Ph.D DEGREE

Innovation Science and Technologies

Cycle XXXII

TITLE OF THE Ph.D THESIS

Integrate approach to the study of chelating agents for the effects of toxic metal ions

Scientific Disciplinary Sector

CHIM/01

Ph.D Student	Rosita Cappai
Coordinator of the Ph.D Programme	Prof. Roberto Orrù
Supervisor	Prof. Valeria M. Nurchi

Final exam. Academic Year 2018 – 2019
Thesis defence: July 2020 Session

To myself

for never losing the way

A me

per non aver mai perso di vista il mio obiettivo

Acknowledgments

I am most grateful to my research supervisor Professor Valeria Nurchi and Professor Guido Crisponi to believe in me and for their help and guidance in the last years.

I am grateful to Professor Zbignew Sczewczuk for welcoming in his research group, to Remik for his help and to Monika and Professor Piotr Stefanowicz for their big advices and support.

I am most grateful to Professor Chris Orvig for giving me the privilege of joing his group in Vancouver.

I am very grateful to Professor Amelia Santos of Centro de Química Estrutural of Lisbon for giving me the opportunity to work in her lab four years ago when I had still to learn a lot about chemistry and now for our collaboration.

I am thankful to all members of Polish and Canadian research groups.

I am grateful to Joanna for the good moments in the lab and conferences.

I am especially grateful to Magda for our lunches, pizza, coffee and all good moments in Wroclaw and Cagliari as well. I wish a brilliant career to my peptide girl.

I am especially thankful to Marco, Mariangela and Noemi of Studio Bellissimo for our funny moments. I wish you all a lot of success for your scientific careers.

I am grateful to Tom for giving me the opportunity to study his ligands, for being my guide at UBC and for his patience speaking with me.

I am most grateful to Lupe for her help, support and love and for the good moments shared in Vancouver. I know we will meet again guapa.

Finally, I would like to thank my family. This work would have not been possible without the constant support of my parents, Lucia and Giuseppe.

Finally, I would like to thank Giuseppe for always being by my side.

All contributed to make my PhD a great and incredible adventure!!!!!!.

Abstract

Metals are an integral part of many structural and functional components in the body, and the interest on their role in physiological processes, environment and medicine is increasing. Many metal complex are used as metal drugs such as cis-platin for cancer treatment, paramagnetic metal complex as contrast agents for magnetic resonance imaging (MRI); many metal are toxic and metal toxicity may occur due to essential metal overload or exposure to heavy metals from various sources interfering with functions of various organ systems like the central nervous system (CNS), the haematopoietic system, liver, kidneys, etc.

New therapeutic strategies, such as chelation therapy, have been developed based on restoring the normal healthy physiology of the body either by direct administration of essential metals, or by chelating out excess or toxic metals, or using them as carriers for targeted drug delivery, or for tagging biomolecules for diagnostics.

Thermodynamic studies in the characterization of ligands of biomedical interest are crucial in the design of a new drugs.

This thesis is focused on the studies of new molecules that have long been recognized as privileged chelating structures for the design of metal chelating drugs, especially towards hard metal ions, in view of their involvement in metal overload disorders. The approach has been multi-variated, from the chemistry to the biochemistry and biology, which has been possible due to the time spent in others research groups and to the other ones that used to collaborate with us.

Because of my stay (research master thesis) in organic chemistry group at Instituto Superior Tecnico of Lisbon guided by Prof. M. Amelia Santos, three hydroxypyridinones ligands have been synthetized, whose biodistribution studies performed at Centro de Ciencias e Tecnologias Nucleares (C2TN) of Lisbon as well.

In the Research Group of Chemistry and Stereochemistry of Peptides and Protein headed by Prof. Zbigniew Szewczuk at the University of Wroclaw new strategies of synthesis have been

developed involving mimosine peptides derivatives. As opposite to hydroxypyridinones, whose solution equilibria studies have been possible, peptides have been mainly characterized by DFT and biological ones in collaboration with the University of San Sebastian and Cagliari.

In the end, three months of my last year of PhD have been spent in the Medicinal Inorganic Chemistry group at the University of British Columbia (Vancouver) under supervision of Prof. Chris Orvig working on solution studies of radiometal complexes of bisphosphonate-picolinic acid derivatives.

It needs to be tightened up with regard to PhD that it has industrial characterization under that a collaboration with industry is scheduled. At Innovative Materials I could learn about biology field and how to work with cells, particularly our idea was to test hydroxypyrones ligands on proliferation and differentiation of stamina cells. The study is still uncompleted and results about are not shown in the following chapters

This thesis is divided in three chapters:

- **Chapter 1** – **An overview of chelation**

It describes general aspects of chelation therapy, the rule of metal ions in human body and in human diseases.

- **Chapter 2** – **Ligands**

It describes structural and chemical properties of ligands studied and shows NTA(PrHP)3, KC18, KC21, SC and six mimosine-peptides derivatives under focus of this thesis.

- **Chapter 3** – **Experimental: methods**

It describes experimental procedures and techniques applied for thesis's studies.

Keywords

Chelation therapy, stability constants, speciation, metal complexes, ligands, hydroxypyridinones, hydroxypyrones, deferiprone, kojic acid, mimosine, iron, aluminium, copper, zinc, vanadium.

Contents

Chapter 1 – An overview of chelation

Chapter 2 – Ligands

Chapter 3 – Experimental: methods

List of abbreviations

1,2-HP	1-Hydroxy-2-pyridinone
3,2-HP	3-Hydroxy-2-pyridinone
3,4-HP	3-Hydroxy-4-pyridinone
Aβ	β-Amyloid
AD	Alzheimer's disease
BAL	2,3-Dimercaptopropanol, Dimercaprol
BAPTA	1,2-bis(o-aminophenoxy)ethane-N,N,N′,N′-tetraacetic acid
BF	Bifunctional chelator
Bn	Benzyl group
BnCl	Benzyl chloride
BMOV	bis(maltolato)oxovanadium(IV)
Boc	*tert*-butyloxycarbonyl
CcO	c oxidase
CN	Coordination number
CNS	central nervous system
dba	Butylenediamine
DCC	N,N'-dicicloesil carbodiimide
DFO	Desferrioxamine
DFP	Deferiprone
DFT	Density-functional theory
dien	Diethylenetriamine
DMPS	D,L-2,3-Dimercaptopropane-1-sulfonic acid
DMSA	*Meso*-2,3-Dimercaptosuccinic acid

Dpa	propylene diamine
D-pen	D-penicillamine
DTPA	Diethylenetriaminepentaacetic acid
EDPA	N,N′-diacetic-N,N′-di-β-propionic acid
EDTA	ethylenediaminetetraacetic acid
en	Ethylenediamine
EPR	Electron Paramagnetic REsonance
ESI-MS	Electron Spray Ionization Mass Spectrometry
Fmoc	fluorenylmethoxycarbonyl
GLEE	Glass Electrode Evaluation
GSH	Glutathione
HATU	1-[Bis(dimethylamino)methylene]-1H-1,2,3-triazolo[4,5-b]pyridinium 3-oxide hexafluorophosphate
HOBt	Hydroxybenzotriazole
HPLC	High Performance Liquid Chromatograph
HPOs	Hydroxypyrones
HPs	Hydroxypyridinones
HSAB	Hard and Soft Acids and Bases Pearson theory
HSQC	Heteronuclear Single Quantum Coherence
IDA	2,2'-azanediyldiacetic acid
MECAM	(1,3,5-N,N',N''-tris-(2,3-dihydrobenzoyl) triaminomethylbenzene
MIM	Mimosine
NMM	*N*-methylmorpholine
NMR	Nuclear Magnetic Resonance Spectroscopy
NTA	nitriloacetic acid

PET	positron-emission tomography
Phen	Phenylalanine
PyBOP	Benzotriazol-1-yl-oxytripyrrolidinophosphonium hexafluorophosphate
RDA	Recommended Daily Allowance
ROESY	Rotating-frame Nuclear Overhauser Effect Correlation Spectroscopy
ROS	reactive oxygen species
SOD	superoxide dismutase
SPECT	single-photon emission computed tomography
TBTU	2-(1H-Benzotriazole-1-yl)-1,1,3,3-tetramethylaminium tetrafluoroborate
TFA	Trifluoroacetic acid
TOCSY	Total Correlation Spectroscopy
TPEN	N,N,N',N'-tetrakis(2-pyridylmethyl)-ethylenediamine
trien	Triethylenetetramine
TTM	Tetrathiomolybdate
Tyr	Tyrosine
T3P	propylphosphonic anhydride
VO-MPA	bis(methylpicolinato)oxovanadium(IV)
VPA	oxobis(picolinato)vanadium(IV)
WD	Wilson's disease

List of figures

Chapter 1 – An overview of chelation

Chapter 2 – Ligands

Chapter 3 – Experimental: methods

List of tables

Chapter 3 – Experimental: methods

List of publications

This thesis is based on the following published papers:

I. R. Cappai, K. Chand, J. I. Lachowicz, S. Chaves, L. Gano, G. Crisponi, V. M. Nurchi, M. Peana, M. A. Zoroddu, M. A. Santos, A new tripodal-3-hydroxy-pyridinone for iron and aluminium sequestration: synthesis, complexation and in vivo studies, *New. J. Chem.*, **2018**, *42*, 8050-8061.

II. V.M. Nurchi, R. Cappai, K. Chand, S. Chaves, L. Gano, G. Crisponi, M. Peana, M. Zoroddu, M. A. Santos, New strong extrafunctionalizable tris(3,4-HP) and bis(3,4-HP) metal sequestering agents: synthesis, solution and *in vivo* metal chelation, *Dalton Trans.*, **2019**, *48*, 16197-16183. This article has been selected as cover of the journal.

III. V. M. Nurchi, M. G. Jaraquemada-Pelaez, G. Crisponi, J. I. Lachowicz, R. Cappai, L. Gano, M. A. Santos, A. Melchior, M. Tolazzi, M. Peana, S. Medici, M. A. Zoroddu, A new tripodal kojic acid derivatives for iron sequestration: synthesis, protonation, complex formation studies with Fe^{3+}, Al^{3+}, Cu^{2+} and Zn^{2+}, and *in vivo* bioassays, *J. Inorg. Biochem.*, **2019**, *193*, 152-165.

IV. S. Berto, E. Alladio, P. G. Daniele, E. Laurenti, A. Bono, C. Sgarlata, G. Valora, R. Cappai, J. I. Lachowicz, V. M. Nurchi, Oxovanadium(IV) Coordination Compounds with Kojic Acid Derivatives in Aqueous solution, *Molecules*, **2019**, *24*, 3767-3786.

V. J. I. Lachowicz, G. Dalla Torre, R. Cappai, E. Randaccio, V. M. Nurchi, R. Bachor, Z. Szewczuk, L. Jaremko, M. Jaremko, M. B. Pisano, S. Cosentino, G. Orrù, A. Ibba, J. Mujika, X. Lopez, Metal self-assembly mimosine peptides with enhanced antimicrobial activity: towards a new generation of multitasking chelating agents, *Dalton Trans.*, **2020**, *49*, 2862-2879.

VI.   G. Bjorklund, G. Crisponi, V.M. Nurchi, R. Cappai, A. B. Djordjevic, J. Aaseth, A Review on Coordination Properties of Thiol Containing Chelating Agents Towards Mercury, Cadmium, and Lead, *Molecules*, **2019**, *24*, 3247-3279.

Chapter 1

An overview of chelation

1.1 Essential metals

Since the amount of water is about 60% and 75% in adult and children respectively, the role of metal ions in the human body depends on their features in solution affecting the well-being of humans in various ways.

A metal can lose one or more electrons and exist as a solvated cation (M^{n+}).

According to their physiological behavior, a first classification can be done in essential, inert/non-essential, which show no evident effect, and toxic which may lead deleterious effect even at low concentration (Fig.1.1). The US Agency for Toxic Substances and Disease Registry assembles a list of the substances that can cause the most significant problems to human health for their toxicity and potential for human exposure [1].

Essential metals are in the living matter, take part in human living processes and their reduction can be normalized by proper addition of the element. They include **hydrogen** (10%) and **oxygen** (65%) prevailing in water; **carbon** (18%), the main component of endogenous molecules such as proteins, carbohydrates and fats; **nitrogen** (3%) found in amino acids, proteins and nucleic acids.

The four bulk elements [2]: **potassium** (0.25%), **sodium** (0.15%), **magnesium** (0.05%) and **calcium** (1.5%). K and Na are electrolytes which regulate the amount of water in the body and the transmission of electrical signal in nerves; Mg is the constituent of skeleton and muscles, present in more than 300 metabolic reactions whose crucial species is Mg-ATP complex; Ca is the most abundant component of bone and teeth (totally 1.2 kg body weight) as hydroxyapatite $Ca_5(PO_4)_3(OH)_2$.

Phosphorus (1%), found in the blood, bone but even in ATP, DNA as phosphate $(PO_4)^{3-}$.

Sulfur (0.25%), contained in methionine and cysteine (as thiol group) which has antioxidant properties mainly expressed in the glutathione (GSH).

Selenium (0.000019%), essential for several enzymes but not for plants which do not need for their survival but can absorb it.

Chlorine (0.15%), as chloride anion important for balancing cations such as sodium and potassium.

Iodine (0.000016%), employed in the synthesis of thyroid hormones, thyroxin, and triiodothyronine.

Vanadium certainly essential for some living organism [3] is not considered definitively essential [4] despite of its involvement in human biology.

Chromium (0.0000024%), involved as Cr^{3+} in the regulation of blood glucose, is transported into the cells by interaction, not yet completely understood, with insulin.

Manganese (0.000017%), important for the protection of mitochondria from toxic oxidants.

The four trace elements [2]: **iron** (0.006%), as Fe^{2+} is the main component of the hemoglobin, as Fe^{3+} gets a very high affinity from plasma blood transferrin (session 1.5); **cobalt** (0.0000021%), component of B12 vitamin and important for DNA regulation; **copper** (0.0001%), as electron donor employed in several enzymatic reactions; **zinc** (0.0032%), involved in the organization of tertiary structure of proteins via zinc fingers.

Nickel, like cobalt, appears to be much more extensively utilized by anaerobic bacteria in reaction involving CH_4, CO and H_2.

Molybdenum (0.000013%), important for the transformation of inorganic nitrogen into organic forms.

Tungsten, still considered essential for some organisms, is required as a cofactor in prokaryotic enzymes [5,6]
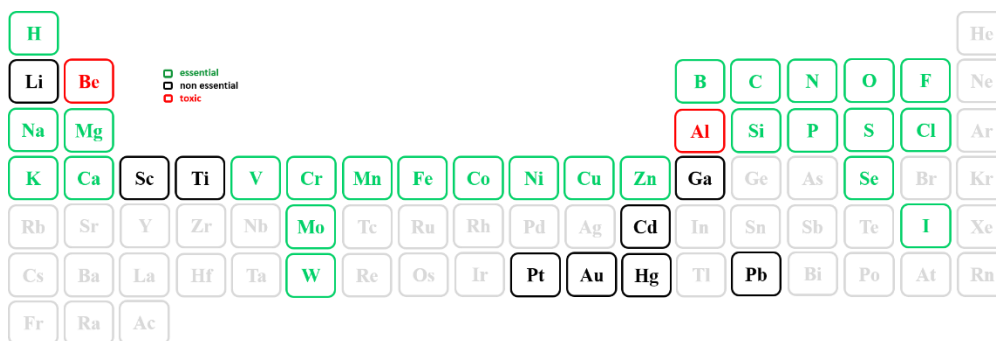
Figure 1.1 *Representation of essential, non-essential and toxic metal ions in the periodic table*

It has to be taken into account that compounds considered toxic can have therapeutic effects in low concentrations, and essential metal in high concentrations can work as toxic as well

as shown in Bertrand diagram (Fig.1.2). Therefore, about metal toxicity, concentration range, speciation form, oxidation state are factors to be considered.
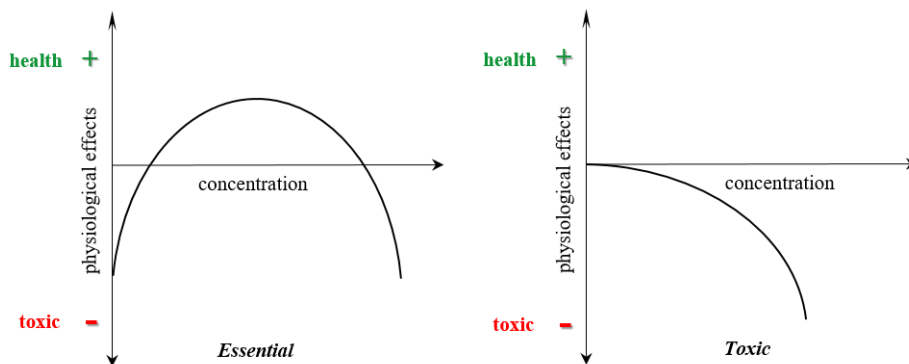
Figure 1.2 *Bertrand diagram*

1.2 Metal intoxication

Nowdays, in the general environment of the modern society, the human exposure to metal ions is increasing and predominantly through food, water, beverages, medicine, cosmetics and so on. Three different categories of metal toxicity can be described:

- **Ingestion and inhalation**

Short-term ingestion can be accidental, as happens to the children, or caused rarely by voluntary episode such as suicide or homicidal involving gastrointestinal and cardio-nervous systems. Long-term ingestion can be done by the accumulation of metals, such as arsenic, with cumulative properties in food or drink involving any organ systems. For instance, $HgCl_2$ salt ingestion intakes kidney [7].

Short-term inhalation is related to environment and occupation giving acute respiratory effects. An example of long-term inhalation may be smoking cigarettes.

- **Chronic intoxication**

It can be caused by environmental and occupational factors.

For instance, occupational Hg exposure in the chloralkali industry (if Hg electrodes are used) and in the manufacture of fluorescent lamps and batteries damages the central nervous system. The elementary Hg^0 is converted to the toxic Hg^{2+} that bind and intoxicate protein thiol groups.

- **Metal overload due to genetic diseases**

Once absorbed, enter the blood through blood cells or plasma proteins such as transferrin and distributed to the body. Their excretion involves gastrointestinal trait due to high capacity of liver and kidney to bind metals [8,9].

The most important ligands historically used in attempts to reduce the body load of toxic metals from the last century are shown in Fig. 1.3.

British Anti Lewisite (**BAL**), synthesized on 1940 at Oxford by Sir Rudolph Peters, was the first antidote for arsenic and lead intoxication though declared to the scientific community only after the end of the second world war [10,11,12].

Ethylenediaminetetraacetic acid (**EDTA**) and diethylenetriaminepentaacetic acid (**DTPA**) were used for the treatment of lead intoxication. Toxic effects can arise from their ability to sequester essential metal ions such as Cu^{2+} and Zn^{2+}. In the 1960s meso-2,3-dimercaptosuccinic acid (**DMSA**) and D,L-2,3-dimercaptopropane-1-sulfonic acid **(DMPS)**, both with a low toxicity and far fewer side effects, had ruled out the clinical uses of BAL [13,14].

In 1968 Peisac and Blumberg proposed the mechanism of reductive chelation to explain that the properties of **D-Penicillamine** (**D-pen**) alone cannot be responsible for the mobilization of copper in Wilson's diseases. **Deferoxamine (DFO)**, commonly named **Desferal**, was initially used in the treatment of iron poisoning and then introduced in the treatment of thalassemia, administered intravenously because of its molecular weight which excludes any oral administration. The first oral iron chelator is **Deferiprone** (**DFP**) considered a suitable alternative to Desferal in the transfusional iron overload; from 2005 the second oral iron chelator in clinical use is **Exjade**.

BAL   **DMSA**   **DMPS**

EDTA   **DTPA**

D-penicillamine   **Exjade**   **Deferiprone**

Desferal
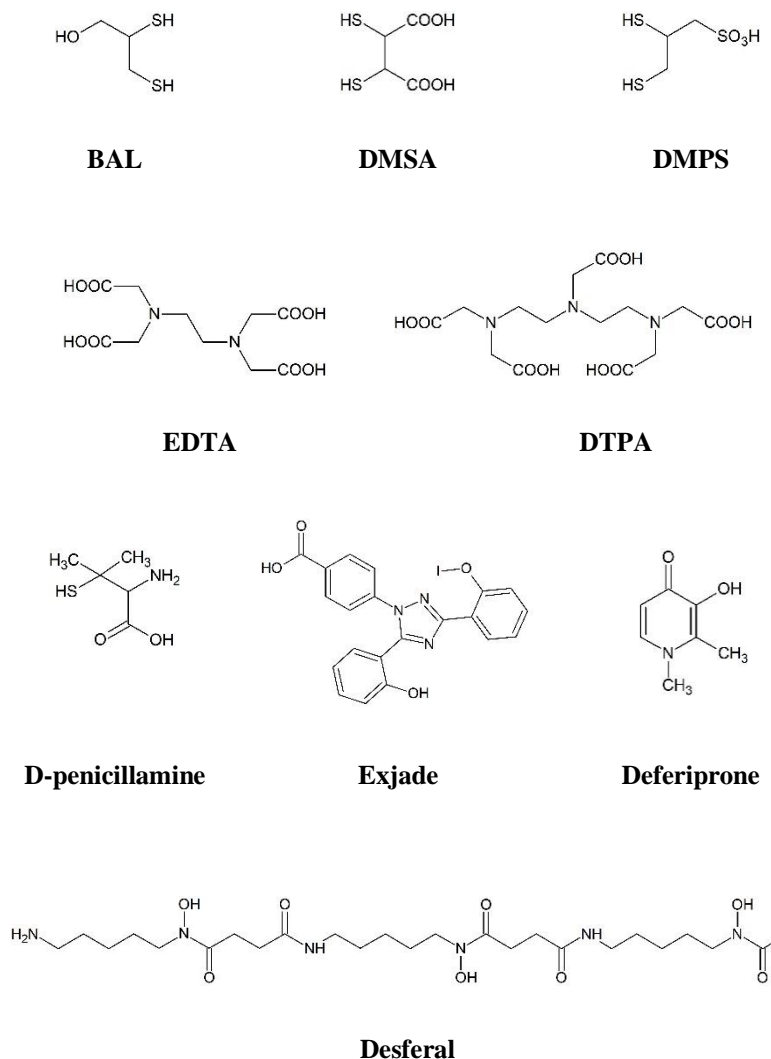
Figure 1.3 Most important ligands historically used in the treatment of toxic metal ions

1.3 Chelating agents

Chelation comes from a Greek word "chele", claw of a lobster, depicting the concept of clinging or holding with a strong grip. Although the first concept of coordination chemistry was born with A. Werner with the idea of coordination numbers (CN) and metal complexes geometry. The term "chelate" was first applied in 1920 to indicate groups which function as two associating units and fasten to a central atom to produce heterocyclic rings [15]. The ring

size, the number of rings formed with a given metal ion and stabilizing or interfering resonance interactions are governed by the structure of the chelating agent, organic or inorganic compounds with ligand binding atoms mainly like S, N and O in chemical groups like those in Table 1.1.

Table 1.1 *Principal chelating donor groups*

Principal Chelating Donor Groups			
$R-NH_2$	Primary amino	R_1-S-R_2	Thioether
R_1 NH R_2	Secondary amino	R_1 R_2 =O R_1 R_2 =S	Keto / Thioketo
R_1 R_2-N R_3	Tertiary amino	$R-O^-$ $R-S^-$	Hydroxylate, Thioalcoholate
R_1 R_2 =NOH	Oxime	$R-COO^-$	Carboxylate
R_1 R_2 =NH	Imino	$R-P(=O)(OH)-O^-$	Phosphonate
R_1 R_2 =NR	Substituted imino	$R-S(=O)(=O)-O^-$	Sulphonate

Chelation therapy acts to eliminate a toxic metal ion from the organism, or to attenuate it toxicity by transforming it in a less toxic compound or by dislocating it from the place where the toxic action is exerted [16].

In the body fluids, metal ions are exposed to the interaction with natural ligands employed in the metabolic functions. A ligand designed to remove a specific metal ion must fulfil certain requirements:

- Low toxicity of both chelator and formed metal complex
- High water solubility
- Selectivity. The ligand must be directed to the target metal ion without any interference from other metal ions naturally present.

- Stability. The chemical affinity between ligand and metal ions must be higher than that with endogenous natural ligands.
- Rapid elimination. The complex must be eliminated without carrying the undesired species to other organs.

However, many complexes with all features described above cannot be used in biological systems because they do not meet other biological requirements such as bioavailability, absorption and membrane permeability. An example is the catechol group not used for the iron removal due to the its toxicity, while Desferal with a lower affinity for Fe^{3+} is more effective and currently employed in the treatment of iron overload.

Molecular size, lipophilicity and charge should be taken into account in the consideration of diffusion through cell membranes: metal ions which can cross blood brain barrier could damage neurological system.

Lipinski et al., in 1997, in a paper entitled *Experimental and computational approaches to estimate solubility and permeability in drug discovery and development settings* [17] analyzed a set of orally delivered drugs and clinical candidates, and defined cut offs that were separately chosen to capture ~ 90% of the ranges for four calculated properties. They proposed *Rule of 5* (Ro5) guidelines and suggested that molecules whose properties fell outside these boundaries would be less likely to be orally absorbed [18].

- Molecular weight < 500 g/mol
- Log P < 5 (with P being the octanol-water partition coefficient)
- Number of hydrogen bond donors ≤ 5
- Number of hydrogen bond acceptors ≥ 10

1.3.1 Chelate effect: a thermodynamic aspect

From the thermodynamic aspect both enthalpy and the entropy can be considered involved in the complex formation in solution. It is known that the equilibrium constants for complex formation reactions

$$M(aq) + L(aq) = ML(aq) \qquad\qquad (1.1)$$

are larger for polydentate ligands than monodentate ones as result of a different number of water molecules "released" from the first coordination sphere as shown in eq 1.2

$$M(H_2O)_x + L(H_2O)_y = ML(H_2O)_z + (x + y - z)H_2O \qquad\qquad (1.2)$$
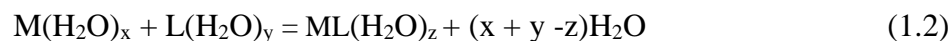
Therefore, multidentate ligands form more stable complexes than monodentate ones following the trend

monodentate < bidentate < tridentate…< hexadentate
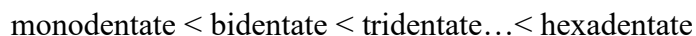
due to the fully available entropy contribution from solvation.
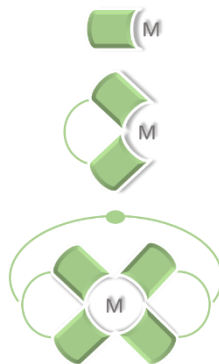
Figure 1.4 Metal complex formation with -mono, -bi and polydentate ligands

In Table 1.2 Cu^{2+} complex formation constants (log β) with ethylenediamine (en), diethylenetriamine (dien) and triethylenetetramine (trien) complexes are reported [19].

Table 1.2 *Complex formation constants of Cu^{2+}-en, Cu^{2+}-dien and Cu^{2+}-trien*

	log β		
Model	**en**	**Dien**	**trien**
denticity	**2**	**3**	**4**
MLH	-	-	23.4 (1)
ML	10.48 (2)	16.15 (4)	20.3 (1)
MLH$_{-1}$	-	6.47 (6)	-
ML$_2$	19.43 (3)	22.23 (8)	-

The increase of log β with increasing denticity gives evidence of the chelate effect. Generally, hexadentate ligands form only one kind of complex and they are preferred, meanwhile ligands with lower denticity can form different kind of complexes depending on total ligand concentration and metal/ligand ratio.

Effectively, the real blooming of coordination chemistry has been achieved, in the 1950's, by Bjerrum and Schwarzenbach with the recognition of chelate effect [20,21] defined as the logarithm to the equilibrium constant for a reaction where *i* independent donors are exchanged by *i* identical donors present in one ligand, thereby expressing the increased stability of the chelates as related to the free energy of the reaction

$$\text{Chelate effect} = \log K_{chel} - \log \beta_2 \tag{1.3}$$

Since it is no possible to determine the stoichiometric coefficients *x*, *y*, and *z* of eq. 1.2, experimentally, a quantitative measure of chelate effect based on $\log \beta_2$ and $\log K_{chel}$ has been proposed for the reactions

$$M(aq) + 2L(aq) = ML_2(aq) \tag{1.4}$$

$$M(aq) + chel(aq) = M(chel)(aq) \tag{1.5}$$
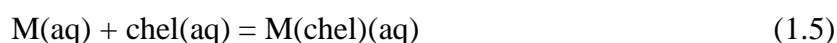
where L is a monodentate and "chel" is a bidentate ligand (L∩L) with the same donor atoms. The complex stability depends on

$$\Delta G = \Delta H - T\Delta S = -RT \ln\beta_i \qquad (1.6)$$

If in a complex i ligands are not associated in one molecule, the enthalpy variation related to bonding often contributes considerably to the free energy, because the unfavorable change in entropy associated with ordering i independent ligands around one ion counteracts the entropy effect of unsolvated groups.

If it is assumed that the enthalpic variation due to the complex formation does not depend on whether the donor groups are independent or joined in a polydentate ligand, the chelate effect should be entirely due to the entropy change. The entropy contribution is often the principal component of increased stability of metal complexes with polydentate ligands, but it is not only given by translation contribution but also by rotation and vibration ones. Preorganization of the ligand involves the freedom of motion of the ligand which increases with entropy: highly preorganized ligand (for example macrocycles) has low entropy because it is approximately in the conformation that exists in the metal complex that is to be formed. However, the enthalpy of reaction can give a contribution to the Gibbs free energy of reaction in complex formation reactions: enthalpy play in the formation of the coordinate bond, which includes both the covalent tendency of the metal ion and of the ligand, as well as the charge neutralization that occurs when they combine [22]. Concentration also contributes to the stability of the complex, especially at low ligand concentration chelates are far more stable than corresponding complexes with monodentate ligands [23].

$$[Cu(H_2O)_6]^{2+} + en \leftrightarrow [Cu(H_2O)_4(en)]^{2+} + 2\ H_2O \qquad \log K_1 = 10.6$$

$$\Delta H^0 = -540\ kJ\ /\ mol \quad \Delta S^0 = +\ 23\ J\ /\ Kmol$$

$$[Cu(H_2O)_6]^{2+} + 2NH_3 \leftrightarrow [Cu(H_2O)_4(NH_3)_2]^{2+} + 2\ H_2O \qquad \log \beta_2 = 7.7$$
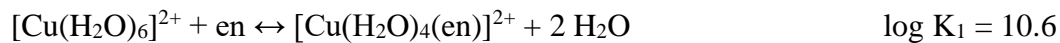
$$\Delta H^0 = -46\ kJ\ /\ mol \quad \Delta S^0 = -\ 8.4\ J\ /\ Kmol$$

Two similar Cu-N bonds are formed in both cases, yet the formation of the chelate is distinctly more favorable. The chelate effect can be traced primarily to differences in reaction entropies between chelated and nonchelated complexes in diluted solutions. The chelation reaction results in an increase in the number of independent molecules in solution, but the nonchelating reaction produces no net change. Therefore, the former has more positive entropy change and hence is the more favorable process [24].

1.3.2 Intrinsic basicity and solvation effect

The intrinsic basicity of donor groups may influence the stability of complexes. For instance, trimethylamine and ammonia in water have similar pKa but they influence differently the complex formation because their intrinsic basicity is masked by solvation effect. The ammonium ion is stabilized by hydrogen bond with the solvent while in trimethylamine the metal groups cannot hydrogen bond to the solvent and exert steric effects on the $(CH_3)_3N^+H$ group formed on protonation and destabilizes its hydrogen bond to the solvent.

Theoretically, the methylation of donor atom may be considered to increase a basicity and the binding strength in the combination with a metal ion due to the increase in the inductive electron release by the methyl group. Then, trimethylamine would be a better donor for metal complex formation than ammonia. However, this does not occur in water because of the steric repulsion of methyl groups for each other and because they break up the hydrogen bond which stabilizes the ammonia complex because the methyl groups do not hydrogen bond with the solvent. On the other hand, the steric repulsions are minimized in the ethylenediamine where the alkyl groups act as bridge groups and their interference with solvation of the metal complex is minimized [25].

1.4 Hard and Soft Acid and Base theory of Pearson (HSAB)

As mentioned in section 1.3, in the design of a proper chelating agents several properties have to be considered, for example the stability and selectivity which depend on the hard/soft behavior both of the ligand coordinating groups and of the metal ion.

In 1923 G. N. Lewis gave a definition of acids and bases by which an acid is an electron-pair acceptor (Lewis acid) and a base is an electron-pair donor (Lewis base)

According to the Hard and Soft Acid and Base (HSAB) theory of Pearson, metal ions are classified in soft and hard [26,27] (Table 1.3) specifically how easily their available orbitals can accept electron density. For a proper interaction, both coordinating molecules (electron donors) and metal ions (electron acceptor) are similar in hardness and softness: large and polarizable ions that prefers large and polarizable ligands and smaller and less polarizable ones that prefer smaller and less polarizable ligands. Therefore, soft metal ions prefer soft ligands and hard metal ions prefer hard metal ions.

Table 1.3 *Metal ions classification according to HSAB*

Acids		
Hard	*Borderline*	*Soft*
H^+, Li^+, Na^+, K^+, Be^{2+}, Mg^{2+}, Ca^{2+}, Sr^{2+}, Ba^{2+}, Al^{3+}, Sc^{3+}, Ga^{3+}, In^{3+}, La^{3+}, Ga^{3+}, Gd^{3+}, Lu^{3+}, Cr^{3+}, Co^{3+}, Fe^{3+}, As^{3+}, Si^{4+}, Ti^{4+}, Zr^{4+}, Hf^{4+}, Th^{4+}, U^{4+}, Pu^{4+}, Ce^{4+}, WO^{4+}, Sn^{4+}, UO^{2+}, VO^{2+}, MoO^{3+}	Fe^{2+}, Co^{2+}, Ni^{2+}, Cu^{2+}, Zn^{2+}, Pb^{2+}, Sn^{2+}, Sb^{3+}, Bi^{3+}, Rh^{3+}, Ir^{3+}	Cu^+, Ag^+, Au^+, Ti^+, Hg^+, Pd^{2+}, Cd^{2+}, Pt^{2+}, Hg^{2+}, Pt^{4+}, Te^{4+}, Br^+, I^+

Bases		
Hard	*Borderline*	*Soft*
H_2O, OH^-, F^-, $CH_3CO_2^-$, PO_4^{3-}, SO_4^{2-}, Cl, CO_3^{2-}, ClO_4^-, NO_3^-, RO^-, NH_3, RNH_2, NH_2NH_2	$C_5H_5NH_2$, C_5H_5N, N_3^-, Br^-, NO_2^-, N_2, SO_3^{2-}	R_2S, RSH, RS^-, I^-, SCN^-, $S_2O_3^{2-}$, CO, CN^-, C_2H_4, R^-, H^-

1.5 Iron

Iron (Fe), atomic number 26, group 8, is the fourth most abundant metal in the earth's crust. It is an essential element for life and plays an important role in many biological processes such as energy generation, DNA synthesis and particularly in hemoglobin which absorbs oxygen and distributes it to the tissues. Table 1.4 shows iron distribution among the various chemical species in human beings [28]. Non-heme iron is stored by ferritin and transferred by transferrin both non saturated with Fe^{3+}.

Table 1.4 Iron distribution in the human body

Compartment	%
Haemoglobin	67.6
Myoglobin	4.1
Transferrin	0.8
Ferritin tissue and serum	27.0, 0.002
Enzymes	0.5

It exists in aerobic aqueous solution primarily as insoluble hydroxides, making its acquisition difficult for microorganisms. To overcome this challenge, many microorganisms secrete low molecular weight iron chelators called siderophores. After sequestering available iron, the ferric complex is incorporated into the cell, and iron is released from the siderophore by reduction of the iron or hydrolysis of the siderophore [29].

The dependence of life upon this transition metal is due to its redox chemistry. Iron exists in two distinct oxidation states, ferrous Fe^{2+} and ferric Fe^{3+} ones, being able to act as an electron donor and acceptor. However, such redox activity can generate reactive oxygen species (ROS) capable of causing a wide range of biological injury. Fe^{3+} is the relatively biologically inactive form of iron, however, it can be reduced to the active Fe^{2+}, depending on the conditions, particularly pH [30], and oxidized back through Fenton type reactions (eq.1.7), with production of hydroxyl radicals; free radicals and other strongly oxidizing species may react with endogenous molecules such as lipids and proteins causing a wide range of

biological injury. Its participation in the oxidation-reduction process is known as the Haber-Weiss reaction (eq.1.9) in which iron catalyzes the hydrogen peroxide reaction to form hydroxyl radical and anion [31,32, 33].

$$Fe^{3+} + O_2^{\cdot-} \rightarrow Fe^{2+} + O_2 \tag{1.7}$$

$$Fe^{2+} + H_2O_2 \rightarrow Fe^{3+} + OH^{\cdot} + OH^{-} \tag{1.8}$$

$$O_2^{\cdot-} + H_2O_2 \rightarrow O_2 + OH^{\cdot} + OH^{-} \tag{1.9}$$

Iron coordination number is 6 associated with octahedral geometry for both Fe^{2+} and Fe^{3+}. It is also possible CN 4 and 5 associated respectively with tetrahedral and trigonal bipyramidal or square pyramidal geometries [2].

1.5.1 Iron disorders

Even if iron is required for a variety of cellular processes, a balance between iron uptake, usage, and storage must be maintained. Despite of that, abnormalities of iron status may occur. Iron deficiency is one of the most common human disorders. *Anaemia* is a decrease in the total amount of red blood cells or hemoglobin in the blood affecting approximately 30% of the world's population, of all ages and sexes, mainly those with inadequate dietary, rapid growth, blood loss or pregnant women owing to increased iron requirements by the foetus [34].

In contrast to iron deficiency, iron overload can occur since there is no physiological mechanism for iron elimination; This is less common but with more toxic side effects and higher mortality rates in humans. In fact, iron overload is the most common metal overload toxicity condition with the highest mortality rate worldwide.

The main causes are genetic defects of increased iron absorption, e.g., idiopathic hemochromatosis, red blood cell transfusions, e.g., thalassaemia. [31,35].

Thalassaemia is due to the absent or defective production of globin chains (α, β, γ, δ) in human hemoglobin. Depending on the type of globin involved, two varieties of thalassemia

can be distinguished, the β - and α –thalassemia respectively. β-thalassemia represents a significant health problem in many areas of the world, mainly in the South East Asia and in the Mediterranean area. Sardinia, Sicily and swampy areas on the Po river are the most affected regions where in the past the natural selection has favoured the survival of people with the mutated gene that causes the malaria disease [28].
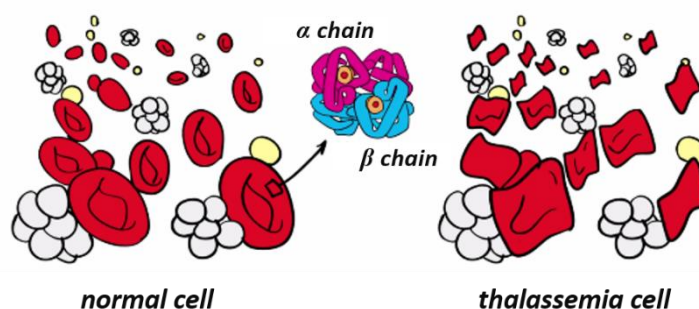
Figure 1.5 *Thalassemia, inherited blood disorder*

The first step in treatment of β-thalassemia involves repeated blood transfusions to reverse the anemic state, and this, in combination with iron absorption from the gastrointestinal tract, leads to iron overload.

1.5.2 Iron chelators

Fe^{3+} is a spherically symmetrical trivalent cation of radius 0.65 Å and classified as a hard Lewis acid. Its preferred CN is 6, producing octahedral complexes. It forms stable bonds with hard ligands (briefly shown in Fig. 1.6) which contain oxyanions as functional groups, such as

- **Catechols**

The strong interaction with Fe^{3+} is due to the high electron density of both oxygen atoms. The complexes forming at pH 7.0 bear a net charge and consequently are unlikely to permeate membranes by simple diffusion. Bidentate catechols form with Fe^{3+} 2:1 complex where iron

atom being not completely protected from the solvent is able to interact with hydrogen peroxide and oxygen to produce free radicals.

The functional cathecol group is found in Enterobactin (found in Gram-negative bacteria such as *Escherichia coli*) a siderophore that binds iron for microbial systems [29].

MECAM (1,3,5-N,N',N''-tris-(2,3-dihydrobenzoyl) triaminomethylbenzene, is one of the molecules synthesized in order to mimic the natural siderophore molecule.

- **Hydroxamates**

Hydroxamates have a lower affinity for iron than catechols, but they form neutral 1:3 metal/ligand complexes at pH 7.4 which are able to permeate membranes by non-facilitated diffusion. Nevertheless, only tetradentate and hexadentate ligands are considered as possible for Fe^{3+} since bidentate hydroxamate ligands, such as L-lysinehydroxamic acid**,** are not strong enough to solubilize Fe^{3+} at pH 7.4 at clinical concentrations. An example of hydroxamate-based hexadentate chelator is Desferal, already shown in Fig. 1.3, isolated from *Streptomyces pilosus*, currently employed in the treatment of β-thalassemia [36,37]. Although Desferal has been available for treating transfusional iron overload from the early 1960s, the era of modern and effective iron-chelating therapy started only 15 years later with the introduction of subcutaneous Desferal infusions by portable pumps [38]. Actually, long-term Desferal therapy is an integral part of the management of thalassaemia and other transfusion-dependent anaemias, with a major impact on wellbeing and survival [39].

- **Aminocarboxylates**

Aminocarboxylates ligands are produced by cereal like wheat, barley, rye, and oat, plants able to secrete phytosiderophores such as mugineic acid, capable of complexing Fe^{3+} and Zn^{2+}. Despite being excellent chelating agents their selectivity is very poor. This lack of selectivity leads to zinc depletion in patients receiving aminocarboxylate based ligands such as EDTA and DTPA [36] shown in Fig. 1.3.

- **Hydroxycarboxylates**

They are more selective for iron than aminocarboxylates since the coordination is only due to oxygen atoms. This family includes rhizoferrin and its precursor citrate [36].

- **Hydroxypyridinones** and **hydroxypyrones**

They will be discussed in detail in Chapter 2.

Cathecol

Enterobactin   **MECAM**
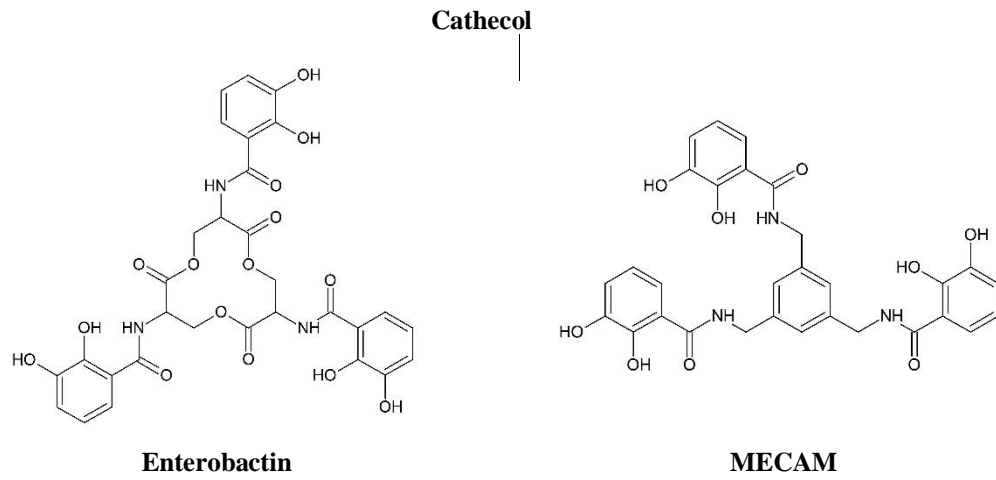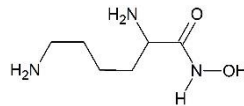
Hydroxamates

L-lysinehydroxamic acid

Aminocarboxylates
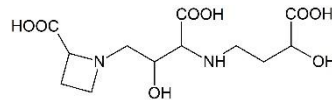
Mugineic acid

Figure 1.6 *Most important iron chelators*

1.6 Aluminium

Aluminium (Al), atomic number 13, group 13, is the most abundant metal in the Earth's crust. It is ubiquitous and although its low bioavailability, it became accessible from diet or environmental exposure. It has been also used in automotive, aeronautic, paper, textile industry, cosmetics and pharmaceutical preparations, veterinary etc. [40,41]. It was only in the 1970s that this metal was suspected to be the cause of different diseases [42].

In water it occurs as solvated ion Al^{3+}, hydrophilic and with a very low ligand exchange rate. Thus, Al^{3+} has a low membrane passage and intestinal absorption; in fact it used in kitchen utensils and in antacids which may occasionally contribute to an income to several g/day apparently without toxic effect. Al^{3+} may form a citrate complex more efficiently absorbed in the intestines than solvated Al^{3+} due to citrated-mediated increased paracellular transport [23]. In spite of that, Al may get in touch with acid solution and accumulate in the organism becoming toxic. For instance, the acidic rain, due sulfur dioxide and nitrogen oxide emission, increases the solubility and the aluminium's bioavailabiliy. CN is 6 associated with octahedral geometry [2].

1.6.1 Aluminium disorders

Actually, aluminium toxicity is associated to several neurodegenerative diseases (Alzheimer and Parkinson), discussed hypothesis and still controversial, but in the past it was associated to haemodialysis treatment. For a long time aluminium contaminated was employed in dialisys, and Al^{3+} accumulated in patients affected by kidney diseases determining osteomalacia and dyalisis dementia. Nowdays the medical technologies have been changed and the use of reverse-osmosis treated water avoids aluminium related problems in haemodialysis patients [23,43].

Alzheimer's disease Alzheimer's disease (AD), described as peculiar disease of cerebral cortex [44], affects more than 25 million people worldwide. It is characterized by extracellular deposition of the β-amyloid peptide (Aβ) and consequent cognitive deficits including memory loss linked with the neuron breakdown and death. However, the role

played by aluminium as well as other elements, e.g. iron, either in the aetiology or pathogenesis of the development of this disease remains unclear [45]. Particularly, some researches posit that aluminium is linked to amyloid deposition both *in vitro* and *in vivo* and X-ray studies give evidence of aluminium accumulation in the neurons since 1980. It is generally accepted that Al^{3+} is neurotoxic, causes lesions in the brain although there is no proved connection with AD's progression [46].

1.6.2 Aluminium chelators

Al^{3+} is trivalent cation of radius 0.54 Å classified as hard Lewis acid. Its preferred coordination number is 6, producing octahedral complexes. It is highly electropositive and not easily polarized. Aluminum-ligand binding is a non-covalent interaction, generally involving ionic or electrostatic bonds [47].

Similar to Fe^{3+} due to the short ionic radius and to the high charge, both they bind to the same plasma proteins. Fe-complexes are more stable than Al-complexes due to the ability of iron to fill its 3*d* orbitals during hexadentate complex formation.

There are no specific chelators for Al^{3+} and their development has been influenced by those in iron chelation, which has been much more extensively studied [48].

Aluminium prefers a coordination with hard donor oxygen-based groups with a single negative charge HO^- and RO^- or with even more effective oxide O^{2-}. Thus, the hydroxide ion forms many complexes of Al^{3+}, while the oxide anion, which is more difficult to generate may be found in polymeric hydrolytic species bridging two (or more) Al^{3+} ions [49]. The most employed aluminium chelators are those shown above (Fig. 1.7) as iron chelators such as catecholates (MECAM), hydroxamates (Desferal), hydroxypyrones and hydroxypyridinones, aminocarboxylates (EDTA) but also bisphosphonate [50,51], hydroxypyridinones-bisphoshonate combined [52] and salicylates [53].

O-TRENSOX

TRENCAMS

HP-bisphosphonate

Bisphosphonate

Salicylates
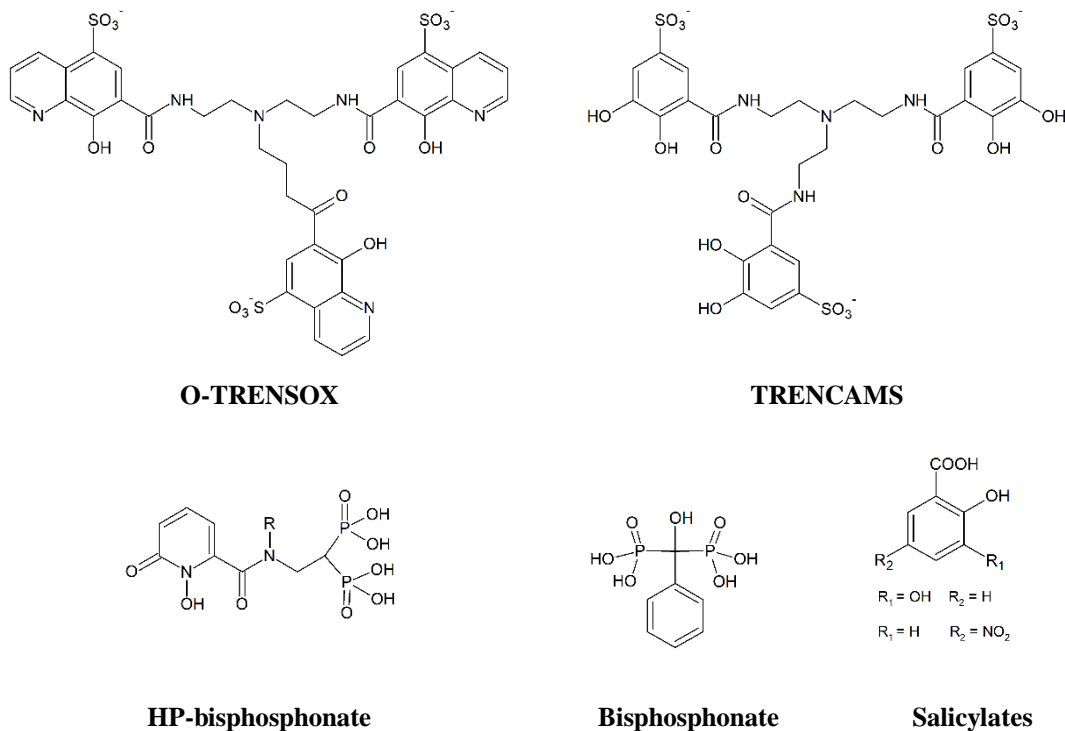
Figure 1.7 Most employed aluminium chelators

O-TRENSOX is found to be slightly more effective than hydroxamate ligand Desferal for the aluminum complexation, while the catecholate ligand TRENCAMS appears the most effective as sequestering agent for Al (pAl 26.2) [54].

1.7 Copper

Copper (Cu), atomic number 29, group 11, is present in different chemical forms throughout the earth crust, in surface and deep water and even, in trace amounts, in the atmosphere [55]. As an essential trace element, it is responsible for several biological functions in human body playing an important role in the development of the brain and nervous system neurotransmitter synthesis. About 70-80 mg of copper are contained in the human body (depending on gender and age) with the highest concentrations in the brain and the liver and

to follow the central nervous system and the heart. About 50% is stored in bones and muscles, 15% in skin, 15% in bone marrow, 8 to 15% in the liver and 8% in the brain [56].

Cu homeostasis is regulated by alterations in both the absorptive efficiency and biliary excretion in the gut [57].

Copper is present in a large number of enzymes, many employed in electron transfer, activation of oxygen such as cytochrome c oxidase (CcO) and superoxide dismutase (SOD), feroxidase, 2-furoate-CoA dehydrogenase, amine oxidase, catechol oxidase, tyrosinase etc.

There are three types of Cu-containing proteins classified on the basis of their visible. UV and EPR spectra as proposed by Bo Malmstrom:

- type 1 (blue proteins) characterized by a single copper atom coordinated by two histidine residues and a cysteine having often methionine
- type 2 characterized by a single copper atom coordinated by N or N/O ligands
- type 3 characterized by a pair of copper centres, each coordinated by three histidine residues with oxygen or hydroxyl anion as a bridge [2].

Copper exists in two oxidation states, Cu^+ and Cu^{2+}, and as with iron, take part in the Fenton reaction: Cu^{2+} in the presence of superoxide anion radical or biological reductants such as ascorbic acid or GSH, can be reduced to Cu^+ which can catalyze the formation of reactive hydroxyl radicals through the decomposition of hydrogen peroxide [58]. The most common coordination number for Cu^{2+} is 4 with square-planar geometry but it may for complexes with CN 5 or 6 [2].

1.7.1 Copper disorders

Since the major way of copper elimination is by biliary excretion, the liver plays a critical role in copper metabolism by regulating biliary copper excretion [59].

Daily copper losses are approximately 1.3 mg/day and in order to preserve copper balance an uptake of 2 mg Cu/day is necessary. It has been assumed that most diets satisfy this requirement because of the presence of copper in most foodstuffs [60]. Even if the main pathologies associated with copper concern its accumulation, there are some diseases due to its deficiency. The most extreme form of Cu deficiency is Menkes disease [61], a

neurodegenerative one involving Cu malabsorption where the transport of copper across the intestinal tract is blocked. It mainly affects children which usually died in the first decade of life [62].

Wilson's disease. Wilson's disease (WD) is a genetic disorder in which excess copper builds up in the body [61]. It may be defined as a disorder due to the inadequate excretion of copper which is not incorporated into its carrier protein (ceruloplasmin) and hence accumulated in the brain, liver, kidneys and cornea. Usually, after an asymptomatic period, hepatic symptoms appear and later neurological ones [63] summarized in Table 1.5 [64].

Table 1.5 *Most common symptoms in WD*

Hepatic	subclinical acute	abnormal liver function test
		mild, self limiting hepatitis
		acute/fulminant liver failure with/without hemodyalisis
	Chronic	active hepatitis with progressive fibrosis
		liver cirrhosis
neurologic	movement and coordination	tremor
		dysphagia, ataxia, rigidity
		concentration and cognitive impairment

1.7.2 Copper chelators

The first Cu^{2+} chelator used in the treatment of WD was BAL (section 1.2 and Fig. 1.8). Given by painful intramuscular injection, it was often associated with fever, leukopenia, haematoma and abscess formation [65]. Alleviation of the painful BAL injections and their associated toxicity became possible with the description by Walshe in 1956 of the potential use of D-pen [66], less toxic and still currently used. Unfortunately, in about 10% of patients, an immunologically induced form of D-pen intolerance develops sooner or later. In 1969 trien had been successful as an alternative orally active chelating agent [67,68].

Tetrathiomolybdate (TTM) because of its rapid action is proving to be a very effective drug for initial treatment of acutely ill Wilson's disease patients [69].

trien   **TTM**
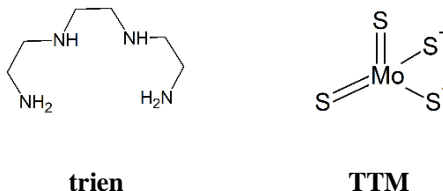
Figure 1.8 Most common copper chelators

1.8 Zinc

Zinc (Zn), atomic number 30, group 12, is the second most abundant trace element in the human body where there are about 3 g. Zinc is in more than 300 enzymes and plays an important role in structure, regulation and catalysis of proteins [70,71]. It is the only metal to have representatives in each of the six fundamental classes of enzymes recognized by the International Union of Biochemistry: oxidoreductase (alcohol dehydrogenase), transferases (RNA polymerase), hydrolases (carboxypeptidase A), lyases (carbonic anhydrase), isomerases (phosphomannose isomerase), ligases (pyruvate carboxylase). Zinc take also part in brain function regulating brain development specially during foetal and early post-natal life [72]. The Recommended Daily Allowance (RDA) of zinc is l5 mg for a male adult, obtained by a balanced diet containing meat and vegetables. However, certain people require more zinc than others; pregnant and lactating women for example, may need as much as 19 mg a day [73].

Zn^{2+} does not have redox reactivity and absorption spectroscopy due to its configuration ([Ar] $3d^{10} 4s^2$]). Coordination number and geometry are due to the ligand size and charge adopting very flexible coordination geometry. Nevertheless, there is a preference for tetrahedral coordination, often distorted, in some proteins [2].

1.8.1 Zinc disorders

The role of zinc in human disorders is related to its interactions with other metal ions (iron and copper) and often with their chelation treatment. Patients receiving regular chelation treatment with Deferiprone for up to one year, showed increased urinary zinc excretion associated with symptoms of dry, itchy, skin patches [74]. Zinc deficiency is an important public health problem identified in mead-eastern countries. It has multiple effects on the immune system such as impaired taste and smell, onset of night blindness dermatitis, diarrhea, alopecia, and mental disturbances. Deregulation of neuronal Zn^{2+} homeostasis has been strongly linked to mitochondrial dysfunction and oxidative stress, making the cation a possible contributor to the activation of patho-physiological pathways involved in brain aging [75].

On the other hand, the exposure to high Zn^{2+} concentrations both *in vitro* and *in vivo* promote neuronal death and elevated neuronal levels are linked to the neuronal loss observed in excitotoxic conditions such as epilepsy, ischemia, and traumatic brain injury [76].

1.8.2 Zinc chelators

Zin chelation has become an important topic in metallo-neurochemistry. To operate effectively, chelators must be specific over other abundant metal ions and cofactors. Intracellular chelators should be neutral and have sufficiently hydrophobic character to diffuse passively across the plasma membrane; extracellular ones generally carry an overall negative charge to minimize translocation across the cell membrane.

The most common intracellular zinc chelator used in zinc metallo-neurochemistry is *N*,*N*,*N*′,*N*′-tetrakis(2-pyridylmethyl)-ethylenediamine (TPEN) employed to study the toxic and neuroprotective effects of zinc chelation. Nevertheless, TPEN binds other transition metals promoting apoptosis.

The most common extracellular zinc chelators nowdays in use in the neuroscience community include EDTA, ethylene glycol-bis(2-aminoethylether)-*N*,*N*,*N*′,*N*′-tetraacetic acid (EGTA), 1,2-bis(*o*-aminophenoxy)ethane-*N*,*N*,*N*′,*N*′-tetraacetic acid (BAPTA), and ethylenediamine-*N*,*N*′-diacetic-*N*,*N*′-di-β-propionic acid (EDPA). Even though the chelators

coordinate zinc tightly and their anionic nature provides an extracellular locale, the high affinity of these chelators for calcium and magnesium render them inappropriate for studying the physiology of zinc [77].

TPEN

EGTA

BATPA

EDPA
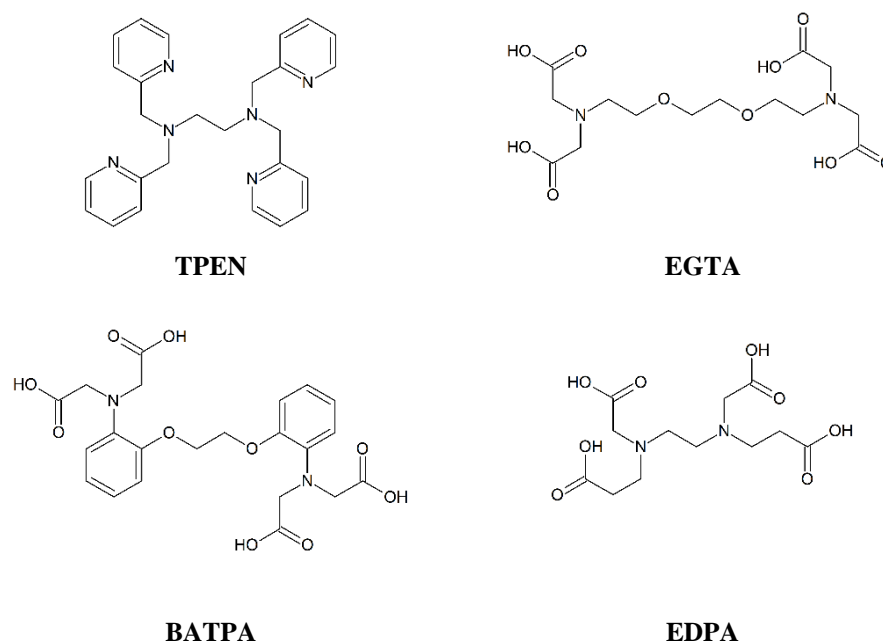
Figure 1.9 *Most common zinc chelators*

1.9 Vanadium

Vanadium, atomic number 23, group 5, is the 21st most abundant element in the Earth's crust and the 2nd most abundant transition metal in sea waters. It is employed in a wide range of alloys in combination with iron, titanium, nickel, aluminium, chromium, and other metals for a diverse range of commercial applications extending from train rails, tool steels, catalysts, to aerospace [78].

Vanadium is present in trace amount in both lithosphere and biosphere, in all mammalian tissues at concentrations of about 10 µM playing a role in the regulation of enzymatic

phosphorylations. It exists in oxidation state from -1 to +5 (most common +3, +4, +5), it is not found in nature as metallic vanadium end it is present mainly in the body as vanadyl ion, VO^{2+}, which may derive from the reduction of V^{5+} by several biological reductants [79]. VO^{2+} has a role in the formation of ROS in Fenton reaction as described for iron and copper. Vanadate, VO_4^{3-}, and vanadyl are inhibitor of certain phosphatase. Much of the biochemistry of vanadium is intricately related to the redox and coordination chemistry of this element. Vanadium can adopt the coordination number from 4 to 8 forming, in ascending order, tetrahedral, tetragonal-pyramidal or trigonal-bipyramidal, octahedral or trigonal-prismatic, pentagonal-bipyramidal or capped trigonal-prismatic and dodecahedra1 (CN = 8) complexes.

1.9.1 Vanadium disorders

Vanadium poisoning is known to occur particularly by exposure, mainly inhalation because of occupational factors, to vanadium compounds such as vanadium oxides with symptoms resemble those of influenza. The bones, liver, and kidneys retain vanadium with a biological half-life of 20-100 h. The excretion takes place mainly through the urine, probably as V^{4+} coordinated to transferrin [80].

Vanadium exerts antitumoral properties through inhibition of cellular tyrosine phosphatases and/or activation of tyrosine phosphorylases; antiproliferative or, in some cases, proliferative effects on various types of cells Vanadium caused also, significant reduction of the tumor cell proliferation; also cytotoxic effects via interactions with DNA.

Diabetes It is characterized by a high concentration of glucose in the blood, which depends on a deficiency of insulin in the human body. Insulin is a hormone secreted in pancreas, normally promotes glucose uptake by the liver and intestine at levels which occur naturally after ingestion of a meal.

Type 1 diabetes goes along with absent or residual insulin supply and concerns children and young people; diabetes type 2 depends on insufficient response of the cellular insulin receptor to insulin and concerns people over 50. Vanadium compounds have been recognized positive in the glucose uptake can be increased by vanadium compounds. Vanadium compounds can

never completely substitute for insulin; however, many of the observed *in vitro* and *in vivo* effects are insulin-like [81,82].

1.9.2 Vanadium chelators

V^{3+}, VO^{2+}, VO^{3+} and VO_2^+ are all classified as hard acids and according to HSAB theory the best chelating ligands are those containing nitrogen and oxygen [5]. Vanadium, specially V^{5+} and V^{4+}, acts in its complexes as both antidiabetes and anticancer, Fig. 1.10. Examples are maltol derivatives which acts an insulin mimetic agents such as bis(maltolato)oxovanadium(IV), (BMOV), oxobis(picolinato)vanadium(IV), (VPA), and bis(methylpicolinato)oxovanadium(IV), (VO-MPA); methoxybenzyl-*cyclo*pentadienil for human kidney cancer cells and *o*-phenanthroline for leukemia and myeoloma ones [81,82].
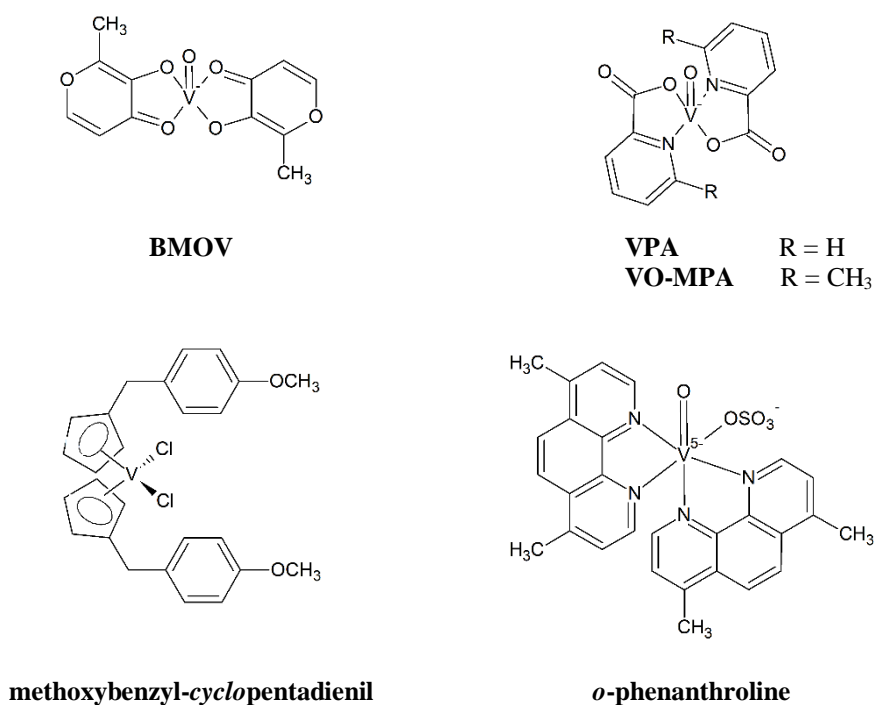

BMOV

VPA   R = H
VO-MPA   R = CH$_3$

methoxybenzyl-*cyclo*pentadienil   ***o*-phenanthroline**

Figure 1.10 *Vanadium chelators and vanadium complexes employed as antidiabetes and anticancer*

1.10 Radiomedicinal chemistry

Nuclear medicine is based on the use of radioactive nuclides for diagnostic and therapeutic purposes. The main clinical use concerns positron-emission tomography (PET) or single-photon emission computed tomography (SPECT) giving a representation of drug distribution *in vivo* difficult to individuate with conventional imaging techniques (MRI, X-ray).

Biological and radioactive drugs are often composed by bifunctional chelators (BFCs), with the aim to make strong complexes and not leave free metal ions *in vivo* [83]. In Fig. 1.11 potential applications of each element in diagnostic and/or therapeutic radiopharmaceuticals are shown [84].

In our research particular attention has been gone to ^{90}Y (t $_{1/2}$ = 64.0 h); ^{44}Sc (t $_{1/2}$ = 58.6 h); ^{111}In (t $_{1/2}$ = 67.2 h); ^{177}Lu (t $_{1/2}$ = 177.0 h).

Yttrium is predominantly found as Y^{3+} (ionic radius 0.9-1.08 Å) take position in the transition metal session. However, like **scandium**, is considered a rare-earth element and its chemistry, unlike Sc, is very close to one of lanthanides. Its preferred CN is 8. This role out hydrolysis at low pH (pKa = 7.7, $Y^{3+}_{(aq)} \rightarrow YOH^{2+}_{(aq)}$) [84].

Indium is trivalent cation In^{3+} (ionic radius 0.62-0.92 Å) considered a borderline-hard metal (CN = 8), despite of its tendency to form stable complexes with soft donor groups [85]. In water its pKa (pKa = 4.0, $In^{3+}_{(aq)} \rightarrow InOH^{2+}_{(aq)}$) is generally nonproblematic for radiolabeling. It becomes completed saturated with CN 8.

Lutetium, Lu^{3+}, (ionic radius 0.86-1.03 Å) is the smallest of the lanthanide series with CN 8. As Y^{3+} the high pKa (pKa = 7.6, $Lu^{3+}_{(aq)} \rightarrow LuOH^{2+}_{(aq)}$) makes metal hydrolysis nonproblematic during radiolabeling [86].
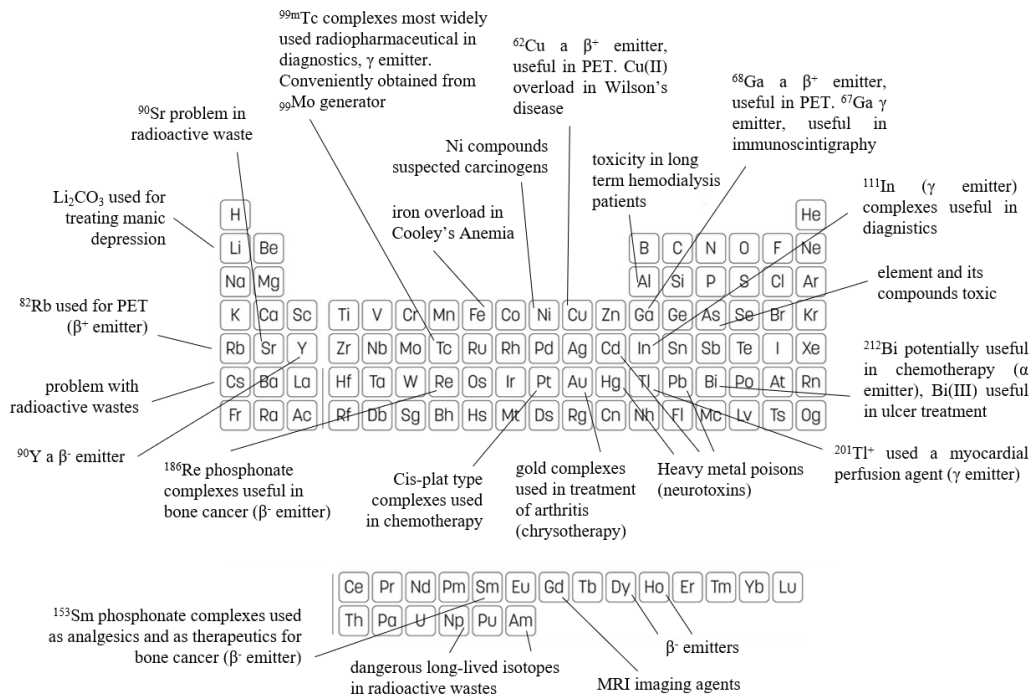
Figure 1.11 *Representation of radiopharmaceutical application/properties in the periodic table*

1.11 References

[1] ATSDR. *ATSDR Substance Priority List*; ATSDR: Atlanta, GA, USA, **2017**

[2] R. R. Crichton, *Biological Inorganic Chemistry-An Introduction*, **2008**, Elsevier

[3] D. C. Crans, J. J. Smee, E. Gaidamauskas, L. Yang, *Chem. Rev*. **2004**, *104*, 849-902

[4] M. A. Zoroddu, J. Aaseth, G. Crisponi S. Medici, M. Peana, V. M. Nurchi, *J. Inorg. Biochem*., **2019**, *195*, 120-129

[5] G. Crisponi, V. M. Nurchi, M. Crespo-Alonso, L. Toso, *Curr. Med. Chem*., **2012**, *19*, 2794-2815

[6] J. Aaseth, G. Crisponi, O. Andersen, *Chelation therapy in the treatment of toxic metal ions*, **2016**, Elsevier

[7] F. P. Brunner, D. de Rougemont, M. Robbiani, H. Seiler, G. Thiel, *Nephron*, **1985**, *41*, 94-99

[8] H.G. Seiler, A. Sigel, H. Sigel, *Handbook on Metals in Clinical and Analytical Chemistry,* **1994,** Mercel Dekker Inc

[9] W. Mertz, *Proc. Nutr. Soc.,* **1974**, *33*, 307-313

[10] M. G. Ord, L. A. Stocken, *Trends Biochem. Sci*., **2000**, *25*, 253-256

[11] R. A. Peters, L. A. Stocken, R. H. S. Thompson, *Nature,* **1945**, *156*, 616-619

[12] H. V. Aposhian, R. M. Maiorino, D. Gonzalez-Ramirez, M. Zuniga-Charles, Z. Xu, K. M. Hurlbut, P. Junco-Munoz, R. C. Dart, M. M. Aposhian, *Toxicology*, **1995**, *97*, 23-38

[13] S. J. S. Flora, V. Pachauri, *Int. J. of Environ. Res. Public Health*, **2010**, *7*, 2745-2788

[14] O. Andersen, J. Aaseth, *Environ. Health Perspect*., **2002**, *110*, S887-S890

[15] G. T. Morgan, H. D. K. Drew, *J. Chem. Soc.* **1920**, *117*, 1456-1465

[16] E. J. Baran, *Curr. Med. Chem*., **2010**, *17*, 3658-3672

[17] C. A. Lipinski, F. Lombardo, B. W. Dominy, P. J. Feeney, *Adv. Drug Deliv. Rev.*, **1997**, *23*, 3-25

[18] M. Q. Zhang, B. Wilkinson, *Curr. Op. Biotech.*, **2007**, *18*, 478-488

[19] V. M. Nurchi, G. Crisponi, G. Sanna, I. Perez-Toro, J. Niclos-Gutierrez, M. J. Gonzalez-Perez, A. Dominguez Martin, *J. Inorg. Biochem.*, **2019**, *194*, 26-33

[20] G. Schwarzenbach, *Adv. Inorg. Radiochem.*, **1961**, *3*, 257

[21] G. Schwarzenbach, *Helv. Chim. Acta*, **1952**, *35*, 2344

[22] V. Vallet, U. Wahlgren, I. Grenthe, *J. Am. Chem. Soc.*, **2003**, *125*, 14941-14950

[23] O. Andersen, *Chem. Rev.* **1999**, *99*, 2683-2710

[24] D. F. Shriver, P. Atkins, C. H. Langford, *Inorganic Chemistry*, 2nd ed., **1994**, Oxford University Press

[25] A. E. Martell, R. D. Hancock, R.J. Motekaitis, *Coord. Chem. Rev.*, **1994**, *133*, 39-65

[26] G. Pearson, *J. Am. Chem. Soc.*, **1963**, *85*, 3533-3539

[27] R. G. Pearson, *J. Chem. Educ.*, **1968**, *45*, 581-587

[28] G. Crisponi, V. M. Nurchi, R. Silvagni, G. Faa, *Polyhedron*, **1999**, *18*, 3219-3226

[29] E. A. Dertz, A. Stintzi, K. N. Raymond, *J. Biol. Inorg. Chem.*, **2006**, *11*, 1087-1097

[30] M. Strlic, T. Radovic, J. Kolar and B. Pihlar, *J. Agric., Food Chem.*, **2002**, *50*, 6313-6317

[31] D. S. Kalinowski, D. R. Richardson, *Pharmacol. Rev.*, **2005**, *57*, 547-583

[32] C. C. Winterbourn, *Toxicol. Lett.*, **1995**, *82/83*, 969-974

[33] M. Andejelkovic, J. V. Camp, B. De Meulenaer, G. Depaemelaere, C. Socaciu, M. Verloo, R. Verhe, *Food Chem.*, **2006**, *98*, 23-31

[34] A. Zu, M. Kaneshiro, J. D. Kaunitz, *Dig Dis Sci,* **2010**, *55*, 548-559

[35] G. J. Kontoghiorghes, *Analyst*, **1995**, *120*, 845-851

[36] Z. D. Liu, R. C. Hider, *Coord. Chem. Rev*., **2002**, *232*, 151-171

[37] G. Faa, G. Crisponi, *Coord. Chem. Rev*., **1999**, *184*, 291-310

[38] M.D.A. Cohen, M.D.E.Schwartz, J. Pediatr., **1978**, *92*, 643-647

[39] C. Hershko, A. M. Konijn, G. Link, *Br. J. Hematol*., **1998**, *101*, 399-406

[40] C. Exley, *J. Inorg. Biochem*., **2003**, *97*, 1-7

[41] S. L. Hem, *Vaccine*, **2002**, *20*, S40-S43

[42] G. Crisponi, V. M. Nurchi, G. Faa, M. Remelli, *Monatsh Chem*., **2011**, *142*, 331-340

[43] D. J. Brown, K. N. Ham, J. K. Dawborn, J. M. Xipell, *The Lancet*, **1982**, *320*, 343-345

[44] R. A. Stelzmann, H. N. Schnitzlein, F. R. Murtagh, *Clin. Anat*., **1995**, *8*, 429-431

[45] R. J. Ward, Y. Zhang, R. R. Crichton, *J. Inorg. Biochem*., **2001**, *87*, 9-14

[46] L. E. Scott, C. Orvig, *Chem. Rev*., **2009**, *109*, 4885-4910

[47] R. A. Yokel, *Coord. Chem*. Rev., **2002**, *228*, 97-113

[48] W. R. Harris, *Clinical Chemistry*, **1992**, *38*, 1809-1818

[49] E. Martell, R. J. Motekaitis, R. M. Smith, *Polyhedron*, **1990**, *9*, 171-187

[50] E. Gumienna-Kontecka, R. Silvagni, R. Lipinski, M. Lecouvey, F. Cesare Marincola, G. Crisponi, V. M. Nurchi, Y. Leroux, H. Kozlowski, *Inorg. Chim. Acta*, **2002**, *339*, 111-118

[51] G. Crisponi, A. Dean, V. Di Marco, J. I. Lachowicz, V. M. Nurchi, M. Remelli, A. Tapparo, *Anal. Bioanal. Chem*., **2013**, *405*, 585-601

[52] T. Bailly, R. Burgada, T. Prangé, M. Lecouvey, *Tetrahedron Lett*., **2003**, *44*, 189-192

[53] S. Giroux, S. Aury, P. Rubini, S. Parant, J. R. Desmurs, M. Dury, *Polyhedron*, **2004**, *23*, 2393-2404

[54] F. Biaso, P. Baret, J. L. Pierre, G. Serratrice, *J. Inorg. Biochem*., **2002**, *89*, 123-130

[55] M. Tegoni, D. Valensin, L. Toso, M. Remelli, *Curr. Med. Chem.*, **2014**, *21*, 3785-3818

[56] M. Angelova, S. Asenova, V. Nedkova, R. Koleva-Kolarova, *Trakia J. Sci.*, **2011**, *9*, 88-98

[57] I. Iakovidis, I. Delimaris, S. M. Piperakis, *Mol. Biol. Int.*, **2011**, 1-14

[58] A. Ahuja, K. Dev, R. S. Tanwar, K. K. Selwal, P. K. Tyagi, *J. Trace Elem. Med. Biol.*, **2015**, *29*, 11-23

[59] M. Patil, K. A. Sheth, A. C. Krishnamurthy, H. Devarbhavi, *J. Clin. Exp. Hepatol.*, **2013**, *3*, 321-336

[60] W. DM, *Semin. Hematol.*, **1983**, *20*, 118-128

[61] N. Horn, L. Birk Møller, V. M. Nurchi, J. Aaseth, *J.Inorg. Biochem.*, **2019**, *190*, 98-112

[62] D. M. Danks, *Ann. Rev. Nutr.*, **1988**, *8*, 235-257

[63] E. A. Roberts, D. W. Cox, *Baillières Clin. Gastroenterol.*, **1998**, *12*, 237-256

[64] D. Huster, *Best Pract. Res. Cl. Ga.*, **2010**, *24*, 531-539

[65] J. M. Walshe, *Q. J. Med.*, **1996**, *89*, 553-555

[66] M. T. Lorincz, *Ann. N. Y. Acad. Sci.*, **2010**, *1184,* 173-187

[67] J. M. Walshe, *The Lancet*, **1982**, *319*, 643-647

[68] Y. Cao, M. A. Skaug, O. Andersen, J. Aaseth, *J. Trace Elem. Med. Bio.*, **2015**, *31*, 188-192

[69] G. J. Brewer, *J. Cell. Mol. Med.* **2003**, *7*, 11-20

[70] P. Chellan, P. J. Sadler, *Phil. Trans. R. Soc.*, **2015**, *373*, 20140182

[71] R. J. Cousins, *Proc. Nutr. Soc.* **1998**, *57*, 307-311

[72] C. T. Chasapis, A. C. Loutsidou, C. A. Spiliopoulou, M. E. Stefanidou. *Arch. Toxicol.*, **2012**, *86*, 521-534

[73] D. Bhowmik, K. P. Chiranjib, S. Kumar, *Int. J. Pharm. Biomed. Sci.* **2010**, *1*, 05-11

[74] G. Crisponi, V. M. Nurchi, M. Crespo-Alonso, G. Sanna, M. A. Zoroddu, G. Alberti, R. Biesuz, *PLoS One*, **2015,** *10*, e0133050

[75] A. H. Shankar, A. S. Prasad, *Am. J. Clin. Nutr*., **1998**, *68*, 447S-63S

[76] V. Frazzini, E. Rockabrand, E. Moccheggiani, S. L. Sensi, *Biogerontology*, **2006**, *7*, 307-314

[77] R. J. Radford, S. J. Lippard, *Curr. Opin. Chem. Biol*., **2013**, *17*, 129-136

[78] R. R. Moskalyk, A. M. Alfantazi, *Miner. Eng*., **2003**, *16*, 793-805

[79] N. D. Chasten, *Copper*, *Molybdenum and Vanadium in Biological Systems*, **1983**, Springer

[80] D. Rehder, *Angew. Chem., Int. Ed. Engl*., **1991**, *30*, 148-167

[81] A. Sigel, H. Sigel, R. K. O. Sigel, *Interrelations between Essential Metal Ions and Human Diseases*, **2013**, Chapter 5 by D. Rehder, Springer

[82] K. H. Thompson, J. H. McNeill, C. Orvig, *Chem. Rev*., **1999**, *99*, 2561-2571

[83] T. I. Kostelnik, C. Orvig, *Chem. Rev.*, **2019**, *119*, 902-956

[84] A. E. Martell, R. D. Hancock, *Metal Complexes in Aqueous Solutions*, **1996**, Springer

[85] Y. Sun, E. A. Martell, R. J. Motekaitis, M. J. Welch., *Tetrahedron*, **1998**, *54*, 4203-421

[86] S. A. Cotton, *Lanthanide and Actinide Chemistry*; **2006**, Wiley

Chapter 2

Ligands

2.1 Hydroxypyridinones

Hydroxypyridinones (HPs) are a family of *N*-hetocyclic chelators with a hydroxyl group in *ortho* to a ketone group. They combine the characteristics of both catechol and hydroxamate groups yielding a five-membered ring chelates in which metal ions is coordinated by two oxygen donor atoms. Due to the high affinity and selectivity for trivalent and hard metal ions, they behave as strong chelators for Fe^{3+} and Al^{3+} HPs [1]. They can be obtained from natural compounds, such as maltol and kojic acid, and easily functionalized for biomedical applications. They have been considered in the design of new pharmaceutical drugs for the treatment of metal overload, neurodegenerative diseases (AD), diabetes, cancer and so on [2] (Fig. 2.1).

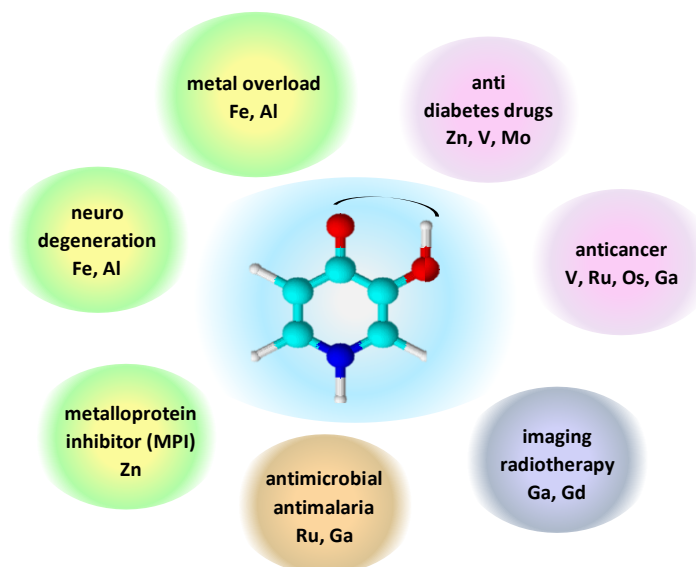**Figure 2.1** *HPs applications*

2.1.1 Bidentate HPs

There are three main HPs sub-groups (Fig. 2.2) such as 1-hydroxy-2-pyridinones (1,2-HPs), 2-hydroxy-3-pyridinones (2,3-HPs) and 3-hydroxy-4-pyridinones (3,4-HPs), all of them very stable at pH 7.4.
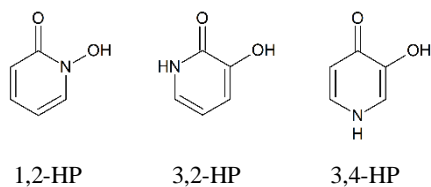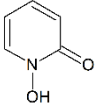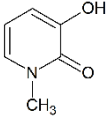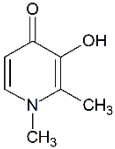
Figure 2.2 *Three main HPs groups*

The 1,2-HPs are typically the most acidic (pKa < 7) and thus better chelators than the 3,2-HPs or the 3,4-HPs in acidic medium. Nevertheless, since they are in the anionic form at the physiological pH, they are quite hydrophilic. At pH 7.4 both 3,2-HPs and 3,4-HPs are neutral ligands and form also neutral 3:1 ligand/metal complexes, important aspect for biological applications. However, 3,4-HPs show the highest basicity (pKa ca. 9.5–9.9) of the hydroxyl group and the highest metal chelating affinity at the physiological pH making them the most studied HPs. The 3,4-HPs are rather stable under biological conditions and easily extra-functionalized, mainly at position 1 (ring-N) but also at C2, C5, and C6 [3].

Table 2.1 *pK$_a$ and pFe values for 1,2-Hs, 3,2-HPs and 3,4-HP*

		pK$_{a1}$	pK$_{a2}$	logβ$_3$	pFe
1-hydroxypyridin-2-one		-	5.8	27	16
1-methyl-3-hydroxypyridin-2-one		0.2	8.6	32	16
1,2-dimethyl-3-hydroxypyridin-4-one (DFP)		3.6	9.9	37.2	20.5

The earliest record of the synthesis of a 3,4-HP dates back to 30s when pyromeconic acid was converted to the 3-hydroxy-1-methylpyridin4-one via Michael addiction reaction [4]. This synthetic approach, including even kojic acid and maltol, has been widely adopted to

prepare a range of 3,4-HPs, for instance DFP [5]. The most important bidentate 3,4-Hp is DFP, clinical chelating agent in the treatment of iron overload since 2000.
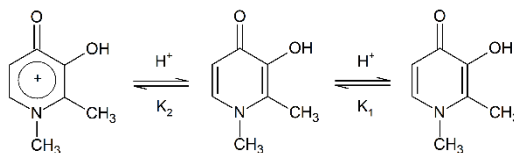
Figure 2.3 *DFP protonation steps*

Different DFP derivatives have been synthesized mainly involving substitutions in positions 1 and 2 with aliphatic and aromatic groups to improve the chelating properties. Both intramolecular hydrogen bond and negative inductive effect, stabilizing the ionized species, lead to a reduction of protonation and iron complex formation constants with hydroxyalkyl substituents in position 2 increasing the corresponding pFe^{3+} values at pH 7.4.

Conversely, the introduction of a hydroxyl function in position 2 does not induce similar effects and instead results in a decrease in lipophilicity as compared to the simple alkyl derivatives. Only a few derivatives with hydrogen in position 1 are known: 5-hydroxy-2-(hydroxymethyl)pyridin-4-one (P1), with its tautomeric forms is one of them. The tautomeric transformation in the presence of metal ions occurs at lower pH than in the free ligand. P1 (pFe 22) should be considered a more efficient iron chelator than DFP because of the higher stability of complex due to tautomers [6].
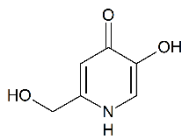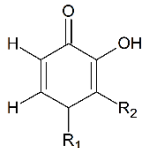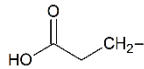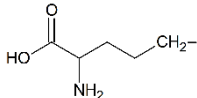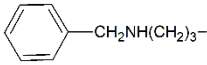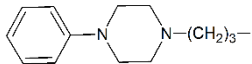
Figure 2.4 *P1. The corresponding HP to kojic acid (see below)*

Unlike formation constants, pM allow directly to compare chemically different ligands. pM = -log $[M]_{free}$ where $[M]_{tot} = 10^{-6}$ M and $[L]_{tot} = 10^{-5}$ M at pH 7.4 [7]. Table 2.2 contains the pM values of some bidentate 3,4-HPs with different N-substituents. In spite of molecular weight of bidentate 3,4-HPs is usually < 500 Da their N-derivatization is helpful to change the lipophilicity, solubility and improve chemical-biological features.

Table 2.2 *Bidentate 3,4-HPs: the effect of different substituents groups on position 1 and 2*

Name	R₁	R₂	pFe	pAl
DFP	CH_3	CH_3	20.7	16.1
CP94	CH_2CH_3	CH_2CH_3	19.7	-
Car-HP		CH_3	21.3	15.0
Orn-HP		CH_3	21.9	15.8
Apb-HP		CH_3	21.0	15.8
Pip-HP		CH_3	17.4	14.6

Based on their pFe and pAl, DFP can only compete for Fe at higher concentration (C = 10^{-3} M) [3].

2.1.2 Tetradentate HPs

In the tetradentate HPs the attachment of two 3,4-HPs chelating moieties allow to increase the metal chelating capacity but also to extra-functionalize the ligand for eventual specific bio-target. Many 3,4-(HP)$_2$ have been synthesized and studied by Prof. Maria Amelia Santos group using polycarboxylic acid as backbone such as *cis*,*cis*-1,3,5-trimethylcyclohexane-1,3,5-tricarboxilicacid (Kemp acid), EDTA, 2,2'-azanediyldiacetic acid (IDA), 2-[bis[2-[bis(carboxymethyl)amino]ethyl]amino]acetic acid (DTPA), nitriloacetic acid (NTA) and nitromethantrispropionic acid for KC21 ligand (paper II).

In Fig. 2.5 KEMP(NPrHP)$_2$ [8]; IDAPr(3,4-HP)$_2$ [9]; EDTAPr(3,4-HP)$_2$ [10,11]; IDAPipPr(3,4HP)$_2$ [12]; DTPA(PrHP)$_2$ [13] and NTA(PrHP)$_2$ [14] are shown. In their iron complexes the metal ion is bis-chelated forming Fe$_2$HxL$_3$ species; being one hydroxyl group a bridge between two metal ions, Fe$_2$(OH)$_2$L$_2$ may be formed.

pFe 20.5   pAl 18.1   pFe 25.8   pAl 18.8

KEMP(NPrHP)$_2$ **IDAPr(3,4-HP)$_2$**

pFe 26.3   pAl 19.0   pFe 25.7   pAl 18.0

EDTAPr(3,4-HP)$_2$ **IDAPipPr(3,4HP)$_2$**

pFe 20.6   pAl 18.2   pFe 23.6   pAl 21.4

DTPA(PrHP)$_2$ **NTA(PrHP)$_2$**
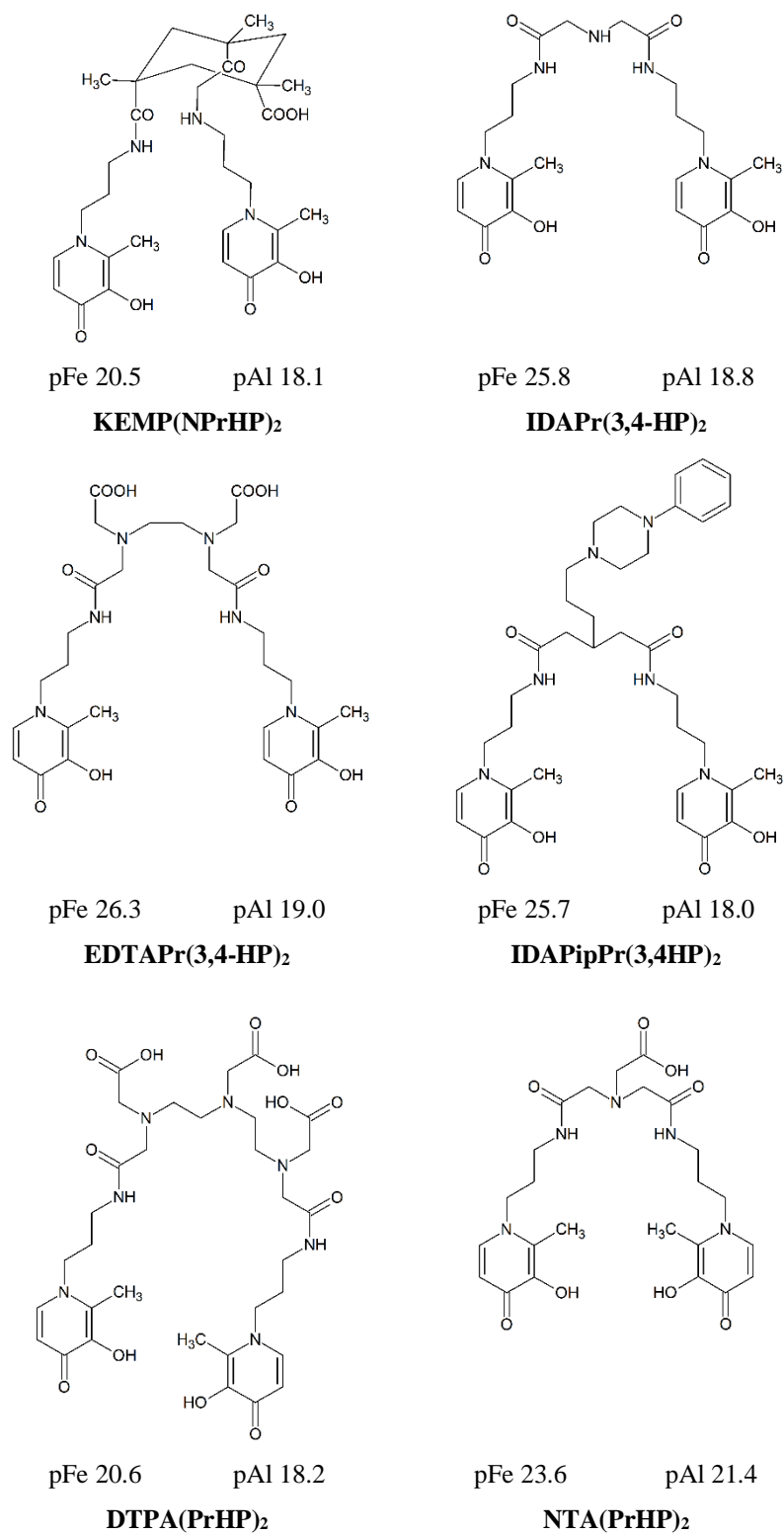
Figure 2.5 *3,4-(HP)$_2$*

4-amino-N^1,N^7-bis(3-(3-hydroxy-2-methyl-4-oxopyridin-1(4*H*)-yl)propyl)-4-(3-((3-(3-hydroxy-2-methyl-4-oxopyridin-1(4*H*)-yl)propyl)amino)-3-oxopropyl)oxohheptaediamide (KC21) is the last tetradentate 3,4-HP synthesized in the present work containing an extra free amino group not involved in the coordination and therefore destinated to future applications. Considering both pFe and pAl it is the strongest bis chelator till now.

KC21

pFe 25.8   pAl 19.1
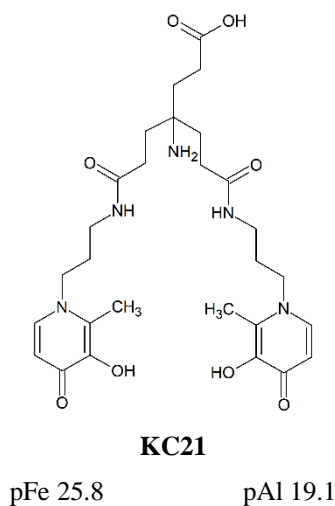
Figure 2.6 KC21. Solution equilibria studies are reported in paper II

2.1.3 Hexadentate HPs

Hexadentate HPs allow fill up the metal coordination sphere forming a 1:1 complex thermodynamically more stable than ones with 3,4-HPs and 3,4-(HP)$_2$.
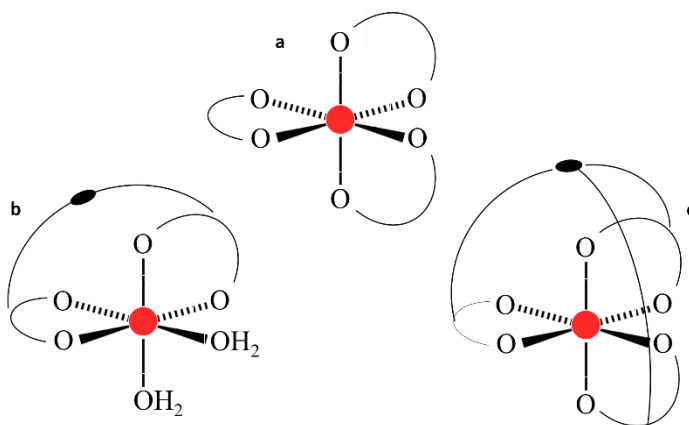
Figure 2.7 *Coordination model for: (a) 1:3 M³⁺-mono HP; (b) 1:1 M³⁺-bis HP; (c) 1:1 M³⁺ tris HP*

The following step of research group mentioned above concerns the synthesis, solution and *in vivo* studies as potential iron and aluminium chelating agents, of hexadentate HPs in which three 3,4-HP-alkylamino arms are attached to cyclic triscarboxylic or aminotriscarboxylic acid backbones: Kemp acid in Kemp(PrHP)₃ and Kemp(BuHP)₃; NTA and nitrilopropionic acid (NTP) in NTA(BuHP)₃ and NTP(BuHP)₃ respectively differing in the peptide bond position and in HP-chains [15,16].

Kemp(PrHP)₃	n = 1	**NTA(BuHP)₃**	p = 1, n = 2
pFe 28.0	pAl 21.2	pFe 27.9	pAl 22.0
Kemp(BuHP)₃	n = 2	**NTP(PrHP)₃**	p = 2, n = 1
pFe 26.8	pAl 21.8	pFe 29.4	pAl 22.4
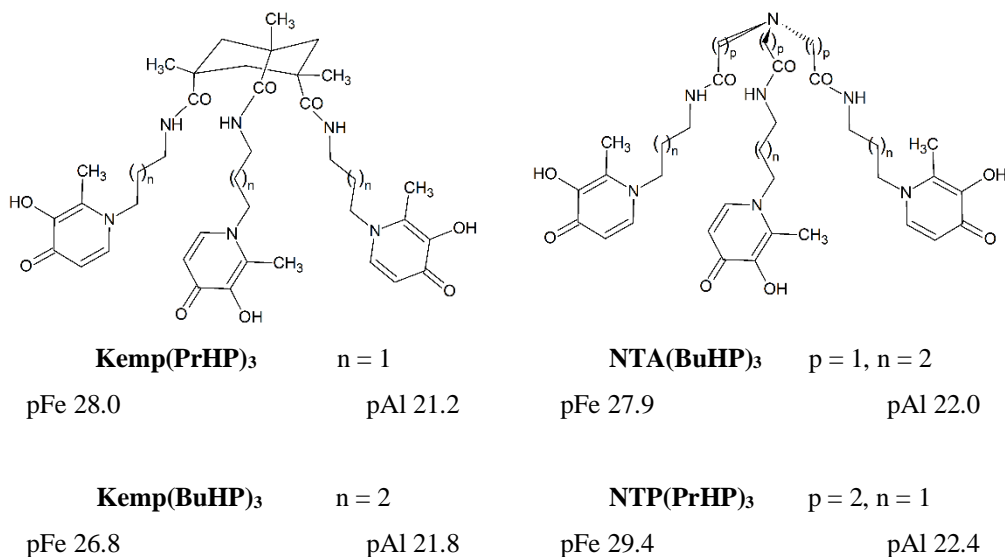
Figure 2.8 *3,4-(HP)₄*

2,2',2''-Nitrilotris(N-(3-(3-hydroxy-2-methyl-4-oxopyridin-1(4*H*)-yl)propyl)acetamide) NTA(PrHP)$_3$ (see paper I) shows a propyl chain between HP unit and peptide bond, and NTA as backbone being between the previous NTA(BuHP)$_3$ and NTP(PrHP)$_3$. The reduced molecular weight may increase membrane crossing ability, however decreasing metal chelation capacity based on pM values.

NTA(PrHP)$_3$ p = 1, n = 3

pFe 26.3   pAl 19.8
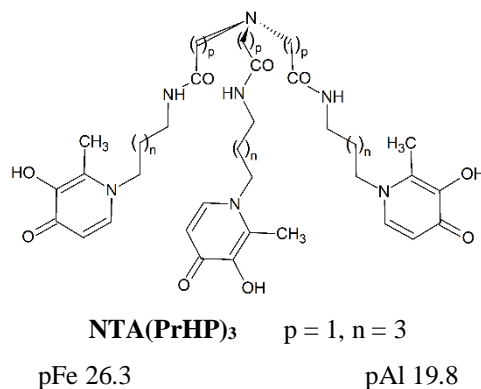
Figure 2.9 *NTA(PrHP)$_3$. Solution equilibria studies are reported in paper I*

4-amino-7-((2-(3-hydroxy-2-methyl-4-oxopyridin-1(4*H*)-yl)propyl)amino)-4-(3-((2-(3-hydroxy-2-methyl-4-oxopyridin-1(4*H*)-yl)propyl)amino)-3oxopropyl)-7-oxoheptanoic acid (KC18) (paper II) is the corresponding tris of KC21. Its pM values make it the strongest hexadentate 3,4-HP synthesized until now not leading to the breakdown of essential zinc (studied as well) showing also an excellent in vivo metal sequestering ability.

KC18

pFe 29.5   pAl 23.8
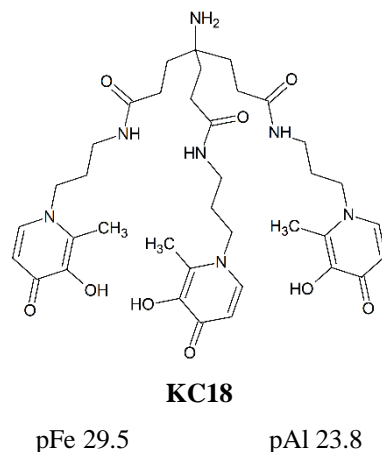
Figure 2.10 *KC18. Solution equilibria studies are reported in paper II*

2.2 Hydroxypyrones

Hydroxypyrones (HPOs) are a family of *O*-heterocyclic compounds with close hydroxyl and ketone groups as oxygen donors like in HPs. They form stable and, in some cases, neutrally charged complexes with several meta ions such as trivalent cations (Fe^{3+}, Al^{3+}) but even bivalent ones (Cu^{2+}, Zn^{2+}, VO^{2+}). HPOs and HPs differ mainly in aromaticity and in proton affinity (higher in HPs) [17].

The most common HPOs are 3-hydroxy-2-methyl-4*H*-pyran-4-one (maltol) and 5-hydroxy-2-(hydroxymethyl)-4*H*-pyran-4-one (kojic acid).

Maltol, and its analogue 2-ethyl-3-hydroxy-4*H*-pyran-4-one (ethyl maltol) have been identified in a wide variety of heated materials such as bread crusts, coffee and cocoa beans, cereals. They are white, crystallize readily, have low melting points, sublime at room temperature, contribute to the odor of caramel, and cotton candy and thus are used as food additive [18].

Kojic acid was first reported as a crystalline substance from the mycelia of *Aspergillus orgzae* grown on steamed rice. It crystallizes in the form of colorless needles and it is readily soluble in water, ethanol, and acetone. As maltol, kojic acid is employed in food industry and specially in cosmetics to preserve colors: on cut fruits it prevents oxidative browning, in

seafood preserves pink and red colors and in cosmetics lightens the skin [19,20]. Previously, P1 has been mentioned as corresponding HP of kojic acid (Fig. 2.4)

| maltol | ethyl maltol | kojic acid |
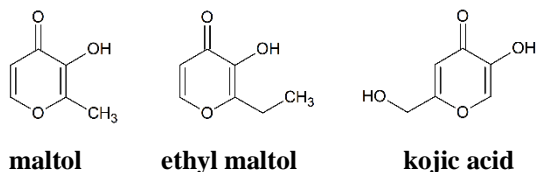
Figure 2.11 *Most common HPOs*

2.2.1 Tetradentate HPOs

Tetradentate HPOs take part in metal ions coordination by two kojic acid moieties improving chelating ability. Several kojic acid derivatives have been synthetized and in the last decade by Profs. Valeria M. Nurchi and Guido Crisponi group working on alkylation at position 6 by Mannich reaction (without protection of the phenolic group) [21] (L ligands series) or on hydroxy-methyl at position 2 (S ligands series) in the heterocyclic ring. Based on kojic acid, which can form 1:1, 1:2 and 1:3 metal/ligand complex, all of them have been studied and characterized.

L ligands in Fig. 2.12 have been synthetized using vanillin, ortho-vanillin, methylamine, benzylamine, piperazine, N-benzylmethylamine, diethylaminoethylamine and ammonium hydroxide as linker. They form Fe_2L_3 binuclear unprotonated complexes at pH 7.4 excluding L7, mono derivative which forms FeL_2H_x complex [22,23,24,25].

Even if different linkers are not involved in metal coordination, they play an important role in the chelation ability of ligand: in Table 2.3 pFe values are reported and it can be seen that L1 has highest value followed by L3.
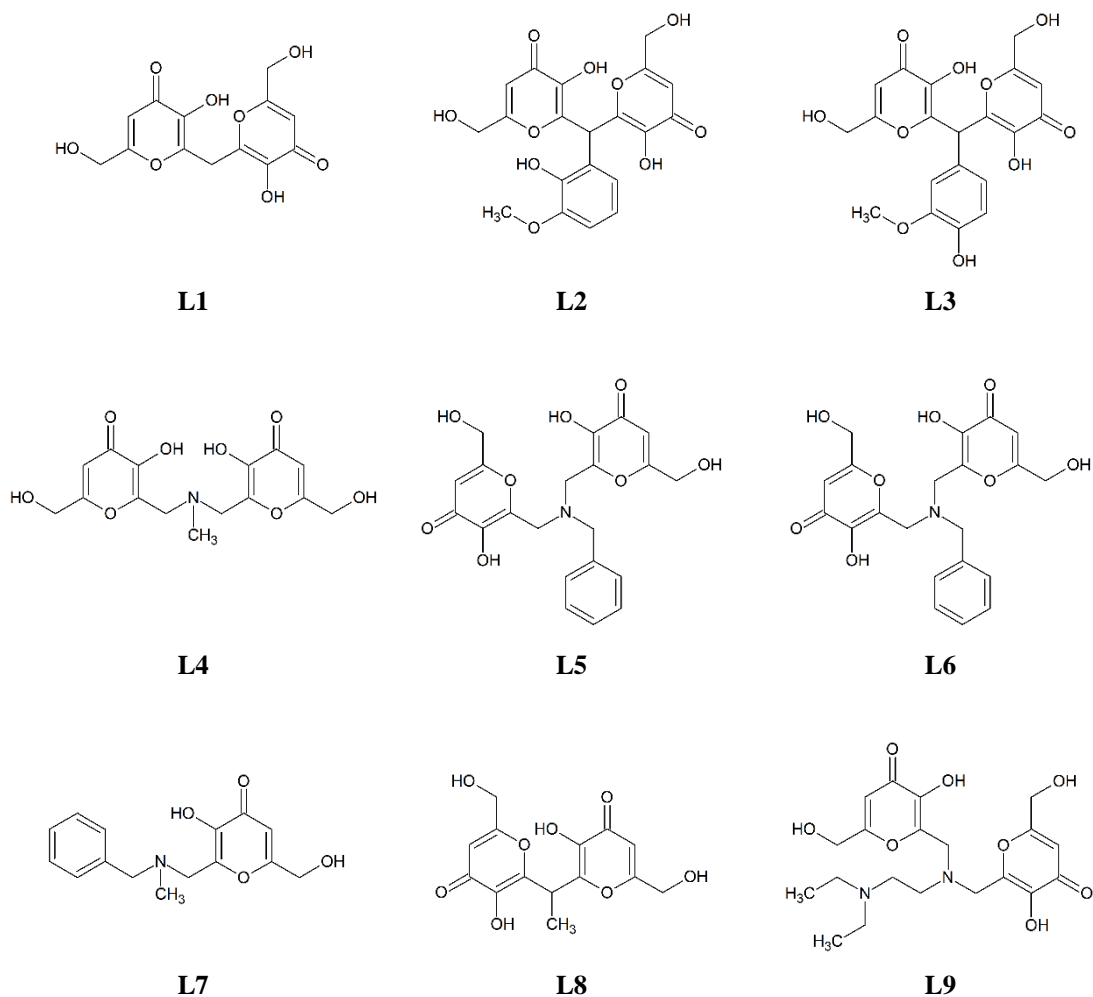
Figure 2.12 *L ligands, kojic acid derivatives synthetized by Nurchi and Crisponi group*

Table 2.3 *pFe values of L ligands*

	L1	L2	L3	L4	L5	L6	L7	L8	L9
pFe	23.1	18.9	22.2	18.1	19.3	17.7	16.7	20.2	17.7

S ligand have been synthetized according to a very easy and cheap method using ethylene diamine (en), propylene diamine (dpa) and butylenediamine (dba) as linkers. The linker length affects both the protonation and complex formation equilibria and nitrogen atoms take

part in the coordination of Cu^{2+} and Zn^{2+} ions studied as well. Data in Table 2.4 evidence that all ligands are comparable in the chelation of each metal ion [26].
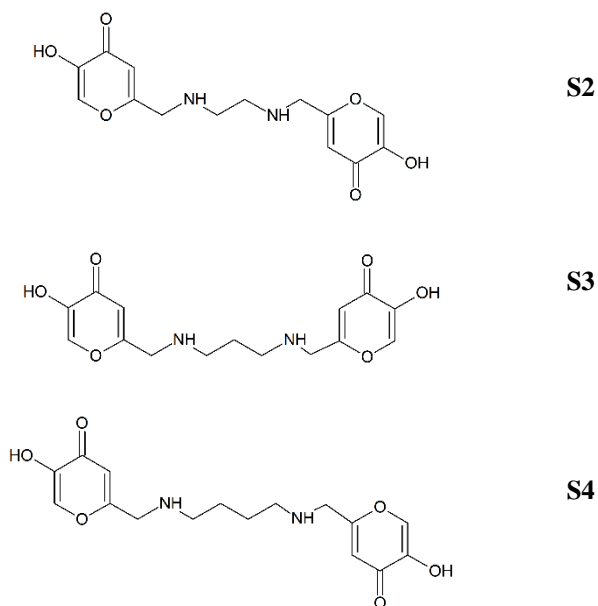
Figure 2.13 *S ligands, kojic acid derivatives synthetized by Nurchi and Crisponi group*

Table 2.4 *pM values of S ligands*

	S2	S3	S4
pFe	19.2	18.9	18.7
pAl	13.9	13.2	12.1
pCu	11.7	10.6	8.8
pZn	6.3	6.7	7.5

2.2.2 Hexadentate HPOs

By the use of tris(2-aminoethyl)amine our group synthetized 6,6′,6″-(((nitrilotris(ethane-2,1-diyl))tris(azanediyl))tris(methylene))tris(3-hydroxy-4H-pyran-4-one (SC). Fe^{3+}, Al^{3+}, Cu^{2+} and Zn^{2+} complexation studies and *in vivo* bioassays have been performed (see paper III).

SC
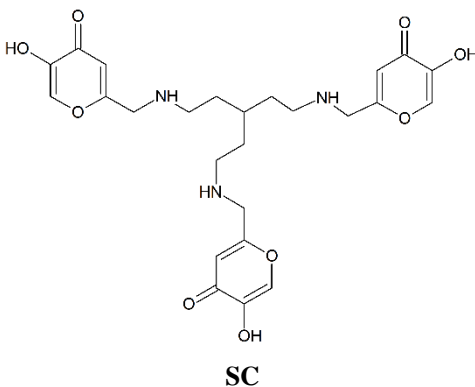
pFe 19.5   pAl 13.7

pCu 14.6   pZn 11.4

Figure 2.14 *SC ligand and its pM values. Solution equilibria studies are reported in paper III*

2.3 Mimosine

Mimosine (β-[N-(2-hydroxy-4-oxypyridyl)]-α-aminopropionic acid) (MIM) was first discovered in 1936 from *Mimosa pudica*. It has same empirical formula $(C_4H_5O_2N)_x$ and solubility with leucaenine (leucenol) but different melting points and optical activity. Mimosine is structurally similar to DOPA, tyrosine (Tyr) and phenylalanine (Phe) and DFP. Mimosine has zwitterionic character and its six-membered rings are nearly planar. The strong intermolecular forces and close packing of the molecules in the crystal depend on the high value of the melting point (227-228 °C)
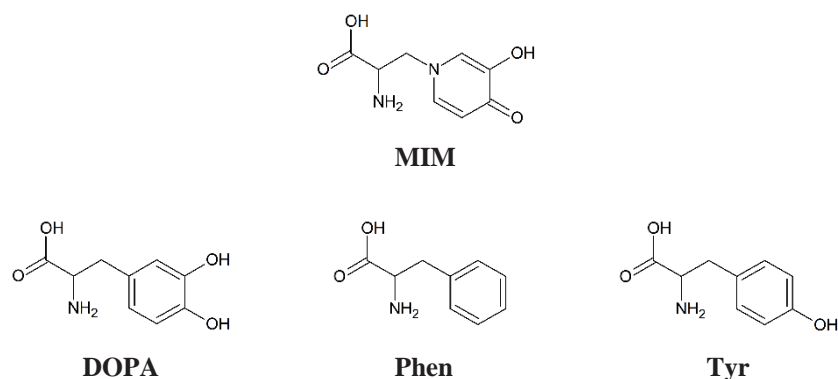
Figure 2.15 *Mimosine and structurally similar molecules*

Mimosine is involved in several biological process. It acts in cell cycle blocking particularly blocking entry into S phase (late G1 phase) and suppressing elongation of DNA replication (S phase). It was found that mimosine inhibited cell cycle progression in human breast cancer cells, and reduced DNA synthesis by more than 90% of the control within 4 h of treatment with 400 μM. It has been reported its induction of apoptosis especially in HL60 human promyelocytic leukemia cells [27]. Mimosine has also antimicrobial [28], anti-inflammatory [29] and anticancer activities [30].

The first values of protonation constants have been proposed on 1946 [31] (pK_1 2.1, pK_2 7.2, pK_3 9.2) and iron complex formation constants on 1973 [32].

Due to the HP residue and to the α-amino carboxylic group, mimosine is a very effective ligand for binding metal ions such as Fe^{3+}, Cu^{2+}, Zn^{2+}, Ni^{2+}.

There was a section, in Chapter 1, on metal used as cofactor by proteins. The metal ion-protein bond changes protein structure and properties. Even peptides that self-assemble through metal-ligand complexes have very different structures and functions from the original ones. Thus, the building blocks formation in stable structure, by covalent or non-covalent bond, is a growing process in nanotechnology.

Mimosine is nonproteinogenic amino acid. Nonproteinogenic amino acids are incorporated biosynthetically into proteins during translation. There are 22 genetically encoded,

proteinogenic, amino acids, 20 in the standard genetic code and 2 more that can be incorporated by special translation mechanisms [33].

Six MIM-based peptides (containing one, two and three MIM residues) have been synthetized (see paper V) which may reach a metal binding affinity comparable to DFP. In addition, the antimicrobial activities of the synthesized complexes against Gram positive, Gram negative bacteria and have been also investigated.
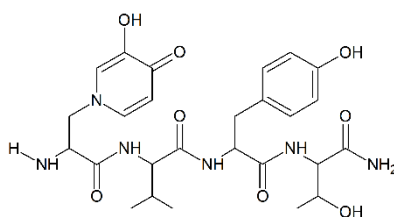
1   **H-Mim-Val-Tyr-Thr-NH₂**
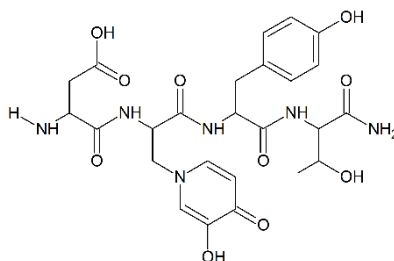
2   **H-Asp-Mim-Tyr-Thr-NH₂**
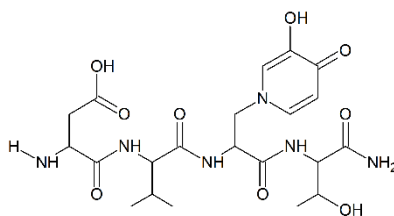
3   **H-Asp-Val-Mim-Thr-NH₂**

4   **H-Mim-Gly-Mim-Gly-OH**

5 **H-Mim-Gly-Pro-Gly-Mim-Gly-OH**
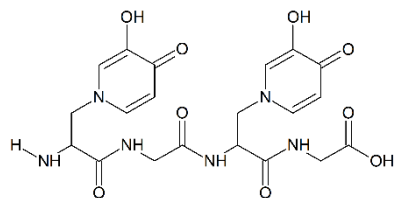
6 **H-Mim-Gly-Pro-Gly-Mim-GlyGly-Mim-OH**
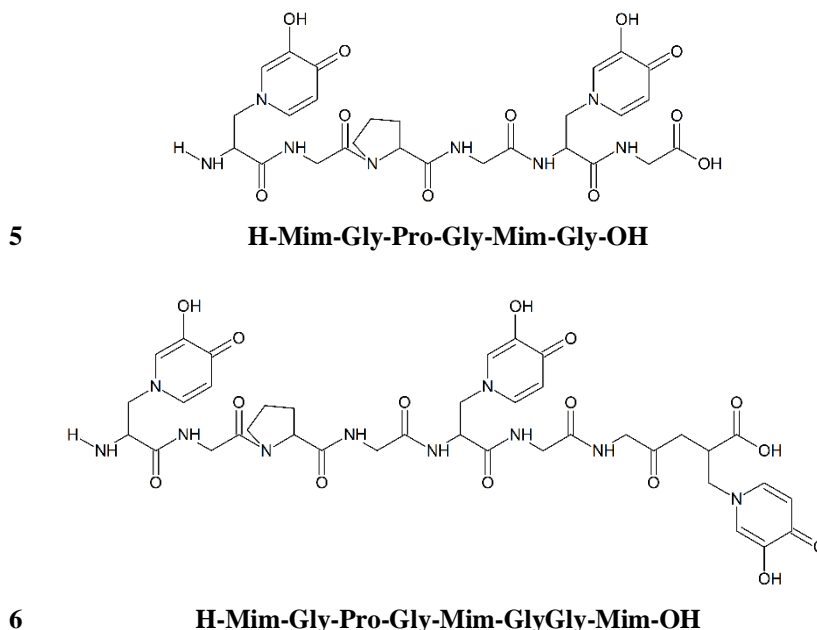
Figure 2.16 *Six MIM-based peptides: the first three N-terminus peptides contain one MIM unit, the next two C-terminus contain two MIM units and the last C-terminus contains three MIM units.*

2.4 Biphosphonate and picolinc acid derivatives

Bisphosphonates (BPs) have clinical application in bone diseases Paget's disease. They reduce hypercalcemia associated, bone pain and prevent progression of bone disease because of their high binding affinity for calcium phosphates. For this reason, some ^{99m}Tc bisphosphonate compounds are used in nuclear medicine in diagnosing certain skeletal diseases. In patients with osteoporosis, they prevent further bone loss and reduce fracture rates. During my three months of research in the Prof. Chris Orvig's group at The University of British Columbia solution studies of two biphosphonate-picolinic acid derivatives have been performed, Phospa and Dipedpa in Fig. 2.17 differing of CH_2 in the phosphonate chain. Their La^{3+} complexes have application in medicinal treatment of bone disorders [34,35,36].

Experiments are still in progress and data collected till now cannot be published in this thesis.
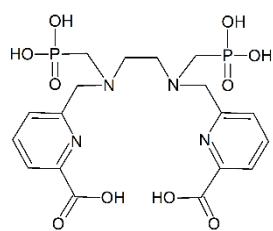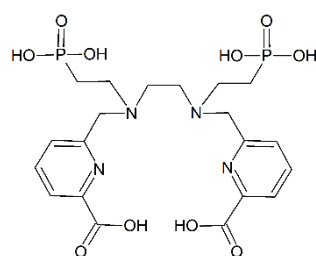
Phospa   **Dipedpa**

Figure 2.17 *Biphosphonate-picolinic acid derivatives studied at UBC*

2.5 References

[1] A. Cilibrizzi, V. Abbate, Y. L. Chen, Y. Ma, T. Zhou, R. C. Hider, *Chem. Rev.*, **2018**, *118*, 7657-7701

[2] M. A. Santos, S. M. Marques, S. Chaves, *Coord. Chem. Rev.*, **2012**, *256*, 240-259

[3] M. A. Santos, S. Chaves, *Future Med. Chem.*, **2015**, *7*, 383-410

[4] J. W. Armit, T. J. Nolan, *J. Chem. Soc.*, **1931**, *0*, 3023-3031

[5] G. J. Kontoghiorghes, L. Sheppard, *Inorg. Chim. Acta*, **1987**, *136*, L11-L12

[6] J. I. Lachowicz, V. M. Nurchi, G. Crisponi, M. G. Jaraquemada-Pelaez, M. Arca, A. Pintus, M. A. Santos, C. Quintanova, L. Gano, Z. Szewczuk, M. A. Zoroddu, M. Peana, A. Dominguez-Martin, D. Choquesillo-Lazarte, *Dalton Trans.*, **2016**, *45*, 6517-6528

[7] V. M. Nurchi, G. Crisponi, T. Pivetta, M. Donatoni, M. Remelli, *J. Inorg. Biochem.*, **2008**, *102*, 684-692

[8] M. A. Santos, R. Grazina, P. Buglyo, S. Gama, E. Farkas, *Polyhedron*, **2002**, *21*, 2609-2616

[9] M. A. Santos, S. Gama, L. Gano, G. Cantinho, E. Farkas, *Dalton Trans.*, **2004**, *7*, 3772-3781

[10] M. A. Santos, S. Gama, L. Gano, E. Farkas, *J. Inorg. Biochem.*, **2005**, *99*, 1845-1852

[11] S. Gama, P. Dron, S. Chaves, E. Farkas, M. A. Santos, *Dalton Trans.*, **2009**, *21*, 6141-6150

[12] S. Gama, M. Gil, L. Gano, E. Farkas, M. A. Santos, *J. Inorg. Biochem.*, **2009**, *103*, 288-298

[13] A. Irto, P. Cardiano, K. Chand, R. M. Cigala, F. Crea, C. De Stefano, L. Gano, G. Gattuso, S. Sammartano, M. A. Santos, *J. Mol. Liq.*, **2019**, *281*, 280-294

[14] A. Irto, P. Cardiano, K. Chand, R. M. Cigala, F. Crea, C. De Stefano, L. Gano, G. Gattuso, S. Sammartano, M. A. Santos, *J. Mol. Liq.*, **2018**, *272*, 609-624

[15] S. Chaves, A. Capelo, L. Areias, S. M. Marques, L. Gano, M. A. Esteves, M. A. Santos, *Dalton Trans.*, **2013**, *42*, 6033-6045

[16] S. Chaves, S. Marques, A. M. F. Matos, A. Nunes, L. Gano, T. Tuccinardi, A. Martinelli, M. A. Santos, *Chem. Eur. J.*, **2010**, *16*, 10535-10545

[17] K. H. Thompson, C. A. Barta, C. Orvig, *Chem. Soc. Rev.*, **2006**, *35*, 545-556.

[18] D. T. LeBlanc, H. A. Akers, *Food Technol.*, **1989**, 78-84

[19] A. Beélik, Adv. *Carbohyd. Chem.*, **1956**, *11*, 145-183

[20] M. Y. Kwak, J. S. Rhee, *Biotechnol. Bioeng.*, **1992**, *39*, 903-906

[21] H. N. Barham, G. N. Reed, *J. Am. Chem. Soc.*, **1938**, *60*, 1541-1545

[22] V. M. Nurchi, G. Crisponi, J. I. Lachowicz, S. Murgia, T. Pivetta, M. Remelli, A. Rescigno, J. Niclós-Gutíerrez, J. M. González-Pérez, A. Domínguez-Martín, A. Castiñeiras, Z. Szewczuk, *J. Inorg. Biochem.*, **2010**, *104*, 560-569

[23] L. Toso, G. Crisponi, V. M. Nurchi, M. Crespo-Alonso, J. I. Lachowicz, M. A. Santos, S. M. Marques, J. Niclós-Gutíerrez, J. M. González-Pérez, A. Domínguez-Martín, D. Choquesillo-Lazarte, Z. Szewczuk, *J. Inorg. Biochem.*, **2013**, *127*, 220-231

[24] V. M. Nurchi, G. Crisponi, M. Arca, M. Crespo-Alonso, J. I. Lachowicz, D. Mansoori, L. Toso, G. Pichiri, M. A. Santos, S. M. Marques, J. Niclós-Gutiérrez, J. M. González-Pérez, A. Domínguez-Martín, D. Choquesillo-Lazarte, Z. Szewczuk, M. A. Zoroddu, M. Peana, *J. Inorg. Biochem.*, **2014**, *141*, 132-143

[25] L. Toso, G. Crisponi, V. M. Nurchi, M. Crespo-Alonso, J. I. Lachowicz, D. Mansoori, M. Arca, M. A. Santos, S. M. Marques, L. Gano, J. Niclós-Gutíerrez, J. M. González-Pérez, A. Domínguez-Martín, D. Choquesillo-Lazarte, Z. Szewczuk, , *J. Inorg. Biochem.*, **2014**, *130*, 112-121

[26] V. M. Nurchi, G. Crisponi, J. I. Lachowicz, M. G. Jaraquemada-Pelaez, C. Bretti, M. Peana, S. Medici, M. A. Zoroddu, *J. Inrg. Biochem.*, **2018**, *189*, 103-114

[27] B. C. Q. Nguyen, S. Tawata, *Phytother. Res.*, **2016**, *30*, 1230-1242

[28] R. Anitha, S. Jayavelu, K. Murugesan, *Phytother. Res.*, **2005**, *19*, 992-993

[29] S. Mistry, R. Patidar, V. Vyas, J. Jena, K. R. Dutt, *J. Pharm. Sci. & Res.*, **2012**, *4*, 1789-1791

[30] A. Zalatnai, J. Bocsi, *Anticancer Res.*, **2003**, *23*, 4007-4009

[31] A. F. Bickel, J. P. Wibaut, *Recueil des Travaux Chimiques des Pays-Bas*, **1946**, *65*, 65-83

[32] W. C. Tsai and K. H. Ling, *J. Chin. Biochem. Soc.*, **1973**, *2*, 70-86

[33] G. Barrett, *Chemistry and Biochemistry of the Amino Acids*, **1985,** Spinger

[34] E. W. Price, B. M. Zeglis, J. S. Lewis, M. J. Adam, C. Orvig, *Dalton Trans.*, **2014**, *43*, 119-191

[35] Y. Mawani, J. F. Cawthray, S. Chang, K. Sachs-Barrable, D. M. Weekes, K. M. Wasan, C. Orvig, *Dalton Trans.*, **2013**, *42*, 5999- 6011

[36] X. Wang, M. de G. Jaraquemada-Pelaez, C. Rodríguez-Rodríguez, Y. Cao, C. Buchwalder, N. Choudhary, U. Jermilova, C. F. Ramogida, K. Saatchi, U. O. Hafeli, B. O. Patrick, C. Orvig, *J. Am. Chem. Soc*. **2018**, *140*, 15487-15500

Chapter 3

Experimental: methods

3.1 Reagents

Kojic acid, maltol, tren, L-mimosine, NaOH, HCl, NaCl, $FeCl_3$, $AlCl_3$, $ZnCl_2$, $CuCl_2$ and vanadyl sulphate were purchased from Sigma Aldrich.

Metal ions standard solution have been prepared dissolving chloride salt in pure double distillated water and adding the proper amount of HCl to prevent the hydrolysis. Fe^{3+} solution was standardized by spectrophotometric analysis of Fe^{3+}-Desferal complex; Al^{3+}, Zn^{2+} and Cu^{2+} by EDTA titration and vanadyl sulfate by redox titration with permanganate solution (Carlo Erba, Milan, Italy), followed by photometric detection.

Fmoc amino acid derivatives were purchased from Novabiochem, Fmoc-Gly-Wang resin from IrishBiotech.

Others chemical for synthesis were purchased from Sigma Aldrich, Acros and Merk Millipore and the organic solvent, from Sigma Aldrich, dried according to standard methods. NMR solvent were purchased from TCI and Sigma Aldrich.

TLC plates coated with silica gel 60 F254 and column chromatographic separation performed with silica gel 230-400 mesh were purchased from Merk.

3.2 Synthesis

From the collaboration between our research group and Prof. Amelia Santos group three new ligands (HPs) have been synthesized: NTA(PrHP)$_3$ in paper I, KC18 and KC21 in paper II. SC ligand, paper III and IV, has been synthesized in Cagliari by our group. MIM-peptides derivatives, paper V, have been synthesized in Poland.

3.2.1 NTA(PrHP)₃, KC18 and KC21

NTA(PrHP)$_3$, KC18 and KC21 come from the conjugation of two or three HPs units by coupling reaction.

The design of synthesis consists in a formation of polydentate 3,4-HPs by attachment of three *N*-alkylamine-3,4-HPs arms to suitable aminopolycarboxylic (NTA) acid to form hexadentate ligand. The design has been developed to the use of policarboxylic acid with free amino group (nitromethanetrispropionic acid) skeletons as the anchoring point for the three carboxylic acids giving also a spacer containing methyl groups and an amide bond between the apical tertiary amine and the 3,4-HPs moieties [1].

Shortly, the synthesis follows these steps [2,3]:

- protection of hydroxyl group of maltol by benzyl chloride (by BnCl)
- Michael type addition by amine with opening and closure of heterocyclic ring to convert HPO to HP
- coupling reaction with proper coupling agents
- hydrogenation to re-establish OH function (by Pd/C)

Table 3.1 Reagents of HPs's synthesis

Ligand	linker	amine	Coupling agents
NTA(PrHP)$_3$	NTA	propylenediamine	*N*-methylmorpholine (NMM)
			propylphosphonic anhydride (T3P)
KC18,	Nitromethanetrispropionic	propylenediamine	*N*-methylmorpholine (NMM)
KC21	acid		propylphosphonic anhydride (T3P)

3.2.2 SC

SC, as the others S ligands shown in the previous chapter, has been obtained by an easy and low-cost synthesis from kojic acid by reacting tren with the methylhydroxyl group of kojic acid [4].

3.2.3 Solid-phase peptide synthesis

Solid-phase peptide synthesis (SPPS) represents a big evolution in the synthesis of larger peptides. Bruce Merrield, considered a father of SPPS, had the idea to generate peptide bonds on an insoluble resin, a polymer support, where a single cleavage step permits to obtain the

desired peptide in solution. In this type of the synthetic approach several issues such as the matrix swelling, type of linker groups, protecting groups in the amino acid residues, etc. must be considered.

The main advantages of this synthetic approach are: simplicity and speed carrying out all the reactions in a single reaction vessel, and efficiency avoiding the large losses typical of intermediates purification, obtaining high yields of final products through the use of excess reactants [5].
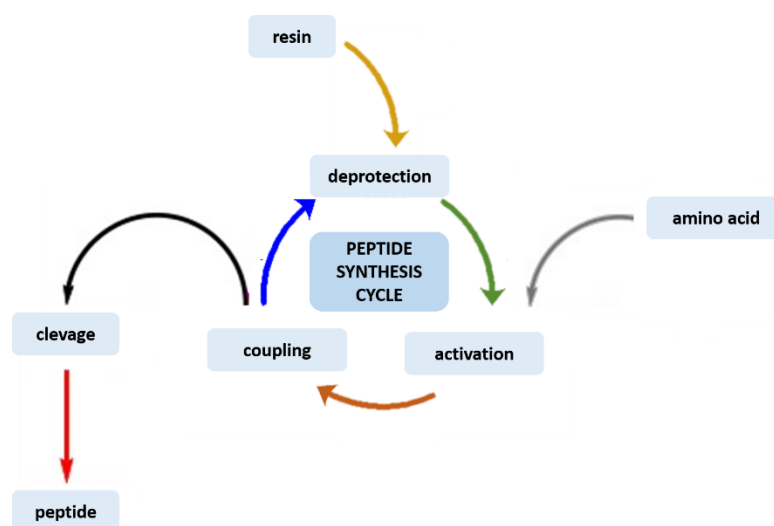
Figure 3.1 SPPS scheme
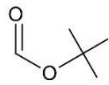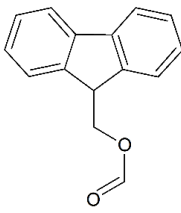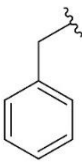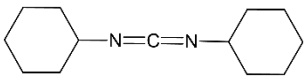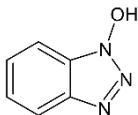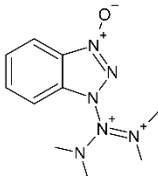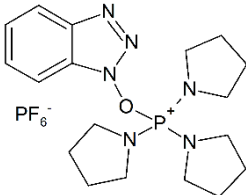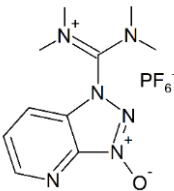
Appropriate protecting groups are required to prevent the formation of undesired bonds and side reactions. A protecting group has to be easily introduced into the functional group, has to be stable to a broad range of reaction conditions and it has to be safely removed at the end of the synthetic process or when the functional group requires manipulation. Because most peptide syntheses are carried out in the *C* to *N* direction, α-aminoprotecting groups (temporary protecting groups) are removed several times during the synthesis, and therefore, removal must be done in mild conditions in order to not affect the remaining protecting groups or even the peptidic chain. There are (Fig. 3.2):

- N protecting groups

- C protecting groups
- C activating groups

Protected amino acids are commercially available or may be protected by synthesis. The most common N protecting groups for SPPS are the *tert*-butyloxycarbonyl (Boc) and 9-fluorenylmethoxycarbonyl (Fmoc) removed, respectevely by acid such has trifluoroacetic acid (TFA) and base such as piperidine. One of the most common C protecting group is the benzyl group (Bn) usually used in the presence of Boc group. Most of the coupling agents of SPPS are used even in solution synthesis such as N,N'-dicicloesil carbodiimide (DCC), Hydroxybenzotriazole (HOBt), 2-(1H-Benzotriazole-1-yl)-1,1,3,3-tetramethylaminium tetrafluoroborate (TBTU) and benzotriazol-1-yl-oxytripyrrolidinophosphonium hexafluorophosphate (PyBOP) and 1-[Bis(dimethylamino)methylene]-1H-1,2,3-triazolo[4,5-b]pyridinium 3-oxide hexafluorophosphate (HATU) used in MIM-peptides sytnhesis [6,7]. In Table 3.2 most common N and C protecting grups and coupling agents are shown.

Table 3.2 *Most common protecting groups. Some of them have been used in MIM-peptide synthesis*

N protecting groups	
Boc	Fmoc

C protecting groups

Bn

Couplin agents

DCC	HOBt	TBTU

PyBOP	HATU

In the end, it is important to understand the nature of the resin. The use of a polimeric solid support requires the insolubility in the synthesis conditions that allows purification by filtration giving speed and simplicity, to the method and the swelling in the reaction medium: resin beads must be permeated by solvent and reagent molecules and that the growing of peptide chain will proceed only if the solvent swell the resin [8,9].

The most commonly available resins are Wang and Rink resin shown in Fig. X. In addition to protected amino acids, protected amino acids on polimeric support are commercially available as well such as Fmoc-Gly-Wang resin used for peptide H-Mim-Gly-Mim-Gly-OH as reported in paper V.

Wang resin   **Rink resin**

MBHA-Rink resin   **2-chlorotrityl chloride resin**
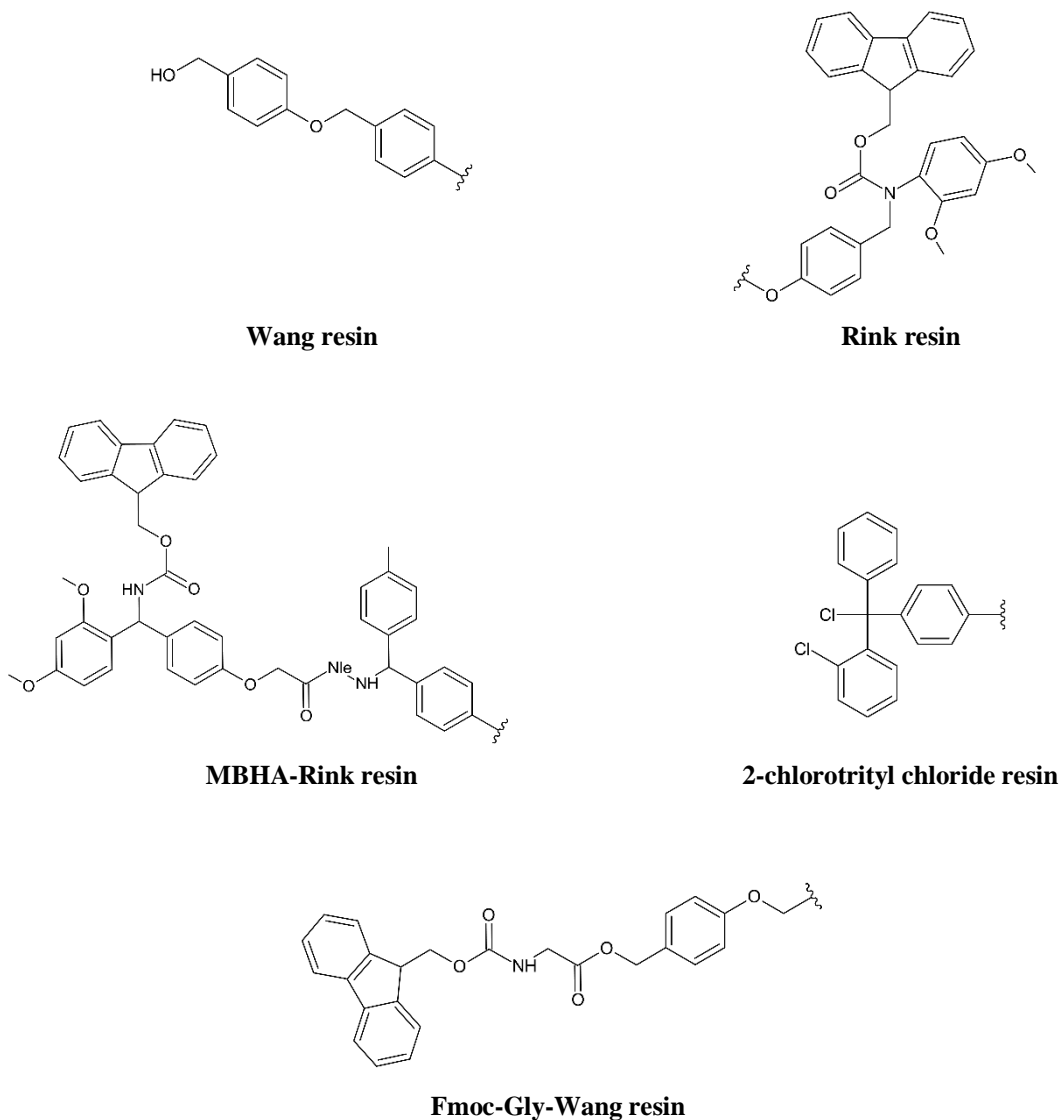
Fmoc-Gly-Wang resin

Figure 3.2 Top row: Wang and Rink resin, the most common one used in SPPS; bottom rows: MBHA-Rink resin employed for peptides 1-3, Fmoc-Gly-Wang resin employed for peptide 4 and 2-chlorotrityl chloride resin employed for peptide 5-6.

3.3 Solution studies

The determination of speciation model provides the stoichiometry of the formed species (M:L ratio) at different pH and controlled temperature and ionic strength by the calculation of protonation and complex formation constants. A generic system can be described by the following equation

$$pM + qL + rH = M_pL_qH_r \tag{3.1}$$
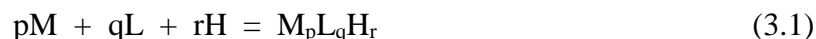
$$\beta_{pqr} = [M_pL_qH_r] / [M]^p[L]^q[H]^r \tag{3.2}$$

where M, L and H are metal, ligand and proton consisting the system of which charges and solvent are omitted for simplicity. Species in brackets square represent the equilibrium concentrations. β_{pqr} is the cumulative constant. In the following equations concentrations are used instead of activities because most of experiments are carried out at specific ionic strength and temperature (NaCl 0.1M, 25°C).

The first step in solution studies is the determination of ligand protonation constants K.

$$L + H = HL \qquad\qquad K_1 = \frac{[HL]}{[L][H]} \tag{3.3}$$

$$HL + H = H_2L \qquad\qquad K_2 = \frac{[H_2L]}{[HL][H]} \tag{3.4}$$

$$H_{(n-1)}L + H = H_nL \qquad\qquad K_n = \frac{[H_nL]}{[H_{(n-1)}L][H]} \tag{3.5}$$
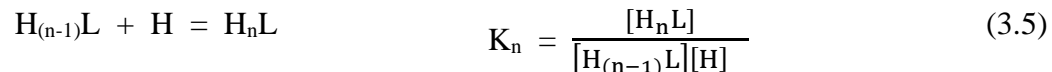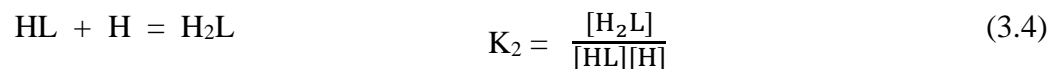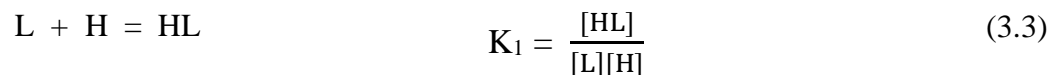
The K protonation constants regard protonation reactions, i.e. the reverse of acid dissociation reactions. The relationship between protonation and dissociation constants can be expressed through the following equation:

$$\log K_H{}^{(k)} = \log \frac{1}{K_a^n} = pK_a{}^{(n)} \tag{3.6}$$

where $k = 1 + m - n$, m is the highest dissociation constants, n indicates a nth consecutive dissociation constant, $1 \leq n \leq m$, and k applies to a kth consecutive protonation constant, $1 \leq k \leq m$ [10].

The protonation constants K in equations 3.3 – 3.5 can be expressed also as cumulative constants β. β gives just a cumulative information while K express directly the acidic strength specifically for each step. The following equations report the β constants with the related protonation reactions.

$$L + H = HL \qquad\qquad \beta_1 = \frac{[HL]}{[L][H]} \tag{3.7}$$

$$L + 2H = H_2L \qquad\qquad \beta_2 = \frac{[H_2L]}{[L][H]^2} \tag{3.8}$$

$$L + nH = H_nL \qquad\qquad \beta_n = \frac{[H_nL]}{[L][H]^n} \tag{3.9}$$
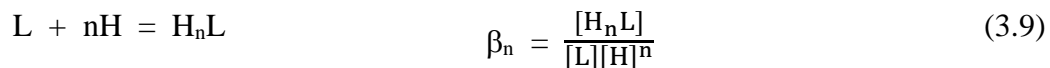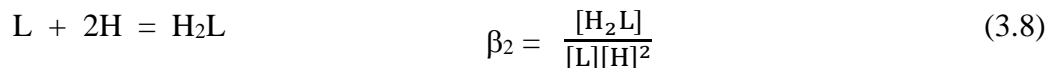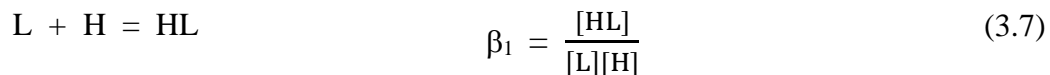
The second step is the determination of complex formation constants

$$M + L = ML \qquad\qquad \beta_1 = \frac{[ML]}{[M][L]} = K_1 \tag{3.10}$$

$$M + 2L = ML_2 \qquad\qquad \beta_2 = \frac{[ML_2]}{[M][L]^2} = K_1 \cdot K_2 \tag{3.11}$$

$$M + nL = ML_n \qquad\qquad \beta_n = \frac{[ML_n]}{[M][L]^n} = K_1 \cdot K_2 \cdot \ldots K_n \tag{3.12}$$
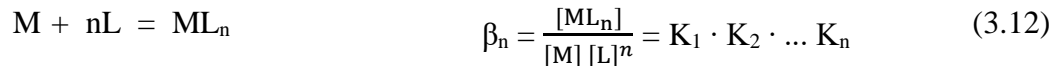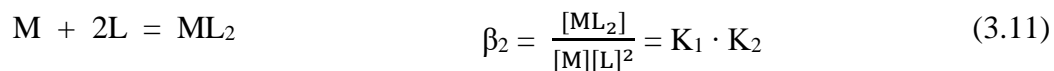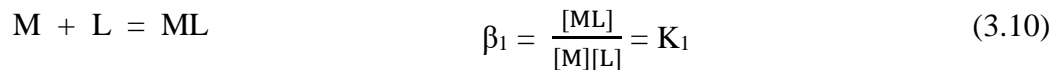
Mass balance needs to be taken into account.

$$C_M = [M] + [ML] + [ML_2] + .. + [ML_n] = [M] + \sum_{n=1}^{n} \beta_n [M][L]^n \tag{3.13}$$

$$C_L = [L] + [HL] + [H_2L] + .. + [H_pL] + [ML] + 2[ML_2] + n[ML_n] =$$
$$= [L] + \sum_{p=1}^{p} X_p[H]^p[L] + \sum_{n=1}^{n} \beta_n [M][L]^n \tag{3.14}$$

$$C_H = [H] - [OH] + [HL] + 2[H_2L] + .. + p[H_pL] =$$
$$= [H] - K_W[H]^{-1} + \sum_{p=1}^{p} PX_p [H]^p[L] \tag{3.15}$$

where brackets concentration are free concentrations corresponding to analytical ones.

These equations can be solved by experiment methods such as potentiometric/spectrophotometric titration. Considering that there could be a competition between the metal and proton donor sites in the ligand, in each titration point the free proton concentration can be measured and three mass balance can be written [11]. Currently, there are many programs [12] able to process hundreds of experimental points [13].

3.4 Potentiometry

Potentiometry is one of the techniques used for the determination of both protonation and complex formation constants of our systems. The method involves the use of glass electrode

which measures the potential correlated to the proton activity (aH^+) and to the pH through Nerst law:

$$E = E^0 + \frac{RT}{F} \cdot \ln a_{H+} \tag{3.16}$$

where E^0 is the standard potential, R the universal gas constant, T the absolute temperature, F the Faraday constant and a_{H+} activities of H^+ ions.

With high and constant concentration of ionic strength, the activity coefficients, γ, is constant to vary the concentration of the other species in solution when they are lower than 10% than ionic medium. Thus, γ can be incorporated into the E^0 giving [14]

$$E = E^0 + \frac{RT}{F} \cdot \ln [H^+] \tag{3.17}$$

3.4.1 Calibration

Glass electrode calibration must be done daily before starting the measurements. It may be performed through solutions [15] or through an acid strong-base strong titration [16] where the acid concentration is known.

The determination of thermodynamic constants happens in a specific range of concentration, the reason why the activity coefficient must be constants, as already mentioned, because of the ionic strength. Buffer solutions allow to calibrate the electrode compared to the proton activity while the acid-base titration to the concentration. This is the reason why in solution studies the calibration is performed by a titration.

The elaboration data is based on Gran's method. Currently, GLEE (glass electrode evaluation) [17], part of HyperQuad program, can be used to calculate the slope and the electrode standard potential linearizing the titration curve

$$E = E^0 + \log[H^+] \qquad (3.18)$$

where E is the measured potential.
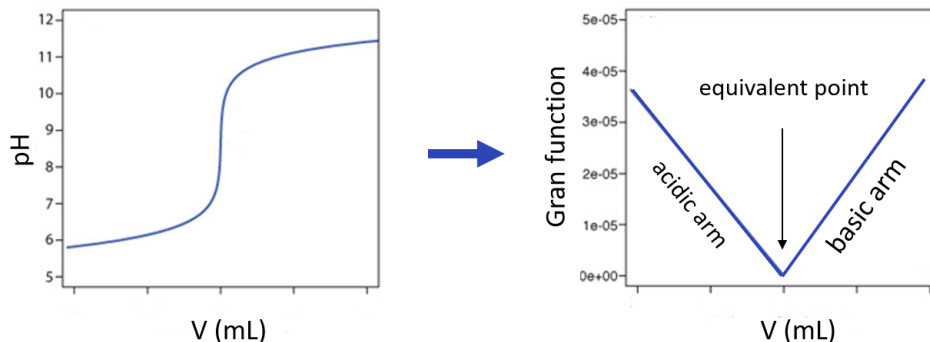
Figure 3.3 Gran plot

The optimal case should show all points fitted by two lines, the first relative to the acid (beginning of titration) and the second relative to the base (end of titration) converging in a single point. This intersection gives an estimation of the equivalent volume which should be the same for acid and base ideally. In case of base contamination, for example carbonate, it may happen that there is no a converging point but that the second arm starts later.
About it, the alkalinity level can be calculated:

$$\text{Alkalinity level \%} = \frac{V_e \text{ base} - V_e \text{ acid}}{V_e \text{base}} \cdot 100 \qquad (3.19)$$

For daily calibration we use to prepare 20 mL of sample containing 1 mL HCl standard 0.1 M and 2 mL NaCl 1 M to reach 0.1 M ionic strength titrated by NaOH 0.1 M. NaOH solution is prepared according to [18] and we use to consider 2% the limit of alkalinity level.

3.5 Spectrophotometry

Spectrophotometry is based on Lambert-Beer law

$$A = \varepsilon \cdot l \cdot C \qquad (3.20)$$

Where A is the absorbance, ε the absorptivity characteristic for each species, l is the optical path length and C the molar concentration of absorbing species. In a multicomponent system total contribution is done by the sum of contribution of each component.

$$A = (\varepsilon_1 C_1 + \varepsilon_2 C_2 + .. + \varepsilon_n C_n) \cdot l \qquad (3.21)$$

The UV-visible spectrophotometry measuring the electromagnetic radiation absorbed by molecules in the ultraviolet range (200-400 nm) and visible (400-800 nm) [14].

3.5.1 Resolution of Gaussian peaks

Gaussian is the characteristic shape of spectra. Generally, the gaussian density function is defined in statistics

$$\Phi (x) = \frac{1}{\sigma(2\pi)^{1/2}} \exp \left[- \frac{(x- \mu)^2}{2\sigma^2} \right] \qquad (3.22)$$

where μ and σ are the expectation value and the standard deviation.
In case of experimental signal like spectra eq. 3.18 becomes

$$Y = H \exp \left[- k \frac{(X - X\prime)^2}{2W^2} \right] \tag{3.23}$$

where H is the peak height, X' the maximum abscissa, W the width of the band at half height and k = 8 ln 2 = 5.545 the proportionally factor for the substitution of σ with W.

The Gaussian peak described by the eq. 3.19 may be normalized to have general results for a single peak. In case of many overlapped peaks, position, width and height give a contribution to each other peaks.

It follows that the decomposition of Gaussian peaks has to be studied as a function of the degree of overlapping between them and of the height and half band width ratios. Crisponi et al. [19] described a method based on the examination of the elements of dispersion matrix, obtained in a nonlinear least squares procedure.

3.5.2 Potentiometric-spectrophotometric titrations

Potentiometric-spectrophotometric titrations have been performed with an automatic Dosimat 665 Metrohm connected to Metrohm 691 pHmeter, with 888 Titrando Metrohm including 801 stirrer and 916 Ti-Touch Metrohm at UBC and with Varian Cary 50 and Varian Cary 60 spectrophotometer. Data have been elaborated by Hyperquad programs, particularly Hyperquad2013 and Hyss for potentiometric data [20] and HypSpec for UV-Vis data.

The sample, 20 mL, has been maintained at 25°C by thermostatic bath under inert condition by argon insufflation. The spectra have been collected by 0.2 cm and 1 cm (cuvette batch system for metal complexes at acidic pH) optical path. The fiber immersed in the titration cell allowed to collect simultaneous potentiometric and spectrophotometric data.

3.6 Nuclear Magnetic Resonance Spectroscopy (NMR)

NMR spectroscopy is one of the most versatile technique which can find application in several fields such as chemistry, medicine and biology giving information about the nature and numbers of atoms and the structural relationship between them.

Nucleus under NMR investigation are described by nuclear magnetic moment

$$\mu = \frac{\gamma \, I \, h}{2\pi} \tag{3.24}$$

where γ is gyromagnetic ratio (constant and different for each nucleus), h is the Plank's constant and I is a spin angular momentum. The atomic nucleus has a property called spin so it is a spinning charged particle, and it generates a magnetic field. For each nucleus with spin, the number of allowed spin states it may adopt is quantized and is determined by its nuclear spin quantum number, I. For each nucleus, I is a physical constant and there are $2I + 1$ allowed spin states with integral differences ranging from $+I$ to $–I$. Only nucleus with $I \neq 0$ can be studied by NMR such as ^1H and ^{13}C while ^{12}C, ^{16}O, which have $I = 0$, cannot be studied.

When an external magnetic field is applied, electrons surrounding nucleus generate an opposite magnetic field and the nucleus begins to process about its axis of spin with angular frequency ω, Larmor frequency, directly proportional to the strength of the applied magnetic field. If the sample is irradiated with an electromagnetic radiation with a frequency equal to the frequency of Larmor, there is an interaction of the magnetic component of radiation with magnetic moments nuclear (also these oscillating at the Larmor frequency). Each radiation absorption involves a change of orientation of the nuclear spin that rotates from aligned with the field to opposite the field. When this spin transition occurs, nuclei are in resonance with the applied radiation [21].

NMR spectroscopy have been used for the characterization of all ligands studied in this thesis, particularly Bruker Advance II 300 MHz and 400 MHz. NMR titration have been performed to support potentiometric and UV-vis techniques with Bruker Ascend 400 MHz with 1D HSQC (Heteronuclear Single Quantum Coherence) and TOCSY (Total Correlation

Spectroscopy) and 2D ROESY (Rotating-frame Nuclear Overhauser Effect Correlation Spectroscopy). The importance of NMR in solution studies is not only the evaluation of stability constants in a range of pH out of potentiometry but specially the attributions. All data have been elaborated by HypNMR program. For peptides 700 MHz and 950 MHz have been used.

3.7 Electron Paramagnetic Resonance (EPR)

EPR spectroscopy is used for studying materials with unpaired electrons. The basic concepts of EPR are analogous to those of NMR but electron spins are excited instead of atomic nuclei spins. EPR spectroscopy is particularly useful for studying metal complexes or organic radicals. EPR studies for SC ligand have been performed at Torino University.

3.8 Electron spray ionization Mass Spectrometry (ESI-MS)

Mass spectrometry is an analytical technique useful for measuring the mass-to-charge ratio (m/z) of one or more molecules present in a sample. Typically, mass spectrometers can be used to identify unknown compounds via molecular weight determination and to determine structure es of molecules.

The complete process involves the conversion of the sample into gaseous ions, with or without fragmentation, which arrive to the detector according to their characteristic m/z ratio.

The signals are displayed graphically as a spectrum showing their relative abundance.

ESI-MS is a soft ionization technique, very sensitive in the study of micro-volumes, non-volatile and thermally labile molecules. Coupled with high performance liquid chromatograph (HPLC) becomes a very powerful technique in the analysis of small and large

molecules with different polarities. ESI uses electrical energy to transfer ions from solution into the gaseous phase through three steps: (1) dispersal of a fine spray of charge droplets, followed by (2) solvent evaporation and (3) ion ejection from the highly charged droplets. In an ESI source, a continuous flow of sample solution is passed through a quartz silica capillary tube, which is maintained at a high voltage. The charged droplets generated at the exit of the electrospray pass down a pressure gradient and potential gradient toward the analyzer region of the mass spectrometer. To obtain structural information, a desired ion can be mass selected and further fragmented applying a collision energy. The fragment ions can then be mass analyzed by a second mass analyzer of a quadrupole mass spectrometer system [22,23].
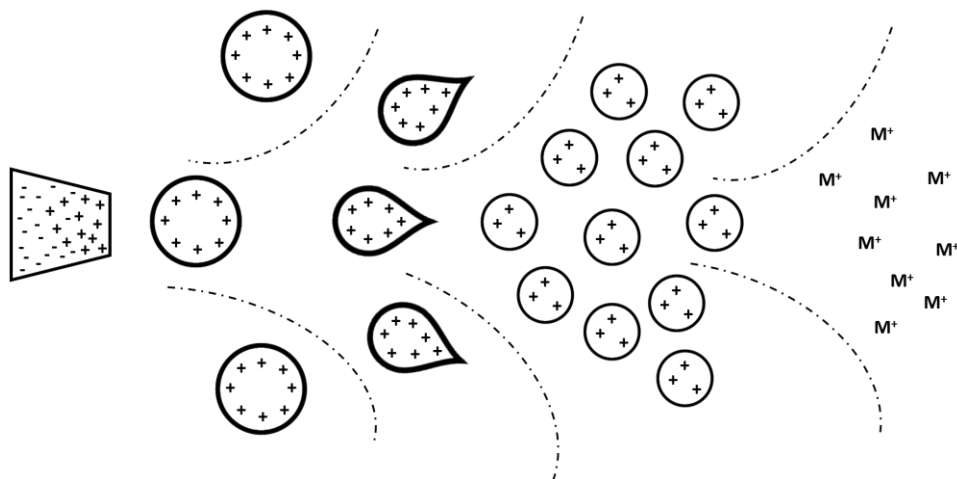
Figure 3.4 Mechanism of ESI

All ligands have been analyzed by mass spectrometer equipped with ESI source. Particularly, HPs have been characterized by 500 MS LC Ion Trap (Varian Incc., Palo Alto, CA, USA) and 310 ESI LC-MS-MS; peptides by microTOF-Q and FTICR (Fourier Transform Ion Cyclotron Resonance) PAex-Qe Ultra 7T (both Bruker Daltonics, Bremen, Germany).

3.9 Density functional theory (DFT)

Density-functional theory (DFT) is a computational quantum mechanical modelling method used in physics and chemistry to investigate the electronic structure. DFT was born with Thomas–Fermi model for the electronic structure of materials but the real input is due to Walter Kohn and Pierre Hohenberg in the framework of the two Hohenberg–Kohn theorems (H–K) only for non-degenerate ground states in the absence of a magnetic field, although they have since been generalized to encompass these [24].

DFT studies are very useful to complete solution studies specially for a determination of coordination model. For example, in HPs iron complexes we could confirm hexacoordination with octahedral geometry.

Portuguese group applied DFT for HPs iron complexes giving a geometry information, angles and bond lengths. SC ligand has been studied by DFT in Udine University and MIM-peptides in San Sebastian University.

3.10 Biodistribution studies

Biodistribution studies are *in vivo* test distribution or localization studies performed to support drug development. Temporal biodistribution profiles may be used to address kinetics and reversibility of target accumulation. Biodistribution studies are often performed using radioactive tracers [25]. The set of animals used in each experiment should be of the same sex, strain and of about the same weight. After the time intervals stipulated for each product the animals should be sacrificed and the organs liver, lung, kidney, stomach, heart, intestine, muscles, bone and blood have to be removed and placed in containers for counting. Biodistribution studies have been performed for NTA(PrHP)$_3$, KC18, KC21 and SC ligands at Centro de Ciencias e Tecnologias Nucleares (C2TN) of Lisbon.

CD1 mice (randomnly bred, Charles River from CRIFFA, France) of 22-25 g body weight were injected by ^{67}Ga citrate used as radiotracer. Ligands were administrated by

intraperitoneal injection and mice sacrificed by cervical dislocation at established time post-administration.
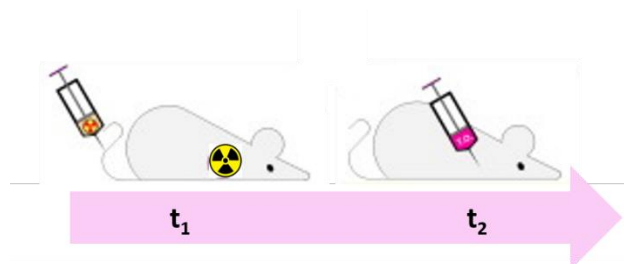
Figure 3.5 *Experimental steps of biodistribution studies*

3.11 References

[1] S. Chaves, S. Marques, A. M. F. Matos, A. Nunes, L. Gano, T. Tuccinardi, A. Martinelli, M. A. Santos, *Chem. Eur. J*., **2010**, *16*, 10535-10545

[2] B. Xu, X. L. Kong, T. Zhou, D. H. Qiu, Y. L. Chen, M. S. Liu, R. H. Yang, R. C. Hider, *Bioorg. Med. Chem. Lett*., **2011**, *21*, 6376-6380

[3] T. Zhou, X. L. Kong, Z. D. Liu, D. Y. Liu, R. C. Hider, *Biomacromolecules*, **2008**, *9*, 1372-1380

[4] V. M. Nurchi, G. Crisponi, J. I. Lachowicz, , C. Bretti, M. Peana, S. Medici, M. A. Zoroddu, *J. Inorg. Biochem*., **2018**, *189*, 103-114

[5] J. M. Palomo, *RSC Adv*., **2014**, *4*, 32658-32672

[6] A. Isidro-Llobet, M. Alvarez, F. Albericio, *Chem. Rev.*, **2009**, *109*, 2455-2504

[7] W. C. Chan, P. D. White, *Fmoc solid phase peptide synthesis*, 2000, Oxford University

[8] V. K. Sarin, S. B. H. Kent, R. B. Merrifield, *J. Am. Chem. Soc.*, **1980**, *102*, 5463-5470

[9] S. Angot, N. Ayres, S. A. F. Bon, D. M. Haddleton, *Macromolecules,* **2001**, *34*, 768-774

[10] K. K. Govender, I. Cukrowski, *J. Phys. Chem.*, **2009**, **113**, 3639-3647

[11] A. Braibanti, V. Carunchio, *I complessi metallici in soluzione*, **1996**, Aracne Editrice

[12] http://www.hyperquad.co.uk/

[13] P. Gans, A. Sabatini, A. Vacca, *Talanta*, **1996**, *43*, 1739-1753

[14] R. Cozzi, P. Protti, T. Ruaro, *Analisi chimica strumentale A,* 2nd ed.*,* **1997**, Zanichelli

[15] C. Maccà, *Anal. Chim. Acta*, **2004**, *512*, 183-190

[16] P. Gameiro, S. Reis, J. L. F. C. Lima, B. de Castro, *Anal. Chim. Acta*, **2000**, *405*, 167-172

[17] P. Gans, B. O'Sullivan, *Talanta*, **2000**, *51*, 33-37

[18] A. Albert, E. P. Serjeant, *Ionization constants of acids and bases: a laboratory manual*, **1962**, Methuen

[19] G. Crisponi, F. Cristiani, V. M. Nurchi, *Anal. Chim. Acta*, **1993**, *281*, 197-206

[20] L. Alderighi, P. Gans, A. Ienco, D. Peters, A. Sabatini, A. Vacca, *Coord. Chem. Rev.*, **1999**, *184*, 311-318

[21] J. Keleer, *Understanding NMR Spectroscopy* 2nd ed., **2011**, Wiley

[22] C. S. Ho, C. W. K. Lam, M. H. M. Chan, R. C. K. Cheung, L. K. Law, L. C. W. Lit, K. F. Ng, M. W. M. Suen, H. L. Tai, *Clin. Biochem. Rev.*, **2003**, *4*, 3-12

[23] S. Banerjee, S. Mazumdar, *Int. J. Anal. Chem.*, **2012**, 1-40

[24] S. B. Trickey, *Advanced in quantum chemistry*, **1990**, Elsevier

[25] A. S. Faqi, *A Comprehensive Guide to Toxicology in Nonclinical Drug Development,* 2nd ed., **2017**, Elsevier

Paper I

A new tripodal-3-hydroxy-pyridinone for iron and aluminium sequestration: synthesis, complexation and in vivo studies

R. Cappai, K. Chand, J. I. Lachowicz, S. Chaves, L. Gano, G. Crisponi, V. M. Nurchi, M. Peana, M. A. Zoroddu, M. A. Santos, *New. J. Chem.*, **2018**, *42*, 8050-8061.

A new tripodal-3-hydroxy-4-pyridinone for iron and aluminium sequestration: synthesis, complexation and *in vivo* studies†

Rosita Cappai,‡[ab] Karam Chand,‡[a] Joanna I. Lachowicz,[b] Sílvia Chaves, [ID][a] Lurdes Gano, [ID][c] Guido Crisponi, [ID][b] Valeria M. Nurchi, [ID]*[b] Massimiliano Peana, [ID][d] Maria Antonietta Zoroddu[d] and M. Amélia Santos [ID]*[a]

Elevated levels of iron and aluminium in the body can lead to tissue damage, organ failure and eventually death. To reduce complications of metal overload, specific chelating agents have been used. Following our recent developments in a series of hexadentate 3-hydroxy-4-pyridinones (3,4-HP) with high M^{3+} sequestering capacity, we herein present a novel tripodal homologue, whose design involves one methylene truncation on the linkers. This truncation aimed to reduce the ligand molecular weight and concomitant improvement in the membrane crossing ability and accessibility to cytoplasmic iron pools, but still retaining the capacity for the formation of a 1:1 (M^{3+}:L) complex with high thermodynamic stability and kinetic inertness. Besides the synthesis of a new ligand, solution studies have been performed to evaluate the acid–base properties and complexation capacity towards Fe(III) and Al(III) using potentiometry and a panoply of spectrometric techniques. The pFe and pAl values show some decrease, as compared with the non-truncated homologues, but still represent an improvement of, respectively, 7- and 4-orders of magnitude, as compared to the marketed drug deferiprone. The ability of this new ligand to facilitate metal-mobilization from the body was investigated using a mice model injected with ^{67}Ga. The new chelator possessing high pM^{3+} values shows promising ability to remove Fe and Al under *in vivo* conditions.

1. Introduction

Iron (Fe) is an essential element for cellular metabolism, mainly due to its high affinity for oxygen and its characteristic redox chemistry. However, when in excess, such as the severe iron-overload situation in transfusional hemosiderosis (caused by the parenteral administration of iron to treat β-thalassemia major), it becomes extremely toxic due to its redox cycling and generation of reactive oxygen species (ROS) which may interact with several endogenous biomolecules and lead to serious pathological situations.[1]

The ubiquitous aluminium (Al) is a non-essential element, but it is the most environmentally abundant toxic element in our biosphere. Health hazards associated with Al have been recently reviewed, and they come from industrial, alimentary or pharmaceutical sources.[2] Although Al bioavailability is usually low, when in contact with acid solutions or complexing agents, it can accumulate in specific organs, namely in the brain (*e.g.* dialysis encephalopathy syndrome and Alzheimer's disease)[3,4] and in the skeletal system (osteomalacia).[5]

To control Fe and also Al overload toxicity, the use of chelating agents has been considered as one of the best therapeutic strategies. The iron chelators in clinical use, such as desferrioxamine (Desferal, DFO), deferiprone (DFP) and deferasirox (ICL670), have also been utilized for mobilization and depletion of aluminium overload,[2,6] due to the similarities between Fe^{3+} and Al^{3+} (ionic radii 64 and 50 pm, respectively). However, all these drugs have some recognized limitations and so there has been a continuous demand for the development of new non-toxic iron-sequestering agents.[7] In particular, 3-hydroxy-4-pyridinones (3,4-HP), as analogues of DFP, appeared as one of the most explored chelating units in the discovery of new therapeutics for Fe-overload[8,9] and Al-overload[10] as well as several metal-related disorders.[11] Many strategies have

[a] Centro de Química Estrutural, Instituto Superior Técnico, Universidade de Lisboa, Av. Rovisco Pais 1, 1049-001 Lisboa, Portugal. E-mail: masantos@ist.utl.pt

[b] Dipartimento di Scienze Chimiche e Geologiche, Università di Cagliari, Cittadella Universitaria, 09042 Monserrato-Cagliari, Italy

[c] Centro de Ciências e Tecnologias Nucleares (C2TN), Instituto Superior Técnico, Universidade de Lisboa, Estrada Nacional 10, 2695-066 Bobadela LRS, Portugal

[d] Dipartimento di Chimica e Farmacia, Università di Sassari, Via Vienna 2, 07100 Sassari, Italy

† Electronic supplementary information (ESI) available. See DOI: 10.1039/c8nj00116b

‡ Authors contributed equally.
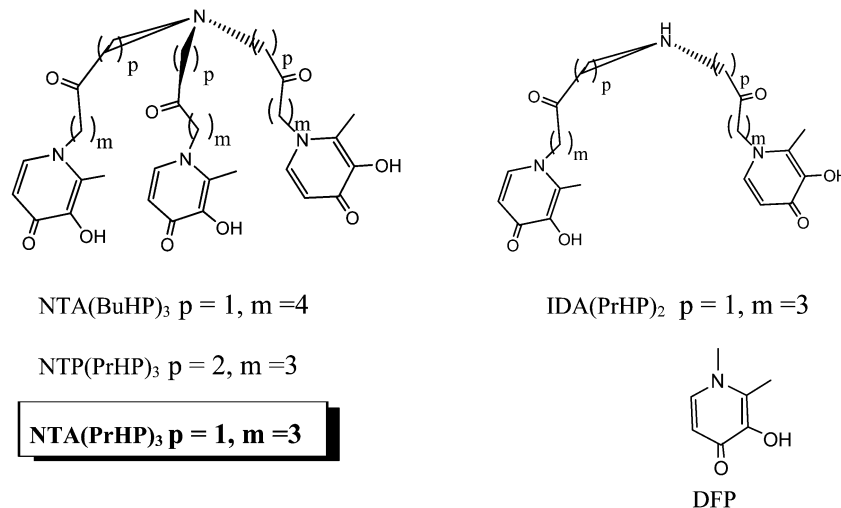
Fig. 1 Structure of the ligand in the study, NTA(PrHP)$_3$, and a selection of analogous 3,4-HP-based ligands.

been based on structural modifications of bidentate 3,4-HP mono-chelators to improve bioavailability or to provide relevant biological roles for several therapeutic applications, namely for neurodegenerative disorders.[12,13] Also, the development of multidentate 3,4-HP, by appending two or three HP units to the same scaffold, has challenged several authors in view of new therapeutic or diagnostic agents.[10,11,14,15] Indeed, such polydentate ligands, especially the hexadentate derivatives, present advantages over the simpler bidentate 3,4-HPs to sequester M^{3+} because they fulfill the metal coordination by the formation of 1:1 (M^{3+}:L) complexes with improved thermodynamic stability and kinetic inertness.

We have reported the development of tetradentate bis-(3-hydroxy-4-pyridinone), IDA(PrHP)$_2$,[16] and, later, also hexadentate tris-(3-hydroxy-4-pyridinone) ligands (e.g. NTA(BuHP)$_3$ and NTP(PrHP)$_3$)[17] (Fig. 1), through the attachment of, respectively, two and three 3,4-HP units to iminobis- and iminotris-carboxylic acid anchoring skeletons. In order to further explore hexadentate 3,4-HPs previously reported we have developed and present herein the study of a new tripodal analogue, NTA(PrHP)$_3$, which, as compared to both iminotriscarboxylic-hydroxypyridinone analogues (NTA(BuHP)$_3$ and NTP(PrHP)$_3$), has linker chains (between the apical tertiary amine and 3,4-HP chelating moieties) truncated in the 1-methylene group. The design strategy of this ligand was based on the assumption that the size of the linker could still be long enough to allow the wrapping of the metal ion by the 3,4-HP moieties, as herein indicated by molecular modeling. On the other hand, such truncation, by reducing the ligand molecular weight, could represent an advantage for the membrane crossing ability and accessibility to cytoplasmic iron pools. Specifically, herein, we describe the synthesis of a new hexadentate compound, followed by the study of its physico-chemical properties and of its metal complexes in solution, especially the complexation ability towards Fe(III) and Al(III). The in vivo behavior as a potential sequestering agent is also assessed, namely on its ability for Ga-67 mobilization from mice previously injected with this radiotracer, as an animal model of Fe- or Al-overload.

The results are further discussed and rationalized in comparison with other ligands, namely the previously reported homologous poly- and mono-(3,4-HP).

2. Experimental

General

Unless stated otherwise, all the chemicals were of analytical reagent grade and used as supplied without further purification. Whenever necessary, the organic solvents were dried according to standard methods.[18] The chemical reactions were monitored by TLC using alumina plates coated with silica gel 60 F254 (Merck). Column chromatography separations were performed on silica gel Merck 230–400 mesh (Geduran Si 60). The melting points (m.p.) were measured using a Leica Galen III hot stage apparatus and are uncorrected. ^{1}H- and ^{13}C-NMR spectra for the synthesis of the compounds were recorded on Bruker Advance II 300 MHz and 400 MHz spectrometers. Chemical shifts are reported as parts per million, ppm (δ), from internal reference TMS (tetramethylsilane) and coupling constants (J) in Hertz. The following abbreviations are used: s = singlet, d = doublet, t = triplet, and m = multiplet. Mass spectra (ESI-MS) were recorded on a 500 MS LC Ion Trap (Varian Inc., Palo Alto, CA, USA) mass spectrometer equipped with an ESI ion source, operated in the positive or negative ion mode. Elemental analyses were performed using a Fisons EA1108 CHNF/O instrument and were within a limit of ±0.4%.

For solution studies, NaOH, NaCl, FeCl$_3$, AlCl$_3$ and HCl solutions were purchased from Aldrich. All the reagents were used without any further purification. Carbonate-free 0.1 M NaOH solution was prepared as previously reported.[19] The metal ion standard solutions were prepared by dissolving the required amount of chloride salts in pure double distilled water and adding a stoichiometric amount of HCl to prevent hydrolysis. Fe^{3+} solution was standardized by spectrophotometric

analysis of the Fe^{3+}–Desferal complex, while Al^{3+} solution was standardized by EDTA titration.

Synthesis

3-(Benzyloxy)-2-methyl-4H-pyran-4-one (2). To a solution of maltol (1) (30 g, 0.237 mol) in methanol (100 mL) NaOH solution (10.46 g in 30 mL of H_2O) was added dropwise with stirring. When the mixture became a clear solution, BnCl (26.99 g, 0.213 mol) was added dropwise over 0.5 h and the reaction mixture was heated for 12 h. The reaction mixture was cooled to room temperature, filtered to remove the inorganic salt, and the filtrate solution was concentrated under reduced pressure. The crude mixture was taken in CH_2Cl_2 (300 mL) and washed with 5% NaOH aqueous solution (2×100 mL) to remove the excess maltol. The organic layer was washed with brine and dried over anhydrous sodium sulfate and finally evaporated to give the desired compound as an oily material with 82% yield. ^{1}H NMR (400 MHz, MeOD-d_4), δ (ppm): 7.93 (1H, d, J = 8.0 Hz, H-6, Py), 7.37–7.44 (5H, 2d and 3t, Ph), 6.43 (1H, d, J = 8.0 Hz, H-5, Py), 5.10 (2H, s, OCH_2Ph), 2.14 (3H, s, CH_3), ^{13}C NMR (400 MHz, MeOD-d_4), δ (ppm): 13.68, 73.38, 116.14, 128.15, 128.79, 136.78, 143.46, 155.16, 161.21, 175.98; m/z (ESI-MS): calculated for $C_{13}H_{12}O_3$ = 216.23, obtained 239.13 (M + Na)$^+$.

1-(3-Aminopropyl)-3-(benzyloxy)-2-methylpyridin-4(1H)-one hydrochloride (3). A mixture of 3-(benzyloxy)-2-methyl-4H-pyran-4-one (2), 1,3-propylenediamine (5.65 g; 0.076 M) and 2 M sodium hydroxide solution (8 mL) was heated to reflux for 16–18 h. The completion of the reaction was monitored by TLC. On completion, the reaction mixture was cooled and concentrated under reduced pressure to give an oily mass. The oily mass so obtained was acidified (until pH = 1–2) with 4 M HCl solution under ice cold conditions. The acidic aqueous solution was then washed with diethyl ether (3×75 mL). Finally the acidic aqueous solution was basified (pH = 9–10) with 10 M NaOH solution and extracted with ethyl acetate (3×100 mL). The combined ethyl acetate solution was washed with brine solution and dried over anhydrous sodium sulfate. The ethyl acetate solution was concentrated under reduced pressure and subjected to precipitation in the form of a salt by treating it with saturated hydrochloride methanol. The salt so obtained was filtered and dried to give the desired compound 3 as a light brown solid in 40% yield; ^{1}H NMR (400 MHz, D_2O), δ (ppm): 7.64 (1H, d, J = 8.0 Hz, 6-HPy), 7.32 (5H, s, Ph), 6.50 (1H, d, J = 8.0 Hz, 5-HPy), 4.91 (2H, s, OCH_2Ph), 3.96 (2H, t, J = 8.0 Hz, CH_2N), 2.91 (2H, t, J = 8.0 Hz, CH_2–NH_2), 2.01 (3H, s, CH_3), 1.91–1.96 (2H, m, $CH_2CH_2CH_2$); ^{13}C NMR (400 MHz, D_2O), δ (ppm): 12.22, 27.56, 36.33, 51.23, 74.04, 116.38, 128.64, 128.89, 129.72, 135.81, 140.61, 144.72, 145.52, 173.10; m/z (ESI-MS): calculated for $C_{16}H_{20}N_2O_2$ = 272.34, obtained 273.21 (M + H)$^+$.

2,2′,2″-Nitrilotris(N-(3-(3-(benzyloxy)-2-methyl-4-oxopyridin-1(4H)-yl)propyl)acetamide) (4). To a mixture of nitrilotriacetic acid (NTA) (1.83 mmol) in 25 mL of dry DMF, N-methyl-morpholine (12.81 mmol) was added under nitrogen. Few minutes later, when the reaction mixture become a clear solution, propyl-phosphonic anhydride (T3P) solution (6.04 mmol) was added

dropwise under nitrogen and the reaction was stirred for half an hour. Finally, the solution of neutral amine (obtained in MeOH over 1.2 eq. of KOH) (9) (6.04 mmol) in dry DMF was added to it under a nitrogen atmosphere and the reaction was stirred overnight at RT. After completion of the reaction (monitored by TLC), DMF was evaporated to dryness. Finally, the reaction mixture was taken in DCM (200 mL) and washed with brine solution, and the crude reaction mixture was purified by column chromatography over silica in the 9–10% MeOH–DCM system to give the desired compound 4 in 71% yield, m.p.: 93–95 °C; ^{1}H NMR (400 MHz, MeOD-d_4), δ (ppm): 7.73 (3H, d, J = 8.0 Hz, 6-HPy), 7.33–7.40 (15H, m, Ph), 6.47 (3H, d, J = 8.0 Hz, 5-HPy), 5.08 (6H, s, OCH_2Ph), 4.0 (6H, t, J = 8.0 Hz, CH_2N), 3.37 (6H, s, NCH_2CONH), 3.24 (6H, t, J = 8.0 Hz, CH_2NHCO), 2.18 (9H, s, CH_3HPy), 1.86–1.89 (6H, m, $CH_2CH_2CH_2$); ^{13}C NMR (400 MHz, MeOD-d_4), δ (ppm): 11.40, 29.84, 35.78, 51.60, 57.97, 73.05, 116.02, 127.96, 128.02, 128.85, 137.04, 139.83, 143.51, 145.76, 172.04, 173.40; (ESI-MS): calculated for $C_{54}H_{63}N_7O_9$ = 953.46, obtained 976.43 (M +Na)$^+$.

2,2′,2″-Nitrilotris(N-(3-(3-hydroxy-2-methyl-4-oxopyridin-1(4H)-yl)propyl)acetamide) (5). In a hydrogenolysis flask, 2,2′,2″-nitrilotris-(N-(3-(3-(benzyloxy)-2-methyl-4-oxopyridin-1(4H)-yl)propyl)acetamide) (1 mmol) was dissolved in methanol and 10% Pd/C was added to it. The reaction suspension was shaken for 3 h under a H_2 atmosphere (5 bar). The completion of the reaction was monitored by TLC. On completion, the reaction mixture was filtered over celite and the filtrate so obtained was concentrated under reduced pressure to give a white compound 5 in 95% yield, m.p. 118–120 °C; ^{1}H NMR (MeOD-d_4), δ (ppm): 7.60 (3H, d, J = 8.0 Hz, 6-HPy), 6.33 (3H, d, J = 8.0 Hz, 5-HPy), 4.04 (6H, t, J = 8.0 Hz, $CH_2CH_2CH_2$N), 3.36 (6H, s, NCH_2-CONH), 3.26 (6H, t, J = 8.0 Hz, CH_2NHCO), 2.37 (9H, s, CH_3HPy), 1.90–1.96 (6H, t, J = 8.0 Hz, $CH_2CH_2CH_2$); ^{13}C NMR (MeOD-d_4), δ (ppm): 10.56, 30.06, 35.90, 51.98, 58.20, 111.34, 131.24, 137.50, 146.00, 169.23, 172.05; (ESI-MS): calculated for $C_{33}H_{45}N_7O_9$ = 683.32, obtained 684.48 (M + H)$^+$. Analysis calc. for ($C_{33}H_{45}N_7O_9$. 2.2H_2O): C 54.79, H 6.88, N 13.55%; found: C 54.81, H 6.75, N 13.46%.

Solution equilibrium studies

Potentiometric–spectrophotometric measurements. Protonation and complex-formation equilibria were carried out at an ionic strength of 0.1 M NaCl, as previously described.[20] The working ligand concentration was 5.0×10^{-4} M. Complex formation studies were performed at a 1:1 metal/ligand molar ratio. Combined potentiometric–spectrophotometric measurements were performed in the 200–400 nm spectral range for protonation equilibria and in the 400–800 nm range for Fe^{3+} complexation, using 0.2 and 1 cm path lengths, respectively. Complex formation equilibria with Al^{3+} were potentiometrically studied. Protonation and complex formation data were analyzed using HyperQuad2013[21] and HypSpec2[22] programs.

ESI-MS analysis of complexes. The ESI-MS experiments were performed using a Varian 310 ESI LC–MS-MS spectrometer. The samples for analysis were prepared at a concentration of 0.1 mM both in the ligand and in metal ions in water/methanol (50 : 50) solvent. The solutions, once prepared, were incubated for 2 h before measurements. The instrument parameters were: scan

range 250–1000 m/z, needle voltage 6000 V, shield voltage 600 V, housing temperature 60 °C, drying gas temperature 120 °C, nebulizer gas pressure 40 PSI, drying gas pressure 20 PSI, and detector voltage 2000 V. The mass spectrometer was operated in the positive ion mode. Each spectrum was obtained with more than 100 individual scans. The overall charge of the analyzed ions was calculated on the basis of the distance between isotopic peaks. The formulae of the complexes were determined using the Compass Data Analysis program (Bruker Daltonik, Germany).[23]

NMR measurements. NMR experiments were performed using a Bruker Ascend™ 400 MHz spectrometer equipped with a 5 mm automated tuning and matching broad band probe (BBFO) with z-gradients. In particular, all the NMR experiments were carried out with a ligand concentration of 2 mM in D_2O and H_2O–D_2O (90%–10%) solutions at 25 °C in 5 mm NMR tubes.

2-D ^1H–^{13}C HSQC (heteronuclear single quantum coherence) spectra were acquired using a phase-sensitive sequence employing Echo- Antiecho-TPPI gradient selection with a heteronuclear coupling constant J_{XH} = 145 Hz, and shaped pulses for all 180° pulses on the f2 channel with decoupling during acquisition; sensitivity improvement and gradients in back-inept were also used. Relaxation delays of 2 s and 90° pulses of about 10 μs were applied in all the experiments. Solvent suppression for 1D ^1H, 2D ^1H–^1H TOCSY (total correlation spectroscopy) and ^1H–^1H ROESY (rotating-frame Overhauser effect spectroscopy) experiments were achieved using excitation sculpting with gradients. The spin-lock mixing time of the TOCSY experiment was obtained with MLEV17. ^1H–^1H TOCSYs were performed using a mixing time of 60 ms. A combination of 1D, 2D TOCSY, HSQC and ROESY experiments was employed to assign the signals of both free and metal-bound ligand at different pH values as previously reported for similar systems.[24–27] All NMR data were processed using TopSpin (Bruker Instruments) software, and analyzed by Sparky 3.11 and MestRe Nova 6.0.2 (Mestrelab Research S.L.) programs.

Molecular modelling studies

The optimized structures of the iron complex, Fe^{3+}–NTA(PrHP)$_3$, were calculated and compared with the homologue Fe^{3+}–NTA-(BuHP)$_3$, previously reported,[17] as well as the corresponding ligands NTA(PrHP)$_3$ and NTA(BuHP)$_3$. They were fully optimized by quantum mechanical calculations based on Density Functional Theory (DFT) methods included in the Gaussian 03 computational software.[28] A first optimization step was carried out using the B3LYP functional and the LANL2MB basis set, a direct SCF calculation and an SCF convergence criterion of 10^{-5}. The B3LYP hybrid functional has been shown to be an accurate density functional method[29] and it gives good geometries for the first-row transition metal complexes.[30] The B3LYP model is a combination of the Becke three-parameter hybrid functional[31] with the Lee–Yang–Parr correlation functional (which also includes density gradient terms).[32,33] Regarding the basis set, LANL2MB specifies the STO-3G in the first row[34] and Los Alamos ECP plus MBS on Na–Bi.[35] The results of these calculations were then submitted to second optimization using the B3LYP functional with the LANL2DZ basis set that describes the Fe atom through the Los Alamos ECP and an

essentially double-zeta basis set including 3d orbitals and 3d diffuse functions for the valence shell. In this basis set, the remaining atoms are described through the Dunning-Huzinaga full double-ζ basis set.[36]

Pharmacokinetic parameters for the ligand were also calculated using the QikProp program,[37] included in the computational software Maestro.[38]

Biodistribution studies

A ^{67}Ga-citrate injection solution was prepared by dilution of ^{67}Ga citrate from Mallinckrodt Medical B.V. with saline to obtain a final radioactive concentration of approximately 5–7 MBq/100 μL. Biodistribution studies were carried out in groups of 3 female Balb-C mice (randomly bred, Charles River, from CRIFFA, France) weighing *ca.* 22–25 g. Mice were intravenously (i.v.) injected with 100 μL (5.5 MBq) of ^{67}Ga citrate *via* the tail vein immediately followed by an intraperitoneal (i.p.) injection of 0.5 μmol of the ligand in 100 μL saline. Animals were maintained on a normal diet *ad libitum* and were sacrificed by cervical dislocation at 15 min, 1 h and 24 h post-administration. The administered radioactive dose and the radioactivity in sacrificed animals were measured using a dose calibrator (Capintec CRC25R). The difference between the radioactivity in the injected and sacrificed animal was assumed to be due to whole body excretion. Tissue samples of main organs were then removed for counting in a gamma counter (Berthold LB2111, Berthold Technologies, Germany). Biodistribution results were expressed as percent of injected activity per gram of organ (%I.A./g) and presented as mean values ± SD. Biodistribution data were evaluated by analysis of variance. The level of significance was set at 0.05 (two-sided). Animal studies were carried out under the supervision of well-experienced researchers in laboratory animal facilities licensed by the National Authority in compliance with the principles of laboratory animal science on animal care, protection and welfare. The research project was also approved by the National Authority according to the National and European Legislation.

3. Results and discussion

Synthesis and characterization

The new tripodal chelator NTA(PrHP)$_3$ was designed to contain three 3,4-HP coordinating groups attached to an imino-tricarboxylic skeleton (Fig. 1), following a general strategy recently proposed by our group for tripodal hexadentate 3,4-HP-based ligands,[17] but with a 1-atom-truncated spacer to reduce molecular weight and potentially improve the membrane crossing ability. This ligand was synthesized through a straightforward method outlined in Scheme 1. 3.3 mole equivalents of 1-(3′-aminopropyl)-3-benzyloxy-2-methyl-4-pyridinone were used to be condensed with 1 mole equivalent of iminotriacetic acid (NTA), in the presence of a base (*N*-methyl-morpholine, 7 mole equivalent) and the coupling agent propylphosphonic anhydride (T3P, 3.3 mole equivalents), in dry DMF. Purification by silica-gel chromatography column with a mixture of DCM–MeOH as the eluent afforded the tris-benzyloxypyridinone, NTA(PrHPBz)$_3$, in 71% yield. Removal of
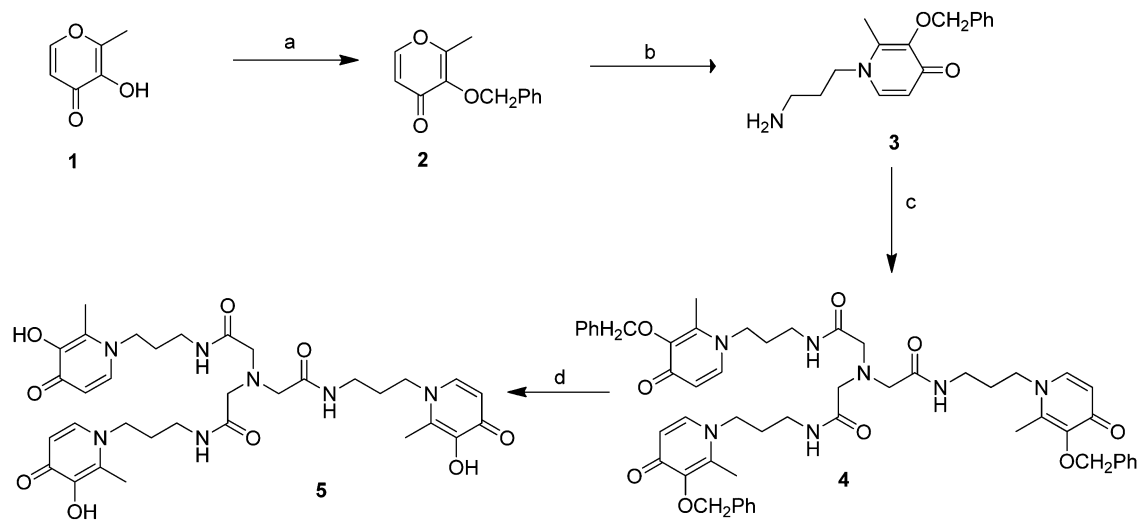
Scheme 1 Synthesis of NTA(PrHP)$_3$, reagents and conditions: (a) MeOH, NaOH (1.1 eq.), benzyl chloride (0.9 eq.), reflux; (b) 2 M NaOH, MeOH, 1,3-diaminopropane, reflux; (c) NTA (1 mole eq.), NMM, (7 mole eq.), T3P (3.3 mole eq.), dry DMF, RT; (d) MeOH, H$_2$, Pd/C.

the benzyl protecting groups by standard hydrogenolysis (5 bar atm H$_2$, over 10% Pd/C) lead to the final product, NTA(PrHP)$_3$, as a beige powder (95%).

Protonation equilibria. The protonation equilibria of the ligand NTA(PrHP)$_3$ (Scheme 2) have been studied by potentiometry, UV-vis spectrophotometry and ^{1}H-NMR spectroscopy.

The protonation constants reported in Table 1 were evaluated at 25 °C and an ionic strength of 0.1 M NaCl by potentiometric titration, except that related to the formation of the species LH$_7^{4+}$, evaluated from the ^{1}H NMR spectra collected between pH 2.8 and 1.0. The corresponding distribution curves are shown in Fig. 2.

The attribution of each calculated stepwise protonation constant to individualized protonation processes of specific basic groups in the molecule, useful in discussing the present results, in comparison with those of the NTA(BuHP)$_3$ and NTP(PrHP)$_3$, was based on the spectrophotometric and ^{1}H-NMR results.

Table 1 Protonation constants of NTA(PrHP)$_3$ (L = deprotonated ligand) (total and stepwise) evaluated from the potentiometric titration at 25 °C and 0.1 M NaCl ionic strength. The stepwise protonation constants of homologous ligands NTA(BuHP)$_3$ and NTP(PrHP)$_3$ are also reported in the two last columns for comparison[17]

Species	log β	log K	log $K_{\text{NTA(BuHP)}_3}$	log $K_{\text{NTP(PrHP)}_3}$
LH^{2-}	10.75(2)	10.75	9.98	9.946
LH$_2^-$	20.60(2)	9.85	9.83	9.84
LH$_3$	29.94(3)	9.34	8.94	9.091
LH$_4^+$	34.13(4)	4.19	3.88	6.77
LH$_5^{2+}$	—	—	3.11	3.81
LH$_6^{3+}$	40.17(4)	—	2.35	3.14
LH$_7^{4+}$	41.4(1)	1.2	1.4	2.76

The UV-vis spectra collected in the 3.1–6.8 pH range (Fig. 3A) look similar to those due to the formation of positively charged deferiprone (DFP),[39] and those collected during the basic titration in the 7.8–11.3 pH range (Fig. 3B) similar to those related to the protonation of the phenate group in DFP.[39]
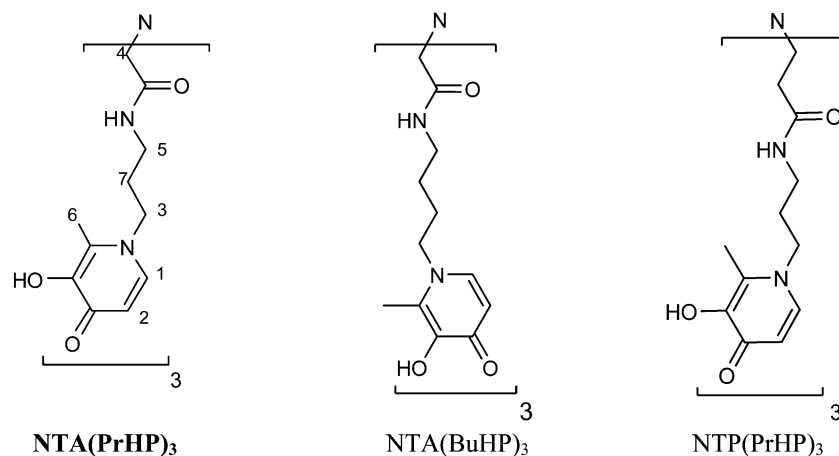
Scheme 2 Schematic structure (and numbering scheme) of NTA(PrHP)$_3$ and of the previously studied homologous ligands, NTA(BuHP)$_3$ and NTP(PrHP)$_3$.
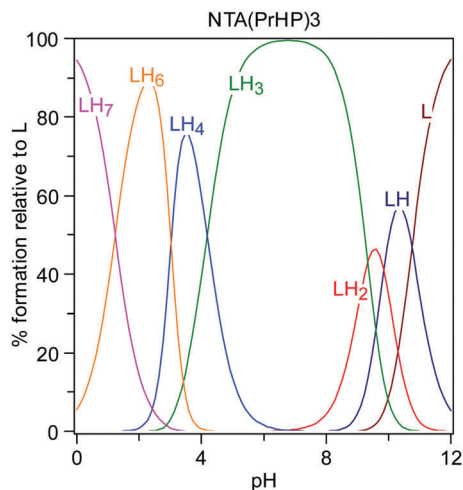
Fig. 2 Speciation plots of ligand NTP(PrHP)$_3$ calculated using the protonation constants in Table 1.

The higher intensity is due to the presence of three 3,4-hydroxypyridinone units in the ligand NTA(PrHP)$_3$. These similarities lead us to attribute the first three protonation steps to the O$^-$ groups in the 3,4-HP units. Analogously, the further three steps were attributed to the protonation of the three 3,4-HP units to give LH$_4^+$, LH$_5^{2+}$ and LH$_6^{3+}$ species (the last two protonation steps take place simultaneously). These protonation steps take place presumably on the three carbonyl groups, as previously reported for DFP,[39] or on the pyridinyl nitrogen atom, as reported by Chaves et al.[17] The spectral data, processed with the HypSpec program,[40] gave the same protonation constants obtained by potentiometric results (Table 1) in the limits of the experimental precision. The last protonation to give the LH$_7^{4+}$ species was observed only in the NMR spectra collected between pH 2.8 and 1.0, and the corresponding protonation constant was evaluated with the HypNMR program. This last step was attributed to the protonation of the apical nitrogen atom. The unexpected low values obtained for these protonation constants may be explained by the formation of intramolecular hydrogen-bonding (CONH$\cdots$N) networks

(maybe trifurcated) that are stronger for NTA(PrHP)$_3$ ($p = 1$) than for NTP(PrHP)$_3$ ($p = 2$), due to the formation of the corresponding 5- and 6-membered intermediates.

All NMR results are reported in the ESI:† the ^{1}H NMR spectra in Fig. S1; the variation of the ^{13}C and ^{1}H NMR chemical shifts, as a function of pH, in Fig. S2, and the intrinsic chemical shifts of the species evaluated by the HypNMR program[22] in Tables S1 and S2. The good fitting remarks the optimal agreement between potentiometric and NMR results.

The individual chemical shift of each nucleus in each chemical species and their variations in the various protonation steps, reported in Tables S1b and S2b (ESI†) for ^{1}H and ^{13}C respectively, provide support to the attribution of the protonation steps to specific basic groups. In particular, the variations of individual chemical shifts of C2, H2, C3, H3 and to a lesser extent C7, H7 confirm the attribution of the last three protonation steps to the pyridinyl nitrogen atoms. The protonation constants of NTA(PrHP)$_3$ are in the same range of those observed for NTA(BuHP)$_3$ and NTP(PrHP)$_3$. It has to also be remarked that the first protonation of the phenolate group is about 0.8 units higher, as well as the first pyridinyl nitrogen atom is about 0.3 units higher.

Complex formation equilibria with Fe^{3+}. Since Fe^{3+} is almost completely complexed at the start of titration, the potentiometric data alone do not allow the calculation of the corresponding formation constants. Therefore, we studied the Fe^{3+}–NTA(PrHP)$_3$ complex formation by a simultaneous spectrophotometric and potentiometric procedure.[20] First we prepared a set of 1 : 1 Fe/L solutions of increasing hydrochloric acid concentration. The ionic strength (0.1 M) was reached with appropriate amounts of HCl and NaCl until pH 1; at more acidic pH values, the ionic strength was no more controlled. A second set of measurements were obtained by titrating with 0.1 M NaOH until pH 2.9, and precipitation occurred at pH > 2.9 for the formation of the uncharged complex FeL (Fig. 4).

Spectrophotometric data, together with the corresponding proton concentrations, processed with the HypSpec program,[40] allowed the calculation of the iron complex formation constants in Table 2, and of the speciation plot as shown in Fig. 5A.
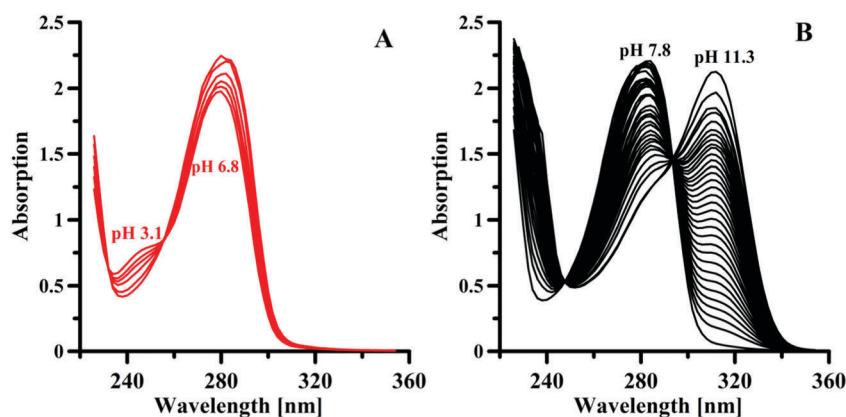
Fig. 3 Representative spectra (0.2 cm optical path) collected during the titration of NTA(PrHP)$_3$ 5.0 × 10^{-4} M: (A) with HCl 0.1 M from pH 6.8 to 3.1; (B) with NaOH 0.1 M from pH 7.8 to 11.3.

Fig. 4 (A) Representative spectra of the system Fe^{3+}–L collected in the pH range 0–2.9 at [NTA(PrHP)$_3$] = [Fe^{3+}] = 5×10^{-4} M. (B) Absorptivity spectra of differently protonated forms of iron complexes with NTA(PrHP)$_3$.

Table 2 Global formation constants for the complexes of NTA(PrHP)$_3$ with the trivalent metal ions M^{3+} (M = Fe, Al) at 25 °C, 0.1 M NaCl ionic strength

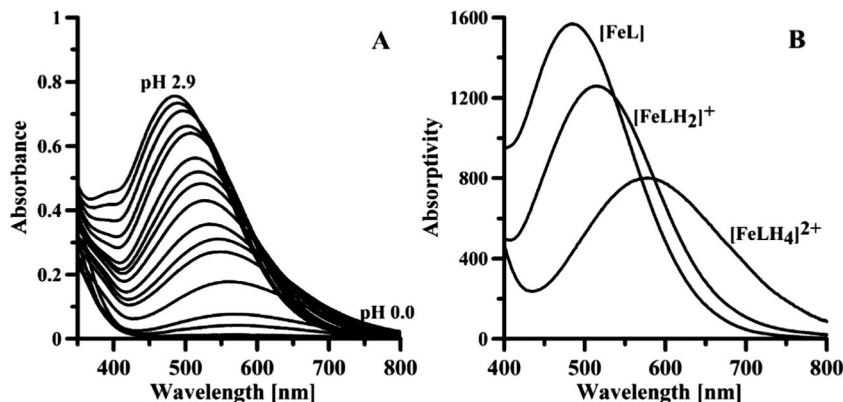| Species	$\log \beta$ (FeLH$_i$)	$\log \beta$ (AlLH$_i$)
ML	33.11(3)	26.58(7)
[MLH]$^+$	—	30.40(7)
[MLH$_2$]$^{2+}$	38.04(4)	33.1(1)
[MLH$_4$]$^{4+}$	40.77(4)	39.0(1)

Anyhow, the formation of more than 80% of this uncharged complex allowed the calculation of reliable stability constants.

The [FeLH$_4$]$^{4+}$ complex, characterized by a band centered at about 580 nm, is observed in the pH range 0–1, which transforms into [FeLH$_2$]$^{2+}$ from pH 1 to 1.8, characterized by a band at 510 nm. Finally, the neutral FeL complex formation was observed in the pH range 1.8–2.9 with a band centered at 480 nm. The absorptivity spectra are presented in Fig. 4B.

According to the profile of the pH dependent absorptivity spectra, the [FeLH$_4$]$^{4+}$ species has the metal ion coordinated by one hydroxypyridinone unit (as in the [FeL]$^{2+}$ complex with DFP)[39] that has lost both the acid protons, the phenolic one for iron coordination and that on the pyridinyl nitrogen atom due to the polarizing effect of the coordinated Fe^{3+}. In the [FeLH$_2$]$^{2+}$ species, iron is coordinated also by a second hydroxypyridinone unit (as in the [FeL$_2$]$^+$ with DFP) that has lost its acidic protons. Finally, already at pH 3 a neutral complex is formed, coordinated by all the three-hydroxypyridinone groups. The formation of this neutral form leads to complex precipitation. The filtered precipitate, dissolved by the addition of hydrochloric acid and properly diluted, gave the same spectra as that previously observed in Fig. 4. A comparison can be done with the analogous complexes with NTA(BuHP)$_3$ and NTP(PrHP)$_3$,[17] whose structures are reported in Scheme 1. The three tris(3,4-HP) chelators are characterized by arms of the type –(CH$_2$)$_p$-C(O)NH-(CH$_2$)$_m$, in which $p + m = 5$ for the previously studied NTA(BuHP)$_3$ and NTP(PrHP)$_3$ chelators, with different peptide bond positions, and $p + m = 4$ for NTA(PrHP)$_3$, which has a shorter arm.

The shorter arm determines a decrease in the strength of iron binding (pFe) of about 1.6 units relative to the non-truncated tris-HP direct homologue (NTA(BuHP)$_3$) and an increase of 0.5 units relative to the bis-HP analogue, IDA(PrHP)$_2$.[16] However the pFe value found for the NTA(PrHP)$_3$–Fe^{3+} system is 7-orders of magnitude higher than that of the 3-hydroxy-4-pyridinone drug (DFP) under clinical use,[41] and so this ligand is still a strong chelator. It has to be noticed that at an iron concentration of 1×10^{-5} M no precipitation occurs, rendering the possible use of NTA(PrHP)$_3$ in vivo. From the complexation data with transferrin (Table 3),[42,43] the new ligand was able to compete with apotransferrin for iron. Although we are aware of the limits of the pM value,[44] it is well recognized as a good parameter for evaluation and comparison of chelation strength.

Complex formation equilibria with Al^{3+}. The complex formation equilibria of NTA(PrHP)$_3$ with Al^{3+} was studied by potentiometric titrations until pH 3.6, where precipitation occurred. As in the case of iron, it was possible to redissolve the filtered precipitate by acid addition and to confirm that it was an aluminium complex from the registered NMR spectra. The complexation scheme is similar to that observed for iron, but with lower values of formation constants (Table 2). The only remarkable difference is the presence of the complex [AlLH]$^+$ formed from the [AlLH$_2$]$^{2+}$, coordinated by two hydroxypyridinone moieties, that loses the pyridinyl proton.

Therefore, similarly to the iron, the aluminium complexation ability of the present ligand can be compared with that of other ligands on the basis of the corresponding pAl values. In fact, as observed with Fe^{3+}, at an aluminium concentration of 1×10^{-5} M no precipitation occurred, thus allowing the use of NTA(PrHP)$_3$ in vivo. Analysis of data in Table 3 shows that for NTA(PrHP)$_3$ the pAl value decreases by 2-orders of magnitude as compared to the corresponding tris-HPs homologues with longer linkers (NTA(BuHP)$_3$ and NTP(PrHP)$_3$), but an increase of, respectively, 1- and 4-orders of magnitude relative to the bis-HP homologue, IDA(PrHP)$_2$, and the marketed mono-HP drug (DFP). Therefore, the new ligand appears as a strong ligand that also seems to compete with apotransferrin for aluminium.
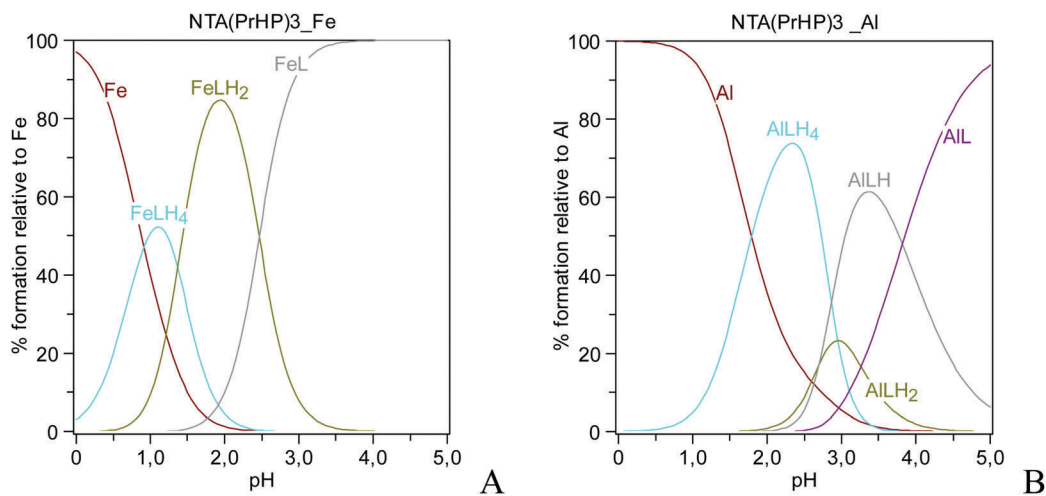
Fig. 5 (A) Speciation plot of the Fe^{3+}–$NTA(PrHP)_3$ complexes relative to $C_{Fe} = C_L = 1 \times 10^{-3}$ M. (B) Speciation plot of the Al^{3+}–$NTA(PrHP)_3$ complexes relative to $C_{Al} = C_L = 1 \times 10^{-3}$ M.

Table 3 pM^a values calculated for the $NTA(PrHP)_3$–M^{3+} system (M = Fe, Al) and for the corresponding complex systems with homologous ligands ($NTA(BuHP)_3$, $NTP(PrHP)_3$, $IDA(PrHP)_2$), DFP and transferrin

	$NTA(PrHP)_3{}^b$	$NTA(BuHP)_3{}^b$	$NTP(PrHP)_3{}^b$	$IDA(PrHP)_2{}^c$	DFP^d	Transferrin
pFe	26.3	27.9	29.4	25.8	19.3	20.3^e
pAl	19.8	22.0	22.4	18.8	16.0	14.5^f

^{a} pM = $-\log[M]$ with $C_L/C_M = 10$ at pH = 7.4, $C_M = 10^{-6}$ M. ^{b} Admitting that there is no precipitation for the low concentration values of pM determination, ref. 17. ^{c} Ref. 16. ^{d} Ref. 42. ^{e} Ref. 43. ^{f} Ref. 44.

Aimed at gaining some support for the equilibrium model, the ^1H NMR spectra of the system $NTA(PrHP)_3$–Al^{3+} were also registered. Comparison of the spectra of the free ligand and ligand–Al systems shows that only the signals of protons H1 and H2 of the three hydroxypyridinone rings present a clear change in the chemical shift. It is possible to remark from spectra 1D (Fig. S3, ESI†) and 2D HSQC (Fig. S4, ESI†) (TOCSY data not showed) that the protons H1 and H2 lose their degeneration and show now three separate signals. From the distribution plot in Fig. 5B this is related to the existence at pH 3.9 of different species in which the Al^{3+} ion is chelated by a different number of DFP units.

Also the three NH signals are affected, which shows that the three new signals separate from that of the free ligand.

ESI-MS studies of metal complex formation. The ESI-MS studies confirm previous results showing the formation of 1:1 metal/ligand stoichiometry complexes for all the metal ions. In the case of Fe^{3+}, the signal at 735.4 m/z corresponds to the $[FeLH]^+$ complex ($[C_{33}H_{43}FeN_7O_9]^+$). Thus, differently from some previously reported MS studies, which indicated for this type of chelators the probable formation of 2:2 instead of 1:1 complexes,[45] the ESI-MS spectrum obtained herein has all the peaks separated by one mass unit, thus identifying a 1:1 FeL complex. Analogously, the signal at 708.5 m/z for Al^{3+} corresponds to the $[AlLH]^+$ complex ($[C_{33}H_{43}AlN_7O_9]^+$). The experimental data agree well with the calculated ones presented in Table 4 and in Fig. S5 (ESI).

Molecular modelling of the iron complexes

Since efforts to obtain adequate crystalline samples of the Fe–$NTA(PrHP)_3$ complex for X-ray diffraction were unsuccessful, molecular modeling studies were performed in order to evaluate the stability of the ferric complexes with the truncated new ligand $NTA(PrHP)_3$ and compared with the data previously obtained for the corresponding homologue with the longer linker $NTA(BuHP)_3$.[17] Hence, molecular simulations were carried out in the same previously adopted conditions, with full geometry optimization of the iron complex by quantum mechanical calculations based on DFT methods included in the Gaussian 03 program software,[28] combining the B3LYP functional[31] with the basis sets LANL2MB[35] and LANL2DZ.[36] No symmetry constrains were imposed during geometry optimization.

Analysis of the energy-minimized structure for the $Fe:NTA(PrHP)_3$ complex shows that it is quite similar to that found for $Fe:NTA(BuHP)_3$, namely in terms of metal hexacoordination and octahedral geometry (Fig. 6), in agreement with our expectations and solution studies. Nevertheless, the ferric complex with $NTP(PrHP)_3$ has an "in" conformation, similar to that found in another tripodal hexadentate complex with CP130,[46] and for both free corresponding ligands ($NTA(PrHP)_3$ and $NTA(BuHP)_3$), while the homologue complex, Fe^{3+}–$NTA(BuHP)_3$, has an "out" conformation, and so with the free electron pair of the apical tertiary N amine pointing away from the metal ion.[17]

The "in" conformation of the N atoms may favor the formation of more stable intramolecular hydrogen bonds although the

Table 4 Experimental and calculated m/z values for pure ligand (L), NTA(PrHP)$_3$, and its complexes with the trivalent metal ions Fe^{3+} and Al^{3+}

Name	Formula	m/z experimental	m/z calculated
[LH$_4$]$^+$	[C$_{33}$H$_{46}$N$_7$O$_9$]$^+$	684.5	684.3
		685.5	685.3
		686.5	686.3
[LH$_3$ + Na]$^+$	[C$_{33}$H$_{45}$N$_7$O$_9$Na]$^+$	706.5	706.3
		707.5	707.3
		708.5	708.3
[FeLH]$^+$	[C$_{33}$H$_{43}$FeN$_7$O$_9$]$^+$	735.4	735.3
		736.4	736.3
		737.4	737.2
		738.2	738.2
		739.2	739.2
[AlLH]$^+$	[C$_{33}$H$_{43}$AlN$_7$O$_9$]$^+$	708.5	708.3
		709.5	709.3
		710.5	710.3

pre-organization of the ligand geometry for the metal coordination can result in their eventual lengthening or even disruption. Fig. 6 also indicates one H-bond between an inward N-amide and a coordinated carbonyl O-atom of another arm.

Concerning the coordination shell, the O–Fe bond lengths are in the range 1.910–1.990 Å and 1.849–1.979 Å for the complexes with NTA(PrHP)$_3$ and NTA(BuHP)$_3$, respectively, in accordance with the values found in the literature for analogous compounds[17] and reflecting also the fact that O(carbonyl)–Fe bonds are longer than O(phenolic)–Fe bonds. On the other hand, the sum of the O–Fe–O angles (O belongs to different arms) should be 540° (3 × 180°) for a regular octahedron and for the herein studied ferric complexes, with NTA(PrHP)$_3$ and NTA(BuHP)$_3$, the values obtained are *ca.* 525° and 532°, respectively. These results show that the ferric complex with NTA(PrHP)$_3$ is more distorted and consequently more strained than the one with NTA(BuHP)$_3$, due to the truncated arm that turns the structure more rigid. These molecular modeling studies are supported by the solution
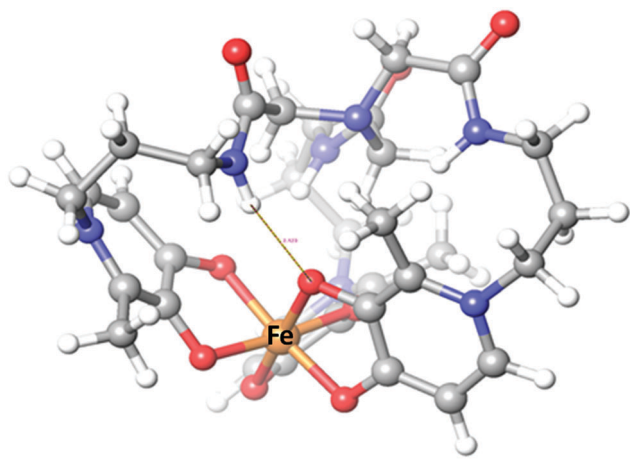
Fig. 6 DFT-minimized structure of the Fe^{3+}–L complex L = NTA(PrHP)$_3$, with indication of H-bond (NH···O bond length/angle of 2.123 Å/165.5°). Coloring of atoms: Fe orange, N blue, O red, C grey and H white.

complexation studies, which show that although the new tris-hydroxypyridinone ligand can form a 1:1 Fe:L hexacoordinated complex with distorted octahedral geometry, the Fe–NTA(PrHP)$_3$ complex is slightly less stable than Fe–NTA(BuHP)$_3$.

Since these two complexes have different number of atoms, their stability must be compared on the basis of the differences between total energy of each complex and that of the corresponding ligand (ΔE). The values obtained, −76 379 kcal mol^{-1} for the NTA(PrHP)$_3$ system and −76 401 kcal mol^{-1} for the NTA(BuHP)$_3$ system, resulted in a difference in the binding energy ($\Delta\Delta E$ = 22 kcal mol^{-1}) and, interestingly, the corresponding log $\Delta\Delta E$ = 1.34 value is close to the difference between the pFe values (1.6) of these ferric systems. Although these values do not take in account solvent effects, they provide support for the formation of 1:1 Fe:L complexes with a distorted octahedral structure, but the Fe^{3+}–NTA(PrHP)$_3$ complex with a lower stability than the higher homologue Fe–NTA(BuHP)$_3$, attributed to the linker truncation and consequently more strained metal coordination geometry.

Pharmacokinetic parameters

The simulation of the pharmacokinetic parameters, calculated by the Maestro software[38] for NTA(PrHP)$_3$ and the respective homologue NTA(BuHP)$_3$, showed quite similar descriptors. Thus, the first ligand presents some minor advantages over the second one, namely in terms of MW (683.76/725.84) and blood–brain barrier permeability expressed as log BB (−3.815/−4.894); it also presents some minor disadvantages, namely in terms of c log P (−1.969/−1.051), oral absorptivity in the gut (18/19) and a number of violations of Lipinski's rule[47] (3/2).

Biodistribution studies

Biodistribution studies were carried out in Balb-C mice to assess the efficacy of the ligand NTA(PrHP)$_3$ as a chelating agent for the mobilization of gallium in ^{67}Ga-citrate injected mice. Since the biodistribution profile of the radiotracer ^{67}Ga-citrate in mice is well-known, we evaluated the effect of the ligand on the biokinetics and elimination of the radiometal by intraperitoneal administration of 0.5 μmole of the NTA(PrHP)$_3$ solution immediately after intravenous administration of the radiotracer. Tissue distribution of ^{67}Ga in major organs up to 24 h is presented in Fig. 7.

These results indicate that the radiometal is rapidly cleared from the bloodstream mainly by the kidneys. Clearance from the major organs is also very rapid and no relevant radioactivity uptake in any organ, except the kidneys, was detected 24 h after injection. The overall rate of radioactivity excretion was high, 43.0 ± 6.2, 80.8 ± 0.3 and 98.2 ± 0.1% I.A, at 15 min, 1 h and 24 h, respectively.

Altogether, data from our animal studies demonstrated that the ligand NTA(PrHP)$_3$ has a high *in vivo* chelating ability promoting a rapid elimination of the radiometal from the animal body, mainly by urinary excretion. This favorable *in vivo* behavior is in agreement with the biodistribution and excretion profiles previously reported for two other tris(hydroxypyridinones) that were considered promising compounds for clinical application
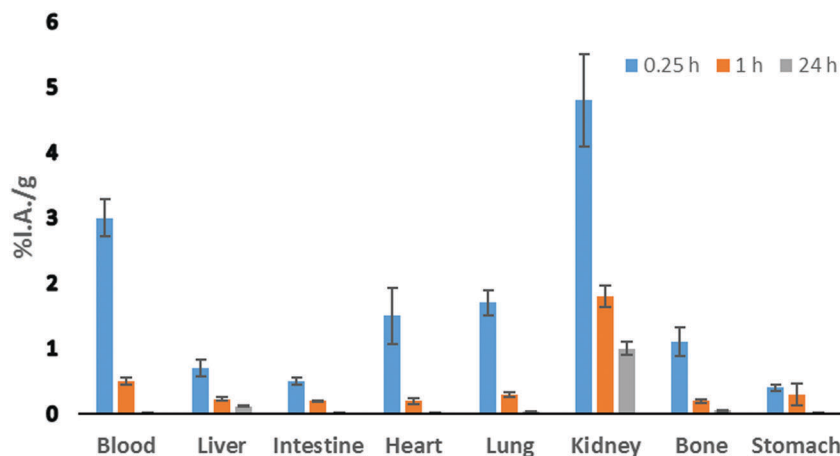
Fig. 7 Biodistribution of ^{67}Ga, after administration of ^{67}Ga-citrate with simultaneous intraperitoneal injection of NTA(PrHP)$_3$, expressed as %I. A./g, at 15 min, 1 h, and 24 h post-injection in female Balb-C mice (n = 3). (%I.A./g means percent of injected activity per gram of organ).
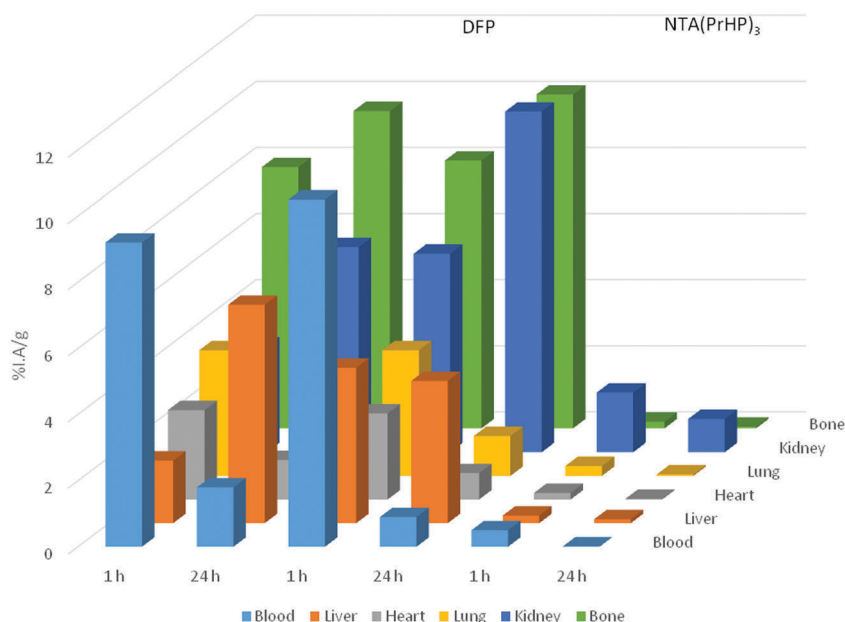
Fig. 8 Biodistribution data in the most relevant organs, expressed as % I.A./g for ^{67}Ga-citrate and ^{67}Ga-citrate with co-administration of DFP or NTA(PrHP)$_3$, 1 and 24 h after administration in female Balb-C mice (n = 3).

as metal removal agents.[11] Direct comparison between the bio-distribution profiles cannot be done since these results were also obtained in mice but in a different strain even though the trend is the same.

To further evaluate the potential usefulness of our ligand to complex *in vivo* and eliminate unwanted trivalent metal ions, we have compared our results with those found with the drug DFP in the same animal model at 1 h and 24 h (Fig. 8). The biodistribution profile of the radiotracer ^{67}Ga-citrate without simultaneous administration of any ligand is also included in the graph for comparative purposes.

Analysis of data at 1 h and 24 h after administration evidenced that the co-administration of the ligand NTA(PrHP)$_3$ has enhanced the clearance of the radiometal ^{67}Ga and the overall excretion rate of

radioactivity from the whole animal body more efficiently than the drug ($\rho < 0.01$). In fact, at 1 h more than 80% of the injected activity was already excreted due to NTA(PrHP)$_3$ while DFP only increased that excretion up to 26.5% I.A. Moreover, no radioactivity retention was detected in most of the organs, except in the kidneys. Therefore, this ligand is very efficient to chelate the radiometal in our animal model which suggests that it can be a very promising candidate as a chelating agent of other trivalent metals.

4. Conclusions

A novel tripodal hexadentate 3,4-HP-based chelator has been synthesized and then studied in solution and *in vivo* for its

properties as a potential iron or aluminium sequestering agent for chelating therapy. The design of this ligand was based on the strategy recently reported, involving the attachment of three amine-alkyl 3,4-HP chelating moieties to an aminotricarboxylic anchoring backbone. The new chelator (NTA(PrHP)$_3$) as compared with the reported homologues (NTA(BuHP)$_3$ or NTP(PrHP)$_3$), has linkers between the apical amine and the 3,4-HP chelating unit, truncated in one methylene. This truncation reduced the molecular weight of the ligand and thus improved some pharmacokinetic descriptors, but at the expense of some reduction of the metal chelating capacity, as confirmed by the molecular modelling of the iron complexes with NTA(PrHP)$_3$ and the corresponding homologous ligand, NTA(BuHP)$_3$. However, NTA(PrHP)$_3$ still presents a high capacity for metal chelation, as indicated by the corresponding pFe and pAl, which are improved by, respectively, 7- and 4-orders of magnitude, as compared with the marketed drug deferiprone. Concerning *in vivo* metal mobilization, the new ligand evidenced excellent ability, with a favourable biodistribution profile and high metal excretion rates. Thus, the new chelator shows promising ability to remove Fe and Al under *in vivo* metal overload conditions.

Conflicts of interest

There are no conflicts to declare.

Acknowledgements

References

1 E. D. Weinberg, *Metallomics*, 2010, **2**, 732.

2 G. Crisponi, V. M. Nurchi, G. Faa and M. Remelli, *Monatsh. Chem.*, 2011, **142**, 331.

3 T. Kiss, K. Gajda-Schrantz and P. Zatta, The role of aluminium in neurotoxic and neurodegenerative processes, in *Metal Ions and Life Sciences, Neurodegenerative Diseases and Metal Ions*, ed. A. Sigel, H. Sigel and R. K. O. Sigel, Wiley & Sons, Chichester, 2006, vol. I, p. 371.

4 C. Exley, *J. Inorg. Biochem.*, 1999, **76**, 133–140.

5 S. M. Ott, N. A. Maloney, J. W. Coburn, A. C. Alfrey and D. J. Sherrard, *N. Engl. J. Med.*, 1982, **307**, 709.

6 R. A. Yokel, A. K. Datta and E. G. Jackson, *J. Pharmacol. Exp. Ther.*, 1991, **257**, 100.

7 V. M. Nurchi, G. Crisponi, J. I. Lachowicz, S. Medici, M. Peana and M. A. Zoroddu, *J. Trace Elem. Med. Biol.*, 2016, **38**, 10.

8 T. Zhou, Y. Ma, X. Kong and R. C. Hider, *Dalton Trans.*, 2012, **41**, 6371.

9 (a) M. A. Santos, *Coord. Chem. Rev.*, 2002, **228**, 187; (b) M. A. Santos, M. Gil, L. Gano and S. Chaves, *J. Biol. Inorg. Chem.*, 2005, **10**, 564.

10 M. A. Santos, S. M. Marques and S. Chaves, *Coord. Chem. Rev.*, 2012, **256**, 240.

11 A. Nunes, M. Podinovskaia, A. Leite, P. Gameiro, T. Zhou, Y. Ma, X. L. Kong, U. E. Scheible, R. C. Hider and M. Rangel, *J. Biol. Inorg. Chem.*, 2010, **15**, 861.

12 M. A. Telpoukhovskaia, B. O. Patrick, C. Rodríguez-Rodríguez and C. Orvig, *Bioorg. Med. Chem. Lett.*, 2016, **6**, 1624.

13 M. A. Santos, K. Chand and S. Chaves, *Coord. Chem. Rev.*, 2016, **327–328**, 287.

14 M. A. Santos and S. Chaves, *Future Med. Chem.*, 2015, **7**, 381.

15 M. T. Ma, L. K. Meszaros, B. M. Paterson, D. J. Berry, M. S. Cooper, Y. Ma, R. C. Hider and P. J. Blower, *Dalton Trans.*, 2015, **44**, 4884.

16 M. A. Santos, S. Gama, L. Gano, G. Cantinho and E. Farkas, *J. Chem. Soc., Dalton Trans.*, 2004, 3772.

17 S. Chaves, S. M. Marques, A. M. F. Matos, A. Nunes, L. Gano, T. Tuccinardo, A. Martinelli and M. A. Santos, *Chem. – Eur. J.*, 2010, **16**, 10535.

18 *Purification of Laboratory Chemicals*, ed. W. L. F. Armarego and D. D. Perrin, Butterworth-Heinemann Press, Oxford, 4th edn, 1999.

19 A. Albert and E. P. Serjeant, *Ionization constants of acids and bases: a laboratory manual*, Methuen, 1962.

20 V. M. Nurchi, G. Crisponi, M. Crespo-Alonso, J. I. Lachowicz, Z. Szewczuk and G. J. Cooper, *Dalton Trans.*, 2013, **42**, 6161.

21 P. Gans, A. Sabatini and A. Vacca, *Talanta*, 1996, **43**, 1739. www.hyperquad.co.uk/HQ2013.htm.

22 C. Frassineti, S. Ghelli, P. Gans, A. Sabatini, M. S. Moruzzi and A. Vacca, *Anal. Biochem.*, 1995, **231**, 374. www.hyperquad.co.uk/hypnmr.htm.

23 Bruker, ESI Compass 1.3; DataAnalysis Version 4.0 (Build 234) Daltonik GmbH http://www.bdal.com.

24 M. Peana, S. Medici, V. M. Nurchi, J. I. Lachowicz, G. Crisponi, M. Crespo-Alonso, M. A. Santos and M. A. Zoroddu, *J. Inorg. Biochem.*, 2015, **148**, 69.

25 S. Medici, M. Peana, L. G. Delogu and M. A. Zoroddu, *Dalton Trans.*, 2012, **41**, 4378.

26 M. Remelli, M. Peana, S. Medici, L. G. Delogu and M. A. Zoroddu, *Dalton Trans.*, 2013, **42**, 5964.

27 V. M. Nurchi, G. Crisponi, M. Arca, M. Crespo-Alonso, J. I. Lachowicz, M. A. Zoroddu, M. Peana, G. Pichiri, M. A. Santos, S. M. Marques, J. Niclos-Gutierrez, M. J. Gonzalez-Perez, A. Dominguez-Martin, D. Choquesillo-Lazarte, Z. Szewczuk, D. Mansoori and L. Toso, *J. Inorg. Biochem.*, 2014, **141**, 132.

28 M. J. Frisch,. G. W. Trucks, H. B. Schlegel, G. E. Scuseria, M. A. Robb, J. R. Cheeseman, J. A. Montgomery, Jr., T. Vreven,

K. N. Kudin, J. C. Burant, J. M. Millam, S. S. Iyengar, J. Tomasi, V. Barone, B. Mennucci, M. Cossi, G. Scalmani, N. Rega, G. A. Petersson, H. Nakatsuji, M. Hada, M. Ehara, K. Toyota, R. Fukuda, J. Hasegawa, M. Ishida, T. Nakajima, Y. Honda, O. Kitao, H. Nakai, M. Klene, X. Li, J. E. Knox, H. P. Hratchian, J. B. Cross, V. Bakken, C. Adamo, J. Jaramillo, R. Gomperts, R. E. Stratmann, O. Yazyev, A. J. Austin, R. Cammi, C. Pomelli, J. W. Ochterski, P. Y. Ayala, K. Morokuma, G. A. Voth, P. Salvador, J. J. Dannenberg, V. G. Zakrzewski, S. Dapprich, A. D. Daniels, M. C. Strain, O. Farkas, D. K. Malick, A. D. Rabuck, K. Raghavachari, J. B. Foresman, J. V. Ortiz, Q. Cui, A. G. Baboul, S. Clifford, J. Cioslowski, B. B. Stefanov, G. Liu, A. Liashenko, P. Piskorz, I. Komaromi, R. L. Martin, D. J. Fox, T. Keith, M. A. Al-Laham, C. Y. Peng, A. Nanayakkara, M. Challacombe, P. M. W. Gill, B. Johnson, W. Chen, M. W. Wong, C. Gonzalez and J. A. Pople, *Gaussian 03, Revision C.02*, Gaussian, Inc., Wallingford CT, 2004.

29 C. W. Bauschlicher, *Chem. Phys. Lett.*, 1995, **246**, 40.

30 A. Ricca and C. W. Bauschlicher, *Theor. Chim. Acta*, 1995, **92**, 123.

31 A. Becke, *Phys. Rev. A: At., Mol., Opt. Phys.*, 1988, **38**, 3098.

32 C. Lee, W. Yang and R. G. Parr, *Phys. Rev. B: Condens. Matter Mater. Phys.*, 1988, **37**, 785.

33 B. Miehlich, A. Savin, H. Stoll and H. Preuss, *Chem. Phys. Lett.*, 1989, **157**, 200.

34 J. B. Collins, P. V. Schleyer, J. S. Binkley and J. A. Pople, *J. Chem. Phys.*, 1976, **64**, 5142.

35 P. J. Hay and W. R. Wadt, *J. Chem. Phys.*, 1985, **82**, 299.

36 T. H. Dunning Jr. and P. J. Hay, in *Modern Theoretical Chemistry*, ed. H. F. Schaefer, III, Plenum, New York, 1976, vol. 3, pp. 1–28.

37 QikProp, version 2.5, Schrödinger, LLC, New York, NY, 2005.

38 Maestro, version 9.3. Schrödinger Inc., Portland, OR, 2012.

39 V. M. Nurchi, G. Crisponi, T. Pivetta, M. Donatoni and M. Remelli, *J. Inorg. Biochem.*, 2008, **102**, 684.

40 P. Gans, A. Sabatini and A. Vacca, *Ann. Chim.*, 1999, **89**, 45. www.hyperquad.co.uk/HypSpec.htm.

41 S. Chaves, M. Gil, S. Marques, L. Gano and M. A. Santos, *J. Inorg. Biochem.*, 2003, **97**, 161.

42 R. J. Motekaitis and A. E. Martell, *Inorg. Chim. Acta*, 1991, **183**, 71.

43 W. R. Harris and J. Sheldon, *Inorg. Chem.*, 1990, **29**, 119.

44 G. Crisponi and M. Remelli, *Coord. Chem. Rev.*, 2008, **252**, 1225.

45 T. Zhou, R. C. Hider and X. Kong, *Chem. Commun.*, 2015, **51**, 5614.

46 G. Xiao, D. Helm, R. C. Hider and P. S. Dobbin, *Inorg. Chem.*, 1995, **34**, 1268.

47 C. A. Lipinski, F. Lombardo, B. W. Dominy and P. J. Feeney, *Adv. Drug Delivery Rev.*, 2012, **64**, 4.

Paper II

New strong extrafunctionalizable tris(3,4-HP) and bis(3,4-HP) metal sequestering agents: synthesis, solution and *in vivo* metal chelation

V.M. Nurchi, R. Cappai, K. Chand, S. Chaves, L. Gano, G. Crisponi, M. Peana, M. Zoroddu, M. A. Santos, *Dalton Trans.,* **2019***, 48,* 16197-16183.

Dalton Transactions

An international journal of inorganic chemistry

rsc.li/dalton

KC18

Fe³⁺
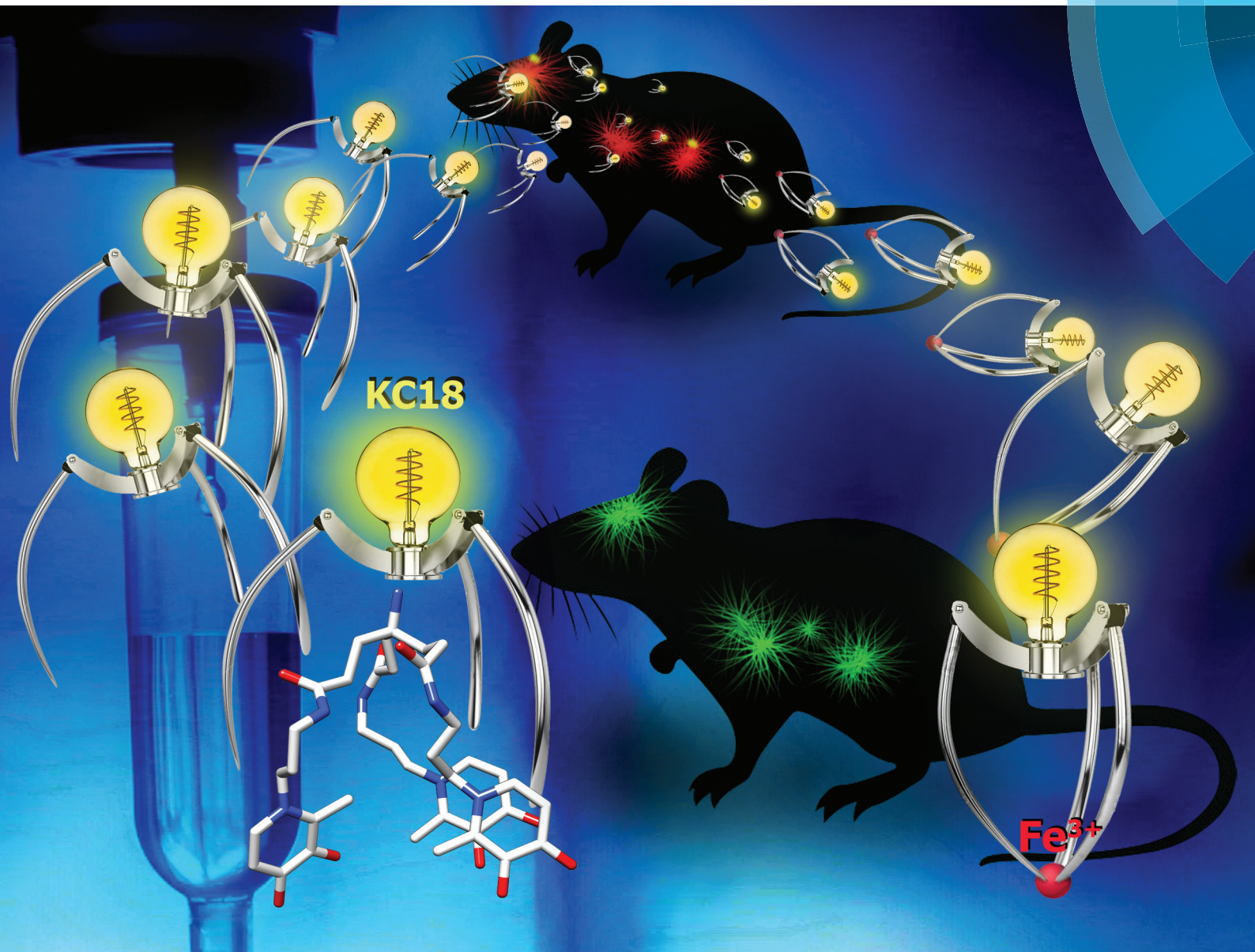
ROYAL SOCIETY OF CHEMISTRY | Celebrating IYPT 2019

PAPER
Valeria M. Nurchi, M. Amélia Santos *et al.*
New strong extrafunctionalizable tris(3,4-HP) and bis(3,4-HP) metal sequestering agents: synthesis, solution and *in vivo* metal chelation

ROYAL SOCIETY OF CHEMISTRY

Check for updates

New strong extrafunctionalizable tris(3,4-HP) and bis(3,4-HP) metal sequestering agents: synthesis, solution and *in vivo* metal chelation†

Valeria M. Nurchi, [ID] *[a] Rosita Cappai, [ID] [a,b] Karam Chand, [ID] [b] Sílvia Chaves, [ID] [b]
Lurdes Gano, [ID] [c] Guido Crisponi, [ID] [a] Massimiliano Peana, [ID] [d]
M. Antonietta Zoroddu [ID] [d] and M. Amélia Santos [ID] *[b]

Finding new multifunctional metal binders to be potentially used in diagnosis or therapy has been a subject of major challenge. Hydroxypyridinones have long been recognized as privileged chelating structures for the design of metal chelating drugs, especially towards hard metal ions, in view of their decorporation in metal overload disorders. Thus, pursuing our strategy of engineering new polydentate 3-hydroxy-4-pyridinones (3,4-HP) with extrafunctionalization capacity for sensing or targeting purposes, we report herein the synthesis and full characterization of a hexadentate (tris-3,4-HP) and a tetradentate (bis-3,4-HP) ligand, possessing three and two 3,4-HP arms *N*-attached to an aminomethanetrispropionic acid backbone, respectively. Thus, as compared with previously reported analogues, each ligand possesses an extra free amino group ready for further functionalization. Their chelating capacity towards Fe and Al was evaluated in aqueous solution, by potentiometric and spectroscopic techniques, and they proved to be strong sequestering agents for these metal ions without depletion of Zn, an essential biometal. Their excellent *in vivo* metal-decorporation capacity was also evidenced in mice injected with a radiotracer (^{67}Ga) as an animal model of metal overload pathological situations. These findings provide encouragement for further ongoing extrafunctionalizations in view of several potential biomedical applications.

1. Introduction

Iron is an essential element for many metabolic functions in organisms. However, when in excess, iron is toxic because it generates superoxide anions and hydroxyl radicals that react readily with biological molecules, including proteins, lipids, and DNA. Abnormal accumulation of iron in the body can be caused by genetic disorders related to iron absorption, such as a primary overload (hemochromatosis) or by a secondary overload associated with other diseases, requiring multiple blood transfusions (*e.g.* treatment of β-thalassemia).[1,2]

Aluminium is a nonessential toxic element that is mainly released into the ecosystem by several anthropogenic activities, thus becoming an environmental risk factor.[3] Al overload is implicated in several diseases, namely neurodegenerative and bone disorders, although Al accumulation has also been associated with some specific cancers.[4]

The use of chelating agents to control the toxicity of metal overload, or metal compartmentalization/accumulation in specific organs, has been generally considered as one of the best therapeutic strategies. Several iron-specific chelating drugs for Fe^{3+} overload were subsequently approved over the last five decades, namely Deferoxamine (DFO), Deferiprone (DFP) and Deferasirox (ICL670). These drugs are, respectively, hexadentate, bidentate and tridentate ligands, with inherently different chelating capacity, bioavailability and drawbacks.[5,6] Despite the recognized higher difficulties in the removal of Al than Fe, namely due to the generally higher Al-compartmentalization, the similarities of Al/Fe physicochemical properties lead to the use of approved iron chelators for Al-decorporation, as DFO for the treatment of Al-overload disorders (osteomalacia and encephalopathy) and also as DFP in situations of Al-accumulation in the brain (neurodegeneration), requiring higher permeability.[7,8]

[a]*Dipartimento di Scienze della Vita e dell'Ambiente, Università di Cagliari, Cittadella Universitaria, 09042 Monserrato-Cagliari, Italy. E-mail: nurchi@unica.it; Fax: +39 0706754478*
[b]*Centro de Quimica Estrutural, Instituto Superior Tecnico, Universidade de Lisboa, Av, Rovisco Pais 1, 1049-001 Lisboa, Portugal. E-mail: masantos@tecnico.ulisboa.pt; Fax: +351 218464455*
[c]*Centro de Ciencias e Tecnologias Nucleares(C2TN), Instituto Superior Tecnico, Universidade de Lisboa, Estrada Nacional 10, 2695-006 Lisboa, Portugal*
[d]*Dipartimento di Chimica e Farmacia, Università di Sassari, Via Vienna 2, 07100 Sassari, Italy*
†Electronic supplementary information (ESI) available. See DOI: 10.1039/C9DT02905B
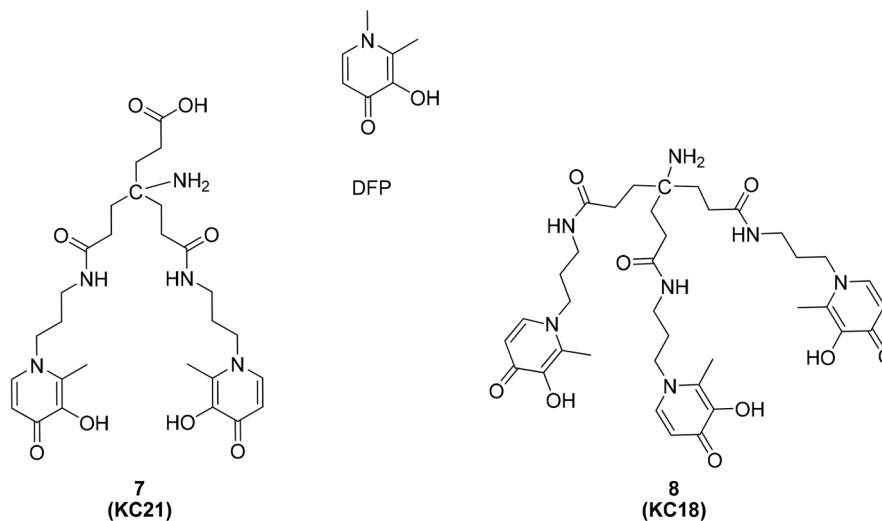
Fig. 1 Structures of the ligands in this study, bis-(3,4-HP) (**7** or KC21) and tris-(3,4-HP) (**8** or KC18), and DFP.

Since the disclosure of DFP (1,2-dimethyl-3-hydroxypyridin-4-one)[9] and its late approval (1999) as an orally active iron-selective chelating drug to treat systemic iron overload,[1] several research groups, including ours, have extensively explored this family of compounds, 3-hydroxy-4-pyridinones (3,4-HPs). The aim of this research was either to overcome one of the main drawbacks of DFP that is associated with the need for relatively high doses of DFP for its clinical use (typically 75–100 mg kg^{-1}, with poor patient compliance),[10] or to improve the pharmacokinetic properties and specific biotargeting capacity in view of its repurposing in a variety of clinical applications.[11–13] In fact, the need for high clinic dosage of DFP in iron-chelating therapy is mainly due to its bidenticity and consequent ligand dilution effects, because three ligands are necessary to complete the metal coordination sphere. Thus, quite a number of polydentate 3,4-HP-based chelators have been developed, specially hexadentate ligands to fulfill the metal coordination by formation of 1 : 1 (M^{3+} : L) complexes with improved thermodynamic and kinetic stability.[14–16] Also a lot of efforts have been made on the extrafunctionalizations of simple bidentate 3,4-HPs, aimed at improving the bio-availability and also biotargeting capacity, in view of other potential applications, namely as potential anti-neurodegeneratives.[11,17–19] Also a hexadentate 3,4-HP ligand, based on a complex synthetic procedure, has already been subjected to extrafunctionalizations aimed at achieving potential antimycobacterial activity.[20–22]

Herein, pursuing our previous strategy, we present two new polydentate 3,4-HPs, *i.e.* a hexadentate and a tetradentate ligand containing, respectively, three and two easily synthesized 3,4-HP units, which are *N*-attached to the carboxylic groups of a backbone anchor. However, as compared with the previously reported tris-3,4-HP[15,16] and bis-3,4HP analogues,[23,24] these new ligands include in their backbone support (aminomethanetrispropionic acid) a free amine group with the capacity to be easily extrafunctionalized to provide

specific sensing or targeting capacity (see Fig. 1). Besides the synthesis and characterization of the ligands, they are evaluated for their physicochemical properties in solution, especially for their acid–base properties and chelating capacity towards Fe^{3+} and Al^{3+}, using potentiometric and spectroscopic techniques, while the structure of the iron complex and the lipo-hydrophilic character of ligands are evaluated on the basis of molecular modeling studies. The zinc chelating capacity is also evaluated to anticipate whether the sequestration of iron can lead to the depletion of this bio-relevant metal ion.

Their *in vivo* metal sequestering capacity is also assessed through their mobilization of ^{67}Ga from mice previously injected with this radiotracer as an animal model of the Fe and Al overload.

2. Experimental

2.1 Equipment and reagents

For the synthesis, all the chemicals (from Sigma-Aldrich and Acros) were of analytical reagent grade and, unless stated otherwise, they were used without further purification. Whenever necessary, the organic solvents were dried according to standard methods.[25] The chemical reactions were monitored by TLC using alumina plates coated with silica gel 60 F254 (Merck). Column chromatography purifications were performed on silica gel Merck 230–400 mesh (Geduran Si 60, Merck). The melting points (m.p.) were measured using a Leica Galen III hot stage apparatus and are uncorrected. Electrospray mass spectra (ESI-MS) were obtained using a LCQ Fleet mass spectrometer operated in the ESI positive and negative ion modes. ^{1}H- and ^{13}C-NMR spectra were recorded using a Bruker Advance II 400 MHz spectrometer. Chemical shifts (δ) are reported in ppm from internal reference TMS (tetramethylsilane) and coupling constants (J) in Hertz. The following abbreviations were used: s = singlet, d = doublet, t = triplet, and

m = multiplet. Elemental analyses were performed using a Fisons EA1108 CHNF/O instrument and the results were within a limit of 0.4%.

For solution studies, NaOH, NaCl, FeCl$_3$, AlCl$_3$, ZnCl$_2$ and HCl solutions were purchased from Aldrich. All the reagents were used without any further purification. Carbonate-free 0.1 M NaOH solution was prepared as previously reported.[16] The metal ion standard solutions were prepared by dissolving the required amount of the respective chloride salts in pure double distilled water, acidified with a stoichiometric amount of HCl to prevent hydrolysis. Fe^{3+} solution was standardized by spectrophotometric analysis of the Fe^{3+}–DFO complex, while Al^{3+} and Zn^{2+} solutions were standardized by EDTA titration.

2.2 Synthesis of the ligands

3-(Benzyloxy)-2-methyl-4H-pyran-4-one (2). To a solution of maltol (1) (30 g, 0.237 mol) in methanol (100 mL), NaOH solution (10.46 g in 30 mL of H$_2$O) was added dropwise with stirring. When this mixture became clear solution, benzyl chloride (26.99 g, 0.213 mol) was added dropwise over 0.5 h and the reaction mixture was heated under reflux for 12 h. Then, it was cooled to room temperature, filtered to remove the inorganic salt, and the filtrate so obtained was concentrated under reduced pressure. The residual oil mixture was taken in CH$_2$Cl$_2$ (300 mL), and washed with 5% NaOH (2 × 100 mL) to remove the excess maltol. The organic layer was washed with brine and water, dried over anhydrous sodium sulphate and, finally, it was evaporated and dried under vacuum to give the title product, as an oily material with 82% yield. ^{1}H NMR (400 MHz, MeOD-d_4), δ (ppm): 7.93 (1H, d, J = 8.0 Hz, H-6, Py), 7.37–7.44 (5H, 2d and 3t, Ph), 6.43 (1H, d, J = 8.0 Hz, H-5, Py), 5.10 (2H, s, OCH$_2$Ph), 2.14 (3H, s, CH$_3$), ^{13}C NMR (100 MHz, MeOD-d_4), δ (ppm): 13.68, 73.38, 116.14, 128.15, 128.79, 136.78, 143.46, 155.16, 161.21, 175.98; m/z (ESI-MS): 239.13 (M + Na)$^+$.

1-(3-Aminopropyl)-3-(benzyloxy)-2-methylpyridin-4(1H)-one hydrochloride (3). To a solution of 3-(benzyloxy)-2-methyl-4H-pyran-4-one (2), (14.84 g, 0.068 mol) and about 10% excess propane-1,3-diamine (6.5 mL; 0.076 mol) in ethanol (12 mL) was added a 2 M NaOH solution (8 mL), and this mixture was heated under reflux until the completion of the reaction (16–18 h), which was monitored by TLC. The reaction mixture was cooled and concentrated under reduced pressure to give an oily residue, which was subsequently acidified in ice cold conditions (until pH = 1–2) with 4 M HCl solution. The acidic aqueous solution was then washed with diethyl ether (3 × 75 mL). Finally this acidic aqueous solution was basified (up to pH = 9–10) with 10 M NaOH solution and extracted with ethyl acetate (3 × 100 mL). The combined ethyl acetate solution was washed with brine solution and dried over anhydrous sodium sulphate. The ethyl acetate solution was concentrated under reduced pressure and subjected to precipitation in the form of a salt by treating it with hydrochloride saturated methanol solution. The salt so obtained was filtered and dried to give the desired compound 3 as a light brown solid in 40%

yield; ^{1}H NMR (400 MHz, D$_2$O), δ (ppm): 7.64 (1H, d, J = 8.0 Hz, 6-HPy), 7.32 (5H, m, Ph), 6.50 (1H, d, J = 8.0 Hz, 5-HPy), 4.91 (2H, s, OCH$_2$Ph), 3.96 (2H, t, J = 8.0 Hz, CH$_2$N), 2.91 (2H, t, J = 8.0 Hz, CH$_2$-NH$_2$), 2.01 (3H, s, CH$_3$), 1.92–1.96 (2H, m, CH$_2$CH$_2$CH$_2$); ^{13}C NMR (100 MHz, D$_2$O), δ (ppm): 12.22, 27.56, 36.33, 51.23, 74.04, 116.38, 128.64, 128.89, 129.72, 135.81, 140.61, 144.72, 145.52, 173.10; m/z (ESI-MS): 273.21 (M + H)$^+$.

7-(3-(3-(Benzyloxy)-2-methyl-4-oxopyridin-1(4H)-yl)propylamino)-4-(3-(3-(3-(benzyloxy)-2-methyl-4-oxopyridin-1(4H)-yl)propylamino)-3-oxopropyl)-4-nitro-7-oxoheptanoic acid (5). To the mixture of nitromethanetrispropionic acid (1.83 mmol) in dry DMF (25 mL), N-methylmorpholine (7.32 mmol) was added under nitrogen atmosphere. A few minutes later, when the reaction mixture became a clear solution, propylphosphonic anhydride (T3P) solution (7.32 mmol) was added dropwise under nitrogen atmosphere and the reaction mixture was stirred for 30 min. Finally, the solution of the neutral amine derivative 3 (obtained from stirring the corresponding hydrochloride amine in MeOH over 1.2 eq. of KOH) (8.05 mmol) in dry DMF was added under a nitrogen atmosphere to the reaction mixture. The reaction mixture was stirred overnight and the completion of the reaction was monitored with TLC. DMF of the reaction mixture was evaporated to dryness under vacuum and the crude mixture so obtained was added to DCM (200 mL) and washed with brine solution. Finally the organic layer was dried over anhydrous sodium sulphate and evaporated under reduced pressure to give an oily material which was then purified through column chromatography, over silica in a 9% MeOH-DCM system, to give the desired compound 5 in 48% yield. M.p. 78–80 °C; ^{1}H NMR (400 MHz, MeOD-d_4), δ (ppm): 7.69 (d, 2H, J = 8.0 Hz, PyH-6″), 7.28–7.37 (m, 10H, Ph), 6.45 (d, 2H, J = 8.0 Hz, PyH-6″), 5.04 (s, 4H, CH$_2$Ph), 3.95 (t, 4H, J = 8.0 Hz, H-3′), 3.29 (t, 2H, J = 8.0 Hz, H-2), 3.15 (t, 4H, J = 8.0 Hz, H-1′), 2.20 (brs, 10H, H-3, H-5 & H-6), 2.14 (s, 9H, CH$_3$Py), 1.81 (t, 4H, J = 8.0 Hz, H-2′); ^{13}C NMR (100 MHz, MeOD-d_4), δ (ppm): 11.41, 29.69, 29.75, 30.51, 36.01, 51.70, 73.07, 92.84, 115.95, 127.94, 128.01, 128.80, 137.02, 139.85, 143.63, 145.69, 172.66, 173.24; m/z (ESI-MS): 786.39 (M + H)$^+$.

N^1,N^7-Bis(3-(3-(benzyloxy)-2-methyl-4-oxopyridin-1(4H)-yl)propyl)-4-(3-(3-(3-(benzyloxy)-2-methyl-4-oxopyridin-1(4H)-yl)propylamino)-3-oxopropyl)-4-nitroheptanediamide (6). To the mixture of nitromethanetrispropionic acid (1.83 mmol) in 25 mL of dry DMF, N-methylmorpholine (12.81 mmol) was added under nitrogen atmosphere. A few minutes later, when the reaction mixture became clear, the solution of propylphosphonic anhydride (T3P) (8.05 mmol) was added dropwise under nitrogen atmosphere and the reaction mixture was stirred for 30 min. Finally, the solution of anhydrous neutral amine 3 (obtained in MeOH over 1.2 eq. of KOH) (8.05 mmol) in dry DMF was added to the reaction mixture under a nitrogen atmosphere. The reaction mixture was stirred overnight and the completion of the reaction was monitored with TLC. Upon completion, DMF was evaporated under vacuum to dryness and the crude mixture so obtained was added to DCM (200 mL) and washed with brine solution. Finally, the organic layer was dried over

Paper

anhydrous sodium sulphate and evaporated under reduced pressure to give an oily material which was then purified through column chromatography over silica in 6% MeOH-DCM system to give the desired compound **6** in 73% yield. M.p. 93–95 °C; ^{1}H NMR (400 MHz, MeOD-d_4), δ (ppm): 7.71 (d, 3H, J = 8.0 Hz, PyH-6″), 7.32–7.40 (m, 15H, Ph), 6.48 (d, 3H, J = 8.0 Hz, PyH-5″), 5.08 (s, 6H, CH_2Ph), 3.99 (t, 6H, J = 8.0 Hz, H-3′), 3.19 (t, 6H, J = 8.0 Hz, H-1′), 2.19–2.26 (m, 21H, H-1, H-2 & CH_3HPy), 1.83–1.88 (m, 6H, H-2′); ^{13}C NMR (100 MHz, MeOD-d_4), δ (ppm): 11.41, 29.69, 29.75, 30.51, 36.01, 51.70, 73.07, 92.84, 115.95, 127.94, 128.01, 128.80, 137.02, 139.85, 143.63, 145.69, 172.66, 173.24; m/z (ESI-MS): 1040.53 $(M + H)^+$.

General procedure for the synthesis of compounds 7 (KC21) and 8 (KC18). In a hydrogenation flask, the benzyl protected compounds (**5** and **6**) (2 mmol) were dissolved in methanol and 10% Pd/C (0.428 or 0.642 g, (4 or 6 mmol)) was added to them. The reaction suspension was shaken for 3–4 h under an H_2 atmosphere at 5 bar pressure. Upon completion of the reaction (monitored by TLC), the reaction mixture was filtered over celite and the filtrate so obtained was concentrated and dried under reduced pressure to afford pure white solid compounds (**7** or **8**) in 93–96% yields.

4-Amino-7-((2-(3-hydroxy-2-methyl-4-oxopyridin-1(4H)-yl)propyl)amino)-4-(3-((2-(3-hydroxy-2-methyl-4-oxopyridin-1(4H)-yl)propyl)amino)-3-oxopropyl)-7-oxoheptanoic acid (7; KC18). Yield 93%. M.p. 135–137 °C; ^{1}H NMR (400 MHz, MeOD-d_4), δ (ppm): 7.65 (d, 2H, J = 8.0 Hz, PyH-6″), 6.40 (d, 2H, J = 8.0 Hz, PyH-6″), 4.10 (t, 4H, J = 8.0 Hz, H-3′), 3.28 (t, 4H, J = 8.0 Hz, H-1′), 2.45 (s, 9H, CH_3Py), 2.31–2.37 (m, 4H, H-6), 2.23–2.28 (m, 4H, H-2), 1.90–1.99 (m, 10H, H-3, H-5 & H-2′); ^{13}C NMR (100 MHz, MeOD-d_4), δ (ppm): 10.50, 29.11, 29.86, 31.13, 31.87, 36.19, 51.66, 56.54, 93.11, 111.35, 131.32, 137.56, 145.98, 169.23, 173.38, 179.12; m/z (ESI-MS): 576.40 $(M + H)^+$; elemental analysis calcd (%) for $C_{28}H_{41}N_5O_8$·2.5 H_2O: C 53.79, H 7.50, and N 11.20; found: C 53.83, H 7.08, and N 11.06.

4-Amino-N^1,N^7-bis(3-(3-hydroxy-2-methyl-4-oxopyridin-1(4H)-yl)propyl)-4-(3-((3-(3-hydroxy-2-methyl-4-oxopyridin-1(4H)-yl)propyl)amino)-3-oxopropyl)heptanediamide (8; KC21). Compound obtained as a white solid (highly hygroscopic) in 96% yield. M.p. 128–130 °C; ^{1}H NMR (400 MHz, MeOD-d4), δ (ppm): 7.66 (d, 3H, J = 8.0 Hz, PyH-6″), 6.42 (d, 3H, J = 8.0 Hz, PyH-5″), 4.09 (t, 6H, J = 8.0 Hz, H-3′), 3.25 (t, 6H, J = 8.0 Hz, H-1′), 2.45 (s, 9H, CH_3HPy), 2.23–2.25 (m, 12H, H-1 & H-2), 1.94–1.96 (m, 6H, H-2′); ^{13}C NMR (100 MHz, MeOD-d_4), δ (ppm): 10.53, 29.71, 29.93, 30.52, 36.08, 51.70, 92.90, 111.30, 131.59, 137.56, 145.88, 168.92, 172.75; m/z (ESI-MS): 740.54 $(M + H)^+$; elemental analysis calcd (%) $C_{37}H_{53}N_7O_9$·4.0 H_2O: C 54.73, H 7.57, and N 12.08; found: C 54.76, H 7.84, and N 12.04.

2.3 Solution equilibrium studies

Potentiometric–spectrophotometric measurements. The study of protonation and complex-formation equilibria was carried out at 25 °C, ionic strength of 0.1 M NaCl, as previously described.[26] The working ligand concentration was 2.0×10^{-4} M for protonation studies, while complex formation studies were performed at a 1 : 1 metal/ligand molar ratio with Fe^{3+} at a concentration of 5.0×10^{-4} M and Al^{3+} and Zn^{2+} at a concentration of 3.3×10^{-4} M. Combined potentiometric–spectrophotometric measurements were performed in the 220–340 nm spectral range for protonation equilibria and in the 300–800 nm range for Fe^{3+} complexation, using fiber optic devices with 0.2 and 1.0 cm path lengths. Complex formation equilibria with Al^{3+} and Zn^{2+} were potentiometrically studied. Protonation and complex formation data were analyzed using HyperQuad2013 and HypSpec2 programs.[27]

NMR (nuclear magnetic resonance) experiments were conducted at 298 K by using a Bruker Ascend™ 400 MHz spectrometer equipped with a 5 mm automated tuning and matching broad band probe (BBFO) with z-gradients, as previously reported.[28–30] The concentrations of the KC18 and KC21 ligands were 1.0 mM, using 90/10 (v/v) H_2O/D_2O solutions and 5 mm NMR tubes. The electrode for NMR titrations was calibrated with standard commercial pH buffered solutions (pH 4.01, 7.01 and 10.01). Proton and carbon resonance assignments were made by a combination of 1D ^{1}H, 2D ^{1}H–^{13}C HSQC (Heteronuclear Single Quantum Coherence) 2D ^{1}H–^{1}H TOCSY (Total Correlation Spectroscopy) and 2D ^{1}H–^{1}H ROESY (Rotating-frame Nuclear Overhauser Effect Correlation Spectroscopy) experiments. The same combination of measurements was used to assign the signals of both the free and metal-bound ligands for a large range of pH values.[31–33] The NMR spectra were processed by using TopSpin software (Bruker Instruments) and analyzed with MestRe Nova 6.0.2 (Mestrelab Research S.L.) and Sparky 3.11 programs.

2.4 Molecular modelling studies

The structures of the ligand KC18 and its respective iron complex (Fe^{3+}–KC18) were fully optimized by quantum mechanical calculations based on Density Functional Theory (DFT) methods included in the Gaussian 03 computational software.[34] During the first step, the optimization was carried out using the B3LYP hybrid functional and the LANL2MB basis set, a direct SCF calculation and an SCF convergence criterion was set to 10^{-5}. In fact, the B3LYP hybrid functional[35] is an accurate density functional method that gives good geometries for the first-row transition metal complexes.[36] This model is a combination of the Becke three-parameter hybrid functional[37] and the Lee–Yang–Parr correlation functional.[38] Regarding the basis set, LANL2MB specifies the STO-3G on the first row and Los Alamos ECP plus MBS on Na–Bi.[39] During the second step, the obtained results were submitted to optimization using the B3LYP functional with the LANL2DZ basis set that describes the Fe atom through the Los Alamos ECP and an essentially double-zeta basis set including 3d orbitals and 3d diffuse functions for the valence shell. In this basis set, the remaining atoms are described through the Dunning-Huzinaga full double-ζ basis set.[40]

The pharmacokinetic parameters for the ligand KC18 were also determined using the QikProp program[41] that is included in the computational software Maestro.[42]

2.5 Biodistribution studies

^{67}Ga-citrate injection solution was prepared by dilution of ^{67}Ga citrate from Mallinckrodt Medical B.V. with saline to obtain a final radioactive concentration of approximately 5–7 MBq per 100 μL. Biodistribution studies were carried out in groups of 3 female CD1 mice (randomly bred, Charles River, from CRIFFA, France) weighing *ca.* 25 g. Mice were intravenously (i.v.) injected with 100 μL (5.5 MBq) of ^{67}Ga citrate *via* the tail vein, immediately followed by intraperitoneal (i.p.) injection of 0.5 μmol of each ligand in 100 μL saline. Animals were fed with a normal diet *ad libitum* and were sacrificed by cervical dislocation at 1 h and 24 h post-administration. The administered radioactive dose and the radioactivity in sacrificed animals were measured using a dose calibrator (Capintec CRC25R). The difference between the radioactivity in the injected and sacrificed animals was assumed to be due to whole body excretion. The tissue samples of main organs were then removed for counting in a gamma counter (Berthold LB2111, Berthold Technologies, Germany). The biodistribution results were expressed as the percentage of injected activity per organ (% I.A.) and as the percentage of injected activity per gram of organ (% I.A. per g) and presented as mean values ± standard deviation. Biodistribution data were evaluated by analysis of the variance. The level of significance was set at 0.05 (two-sided). Animal studies were carried out under the supervision of experienced researchers in animal facilities approved by the national authorities according to the national and European laws.

3. Results and discussion

3.1 Synthesis of the ligands

The synthesis of these polydentate 3,4-HP-based ligands followed a general strategy based on the attachment of the free amino group of *N*-aminoalkyl derivatives of 3,4-HP to the carboxylic acid functions of the backbone support, as previously used in the preparation of several tripodal and bipodal (3,4-HP) structures of hexadentate and tetradentate chelators for hard metal ions (Fe^{3+} and Al^{3+}).[15,24]

However, as compared with the previously reported nitrilo-carboxylic-hexadentate ligands (*e.g.* NTA(BuHP)$_3$, NTP(PrHP)$_3$), these new ligands enclose an amino group in the anchor structure for potential future extrafunctionalizations. Nevertheless, due to the known nucleophilic reactivity of the amino group, we have used a synthetic strategy in which the projected aminomethanetrispropionic acid backbone was replaced with the homologue nitromethanetrispropionic acid throughout the synthetic procedure, but in the final step the nitro group was reduced to the target primary amino group.

The synthetic procedure for the new polypodal 3-hydroxy-4-pyridinones (3,4-HP) is outlined in Scheme 1. It started with the preparation of the *N*-aminopropyl-3,4-HP arm (monomer 3,4-HP), following a strategy previously described.[15] The first step consisted of the protection of the hydroxyl group of the commercially available 3-hydroxy-2-methyl-4*H*-pyran-4-one (maltol, **1**) by reaction with benzyl chloride and the formation of the corresponding 3-benzyloxy derivative (**2**). In the second step, a Michael type addition is engage, with opening and closure of the heterocyclic ring, to convert hydroxypyrone (**2**) into the *N*-substituted hydroxypyridinone (**3**), by reaction with 1,3-diaminopropane. Afterwards, the *N*-aminopropyl-*O*-benzyl-oxi-3,4-HP arms (**3**) were linked to the triscarboxylic anchor structure (nitromethanetrispropionic acid, **4**) *via* amide bond linkages. This reaction was performed in dry DMF, in the presence of a base (*N*-methylmorpholine) and the coupling agent propylphosphonic anhydride (T3P). Depending on the equivalent amount ratio of the monomeric 3,4-HP arms (**3**) to the nitro-tricarboxylic skeleton (**4**), (*ca.* 2 : 1 or 3 : 1), this coupling reaction leads to the formation of bis-(*O*-benzyloxi-3,4-HP) (**5**) (48%) or the tris-(*O*-benzyloxi-3,4-HP) (**6**) (73%), respectively. The purification of these pre-final compounds involved silica-gel column chromatography. The final step consisted of the hydrogenolysis/reduction (5 bar, H$_2$, over 10% Pd/C) for the removal of the benzyl protecting groups of the 3,4-HP chelating moieties and the reduction of the nitro group to the amino group of the anchoring moiety, affording the final products (**7** and **8**) as pure compounds in 93% and 96% yield, respectively.

3.2 Protonation equilibria

The protonation equilibria of the ligands KC18 and KC21 (Fig. 1) have been studied by potentiometry (Fig. 1S and 2S†), UV-vis spectrophotometry and ^{1}H and ^{13}C NMR spectroscopy. The protonation constants reported in Table 1 were obtained at 25 °C and ionic strength of 0.1 M NaCl by potentiometric and spectrophotometric data. The corresponding speciation plots are shown in Fig. 2. The assignment of each calculated stepwise protonation constant to the protonation processes of a specific basic group in the molecule was based on the spectrophotometric and ^{1}H and ^{13}C NMR results. Those based on spectrophotometric results depend on the observed spectral variations shown in Fig. 3 and comparison with those of DFP previously studied.[43] The band corresponding to the completely deprotonated L^{3-} species (312 nm, Fig. 3C) is similar to that of the deprotonated DFP but characterized by an absorbance about three times more intense and it does not change significantly in the first protonation step. Therefore, we attribute $\log K_1 = 11.03$ to the protonation of the spectrally silent amino group. The following three protonation steps are accompanied by a decrease of the band at 312 nm and a concomitant increase of a new band at 282 nm. This last band is similar (always of triple intensity) to that of the neutral form of DFP. An extremely regular decrease/increase of the two bands in each protonation step, and the sharp isosbestic points at 248 and 293 nm are both indicative of an equal contribution of each of the three 3,4-HP moieties to the UV bands.[43] The observed $\log K_2$ 9.81, K_3 9.51 and K_4 9.03 are similar to that of DFP 9.82; the observed slight decrease in these values is in agreement with the decrease expected on a statistical basis ($\log 3 = 0.48$) for three equivalent basic sites.[44]

The determination of the constants related to the protonation of LH_5^{2+} to LH_8^{5+} species was based on the spectral data,
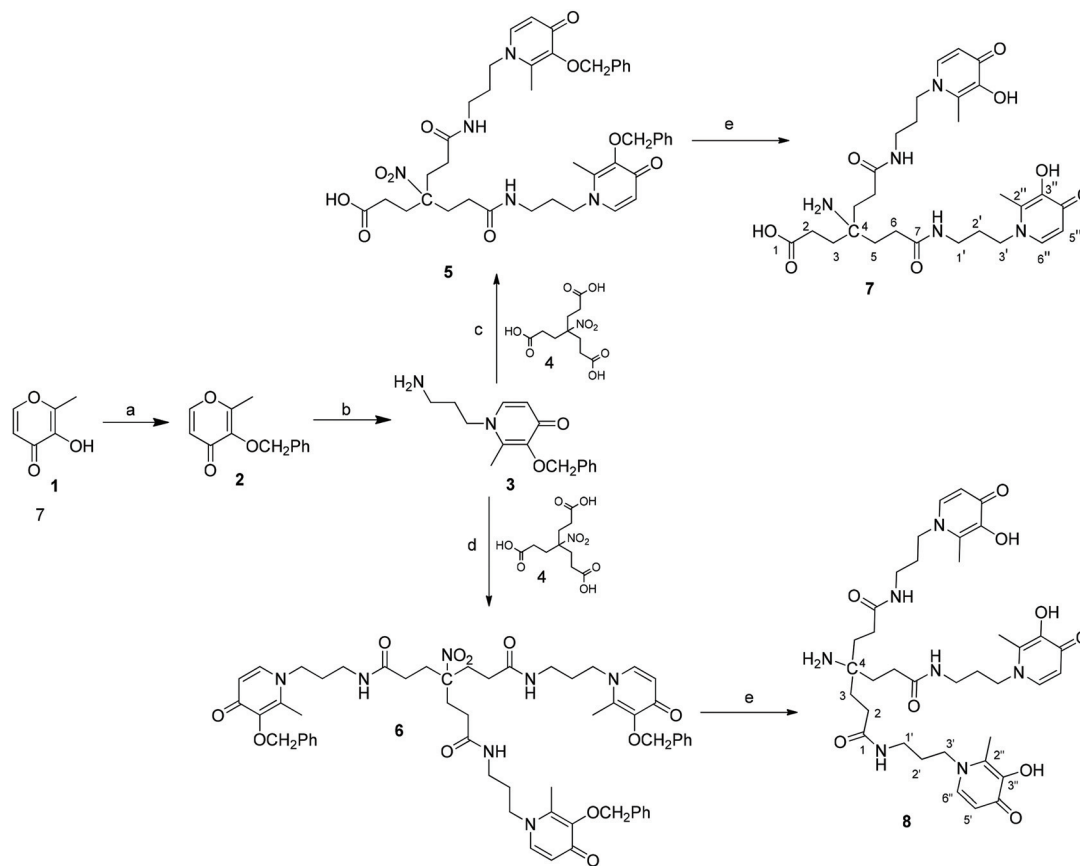
Scheme 1 Reagents and conditions: (a) MeOH, NaOH (1.1 eq.), benzyl chloride (0.9 eq.), and reflux; (b) 2 M NaOH, 1,3-diaminopropane, MeOH, and reflux; (c) NMM (4 eq.), T3P (2.05 eq.), and dry DMF; (d) NMM (7 eq.), T3P (3.3 eq.), and dry DMF; (e) MeOH, H₂, and Pd/C.

Table 1 Protonation constants (log β and log K) of KC18 and KC21 (L = deprotonated ligand) evaluated from potentiometric and spectrophotometric titrations at 25 °C and 0.1 M NaCl ionic strength

	KC18		KC21	
Species	$\log \beta$	$\log K$	$\log \beta$	$\log K$
LH^{2-}	11.03(2)	11.03	10.43(2)	10.43
LH_2^{-}	20.84(1)	9.81	20.19(1)	9.76
LH_3	30.35(2)	9.51	28.87(2)	8.68
LH_4^{+}	39.38(1)	9.03	33.35(2)	4.48
LH_5^{2+}	43.43(4)	4.05	36.67(4)	3.32
LH_6^{3+}	46.75(5)	3.30	39.80(5)	3.13
LH_7^{4+}	49.53(7)	2.80	—	—

collected in the pH range of 3.3–7.5 (Fig. 3B) during spectrophotometric titration, and in the pH range of 1.0–3.0 in a batch procedure on a set of solutions at constant ligand concentration (Fig. 3B). The 0.1 M ionic strength was controlled by proper additions of HCl and NaCl. These data were processed with HypSpec program obtaining, together with the protonation constants in Table 1, the absorptivity spectra in Fig. 4.

The log K_5 4.05, log K_6 3.30 and log K_7 2.80 values were attributed to the protonation of the hydroxypyridinone pyridinic amine. In fact, the intensity decrease of the 282 nm band with a concomitant increase of the 242 nm band is similar to the spectral variations previously observed during the formation of the positively charged hydroxypyridinone molecule.[43] The protonation constants of KC18 can be compared with those of the ligand NTP(PrHP)₃ that bears exactly the same pending arms, attached in this last ligand to a ternary nitrogen atom instead of the quaternary carbon atom bearing attached an amino group. The protonation constants of KC18 for the OH groups in the 3,4-HP units (9.81, 9.51 and 9.03) are slightly lower than those of NTP(PrHP)₃ (9.946, 9.84 and 9.09),[15] while an inverse behavior is observed for the further three protonations of 3,4-HP units (KC18: 4.05, 3.30 and 2.80 and NTP(PrHP)₃: 3.81, 3.14 and 2.76). These small differences can be explained by some dissimilar stabilization through hydrogen bonds, and for the OH groups by the positive charge of KC18 (NH_3^+) in the pH range of 8–10.5.

The protonation equilibria of KC18 were also studied by ¹H and ¹³C NMR titrations in the pH range of 1.6–11.

1D ¹H, 2D H–H TOCSY and 2D H–C HSQC spectra of KC18 and KC21 ligands with proton and H–C correlation assignments are shown in Fig. 5, 3S and 4S,† respectively. From these spectra, it is possible to see that both the ¹H and ¹³C resonances are in fast exchange, showing degeneration of nuclei due to the high symmetry of the ligands. All the resonances of protons and carbons have been unambiguously assigned.
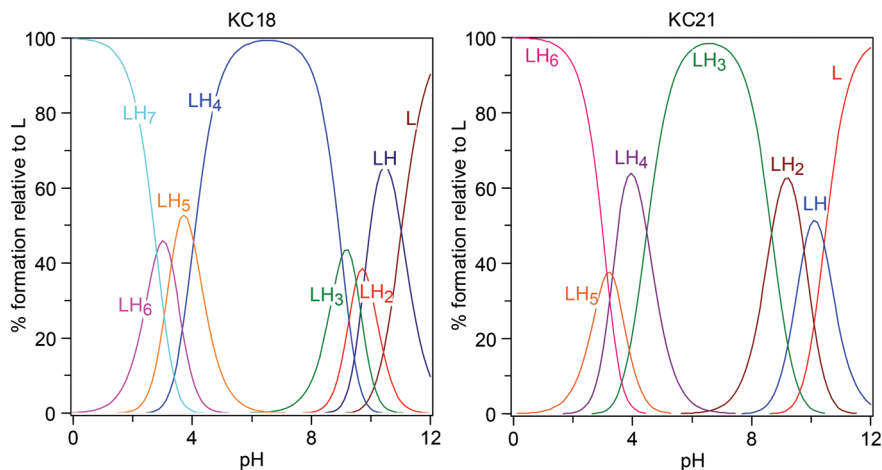
Fig. 2 The speciation plots of the ligands KC18 and KC21 (protonation constants in Table 1).
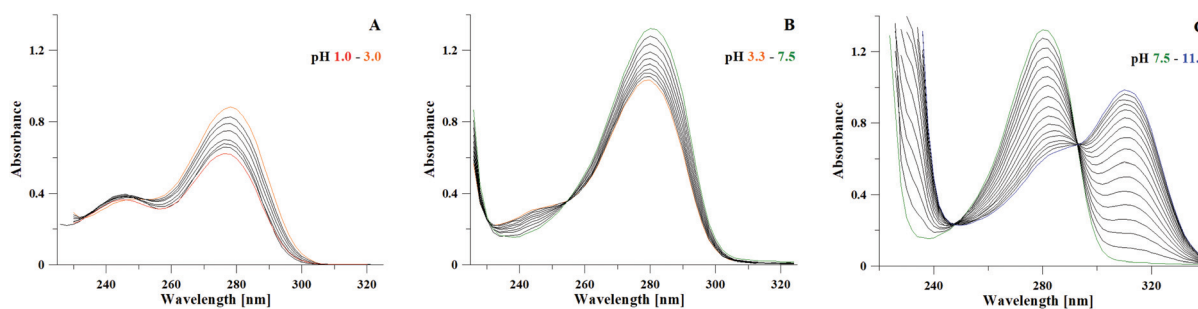
Fig. 3 Representative spectra (with an optical path length of 0.2 cm) recorded during the titration of the KC18 ligand, $C_L = 2.0 \times 10^{-4}$ M: (A) with 1 M HCl at pH in the range from 3.0 to 1.0; (B) and (C) with 0.1 M NaOH at pH in the range from 3.3 to 11.1.
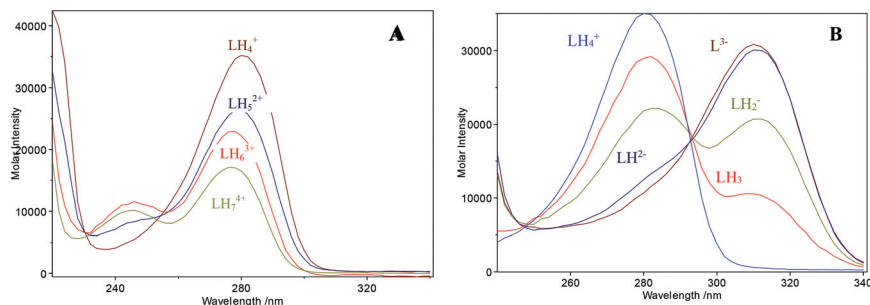
Fig. 4 Calculated absorptivity spectra of differently protonated forms of the ligand KC18 (A) at a pH below 6, (B) at a pH above 7.

Titration of the ligands by NMR has been performed by changing the pH value in the range from 2 to 11 and the ^{1}H and ^{13}C chemical shifts are reported in Tables 1S and 2S† for the KC18 and KC21 ligands, respectively. The pH titration of KC18 as a function of pH is shown in Fig. 6, and the ^{1}H and ^{13}C chemical shifts of each atom are reported in Fig. 5S and 6S† as a function of pH.

It is possible to see that the H1 and H2 proton signals from the pyridinone units show more evident variations in chemical shifts (in particular, H1 > H2), which are in agreement with

the K values obtained from potentiometric titrations ($\log K_5$ 4.05, $\log K_6$ 3.30 and $\log K_7$ 2.80), due to the deprotonation of the three pyridinyl nitrogen atoms from the pyridinone rings. The other protons are only slightly influenced, following the order H4 > H3 > H5 > H6 ≥ H7. The subsequent deprotonations are attributed to the hydroxyl groups of the pyridinone rings (with $\log K$ values of 9.81, 9.51 and 9.03); they are confirmed by the variation in the chemical shifts of the H1 and H2 proton signals observed at pH values ranging from 9 to 10. The last deprotonation, observed by the potentiometric
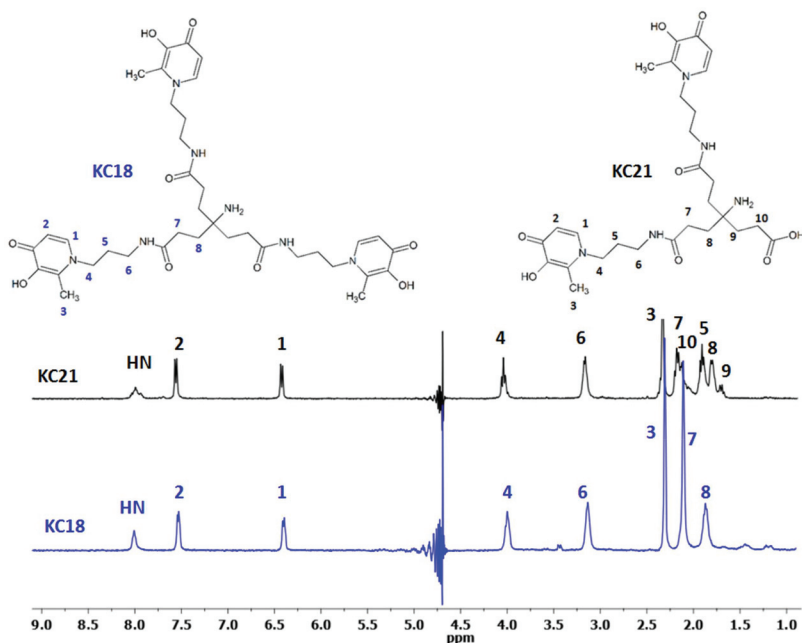
Fig. 5 ^{1}H NMR spectra of KC18 and KC21 ligands with the corresponding proton assignments.
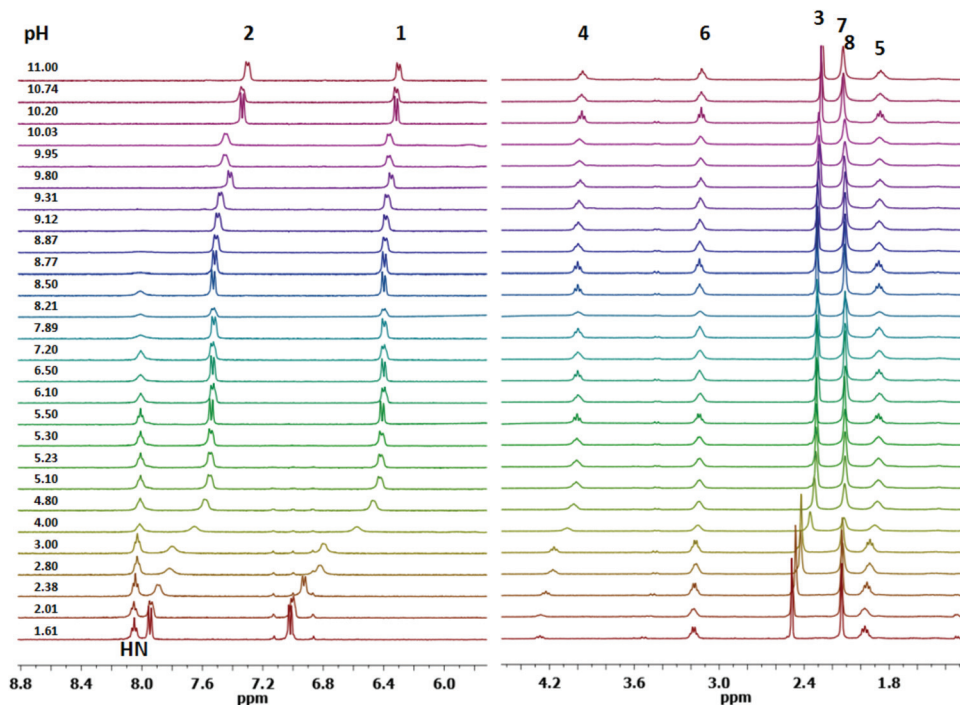
Fig. 6 ^{1}H NMR spectra of the KC18 ligand as a function of pH.

measurement was attributed to the deprotonation of the amine group (log K = 11.03), but it was not identified by NMR spectroscopy in the used pH range. In general, upon increasing the pH value all the proton signals show an upfield shift.

Regarding carbon signals, during the titration from pH 2 to pH 5, the C1 signal shows a downfield shift, following the deprotonation of the pyridinyl nitrogen atom from the pyridinone ring. C2 resonance does not show any change in the chemical shift as well as all the other carbon signals, except C4 resonance that shows an upfield shift.

Above pH 9, following the deprotonation of the OH groups of the pyridinone ring, it is possible to observe a shift of C1

and C2 signals (C2 > C1) towards the higher field. In contrast, a slight downfield shift is observed for the C3 nucleus, and to a lesser extent for the C5 and C6 nuclei.

The protonation constants of the KC21 ligand, which are measured and calculated in the same way as that for KC18, are reported in Table 1. The attribution of protonation constants was made on the basis of UV spectral changes (Fig. 7S†) and of ^1H and ^{13}C NMR chemical shifts as a function of pH (Table 2S and Fig. 8S–10S†) according to what has been discussed above for the ligand KC18. Therefore, $\log K_1 = 10.43$ and $\log K_2 = 9.76$ are assigned to the –OH groups of the pyridinone units. The difference $\log K_1 - \log K_2 = 0.67$ is in line with the value 0.602 expected on a statistical basis for the two equivalent basic groups.[44] $\log K_3 = 8.68$ is attributed to the amino group, on the basis of the high chemical shift variation of H8 and C8 around this value, which is not observed in the case of KC18. The protonation constant of the amino group appears to be much lower than that of KC18, which may be attributed to some H-bond interactions with the carboxylic arm (N–H⋯O, with a 7-membered ring). $\log K_4 = 4.48$ and $\log K_5 = 3.32$ are assigned to the pyridinic amine of hydroxypyridinone units, and $\log K_6 = 3.13$ to the carboxylic group of the backbone.

In Fig. 8S† the ^1H NMR titration of the KC21 ligand as a function of pH is shown. In a similar way to the KC18 ligand, the KC21 ligand also shows variation in the chemical shifts for the protons H1 and H2, with a more evident shift for the H1 proton in the pH range of 2–5. This shift is in agreement with the deprotonation of the pyridinyl nitrogen atom of the two pyridinone rings and of the terminal carboxylic group. Raising the pH value from 5 to 8 does not induce changes in the chemical shifts except for the H7 proton which starts to shift toward higher fields at a pH of 7.6. This behavior can be attributed to the deprotonation of the amine group that occurs at a more acidic pH than that observed for the KC18 ligand. Presumably, the amine group in the KC21 ligand may be involved in hydrogen bond interactions. Upon increasing the pH value above 9, the deprotonation of the OH group of the pyridinone rings results in the variation of the chemical shifts of H1 and H2 signals. The other proton signals remain almost unaffected.

As far as the carbon signals are concerned, the behavior of the KC21 ligand is very similar to that of the KC18 ligand

regarding C2, and C1 signals at pH values ranging from 2 to 5 as well as above 9. In addition, above pH 7.6, some downfield chemical shift variations were observed for C8, C7 and C10, in the order C8 > C7 = C10.

Fig. 10S† shows the trend of ^1H and ^{13}C chemical shifts vs. pH for the KC21 ligand calculated using the formula $\Delta\delta = \delta_{pHi} - \delta_{pH0}$ ppm, where δ_{pH0} is the value of the proton or carbon chemical shift at the first value of pH and δ_{pHi} is the subsequent value of pH.

3.3 Fe^{3+} Complex formation equilibria

Due to the complete complexation of Fe^{3+} at the start of titration, we studied the Fe^{3+}–KC18 complexation by spectrophotometric measurements on a set of 1:1 Fe/ligand solutions with increasing hydrochloric acid concentration. An ionic strength of 0.1 M was reached by adequate addition of HCl and NaCl until pH 1 was reached. Below pH 1, the ionic strength was no longer controlled. The pH was changed by additions of 1 M HCl until the absorption bands between 400 and 800 nm disappeared. In the 0.26–1.00 pH range (Fig. 7A), the increase in the band intensity at 560 nm was specific for the 1:1 Fe^{3+}–DFP complex, and therefore it was attributed to the [FeLH$_5$]$^{5+}$ complex in which the metal ion is coordinated to one of the hydroxypyridinone units. With the increase of pH up to 1.5 the band is shifted at 525 nm (isosbestic point at 624 nm) related to the [FeLH$_3$]$^{3+}$ complex in which Fe^{3+} is coordinated to two hydroxypyridinone units. Finally, at pH 2.29, when precipitation occurred, the complex [FeLH]$^+$ coordinated to all three hydroxypyridinone groups is formed, and is characterized by a band centered at 498 nm with isosbestic point at 550 nm. In addition, the profile of the pH dependent absorptivity spectra (Fig. 7B) is in agreement with the observations for Fe^{3+}–DFP complexes.[43] These data, processed with the HypSpec program (Fig. 11S†),[27] allowed the calculation of the iron complex formation constants given in Table 2 and the speciation plot in Fig. 8.

In the case of Fe^{3+}–KC21 complexes we obtained the complex formation constants as given in Table 2, and the speciation plot as shown in Fig. 8B with a treatment analogous to that for KC18 (Fig. 12S†). With KC21, no precipitation of the complex occurred. In the complexes [FeLH$_4$]$^{4+}$ and [FeLH$_2$]$^{2+}$, one and two hydroxypyridinone units are coordinated to Fe^{3+},

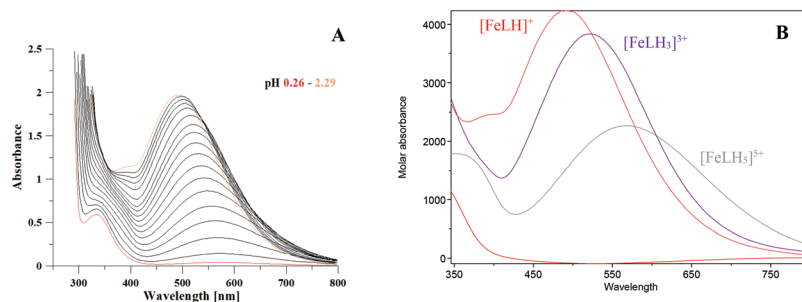**Fig. 7** (A) Representative spectra of the system Fe^{3+}–KC18 obtained in the pH range of 0.26–2.29 at $C_{KC18} = C_{Fe} = 5 \times 10^{-4}$ M (with an optical path length of 1 cm). (B) The absorptivity spectra of differently protonated forms of iron complexes with KC18.

Table 2 Complex formation constants for the complexes of KC18 and KC21 with Fe^{3+}; with $C_L = C_{Fe} = 1 \times 10^{-3}$ M, at 25 °C, and 0.1 M NaCl ionic strength

KC18			KC21		
Species	$\log \beta$	$\log K$	Species	$\log \beta$	$\log K$
$[FeLH_5]^{5+}$	51.488(5)	—	$[FeLH_4]^{4+}$	41.309(2)	
$[FeLH_3]^{3+}$	49.215(7)	2.273	$[FeLH_2]^{2+}$	38.741(3)	1.284
$[FeLH]^+$	45.77(1)	3.45	$[FeLH]^+$	35.19(1)	3.55
			$Fe_2L_3H_3$	102.71(4)	
pFe 29.5			**pFe 25.8**		

Table 3 Complex formation constants for the complexes of KC18 and KC21 with Al^{3+} with $C_{Al} = C_L = 3.33 \times 10^{-4}$ M, at 25 °C, and 0.1 M NaCl ionic strength

KC18			KC21		
Species	$\log \beta$	$\log K$	Species	$\log \beta$	$\log K$
$[AlLH_3]^{3+}$	45.70(2)	2.82	$[AlLH_2]^{2+}$	32.86(1)	3.97
$[AlLH]^{+1}$	40.06(2)	—	$[AlLH]^+$	28.89(1)	—
			$Al_2L_3H_3$	88.44(3)	6.89
			$[Al_2L_3H_2]^-$	81.55(4)	7.38
			$[Al_2L_3H]^{2-}$	74.17(4)	8.52
			$[Al_2L_3]^{3-}$	65.65(4)	—
pAl 23.8			**pAl 19.1**		

respectively. At higher pH values, complete octahedral coordination of Fe^{3+} is achieved *via* the formation of the binuclear $Fe_2L_3H_3$ complex.

The pFe value for KC18 is only slightly higher than the corresponding value of NTP(PrHP)$_3$, (29.4),[15] which may be attributed to a somehow more flexible conformation probably due to the backbone apical carbon atom instead of the amine group. The pFe value obtained for KC18 is also quite close to the value obtained for a previously reported hexadentate ligand (29.8),[20] with a different linkage (C2 instead of N1 atoms) between the 3,4-HP units and the backbone support.

3.4 Al^{3+} complex formation equilibria

The complex formation equilibria of KC18 with Al^{3+} were studied by potentiometric titrations (Fig. 13S†) until pH 4.5, where precipitation occurred. Data analysis gives evidence of the formation of $[AlLH_3]^{3+}$ in which presumably the metal ion is coordinated through two 3,4HP moieties, but still being protonated on the amino group and on the carbonyl and hydroxyl groups of the non-coordinated hydroxypyridinone unit. These last two protons are then lost with a p$K \approx 2.8$ to give the $[AlLH]^+$ complex that bears the positive charge on the protonated amino group. Table 3 provides the complex formation constants for the above complexes and Fig. 9A shows the

related speciation plots. The calculated pAl 23.8 allows classifying KC18 as an extremely strong chelating agent for aluminium. It was not possible to study this system by NMR spectroscopy; in fact, by adding Al^{3+} and Zn^{2+} ions to the KC18 ligand, under the NMR conditions, precipitation occurred, thus preventing NMR analysis.

The complex formation of KC21 with Al^{3+} was studied by potentiometric titrations (Fig. 14S†). At a pH of about 3.5, KC21 forms the species $[AlLH_2]^{2+}$ coordinated to one 3,4-HP unit, the apical NH_2 group and the second 3,4-HP units being still protonated. The proton on the 3,4-HP moiety is lost at a pK value of 3.97, affording the complex $[AlLH]^+$ with the aluminium ion coordinated to both hydroxypyridinone units. In order to complete the octahedral coordination of Al^{3+}, after a pH of 4 the formation of the binuclear $Al_2L_3H_3$ complex begins, in which three hydroxypyridinone units of the three ligands are coordinated to each aluminium ion. The protons in the amino groups of the three coordinated ligands are subsequently lost with pK values of 6.89, 7.38 and 8.52 to form the negatively charged $[Al_2L_3]^{3-}$ species. By adding Al^{3+} and Zn^{2+} ions to the KC21 ligand, under the NMR conditions, the species obtained are slightly more soluble than those obtained with the KC18 ligand. Therefore, NMR analysis has been per-
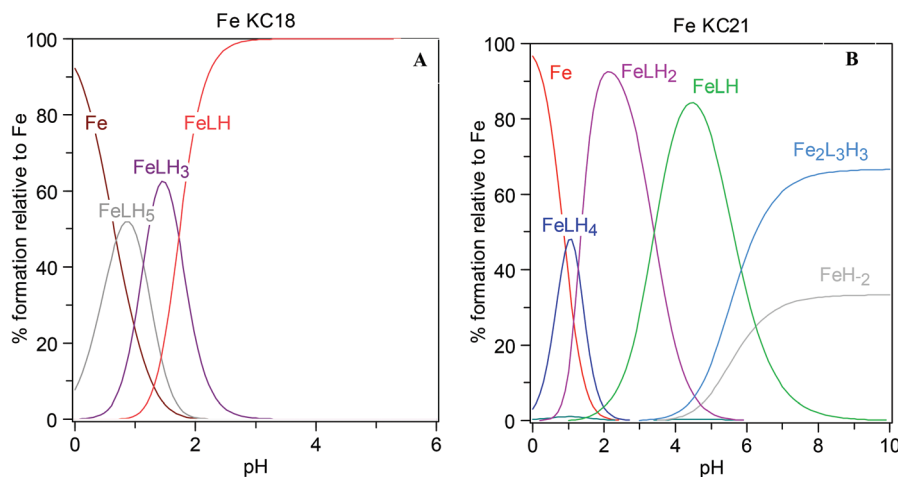
Fig. 8 (A) Speciation plot of the Fe^{3+}–KC18 complexes relative to $C_{KC18} = C_{Fe} = 5 \times 10^{-3}$ M. (B) The speciation plot of the Fe^{3+}–KC21 complexes relative to $C_{KC21} = C_{Fe} = 1 \times 10^{-3}$ M.

Fig. 9 (A) Speciation plot of the Al^{3+}–KC18 complexes relative to $C_{Al} = C_{KC18} = 3.33 \times 10^{-4}$ M. (B) The speciation plot of the Al^{3+}-KC21 complexes relative to $C_{Al} = C_{KC21} = 1 \times 10^{-3}$ M.

formed even though the signals obtained are weak and broad after the addition of the metal ions over the entire pH range. The aromatic and aliphatic regions of ^1H–^{13}C HSQC spectra for KC21:Al^{3+} system at 1 : 1 molar ratio and a pH of 7.5 are shown

Table 4 Global formation constants for the complexes of KC18 and KC21 with Zn^{2+} with $C_{Zn} = C_L = 3.33 \times 10^{-4}$ M, at 25 °C, and 0.1 M NaCl ionic strength

KC18			KC21		
Species	$\log \beta$	$\log K$	Species	$\log \beta$	$\log K$
$[ZnLH_4]^{3+}$	43.94(5)	3.16	$[ZnLH_4]^{3+}$	36.90(5)	4.24
$[ZnLH_3]^{2+}$	40.78(3)	5.04	$[ZnLH_3]^{2+}$	32.66(4)	4.51
			$[ZnLH_2]^{+}$	28.15(3)	—
$[ZnLH]$	30.70(3)	8.93	$Zn_2L_2H_2$	48.27(5)	7.41
$[ZnL]^{-}$	21.77(4)		$[Zn_2L_2H]^{-}$	40.86(5)	9.84
			$[Zn_2L_2]^{2-}$	31.02(7)	
pZn 14.5			**pZn 8. 3**		

in Fig. 15S.† Upon addition of Al^{3+} ions, the signals which show more evident variations are those of the hydroxypyridinone rings, thus indicating that the metal ion is coordinated to both 3,4-HP units. A high pAl value of 19.1 found for KC21 is mainly due to the formation of the binuclear complex.

Also in the case of aluminium the pAl for the KC18 ligand is 1.4 units higher than that for NTP(PrHP)$_3$.

3.5 Zn^{2+} Complex formation equilibria

The complex formation equilibria of KC18 with Zn^{2+} were studied by potentiometric titrations (Fig. 16S†), and the experimental results were processed with Hyperquad program.[27] The calculated complex formation constants are reported in Table 4, and the related speciation plots are shown in Fig. 10A. Analysis of these data indicate the formation of the complex $[ZnLH_4]^{3+}$ in which the metal ion is coordinated through one hydroxypyridinone moiety, with protonation of the amino group, the hydroxy groups of the two non-coordinated 3,4-HP

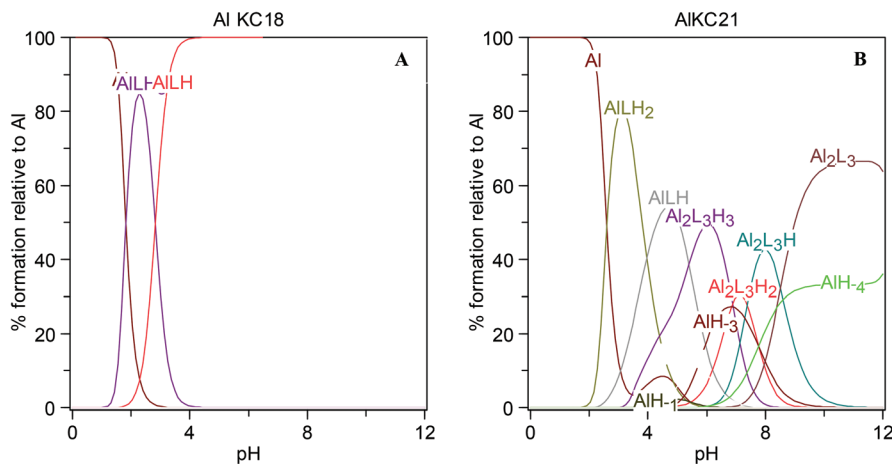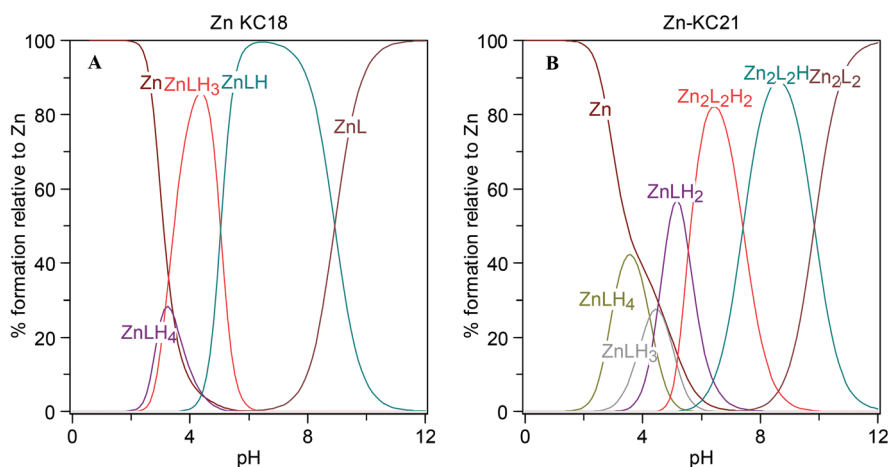**Fig. 10** (A) Speciation plot of the Zn^{2+}-KC18 complexes relative to $C_{Zn} = C_{KC18} = 3.3 \times 10^{-4}$ M. (B) Speciation plot of the Zn^{2+}-KC21 complexes relative to $C_{Zn} = C_{KC21} = 1.0 \times 10^{-3}$ M.

units and also the pyridinic amine group of one 3,4-HP unit. This last proton is lost with a pK value of 3.16 which is attributed to the formation of the $[ZnLH_3]^{2+}$ complex. The simultaneous loss of two protons with a pK value of 5.04 indicates that the coordination of Zn^{2+} may involve either three hydroxypyridinone groups, with the amino group still protonated, or two hydroxypyridinone groups and the amino group. The loss of the last proton at a pK value of 8.93 favors the second hypothesis. However, based on this equilibrium model, the resultant pZn value of 14.5 appears to be quite high for this metal ion (*cf.* pZn = 9.2 for NTP(PrHP)$_3$).[45]

The system Zn^{2+}–KC21 was studied by potentiometry (Fig. 17S†) and NMR spectroscopy. The complex formation constants are reported in Table 4 and the related speciation plots are shown in Fig. 10. The complex $[ZnLH_4]^{3+}$ should involve the coordination to one hydroxypyridinone unit, while the four protons should be attributed to one NH_3^+, two non-coordinated hydroxypyridinone units and one carboxylic group.

The loss of two protons with pK values of 4.24 and 4.51, presumably from the carboxylic group and the charged carbonyl group on the hydroxypyridinone unit, does not change the coordination pattern of the complex. The tetracoordination by the two 3,4-HP groups is accomplished through the formation of the binuclear complex $Zn_2L_2H_2$ with two protons in the amino groups, which are subsequently lost with pK values of 7.41 and 9.84. Alternatively, in these binuclear complexes the amino group could be directly involved in the coordination, and the last protons are lost from the 3,4-HP groups.

In Fig. 18S and 19S,† the aromatic and aliphatic regions of ^{1}H–^{13}C HSQC spectra are shown for the KC21 : Zn^{2+} system at 1 : 1 molar ratio and pH values of 5.8 and 7.5, respectively.

At a pH of 5.8 the H1 and H2 signals of the 3,4-HP rings show only a slight variation. By raising the pH, this variation becomes much more evident, indicating the involvement of the two 3,4-HP units in the coordination to Zn^{2+} ions. The perturbation involves also all the other protons in the linker and those adjacent to the carboxylic group.

The ^{1}H–^{1}H TOCSY spectra of the KC21 : Zn^{2+} system, at 1 : 1 molar ratio and a pH of 7.5, are shown in Fig. 11. In these spectra, the double correlation signals have been determined and can be attributed to the formation of the binuclear Zn^{2+} coordination species. In addition, the large shift ($\Delta\delta = -0.7$ ppm) observed for the amine group resonance can suggest the involvement of this group in the coordination to the Zn^{2+} ions.

Although a pZn value of 8.3 appears to be high, it is lower than that found for KC18.

3.6 Molecular modeling of the KC18 : Fe^{3+} complexes

Efforts to obtain suitable crystalline samples of the Fe–KC18 complex for X-ray diffraction were unsuccessful and so molecular modeling studies were performed under the same previously adopted conditions for analogous tripodal compounds.[15,16] These studies involved full geometry optimization of the iron complex by quantum mechanical calculations based on DFT methods included in the Gaussian 03 program software,[34] combining the B3LYP functional[37] with the basis sets LANL2MB and LANL2DZ.[39,40] No symmetry constraints were imposed during the geometry optimization.

The analysis of the energy-minimized structure of the Fe^{3+}–KC18 complex (Fig. 12) shows metal hexa-coordination and octahedral geometry, which are in agreement with our expectations. Moreover, the ferric complex with KC18 has an "in" conformation (with the NH_2 amine pointing towards the metal ion) similar to that found in complexes with other tripodal hexadentate ligands, such as NTA(PrHP)$_3$[16] and CP130,[46] while the complexes Fe^{3+}-NTP(PrHP)$_3$ and Fe^{3+}-NTA(BuHP)$_3$ have an "out" conformation,[15] with the free electron pair of the apical tertiary N-amine pointing away from the metal ion.

Fig. 12 also indicates the existence of two H-bonds between the inward amine NH_2 and a non-coordinated carbonyl O-atom (2.374 Å/135.6°) as well as with a coordinated carbonyl O-atom (2.219 Å/165°) of another arm.

Regarding the coordination shell, the O–Fe bond lengths in Fe–KC18 are in the range of 1.915–1.987 Å, which are in accordance with the values found in the literature for the Fe^{3+} complexes with NTP(PrHP)$_3$, NTA(PrHP)$_3$ and NTA(BuHP)$_3$,[15,16] indicating that the O(carbonyl)–Fe bonds are longer than the O(phenolic)–Fe bonds. On the other hand, the sum of the O–Fe–O angles (O belong to different arms) should be 540° (3 × 180°) for a regular octahedron and for the herein studied ferric complex with KC18 the value obtained is *ca.* 530°, while it was *ca.* 525° for the one with NTA(PrHP)$_3$. These results show that the ferric complex with KC18 is less distorted than that with NTA(PrHP)$_3$, which is in accordance with the fact that, in this last case, the arms are shorter, causing the structure of the metal coordination geometry to be more rigid. Although the ligands have arms of equal size, since the iron complexes with KC18 and NTP(PrHP)$_3$ have different number of atoms, their simulated stability can be compared on the basis of differences between the total energy of each complex and that of the corresponding ligand (ΔE). The values obtained for each system (KC18 and NTP(PrHP)$_3$) resulted in a difference of the binding energy ($\Delta\Delta E$) of 22 kcal mol^{-1}, evidencing the higher stability of the ferric complex with KC18, which is in agreement with the performed solution studies.

3.7 Pharmacokinetic parameters

The simulation of the pharmacokinetic parameters, calculated by the Maestro software[39,40] for the tris-HP ligand (KC18) and the respective homologue bis-HP ligand (KC21), showed quite similar pharmacokinetic descriptors (see Table 5). However, a more detailed analysis of these calculated descriptors indicate that due to its extra chelating arm the tris-HP ligand KC18, has some minor disadvantages over the bis-HP derivative KC21, namely in terms of MW (739.867/575.61), human serum protein binding (−1.405/−1.393) and blood–brain barrier permeability expressed as log BB (−4.287/−4.097), although the bis-HP derivative has the disadvantage of being quite more hydrophilic, clog P (−0.598/−2.486); nonetheless, they both made the same number (3) of violations of Lipinski's rule.[47]

Overall, although the predicted values for clog P and log K_{hsa} are practically within the range observed in 95% of normal
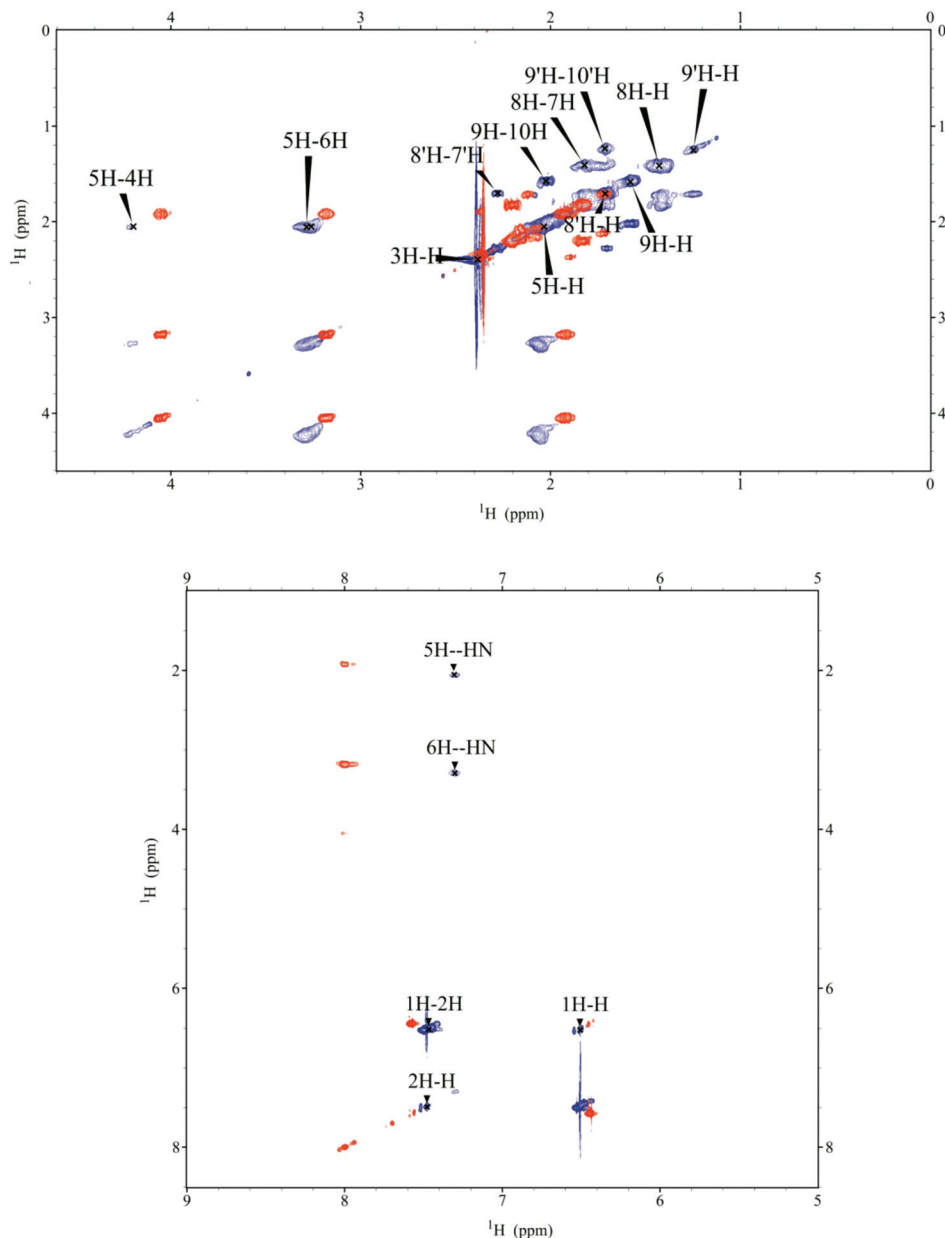
Fig. 11 Aliphatic (up) and aromatic (down) regions of $^1H–^1H$ TOCSY spectra for the KC21 : Zn^{2+} system at 1 : 1 molar ratio and a pH of 7.5.

drugs, the calculated values for log BB warn about possible low absorption through the BBB (blood–brain barrier); also the 3 violations of the Lipinski's Rule of 5 indicates a possible low absorption through the gut. Therefore, the new hexadentate ligand (739.87 Da) may find some limits to its possible use as an oral chelating agent, but we can consider other type of administration or the use of carriers (*e.g.* nanoparticles and liposomes) to facilitate the drug crossing of the biomembranes.

3.8 Biodistribution studies

Taking into consideration the above reported high chelating ability of KC18 and KC21 towards trivalent metal cations in solution, animal studies were further performed to investigate

the efficacy of these ligands as *in vivo* metal chelators. The study was conducted in CD-1 mice through biodistribution studies of the radiometal ^{67}Ga. As the tissue distribution of the radiotracer ^{67}Ga-citrate in mice is well-established, it was injected in the tail vein of the mice followed by an immediately subsequent intraperitoneal administration of 0.5 μmol of each ligand solution. Then, the effect of each ligand on the biodistribution profile and excretion of the radiotracer was assessed at 1 h and 24 h after administration. The biodistribution results of ^{67}Ga in the most relevant organs, expressed as % I.A. per g, are presented in Table 6, in the absence of any chelator (except the radiotracer ^{67}Ga-citrate) and after co-administration of KC18 and KC21 at 1 h and 24 h. The same data, expressed
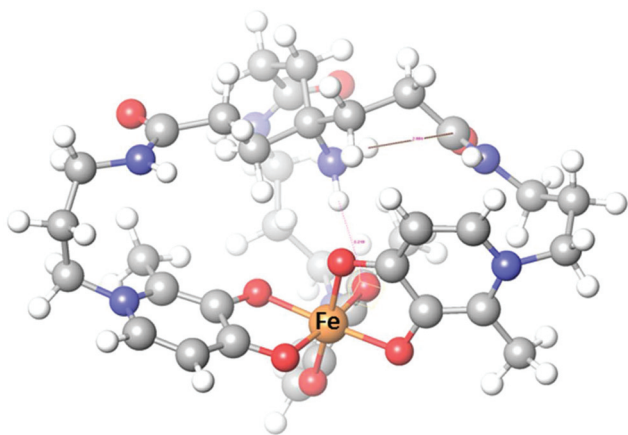
Fig. 12 DFT-minimized structure of the Fe^{3+}–KC18 complex with the indication of H-bonds (NH⋯O bond lengths/angles of 2.374 Å/135.6° and 2.219 Å/165°). Coloring of atoms: Fe orange, N blue, O red, C grey and H white.

Table 5 Pharmacokinetic parameters

Comp. name	M_W[a]	clog P[b]	log K_{hsa}[c]	log BB[d]	Violations of Lipinski's rule of 5[e]
KC18	739.867	−0.598	−1.405	−4.287	3
KC21	575.61	−2.486	−1.393	−4.097	3

95% of normal drugs have: [a] MW < 500; [b] -2 < clog P < -6.5; [c] 1.5 < log K_{hsa} > -1.5; [d] -3.0 < log BB < 1.2; [e] maximum is 4.[41,42]

as % I.A., are also represented in the graphic of Fig. 13, in comparison with the data from ^{67}Ga-citrate and its co-administration with DFP.

This set of results clearly demonstrate that the radiometal ^{67}Ga has a fast blood clearance with a decrease from 0.8 ± 0.4 to 0.06 ± 0.04 and from 0.4 ± 0.1 to 0.03 ± 0.01 with injection of KC18 or KC21, at 1 h and 24 h, respectively. There is also a rather fast clearance from the main organs and almost all the activity was eliminated after 24 h. The low retained activity is localized in the organs related with the excretory pathways,

especially the kidneys. The rate of radioactivity excretion was quite fast with an overall excretion higher than 77.1 ± 6.7 and 88.8 ± 3.6% I.A., at 1 h after administration of KC18 or KC21, respectively. After 24 h the overall percentage of excretion was higher than 96.0% for both ligands.

Altogether, these ^{67}Ga biodistribution and excretion profiles evidenced that both ligands have high *in vivo* chelating ability in this animal model promoting the rapid elimination of the radiometal from the main organs and the whole body. Slight differences in the ^{67}Ga uptake in main organs and in the excretion rate were found at 1 h after administration of KC18 or KC21, which are not relevant after 24 h. Such differences at low time points can be related with different delivery rates and the bioavailability of each ligand. Since the radiotracer and the ligands were injected by different routes, the lower MW of KC21 compared to KC18 and its higher hydrophilic character may explain the fastest availability and metal affinity of KC21 to complex the radiometal and to induce a more rapid elimination.

To evaluate the usefulness of KC18 and KC21 as *in vivo* chelating agent to promote the elimination of undesired trivalent metal cations, we have compared the ^{67}Ga distribution and excretion behavior of the radiotracer ^{67}Ga-citrate with those found after immediate injection of the iron-chelating drug DFP or each of our ligands in the same animal model. The comparative analysis of these data demonstrated that the co-administration of KC18 or KC21 has improved the radioactivity clearance from the main organs and the excretion from whole body more efficiently than the drug at 1 h and 24 h. Similar *in vivo* chelating ability were obtained with other 3,4-HP-compounds under identical experimental conditions. Indeed, the ^{67}Ga excretion pattern induced by the administration of KC18 is in agreement with that found by the administration of the hexadentate ligands NTP(PrHP)$_3$ and NTA(BuHP)$_3$.[15] Moreover, the fastest clearance and overall radioactivity excretion enhancement achieved by injection of the KC21 is also in accordance with the *in vivo* performance of other recently reported 3,4-HP tetradentate chelators such as NTA(PrHP)$_2$[24] or DTPA(PrHP)[48]. Although, the biological studies of DTPA(PrHP)$_2$ were carried out in a different mice strain, a good correlation and a similar trend of the results were obtained.

Table 6 Biodistribution data of ^{67}Ga in the most relevant organs, expressed as percentage of I.A. per g, after administration of ^{67}Ga-citrate with simultaneous intraperitoneal injection of KC18 or KC21 at 1 h and 24 h post-injection in female CD-1 mice (*n* = 3)

	^{67}Ga-citrate		^{67}Ga-(Bis-HP) (KC21)		^{67}Ga-(Tris-HP) (KC18)	
	1 h	24 h	1 h	24 h	1 h	24 h
Blood	2.0 ± 1.4	2.1 ± 0.7	0.4 ± 0.1	0.03 ± 0.01	0.8 ± 0.4	0.06 ± 0.04
Liver	1.5 ± 0.4	4.3 ± 1.1	0.21 ± 0.08	0.10 ± 0.02	0.42 ± 0.05	0.22 ± 0.03
Intestine	1.8 ± 0.7	2.2 ± 0.5	0.4 ± 0.1	0.04 ± 0.01	0.2 ± 0.1	0.06 ± 0.00
Spleen	0.7 ± 0.3	1.9 ± 0.4	0.12 ± 0.04	0.06 ± 0.01	0.24 ± 0.08	0.08 ± 0.02
Heart	1.0 ± 0.5	0.86 ± 0.03	0.17 ± 0.03	0.03 ± 0.00	0.3 ± 0.1	0.04 ± 0.03
Lung	1.4 ± 0.8	2.00 ± 0.04	0.4 ± 0.1	0.05 ± 0.00	0.6 ± 0.3	0.06 ± 0.00
Kidney	2.4 ± 0.4	3.6 ± 0.9	1.6 ± 0.4	1.3 ± 0.1	2.5 ± 0.8	1.3 ± 0.2
Muscle	1.3 ± 0.5	0.82 ± 0.07	0.14 ± 0.03	0.03 ± 0.00	0.24 ± 0.08	0.02 ± 0.00
Bone	7.7 ± 3.8	9.8 ± 1.6	0.22 ± 0.04	0.18 ± 0.06	0.2 ± 0.1	0.07 ± 0.02
Stomach	1.6 ± 0.6	1.0 ± 0.3	4.4 ± 0.2	0.03 ± 0.01	0.8 ± 0.6	0.13 ± 0.02
Excretion (% I.A.)	17.2 ± 3.6	35.4 ± 0.4	88.8 ± 3.6	97.4 ± 0.4	77.1 ± 6.7	96.0 ± 0.4
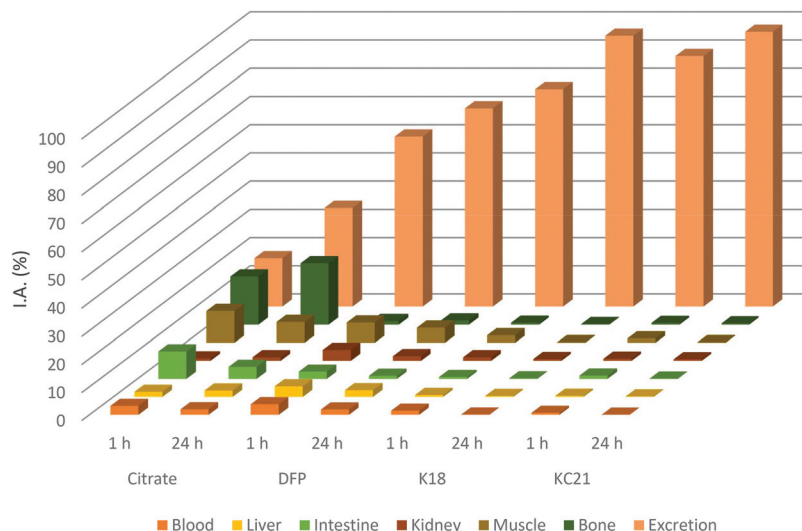
Fig. 13 Biodistribution data in the most relevant organs, expressed as % I.A. for ^{67}Ga-citrate and ^{67}Ga-citrate with co-administration of DFP, КС18 or КС21, at 1 and 24 h after administration in female CD-1 mice (n = 3).

4. Conclusions

Two new strong polydentate 3-hydroxy-4-pyridinone chelators were developed for potential medical application. Particularly, a hexadentate tris(3,4HP) chelator (KC18) and a tetradentate bis(3,4-HP) chelator (KC21) with further capacity for extrafunctionalization and probing were synthesized, characterized and studied *in vitro* and *in vivo* for their properties as iron(III)- and aluminium(III)-sequestering agents. In the main, as compared with other previously reported analogues, these ligands possess in their backbone an extra free amino group with the ability to be attached to other molecules or biosites, to provide targeting or sensing capacity. The ligands demonstrate a very high chelating capacity for those hard metal ions, respectively, pFe = 29.5, 25.8 and pAl = 23.8, 19.1, keeping free the extra-functional amino group. Despite the good ability for Zn complexation, it is lower than with those hard metal ions, thus assuring that their use as Fe- and Al-decorporating agents does not lead to the depletion of this essential bi-charged ion. Both chelators showed excellent *in vivo* metal sequestering capacity and excretion profiles, using mice overload with the radiotracer ^{67}Ga as animal models of Fe and Al overload disorders. Therefore, further studies are due on extra-functionalized analogues for targeting and sensing purposes.

Conflicts of interest

There are no conflicts of interest to declare.

Acknowledgements

References

1 J. B. Porter and M. Garbowski, *Hematol. Oncol. Clin. North Am.*, 2014, **28**, 683–701.
2 G. Crisponi, V. M. Nurchi, R. Silvagni and G. Faa, *Polyhedron*, 1999, **18**, 3219–3226.
3 C. Exley, *Trends Biochem. Sci.*, 2009, **34**, 589–593.
4 G. Crisponi, D. Fanni, C. Gerosa, S. Nemolato, V. M. Nurchi, M. Crespo-Alonso, J. I. Lachowicz and G. Faa, *Biomol. Concepts*, 2013, **4**, 77–87.
5 J. Porter, Treatment of Systemic Iron Overload, in *Metal Chelation in Medicine*, ed. R. R. Crichton, R. J. Ward and R. C. Hider, RSC Publishing, London, 2016.
6 G. Crisponi, V. M. Nurchi, M. Crespo-Alonso and L. Toso, *Curr. Med. Chem.*, 2012, **19**, 2794–2815.
7 G. Crisponi, V. M. Nurchi, V. Bertolasi, M. Remelli and G. Faa, *Coord. Chem. Rev.*, 2012, **256**, 89–104.
8 M. A. Santos, M. A. Esteves and S. Chaves, *Curr. Med. Chem.*, 2012, **19**, 2773–2793.
9 R. C. Hider, G. Kontoghiorghes, J. Silver and M. A. Stockham, *UK Pat.*, 2117766, 1982.
10 E. J. Neufeld, *Blood*, 2006, **107**, 3436–3441.

11 M. A. Santos, S. M. Marques and S. Chaves, *Coord. Chem. Rev.*, 2012, **256**, 240–259.

12 M. A. Santos and S. Chaves, *Future Med. Chem.*, 2015, **7**, 381–408.

13 S. Chaves, L. Piemontese, A. Hiremathad and M. A. Santos, *Curr. Med. Chem.*, 2018, **25**, 97–112.

14 S. Piyamongkol, T. Zhou, Z. D. Liu, H. H. Khodr and R. C. Hider, *Tetrahedron Lett.*, 2005, **46**, 1333–1336.

15 S. Chaves, S. M. Marques, A. M. F. Matos, A. Nunes, L. Gano, T. Tuccinardo, A. Martinelli and M. A. Santos, *Chem. – Eur. J.*, 2010, **16**, 10535–10545.

16 R. Cappai, K. Chand, J. I. Lachowicz, S. Chaves, L. Gano, G. Crisponi, V. M. Nurchi, M. Peana, M. A. Zoroddu and M. A. Santos, *New J. Chem.*, 2018, **42**, 8050–8061.

17 M. A. Santos, K. Chand and S. Chaves, *Coord. Chem. Rev.*, 2016, **327–328**, 287–303.

18 M. A. Telpoukhovskaia, J. F. Cawthray, C. Rodríguez-Rodríguez, L. E. Scott, B. D. G. Page, B. O. Patrick and C. Orvig, *Bioorg. Med. Chem. Lett.*, 2015, **25**, 3654–3657.

19 K. Chand, Rajeshwari, S. Chaves and M. A. Santos, *Metallomics*, 2018, **10**, 1460–1475.

20 A. Nunes, M. Podinovskaia, A. Leite, P. Gameiro, T. Zhou, Y. Ma, X. Kong, U. E. Schaible, R. C. Hider and M. Rangel, *J. Biol. Inorg. Chem.*, 2010, **15**, 861–877.

21 T. Moniz, D. Silva, T. Silva, M. S. Gomes and M. Rangel, *MedChemComm*, 2015, **6**, 2194–2203.

22 M. Rangel, T. Moniz, A. M. N. Silva and A. Leite, *Pharmaceuticals*, 2018, **11**, 110–132.

23 M. A. Santos, S. Gama, L. Gano, G. Cantinho and E. Farkas, *J. Chem. Soc., Dalton Trans.*, 2004, 3772–3781.

24 A. Irto, P. Cardiano, K. Chand, R. M. Cigala, F. Crea, C. De Stefano, L. Gano, G. Gattuso, S. Sammartano and M. A. Santos, *J. Mol. Liq.*, 2018, **272**, 609–624.

25 W. L. F. Armarego and D. D. Perrin, in *Purification of Laboratory Chemicals*, ed. W. L. F. Armarego and D. D. Perrin, Butterworth Heinemann, Oxford, 4th edn, 1999.

26 V. M. Nurchi, G. Crisponi, M. Crespo-Alonso, J. I. Lachowicz, Z. Szewczuk and G. J. Cooper, *Dalton Trans.*, 2013, **42**, 6161–6170.

27 (*a*) P. Gans, A. Sabatini and A. Vacca, *Talanta*, 1996, **43**, 1739–1753http://www.hyperquad.co.uk/HQ2013.htm. (*b*) C. Frassineti, S. Ghelli, P. Gans, A. Sabatini, M. S. Moruzzi and A. Vacca, *Anal. Biochem.*, 1995, **231**, 374–382.

28 J. I. Lachowicz, V. M. Nurchi, G. Crisponi, M. G. Jaraquemada-Pelaez, M. Arca, A. Pintus, M. A. Santos, C. Quintanova, L. Gano, Z. Szewczuk, M. A. Zoroddu, M. Peana, A. Dominguez-Martin and D. Choquesillo-Lazarte, *Dalton Trans.*, 2016, **45**, 6517–6528.

29 L. Toso, G. Crisponi, V. M. Nurchi, M. Crespo-Alonso, J. I. Lachowicz, D. Mansoori, M. Arca, M. A. Santos, S. M. Marques, L. Gano, J. Niclós-Gutíerrez, J. M. González-Pérez, A. Domínguez-Martín,

D. Choquesillo-Lazarte and Z. Szewczuk, *J. Inorg. Biochem.*, 2014, **130**, 112–139.

30 M. Peana, S. Medici, V. M. Nurchi, J. I. Lachowicz, G. Crisponi, E. Garribba, D. Sanna and M. A. Zoroddu, *J. Inorg. Biochem.*, 2017, **171**, 18–28.

31 A. Magri, A. Munzone, M. Peana, S. Medici, M. A. Zoroddu, O. Hansson, C. Satriano, E. Rizzarelli and D. La Mendola, *Int. J. Mol. Sci.*, 2016, **17**, 1240–1259.

32 M. A. Zoroddu, M. Peana, S. Medici, S. Potocki and H. Kozlowski, *Dalton Trans.*, 2014, **43**, 2764–2771.

33 J. I. Lachowicz, V. M. Nurchi, G. Crisponi, G. Jaraquemada-Pelaez, M. Ostrowska, J. Jezierska, E. Gumienna-Kontecka, M. Peana, M. A. Zoroddu, D. Choquesillo-Lazarte, J. Niclos-Gutierrez and J. M. Gonzalez-Perez, *J. Inorg. Biochem.*, 2015, **151**, 94–106.

34 M. J. Frisch, G. W. Trucks, H. B. Schlegel, G. E. Scuseria, M. A. Robb, J. R. Cheeseman, J. A. Montgomery Jr., T. Vreven, K. N. Kudin, J. C. Burant, J. M. Millam, S. S. Iyengar, J. Tomasi, V. Barone, B. Mennucci, M. Cossi, G. Scalmani, N. Rega, G. A. Petersson, H. Nakatsuji, M. Hada, M. Ehara, K. Toyota, R. Fukuda, J. Hasegawa, M. Ishida, T. Nakajima, Y. Honda, O. Kitao, H. Nakai, M. Klene, X. Li, J. E. Knox, H. P. Hratchian, J. B. Cross, V. Bakken, C. Adamo, J. Jaramillo, R. Gomperts, R. E. Stratmann, O. Yazyev, A. J. Austin, R. Cammi, C. Pomelli, J. W. Ochterski, P. Y. Ayala, K. Morokuma, G. A. Voth, P. Salvador, J. J. Dannenberg, V. G. Zakrzewski, S. Dapprich, A. D. Daniels, M. C. Strain, O. Farkas, D. K. Malick, A. D. Rabuck, K. Raghavachari, J. B. Foresman, J. V. Ortiz, Q. Cui, A. G. Baboul, S. Clifford, J. Cioslowski, B. B. Stefanov, G. Liu, A. Liashenko, P. Piskorz, I. Komaromi, R. L. Martin, D. J. Fox, T. Keith, M. A. Al-Laham, C. Y. Peng, A. Nanayakkara, M. Challacombe, P. M. W. Gill, B. Johnson, W. Chen, M. W. Wong, C. Gonzalez and J. A. Pople, *Gaussian 03, Revision C.02*, Gaussian, Inc., Wallingford CT, 2004.

35 C. W. Bauschlicher, *Chem. Phys. Lett.*, 1995, **246**, 40–44.

36 A. Ricca and C. W. Bauschlicher, *Theor. Chim. Acta*, 1995, **92**, 123–131.

37 A. Becke, *Phys. Rev. A: At., Mol., Opt. Phys.*, 1988, **38**, 3098–3100.

38 C. Lee, W. Yang and R. G. Parr, *Phys. Rev. B: Condens. Matter Mater. Phys.*, 1988, **37**, 785–789; B. Miehlich, A. Savin, H. Stoll and H. Preuss, *Chem. Phys. Lett.*, 1989, **157**, 200–206.

39 P. J. Hay and W. R. Wadt, *J. Chem. Phys.*, 1985, **82**, 270–283.

40 T. H. Dunning Jr. and P. J. Hay, in *Modern Theoretical Chemistry*, ed. H. F. Schaefer III, Plenum, New York, 1976, vol. 3, pp. 1–28.

41 *QikProp, version 2.5*, Schrodinger, LLC, New York, NY, USA, 2005.

42 *Maestro, version 9.3*, Schrodinger Inc., Portland, OR, USA, 2012.

43 V. M. Nurchi, G. Crisponi, T. Pivetta, M. Donatoni and M. Remelli, *J. Inorg. Biochem.*, 2008, **102**, 684–692.

44 M. T. Beck and I. Nagypal, *Chemistry of complex equilibria*, Ellis Horwood Ltd, Chichester, 1990.

45 A. C. Mendonça, A. F. Martins, A. Melchior, S. M. Marques, S. Chaves, S. Villette, S. Petoud, P. L. Zanonato, M. Tolazzi, C. S. Bonnet, É. Tóth, P. Di Bernardo, C. F. G. C. Geraldes and M. A. Santos, *Dalton Trans.*, 2013, **42**, 6046–6057.

46 G. Xiao, D. Helm, R. C. Hider and P. S. Dobbin, *Inorg. Chem.*, 1995, **34**, 1268–1270.

47 C. A. Lipinski, F. Lombardo, B. W. Dominy and P. J. Feeney, *Adv. Drug Delivery Rev.*, 2012, **64**, 4–17.

48 A. Irto, P. Cardiano, K. Chand, R. M. Cigala, F. Crea, C. De Stefano, L. Gano, G. Gattuso, S. Sammartano and M. A. Santos, *J. Mol. Liq.*, 2019, **281**, 280–294.

Paper III

A new tripodal kojic acid derivatives for iron sequestration: synthesis, protonation, complex formation studies with Fe^{3+}, Al^{3+}, Cu^{2+} and Zn^{2+}, and *in vivo* bioassays

V. M. Nurchi, M. G. Jaraquemada-Pelaez, G. Crisponi, J. I. Lachowicz, R. Cappai, L. Gano, M. A. Santos, A. Melchior, M. Tolazzi, M. Peana, S. Medici, M. A. Zoroddu, *J. Inorg. Biochem.*, **2019**, *193*, 152-165.

A new tripodal kojic acid derivative for iron sequestration: Synthesis, protonation, complex formation studies with Fe^{3+}, Al^{3+}, Cu^{2+} and Zn^{2+}, and *in vivo* bioassays

Valeria M. Nurchi[a], Maria de Guadalupe Jaraquemada-Pelaez[b], Guido Crisponi[a,*],
Joanna I. Lachowicz[a], Rosita Cappai[a], Lurdes Gano[c], M. Amelia Santos[d], Andrea Melchior[e],
Marilena Tolazzi[e], Massimiliano Peana[f], Serenella Medici[f], Maria Antonietta Zoroddu[f]

[a] *Department of Life and Environmental Sciences, University of Cagliari, Cittadella Universitaria, Monserrato, Cagliari, Italy*
[b] *Medicinal Inorganic Chemistry Group, Department of Chemistry, University of British Columbia, Vancouver, BC, Canada*
[c] *Centro de Ciências e Tecnologias Nucleares (C2TN), Instituto Superior Técnico, Universidade de Lisboa, Estrada Nacional 10, 2695-066 Bobadela LRS, Portugal*
[d] *Centro de Química Estrutural, Instituto Superior Técnico, Universidade de Lisboa, Av. Rovisco Pais 1, 1049-001 Lisboa, Portugal*
[e] *Dipartimento Politecnico, Laboratori di Tecnologie Chimiche, Università di Udine, Via del Cotonificio 108, 33100 Udine, Italy*
[f] *Dipartimento di Chimica e Farmacia, Università di Sassari, Sassari, Italy*

A R T I C L E   I N F O

A B S T R A C T

This work presents the simple and low cost synthesis of a new tripodal ligand, in which three units of kojic acid are coupled to a tris(2-aminoethyl)amine (tren) backbone molecule. The protonation equilibria, together with the complex formation equilibria of this ligand with Fe^{3+}, Al^{3+}, Cu^{2+} and Zn^{2+} ions were studied. The complementary use of potentiometric, spectrophotometric and NMR techniques, and of Density Functional Theory (DFT) calculations, has allowed a thorough characterization of the different species involved in equilibrium. The stability of the formed complexes with Fe^{3+} and Al^{3+} are high enough to consider the new ligand for further studies for its clinical applications as a chelating agent. Biodistribution studies were carried out to assess the capacity the ligand for mobilization of gallium in ^{67}Ga-citrate injected mice. These studies demonstrated that this ligand efficiently chelates the radiometal in our animal model, which suggests that it can be a promising candidate as sequestering agent of iron and other hard trivalent metal ions. Furthermore, the good zinc complexation capacity appears as a stimulating result taking into a potential use of this new ligand in analytical chemistry as well as in agricultural and environmental applications.

1. Introduction

The present study is part of a research project on iron chelating agents for clinical use that we are carrying out along the last ten years [1]. Furthermore, according to the chemical and physical features of the chelators, these can also find application in a variety of fields, as environmental chemistry [2–4], agriculture [5,6] and analytical chemistry. The research we developed in the last years has been centered on tetradentate derivatives of kojic acid (KA) (Fig. 1), obtained by connecting two KA units through linkers anchored in position 6 [7–9], with variations in chemical nature, length, charge, *etc.* These linkers can provide molecules not only with different chelating properties, but

also with different chemical and physical features that determine the properties of the molecule *in vivo* (as intestinal absorption, cellular permeability, bioavailability, and pharmacokinetics). Assembling two KA units in a unique ligand leads to an increase of the stability of the formed iron complexes: the pFe[1] passes from 13.1 for KA to values up to 18–20 for the bis-derivatives. The enthalpic contribution to the stability of the iron complexes with tetradentate ligands should be similar to that of KA, thus, not disturbed by strain effects. Consequently, it is the entropic contribution, due to the preorganization of KA moieties, which determines the remarkable increase of the iron chelating capacity and associated pFe value. Recently, we used a different synthetic strategy, based on connecting two KA units through linear diamines of different

---

* Corresponding author at: University of Cagliari, Cittadella Universitaria, 09042 Monserrato, Cagliari, Italy.
  E-mail address: crisponi@unica.it (G. Crisponi).

[1] pFe is the parameter generally used for evaluating the chelating ability of a ligand, independent both on the proton competition with iron for the same coordinating sites and on the stoichiometry of the formed complexes. It is defined as the concentration, expressed as negative logarithm, of free Fe^{3+} in a solution at pH 7.4 that is 1 μM in metal ion concentration and 10 μM in ligand concentration [12].
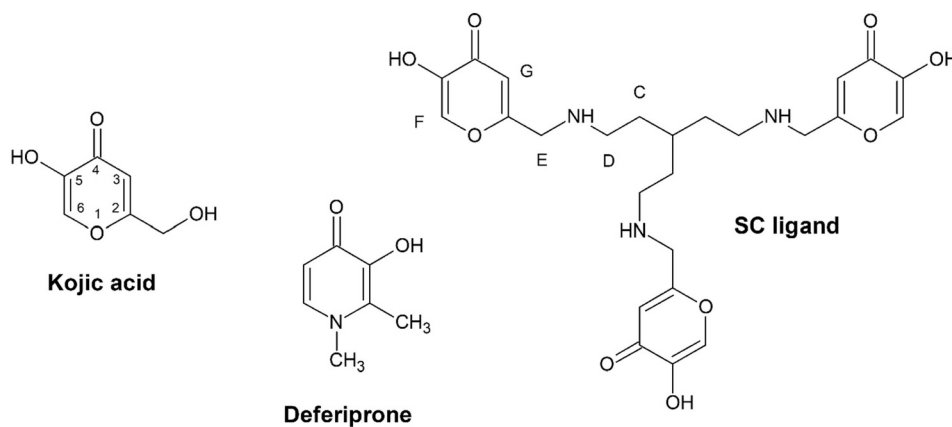
Fig. 1. Molecular structures of kojic acid, deferiprone and of 6,6′,6″-(((nitrilotris(ethane-2,1-diyl))tris(azanediyl))tris(methylene))tris(3-hydroxy-4H-pyran-4-one) (SC ligand). The letters in the structure of SC ligand will be used in NMR attributions.

length, by reacting them with the methylhydroxyl groups in position 2 [10]. The simplicity of synthesis allows an easy and low cost preparation. The different anchoring position of the linker, as well as its length, can affect both protonation and complex formation equilibria. The obtained results remark that the orientation of the oxygen atoms in KA units, related to the anchoring position, strongly affects the protonation constants, while the chelating ability is practically unaffected.

Based on these encouraging results we have explored herein the synthesis of the tripodal KA derivative 6,6′,6″-(((nitrilotris(ethane-2,1-diyl))tris(azanediyl))tris(methylene))tris(3-hydroxy-4H-pyran-4-one), in the following reported as SC ligand, in which three KA units are attached to a tris(2-aminoethyl)amine (tren) backbone.

Potentiometric and spectrophotometric methods, supported by and ^{1}H and ^{13}C NMR spectroscopy and also quantum-mechanical calculations, were thoroughly used to characterize the protonation and the complex formation equilibria with Fe^{3+}, Al^{3+}, Cu^{2+} and Zn^{2+}. Finally, this ligand is bioevaluated for its capacity for metal-mobilization from the body of mice overloaded with Ga^{3+}, and also *in silico* evaluated for its pharmacokinetic properties and druggability [11]. The results are discussed, in comparison with other analogous ligands, in particular the currently marketed chelating drug, Deferiprone (Fig. 1), due to the structural analogy between hydroxypyridinone and hydroxypyrone ligands.

2. Experimental

2.1. Reagents

Kojic acid, tris(2-aminoethyl)amine (tren), NaOH, NaCl, $FeCl_3$, $AlCl_3$, $CuCl_2$, $ZnCl_2$ and HCl were purchased from Aldrich. All the reagents were used without any further purification. Carbonate-free 0.1 M NaOH solution was prepared according Albert and Serjeant [13]. The metal ion standard solutions were prepared by dissolving the required amount of chloride salts in pure double distilled water and adding a stoichiometric amount of HCl to prevent hydrolysis. Fe^{3+} solution was standardized by spectrophotometric analysis using the formation of the colored Fe^{3+}–desferal complex [14], while Al^{3+}, Cu^{2+} and Zn^{2+} solutions were standardized by EDTA titration.

2.2. Synthesis of 6,6′,6″-(((nitrilotris(ethane-2,1-diyl))tris(azanediyl))tris(methylene))tris(3-hydroxy-4H-pyran-4-one)

Kojic acid (1.0 g, 7.04 mmol) was suspended in 20 mL ethanol followed by dropwise addition of tris(2-aminoethyl)amine (350 μL, 2.32 mmol) solved in $CHCl_3$ (2 mL). After stirring the reaction mixture at room temperature for 1 h, the precipitate was filtered and washed with ethyl acetate. The identity and purity of the sample were

confirmed by NMR and elemental analysis. Analytical data: 98.5% yield, ^{1}H NMR (D_2O, 500 MHz) δ 2.83 (t, 6H, $J = 2.81$ Hz), 3.09 (t, 6H, $J = 3.09$ Hz), 4.49 (s, 6H), 6.49 (s, 3H), 7.82 (s, 3H). ^{13}C NMR (D2O, 500 MHz) δ 39.84, 53.86, 62.92, 112.94, 145.16, 168.24, 184.01, 199.25. Elemental analysis (%) calculated for ($C_{24}H_{36}N_4O_{12}$·3H_2O): C 50.35; H 6.34, N 9.79%; found: C 50.53, H 6.21, N 9.72%.

2.3. Potentiometric–spectrophotometric measurements

Potentiometric or combined potentiometric-spectrophotometric measurements for protonation and complex formation equilibria were performed in a thermostatted glass cell equipped with a magnetic stirrer, a Metrohm LL UNITRODE glass electrode connected to a Metrohm 691 pH-meter, a microburet delivery tube connected to a Dosimat 665 Metrohm titrator, an inlet–outlet tube for Argon and a fiber optic dip probe connected to a Varian Cary 50 UV–vis spectrophotometer. Protonation and Fe^{3+} complex formation constants were determined by simultaneous potentiometric and spectrophotometric titrations, while Al^{3+}, Cu^{2+} and Zn^{2+} complex formation constants were potentiometrically determined. Solutions (20 mL at working ligand concentration 5.0×10^{-4} M) were titrated with 0.1 M NaOH at 25.0 °C, and 0.1 M NaCl ionic strength. The electrode was daily calibrated for hydrogen ion concentration by titrating HCl with NaOH in the above experimental conditions and the results were analyzed with Gran procedure [15]. 120 points were generally acquired for each titration. Complex formation studies were performed in triple at 1:1 and 1:2, metal/ligand molar ratios. The reversibility was checked by back titration with HCl in at least one case for each metal/ligand system. Since Fe^{3+} was almost completely complexed when mixing reagents before the base potentiometric titrations, the complex formation equilibria were studied also in strongly acid media (pH 1–3) on sets of solutions at increasing concentrations of HCl until the disappearance of the bands of complexed iron. These measurements were made in batch adjusting the ionic strength by proper additions of HCl and NaCl.

Combined potentiometric spectrophotometric measurements were done in the 200–400 nm spectral range for protonation equilibria, and in the 400–800 nm range for Fe^{3+} complexation, using 0.2 and 1 cm path lengths respectively. Protonation and complex formation data were analyzed using Hyperquad2013 [16] and HypSpec [17] programs. Log β_{pqr} values refer to the overall equilibria $pM + qH + rL \leftrightarrows M_pH_qL_r$ (electrical charges omitted). The hydrolysis constant at 25 °C and 0.1 M ionic strength used in the refinement procedure are reported in Table 1S.

2.4. NMR spectroscopy

Nuclear Magnetic Resonance (NMR) experiments were carried out
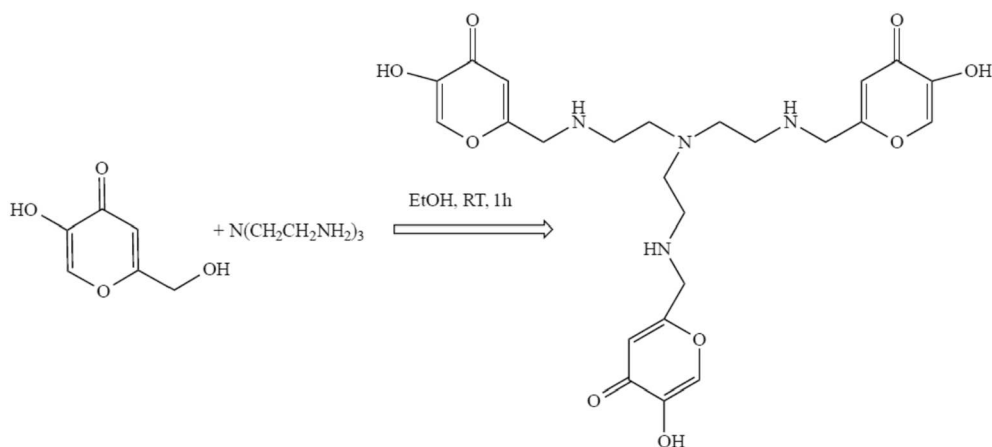
Scheme 1. Scheme of the synthesis of ligand SC starting from KA and tren.

by using a Bruker AscendTM 400 MHz spectrometer equipped with a 5 mm automated tuning and matching broad band probe (BBFO) with z-gradients, as previously described [18–20]. Ligand concentrations varied in the range 2–5 mM, in 90/10 (v/v) H2O/D2O at 298 K using 5 mm NMR tubes. 2D ^1H–^{13}C HSQC spectra (Heteronuclear Single Quantum Coherence) were acquired using a phase-sensitive sequence employing Echo-Antiecho-TPPI gradient with a heteronuclear coupling constant JXH = 145 Hz, and shaped pulses for all 180° pulses on f2 channel with decoupling during acquisition. Sensitivity improvement and gradients in back inept were also used. 2 s and 90° pulses of about 10 μs were employed as relaxation delays of in all the measurements. The suppression of the solvent was performed in 1D ^1H and 2D ^1H–^1H TOCSY (Total Correlation Spectroscopy) experiments by using excitation sculpting with gradients. The spin-lock mixing time of TOCSY experiments was obtained with MLEV17. ^1H–^1H TOCSY spectra were performed using mixing times of 60 ms. A combination of 1D, 2D TOCSY, HSQC experiments was used to assign the signals of both free and metal-bound ligands at different pH values. All NMR data were processed with TopSpin (Bruker Instruments) software and analyzed by Sparky 3.11 and MestRe Nova 6.0.2 (Mestrelab Research S.L.) programs.

2.5. Molecular modelling studies

Density functional theory (DFT) calculations were carried out on the complexes and ligands using the three-parameter hybrid functional B3LYP [21,22] as also previously done for similar systems [23–27]. The LANL2DZ ECP has employed for the metal ions [28], while other elements were treated using a 6–31 + G (25) Gaussian-type basis set. Geometry search for the large Fe3S3 complex has been performed at semiempirical (PM6) level. All calculations were carried out using the Gaussian16 program [29]. The TD-DFT spectra of the Fe^{3+} complexes were calculated with the B3LYP functional at the coordinates of the minimum previously obtained using the def2-TZVP basis set for all elements [30]. The latter calculations were performed using ORCA 4.0 [31].

2.6. Biodistribution studies

^{67}Ga-citrate injection solution was prepared by dilution of ^{67}Ga citrate from Mallinckrodt Medical B.V. with saline to obtain a final radioactive concentration of approximately 5–7 MBq/100 μL. Biodistribution studies were carried out in groups of 3 female CD1 mice (randomly bred, Charles River, from CRIFFA, France) weighing *ca.* 25 g. Mice were intravenously (i.v.) injected with 100 μL (5.5 MBq) of ^{67}Ga citrate *via* the tail vein immediately followed by intraperitoneal (i.p.) injection of 0.5 μmol of the ligand in 100 μL saline. Animals were

maintained on normal diet *ad libitum* and were sacrificed by cervical dislocation at 15 min, 1 h and 24 h post-administration. The administered radioactive dose and the radioactivity in sacrificed animals were measured in a dose calibrator (Capintec CRC25R). The difference between the radioactivity in the injected and sacrificed animal was assumed to be due to whole body excretion. Tissue samples of main organs were then removed for counting in a gamma counter (Berthold LB2111, Berthold Technologies, Germany). Biodistribution results were expressed as percent of injected activity per organ (% I.A.) and as percent of injected activity per gram of organ (%I.A./g) and presented as mean values ± standard deviation. Biodistribution data were evaluated by an analysis of variance. The level of significance was set at 0.05 (two-sided). Animal studies were carried out under the supervision of experienced researchers in animal facilities approved by the national authorities according to the national and European laws.

3. Results and discussion

3.1. Synthesis and characterization

The tripodal chelator SC was designed to contain three KA coordinating groups attached to a tris(2-aminoethyl)amine skeleton (Fig. 1). The ligand was synthesized through the straightforward method outlined in Scheme 1 and detailed in the experimental section, with a 98.5% yield.

The easy and cheap synthesis has to be remarked, together with the extremely high yield. The length of the linker chains between the apical tertiary nitrogen atom and the KA chelating moieties was based on the assumption that it was long enough to allow the wrapping of the metal ion by the KA moieties. A short linker, by reducing the molecular weight of the ligand, could represent a benefit for both the membrane crossing and for the accessibility to cytoplasmic iron pools [32].

3.2. Protonation equilibria

SC ligand is characterized by six protonation sites, the three O– groups in the KA units and the three amino groups of the tren backbone. Potentiometric-spectrophotometric titrations were performed in the 240–370 nm wavelength range (Figs. 1S and 2S), with the aim of evaluating the protonation constants and attributing each protonation step to a given basic group on the molecule (amine or O– groups). The resulting data, processed with HypSpec program [17] allowed the calculation of the six protonation constants in Table 1 and of the absorptivity spectra of the seven differently protonated species in Fig. 2. These spectra permit to ascribe the three last protonation steps with log K 8.04, 7.70 and 7.10 to the O– group in the KA units. In fact, ligand SC, in its completely protonated form LH_6^{3+}, is characterized by a band at

Table 1

Protonation constants of the ligand SC (log β and log K) at 25 °C and 0.1 M NaCl ionic strength[a]. The protonation constants (log K) of tren in the same experimental conditions are from Reference [33].

SC ligand			tren	
Formed species	log β	log K	Formed species	log K
SCH^{2-}	10.18(2)	10.18	TH^+	10.08
SCH_2^-	19.83(1)	9.65	TH_2^{2+}	9.55
SCH_3	28.55(1)	8.72	TH_3^{3+}	8.41
SCH_4^+	36.59(1)	8.04[b]		
SCH_5^{2+}	44.29(1)	7.70[b]		
SCH_6^{3+}	51.39(1)	7.10[b]		

[a] The protonation constant of KA in the same conditions is 7.70 [9].
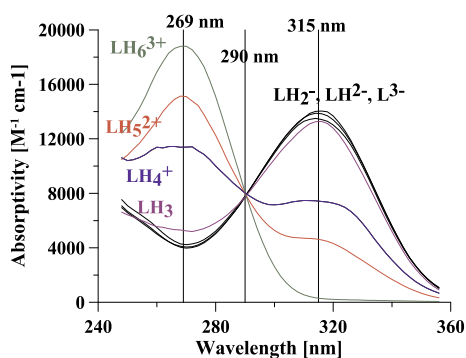[b] Protonation of KA unit.

Fig. 2. Absorptivity spectra of the variously protonated forms of SC ligand, calculated using HypSpec program [17].
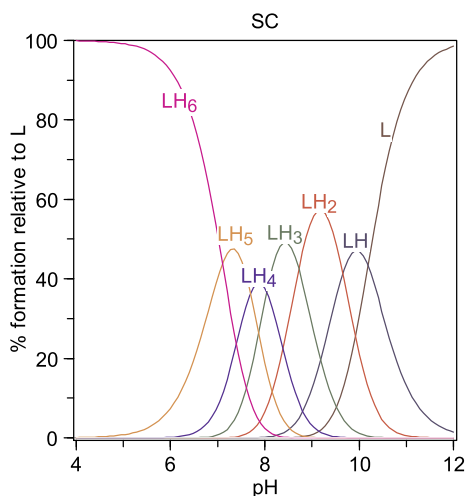

Fig. 3. Speciation plot of SC ligand, calculated using Hyss program [34].

269 nm similar in position to the band of protonated KA, but more intense due to the contribution of three similar chromophore units. Passing to the penta-protonated form LH_5^{2+}, the band at 269 nm decreases in intensity and a new band appears at 315 nm, as in the case of the dissociation of KA. In the second and third dissociation step, until the formation of the neutral LH_3 species, the band at 269 nm decreases and the band at 315 nm reaches its maximum value $\varepsilon = 13{,}000\,M^{-1}\,cm^{-1}$. Fig. 3 presents the speciation plots of SC ligand.

The three following deprotonation steps do not present appreciable spectral variations. Based on the above observations, the first three deprotonation steps were attributed to the dissociation of the OH groups in the KA moieties, and the following three, spectrally silent, to that of the charged amino groups. NMR results support the above

conclusions. The ^{1}H and ^{1}H-^{13}C-HSQC NMR spectra with the assignments of all the protons of ligand SC are reported in Fig. 4.

The ligand shows a very high symmetry in our NMR conditions; indeed, the three KA units, joined by a tris(2-aminoethyl)amine (tren) backbone, give a unique ^{1}H and ^{13}C pattern. In Fig. 5 the ^{1}H NMR spectra as a function of the pH in the range 2.60–9.90 are reported. Table 2S displays ^{1}H and ^{13}C resonance assignments of SC ligand by changing the pH.

The variation in chemical shifts, which starts to appear from pH 6.5 on, points to high field for all the protons, indicating the deprotonation of the nearby sites by raising the pH. As showed in the plot in Fig. 6 the most affected protons are the following in the order F > C = D = G > E from pH 7.10 on. From pH 7.10 on, the observed shifts of C, D and E protons can support the deprotonation of the NH_2^+ sites on the linker.

On the other hand, the change in chemical shifts of the ^{13}C signals reported in the plot in Fig. 7 shows that it pointed toward low field for all the carbons except for G nucleus.

3.3. Iron complex formation equilibria

The complex formation equilibria between Fe^{3+} and SC ligand were studied by a combined potentiometric-spectrophotometric procedure, previously discussed [10]. Furthermore, since Fe^{3+} is almost completely complexed when mixing reagents before the base potentiometric titration, the complex formation equilibria were studied also in strong acidic solutions (pH 0.4–2) on sets of solutions at increasing concentrations of HCl until the disappearance of the bands of complexed iron. These measurements at acidic pH values were made in batch adjusting the ionic strength by proper additions of HCl and NaCl. In the case of four solutions at pH between 0.4 and 0.9 the ionic strength was not 0.1, but determined by the HCl concentration (these points were not taken into account in the calculations). Combined potentiometric-spectrophotometric measurements were done in the 350–700 nm range, using 1 cm path lengths. Some representative spectra collected with both procedures at the same concentration of reagents in a 1:1 ratio are reported in Fig. 3Sb and c. Complex formation data were analyzed using Hyperquad [16] and HypSpec [17] programs. The complex formation constants so evaluated are reported in Table 2, and the related speciation plot in Fig. 8.

As can be seen from the speciation plot, starting from pH = 1 the formation of $[Fe(SC)H_5]^{5+}$, and almost simultaneously of $[Fe(SC)H_4]^{4+}$ is apparent. The first is characterized by a visible band centered at 500 nm, that shifts at 475 nm and increases in intensity with the formation of $[Fe(SC)H_4]^{4+}$. After pH 3 a third species $[Fe(SC)H_3]^{3+}$ appears whose main band is centered at 397 nm. The similarity of the spectral variations with those observed on the system Fe^{3+}/KA, during the formation of the species $[Fe(KA)]^{2+}$, $[Fe(KA)_2]^+$ and $Fe(KA)_3$ [9] (Fig. 3Sa), lead to attribute $[Fe(SC)H_5]^{5+}$ to a complex in which Fe^{3+} is coordinated by one KA unit of SC, $[Fe(SC)H_4]^{4+}$ by two KA units, and $[Fe(SC)H_3]^{3+}$ by all the three KA units. The DFT calculations later presented do not support this last interpretation, and $[Fe(SC)H_3]^{3+}$ should be presumably a polynuclear complex with the same Fe:SC molar ratio. A possible structure of the M:SC 3:3 (where Fe3+ is replaced by Al3+ for simplicity) is reported in Fig. 4S: in this case it is shown that 2 metal ions are completely coordinated by the KA moieties while the third metal ion is bound by two units. Unfortunately, the low melting temperature of ligand SC prevented performing ESI-MS measurements. In the $[Fe(SC)H_3]^{3+}$ complexes, or similar polynuclear complexes, all the nitrogen atoms are protonated. This complex then loses five protons with pK 7.50, 8.62 (two protons), 9.31 and 9.79. The decrease of the intensity of the visible bands from pH 6.70 on (Fig. 3Sc) presumably is indicative of the formation of hydroxo complexes during the first deprotonations where Fe^{3+} is coordinated by only two KA units, and the charged nitrogen atoms then lose their protons in the following steps.
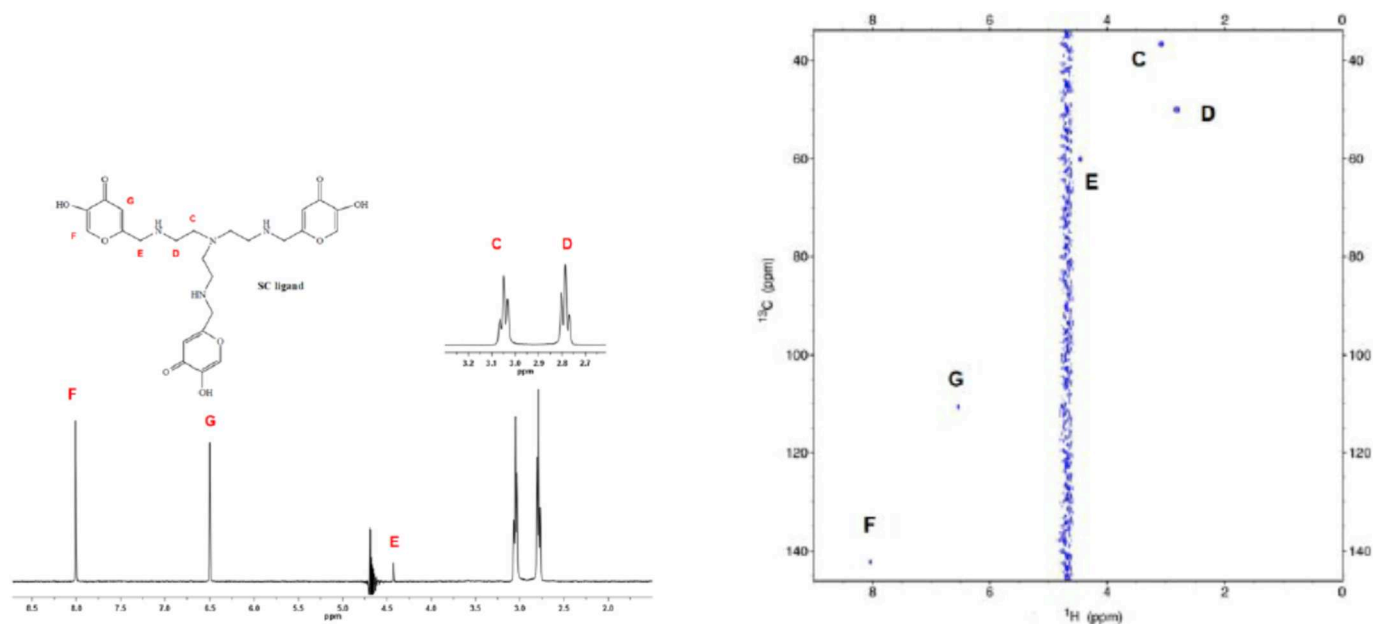
Fig. 4. ^{1}H (left) and ^{1}H-^{13}C-HSQC (right) NMR spectra with the assignments of all the signals.
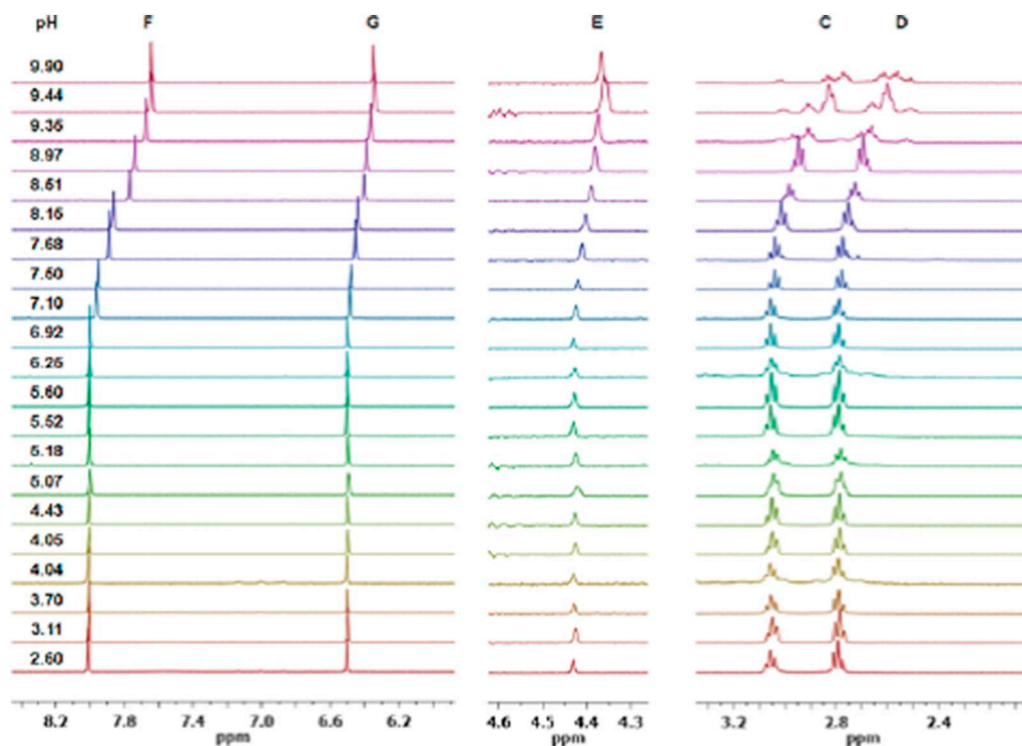
Fig. 5. ^{1}H NMR spectra as a function of pH in the pH range 2.60–9.90.

The complex formation equilibria of the ligand with Fe^{3+} ions were studied also by NMR technique. However, because of the low stability of Fe^{3+} solutions during the experimental condition used for NMR measurements and some broad signals obtained with this system, Ga^{3+} ions were used instead of Fe^{3+} ions as an amenable diamagnetic probe in the NMR measurements.

^{1}H NMR spectra as a function of pH, in the range 3.10–9.60 using a 3:2 SC:Ga^{3+} molar ratio, are reported in Fig. 9.

The ^{1}H chemical shift δΔ variations for the SC:Ga^{3+} and SC:Al^{3+} in a 1:1 molar ratio *versus* SC free ligand by changing the pH are reported in Fig. 10. These plots give evidence of the similar behavior of the two metal ions.

In fact, the behavior of the Ga^{3+}-SC (and presumably Fe^{3+}-SC) system by changing the pH is widely comparable to that of the Al^{3+}-SC system, evidently showing the involvement of the oxygen atoms from the three aromatic rings and the non-involvement of the nitrogen atoms from the linker. At the same time, at pH higher than 8, the signals from the free ligand strongly reappear. The species indicated as FeL in the speciation plot, should be some hydroxylate species, following the NMR behavior where the signals of the free ligands very clearly reappeared at pH higher than 8.
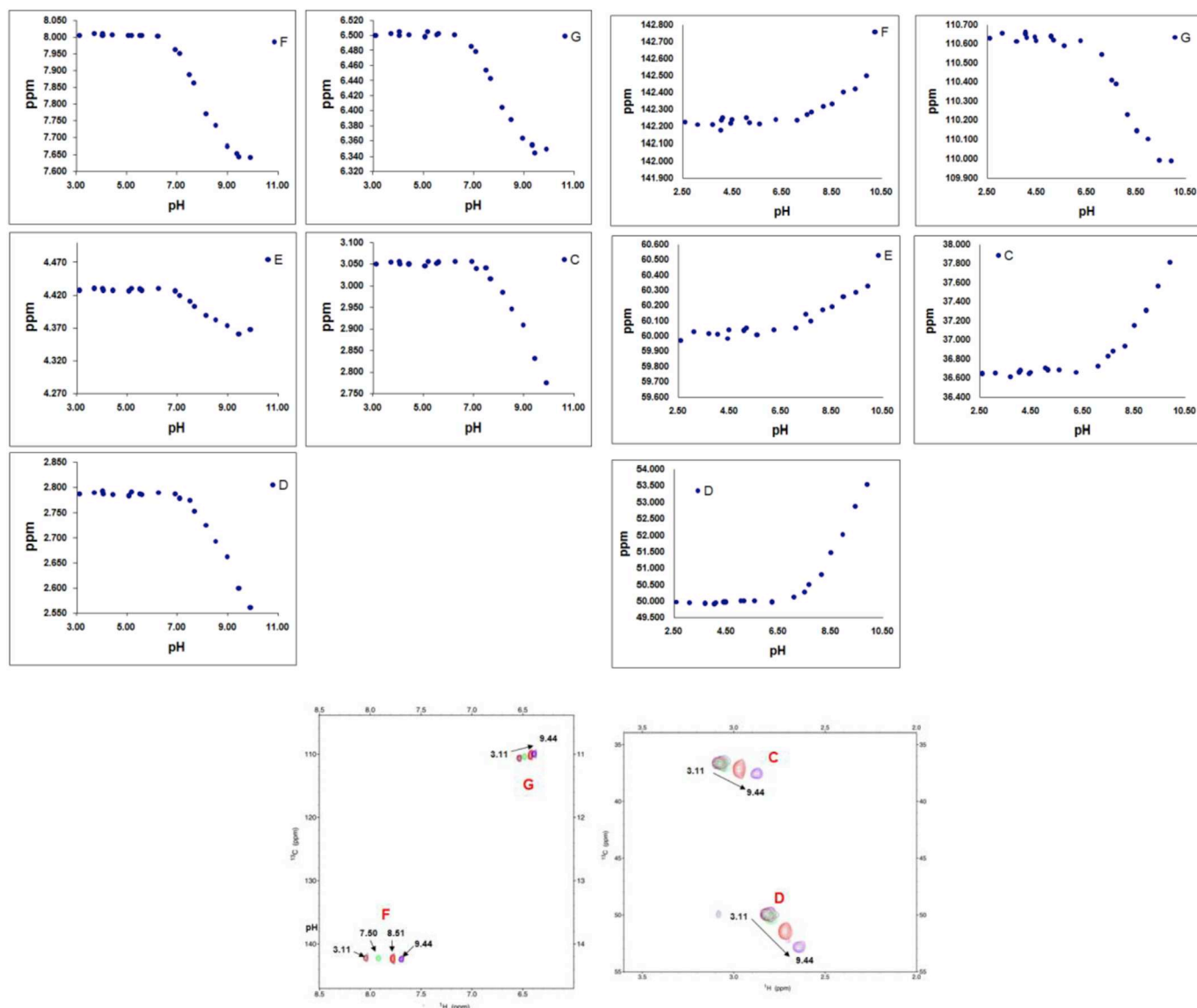
Fig. 6. Trend of ^{1}H and ^{13}C chemical shifts *vs* pH, and some ^{1}H-^{13}C-HSQC spectra at selected pH values.
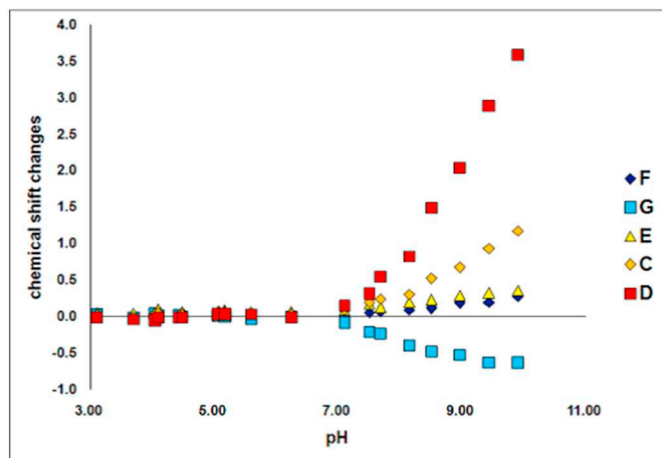
Fig. 7. Trend of ^{13}C chemical shifts *vs* pH.

Table 2

Complex formation constants of the system Fe^{3+}/SC at 25 °C and 0.1 M NaCl ionic strength, calculated with HypSpec program [17].

Formed species	Log β	pK
$[Fe(SC)H_5]^{5+}$	53.5(6)	1.4
$[Fe(SC)H_4]^{4+}$	52.12(7)	4.00
$[Fe(SC)H_3]^{3+}$	48.12(4)	7.50
$[Fe(SC)H_2]^{2+}$	40.62(4)	8.62
Fe(SC)	23.37(5)	9.31
$[Fe(SC)H^{-1}]$	14.06(3)	9.79
$[Fe(SC)H_{-2}]^{2-}$	4.27(4)	–
pFe	**19.5**	

3.4. Aluminium complex formation equilibria

The complex formation equilibria involving Al^{3+} and SC ligand were studied by potentiometric titrations. The formed complexes and the related stability constants are reported in Table 3, and the related
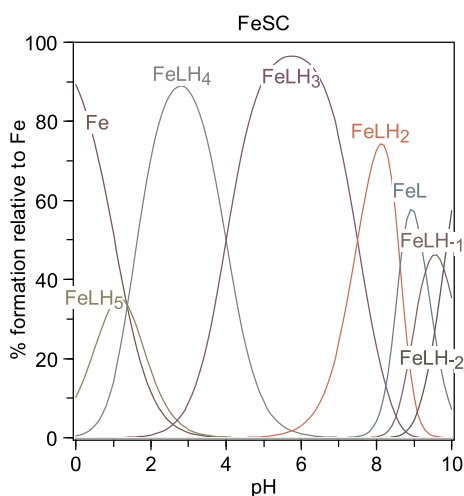
Fig. 8. Speciation plot of the system Fe^{3+}/SC, at $C_{Fe3+} = C_{SC} = 1$ mM, calculated using Hyss program [34].

Fig. 10. ^{1}H Chemical shift variation for the SC:Ga and SC:Al (1:1) systems *vs* that of SC free with changing pH.

speciation plots in Fig. 11. The mechanism of complexation resembles that one of iron, though with lower stability constants. A complex [Al(SC)H$_5$]$^{5+}$ forms from pH 3 on, in which the metal ion is coordinated by one KA unit; almost simultaneously the second [Al(SC)H$_4$]$^{4+}$ species forms, with Al^{3+} ion coordinated by two KA units. Finally, from pH 5 on starts the formation of complex [Al(SC)H$_3$]$^{3+}$ fully coordinated by three KA units, till protonated on the nitrogen atoms. Two of these charged nitrogen atoms lose their protons with pK 8.10 and 8.63, almost one pK unit lower than for pure SC ligand, coming from the effect of the higher total positive charge of the molecule. The obtained pAl value is 5.8 units lower than that with iron, in line with the normal behavior of oxygen-based ligands with these two trivalent metal ions.

The complex formation equilibria of the ligand with Al^{3+} ions were also studied by NMR titrations. ^{1}H NMR spectra are reported in Fig. 12 as a function of the pH in the range 3.07–9.46 at a 1:1 SC:Al^{3+} molar ratio.

Starting from pH 3 a new signal is visible, though together with the signals of the free ligand, showing that the complexes start anyway to form at acidic pH. A further new signal is clearly visible at pH 3.79,

though in a low concentration, together with another one that reaches its maximum around pH 8 and appears as the most important species. At pH higher than 8, this species decreases in intensity while the signals of the free ligand appear more intense suggesting that, at high pH, Al^{3+} ions can be rather involved in the formation of some hydrolytic (mixed ligand-hydroxo) metal complex species.

The formation of Al^{3+}-SC complexes involves the oxygen atoms from the aromatic rings, while nitrogen atoms from the linker are not involved in the interaction with Al^{3+} ions. In fact, the most affected

Fig. 9. ^{1}H NMR spectra as a function of the pH in the range 3.10–9.60 in a 3:2 SC:Ga^{3+} molar ratio. Circles indicate the complexes, asterisks the free ligand.

Table 3
Complex formation constants of the system Al^{3+}/SC at 25 °C and 0.1 M NaCl ionic strength, calculated with Hyperquad program [16].

Formed species	Log β	pK
$[Al(SC)H_5]^{5+}$	51.72(2)	3.64
$[Al(SC)H_4]^{4+}$	48.08(1)	5.63
$[Al(SC)H_3]^{3+}$	42.45(1)	8.10
$[Al(SC)H_2]^{2+}$	34.35(2)	8.63
$[Al(SC)H]^{+}$	25.72(3)	–
pAl	**13.7**	

Table 4
Complex formation constants of the system Cu^{2+}/SC at 25 °C and 0.1 M NaCl ionic strength, calculated with Hyperquad program [16].

Formed species	Log β	pK
$[Cu(SC)H_4]^{3+}$	46.83(2)	3.92
$[Cu(SC)H_3]^{2+}$	42.91(1)	7.26
$[Cu(SC)H_2]^{+}$	35.65(2)	7.53
$Cu(SC)H$	28.12(1)	8.07
$[Cu(SC)]^{-}$	20.05(2)	9.55
$[Cu(SC)H_{-1}]^{2-}$	10.50(2)	
pCu	**14.6**	
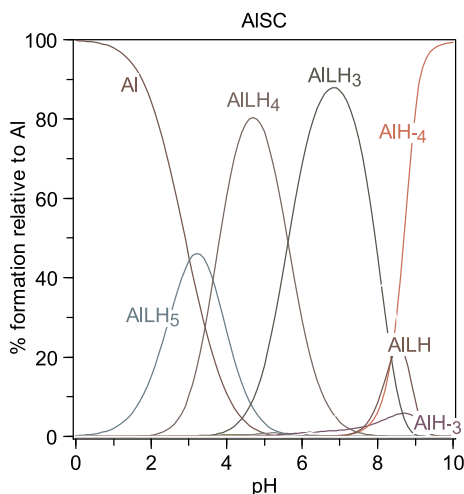
Fig. 11. Speciation plot of the system Al^{3+}/SC ligand, at $[Al^{3+}] = [SC] = 1$ mM, calculated using Hyss program [34].

protons appear to be those on the aromatic rings, mainly F and G protons. The chemical shift values of F and G protons of the Al^{3+}-SC species appear constant in all the range of pH supporting that one predominant species is present in a slow exchange in the NMR scale. The complexed species appears highly symmetric suggesting that all the three aromatic rings are involved in the coordination.

Only one signal is visible for each group of protons indicating that a

relevant interaction between the metal ion and SC ligand is present especially in the range of pH from 6 to 8.

Starting at pH higher than 8 several signals appear for the groups of protons suggesting that aluminium ions are, mostly not more coordinated to the SC ligand. The species indicated as AlSH in the speciation potentiometric plot, should be a hydroxylate species, following the NMR behavior where the signals of the free ligands very clearly reappeared at pH higher than 8.

In Fig. 5S the ^{1}H and ^{13}C $\delta\Delta$ chemical shift variation for F, G, C and D protons for SC:Al^{3+} system at 1:1 molar ratio by changing the pH are reported, and in Table 3S the ^{1}H and ^{13}C resonance assignments at variable pH.

3.5. Copper complex formation equilibria

The complex formation equilibria between Cu^{2+} and ligand SC were studied by potentiometric titrations. The formed complexes and the related stability constants are reported in Table 4, and the speci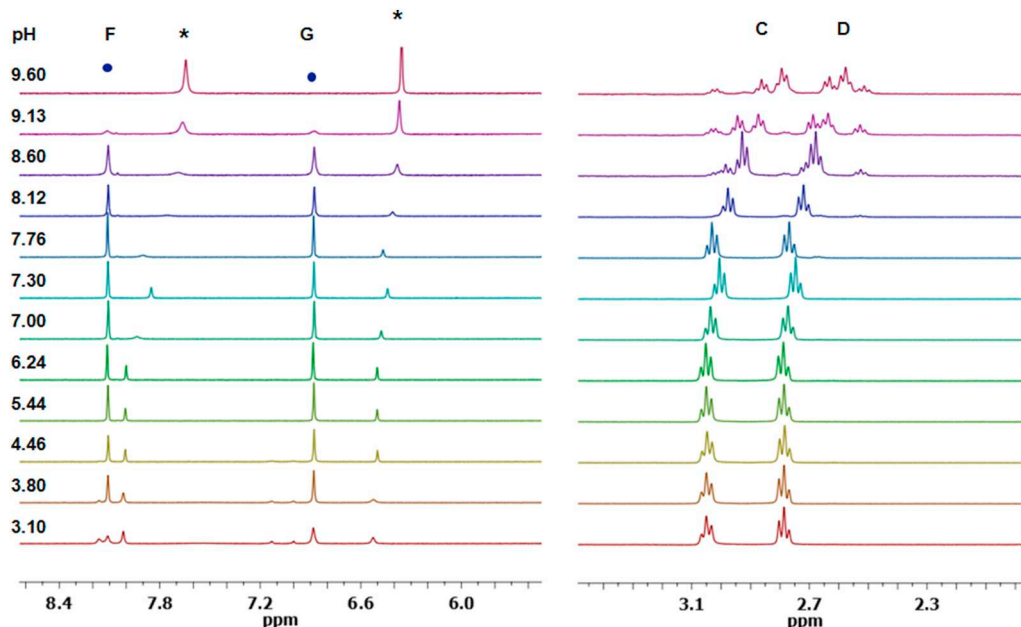ation plot in Fig. 13. Even if the complexation mechanism resembles that with iron and aluminium ions, a completely different situation is present. The first formed species $[Cu(SC)H_4]^{3+}$ is a complex with Cu^{2+} coordinated by two nitrogen atoms. This transforms in $[Cu(SC)H_3]^{2+}$ at pK 3.92 with Cu^{2+} coordinated by all the three nitrogen atoms, analogously to what observed with tren (T) (Table 5 and Fig. 13) [33]. The three remaining protons, lost with pK values almost the same of that measured for the three KA units in pure SC ligand, confirm the above attributions, as well as the similar values of pCu for SC and tren, slightly higher the former.

Fig. 12. Left, ^{1}H NMR as a function of the pH in the range 3.03–9.35 in a 1:1 SC:Al^{3+} molar ratio, at SC concentration 2 mM. On the right, the percentage of the different SC species *vs* pH.
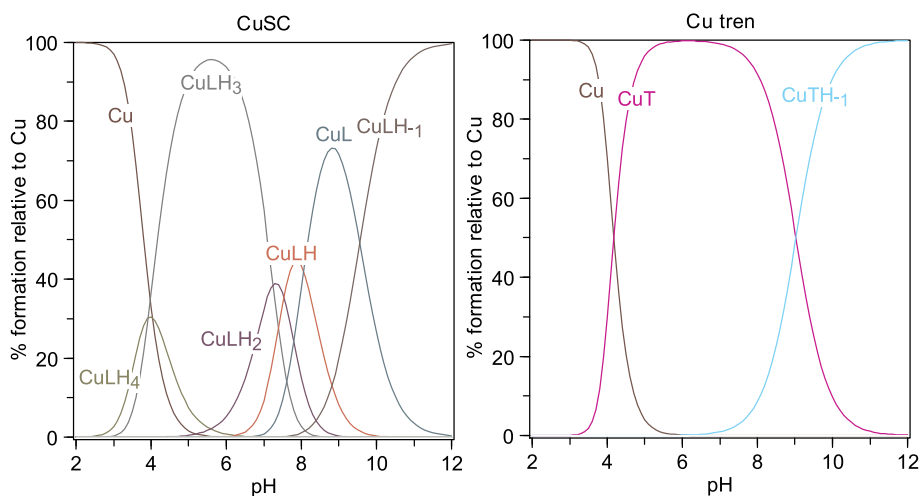
Fig. 13. Speciation plot of the systems left) Cu^{2+}/SC, at $[Cu^{2+}]$ = [SC] = 1 mM, right) Cu^{2+}/tren, at $[Cu^{2+}]$ = [tren] = 1 mM, calculated using Hyss program [34]; tren = T.

Table 5
Complex formation constants of tren (T) with Cu^{2+} and Zn^{2+} at 25 °C and 0.1 NaCl M ionic strength [33].

Formed Species	Cu^{2+}	Zn^{2+}
	$\log \beta$	$\log \beta$
MT	18.83(1)	14.40(2)
MTH_{-1}	9.80(1)	4.09(3)
pM	13.9	9.5

^{1}H NMR studies for SC-Cu^{2+} system using sub-stoichiometric amounts of Cu^{2+} ions, due to its paramagnetic behavior, have been carried out. In Fig. 14 the NMR titration of SC ligand with increasing additions of sub-stoichiometric amounts of Cu^{2+} ions at pH 7.10, from 200:1 to 1:1 SC: Cu^{2+} molar ratio, is reported. The most affected protons are, in this case, F protons from the aromatic ring, while G from the aromatic ring and C and D protons from the linker remain unchanged

till 1:1 molar ratio, where a disappearance of all the signals is visible.

The NMR spectra at 1:1 SC: Cu^{2+} molar ratio at variable pH values are reported in Fig. 15. It is possible to see that whereas C and D protons are still visible since acidic pH, F and G protons disappear. The disappearance of all the signals happen at pH 4.5 and thus, for that reason, the involvement of the nitrogen atoms cannot be demonstrated, but also cannot be excluded by looking to the NMR results only, as clearly visible from the NMR titration analysis obtained by changing the pH from 3.1 to 7.1 for SC:Cu^{2+} 1:1 molar ratio system.

3.6. Zinc complex formation equilibria

The complex formation equilibria between Zn^{2+} and ligand SC were studied by potentiometric titrations. The formed complexes and the related stability constants are reported in Table 6, and the speciation plot in Fig. 16. The results with Zn^{2+} are unexpected, and the pZn value is quite high. Surely, a simple coordination scheme through KA units as with the trivalent metal ions cannot be considered, but rather through
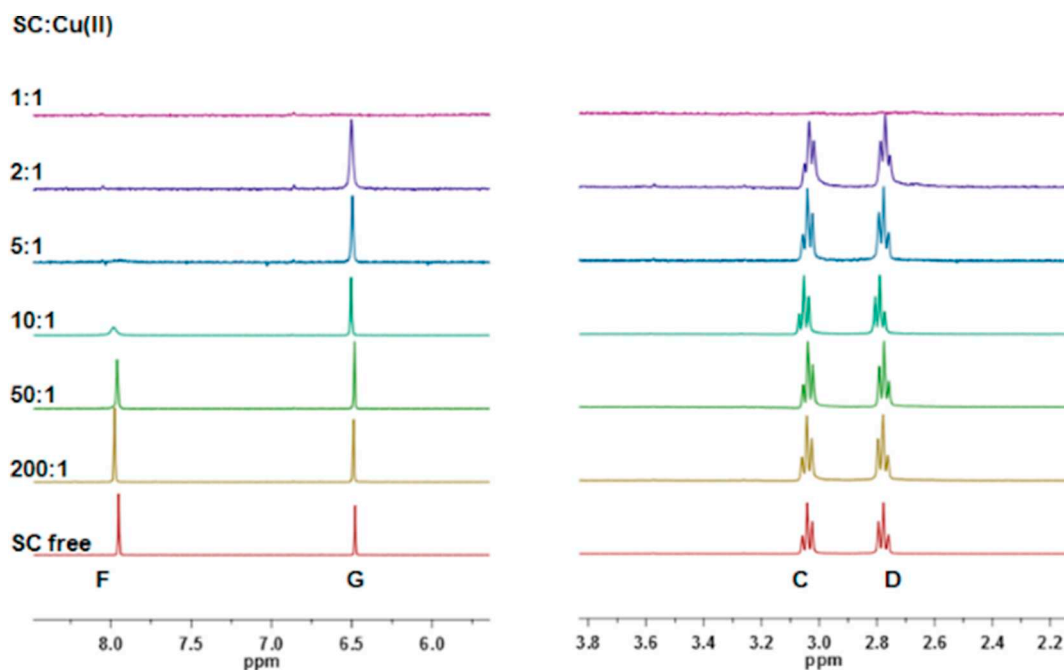
Fig. 14. ^{1}H NMR titration of SC ligand with increasing additions of sub-stoichiometric amounts of Cu^{2+} ions at pH 7.10, from 200:1 to 1:1 SC:Cu^{2+} molar ratios.
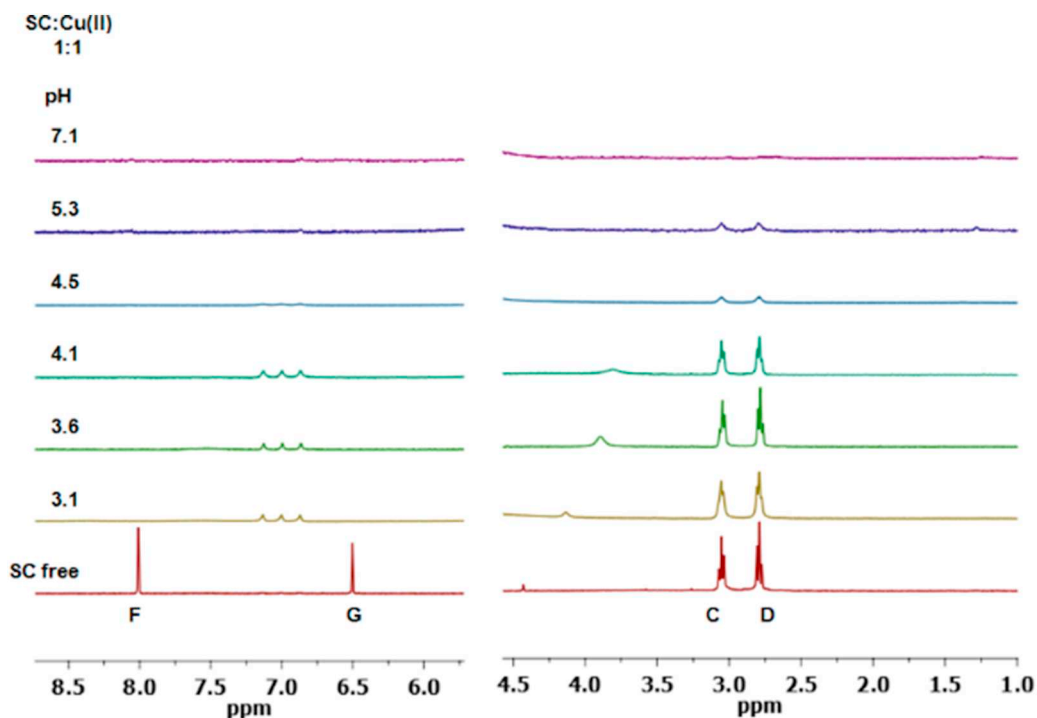
Fig. 15. ^{1}H NMR spectra at 1:1 SC: Cu^{2+} molar ratio at pH values variable from 3.1 to 7.1.

Table 6
Complex formation constants of the system Zn^{2+}/SC at 25 °C and 0.1 M NaCl ionic strength, calculated with Hyperquad program [16].

Formed species	log β	pK
$[Zn(SC)H_4]^{3+}$	43.88(1)	5.24
$[Zn(SC)H_3]^{2+}$	38.64(5)	6.14
$[Zn(SC)H_2]^+$	32.50(1)	7.43
$Zn(SC)H$	25.07(1)	7.89
$[Zn(SC)]^-$	17.18(1)	10.27
$[Zn(SC)H_{-1}]^-$	6.91(1)	
pZn	**11.4**	

nitrogen atoms as in the case of Cu^{2+}. NMR measurements have been used to have an insight on the coordination behavior of Zn^{2+} ions toward SC ligand.

The ^{1}H NMR spectra for the system SC:Zn^{2+} at 1:1 molar ratio, and at pH values from 3.72 to 9.74, are reported in Fig. 17.

In Fig. 18: a) ^{1}H NMR spectrum for the system SC:Zn^{2+} at 1:1 molar ratio at pH 7, and b) ^{1}H-^{13}C-HSQC NMR spectra for the system SC:Zn^{2+} 1:1 molar ratio at different pH values are reported. By the NMR analysis, the proton signals appear with a fast exchange in the NMR scale, as it typically happens for Zn^{2+} systems. In this case, differently from the coordination behavior of the trivalent Al^{3+} and Ga^{3+} ions with SC ligand, the most affected protons are C and D protons from the linker, which shift to higher fields, suggesting the involvement of the nitrogen atoms in the coordination to Zn^{2+} ions. On the other hand, F and G protons are not influenced, unless at higher pH. We also note that E protons are less affected than C and D protons by the addition of Zn^{2+} ions, supporting the idea that only one major species is formed, where the C nucleus is the most affected by the interaction of Zn^{2+} ions with
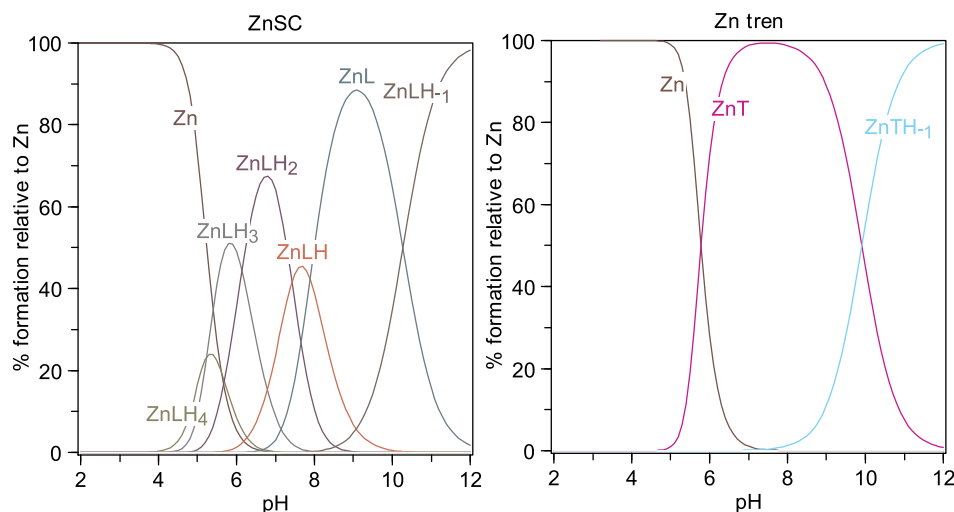
Fig. 16. Speciation plot of the systems left) Zn^{2+}/SC, at $[Zn^{2+}] = [SC] = 1$ mM, right) Zn^{2+}/tren, at $[Zn^{2+}] = [tren] = 1$ mM, calculated using Hyss program [34]; tren = T.
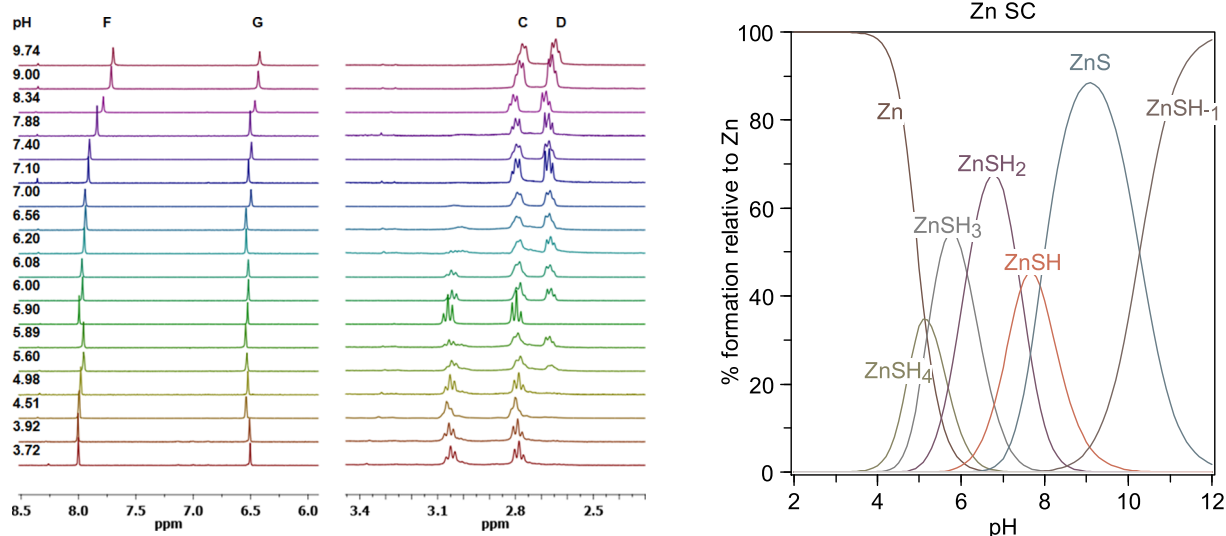
Fig. 17. ^{1}H NMR spectra for the system SC:Zn^{2+} at [SC] = [Zn^{2+}] = 5 mM, at pH values from pH 3.72 to 9.74; on the right the speciation plot at the same concentrations.

SC ligand, following the order C ≫ D ≫ E.

No evidences is found in the NMR results about the possible involvement of the donor atoms on the aromatic rings, unless a very small chemical shifts variation, which can depend from a general different electronic environment after the Zn^{2+} coordination. In agreement with the involvement of the nitrogen donor atoms, the coordination starts at pH higher than 5.9, differently from the starting coordination pH evidenced for Al^{3+}, Ga^{3+}. At pH 7.4 the formation of the species with the higher δΔ values is noted. It is noteworthy that at pH higher than 8, a new species is also visible, though the very low shifts suggest the formation of a species very similar regarding the stoichiometry and the coordination environment of Zn^{2+} ions, but with some differences related to a different protonation state of the SC ligand.

In Fig. 6S the NMR plots for ^{1}H chemical shift δΔ variations for the SC:Zn system 1:1 molar ratio by changing the pH and in Fig. 7S the NMR plots for ^{13}C chemical shift δΔ variations for the SC:Zn system 1:1 molar ratio by changing the pH are reported, respectively.

3.7. X-ray structures of tren complexes

In the following, we report on the structures of the complexes formed by tren with zinc, copper and iron. Fig. 19 reports the X-ray structures of the complexes formed by tren with zinc [35], copper [36] and iron [37] respectively. The length of the bonds between the metal ions and the apical nitrogen atom, and the three terminal nitrogen atoms, are reported in Table 7.

3.8. DFT calculations

The Metal-SC complexes with Zn^{2+} and Al^{3+} ions were initially studied for computational convenience since they are systems with singlet multiplicity. Furthermore, they are good for comparisons, as they have the highest and the lowest stability of the 1:1 complex experimentally found with SC. In Fig. 20 the minimum energy structures of the ZnS complex are displayed: the structures a) and b) have been
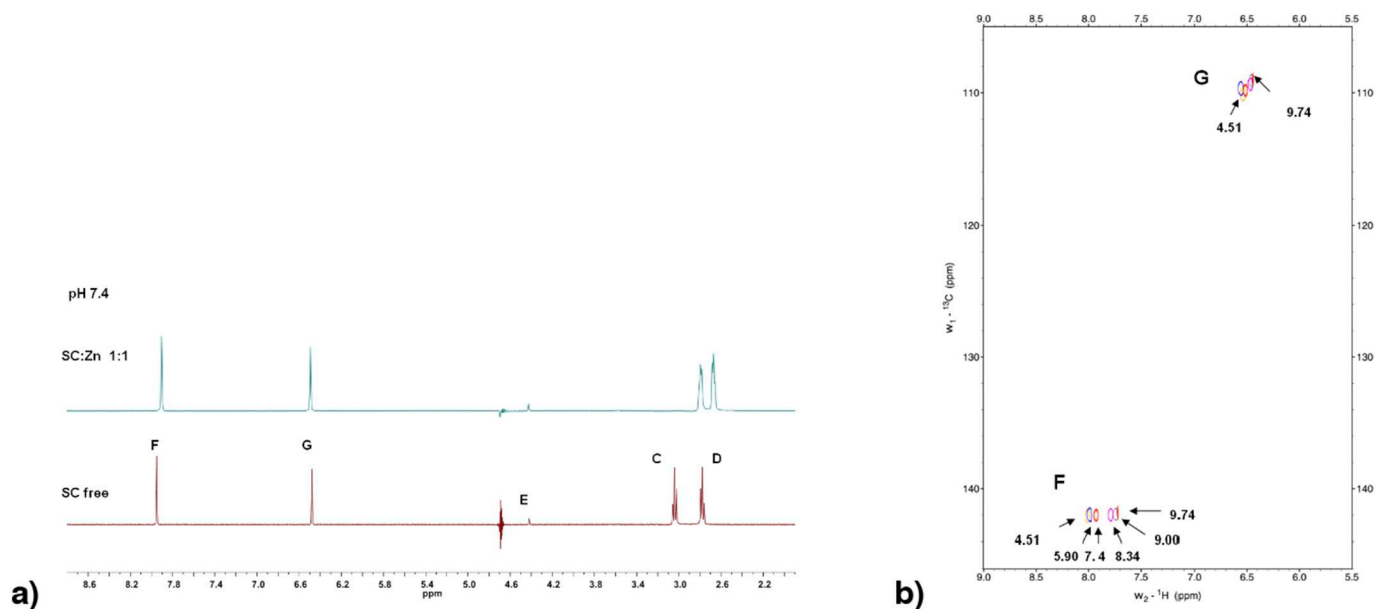
Fig. 18. a) Spectrum of free ligand SC (lower spectrum) and in presence of an equimolar amount of Zn^{2+}, at pH 7.4; b) spectra ^{1}H-^{13}C-HSQC of the system SC:Zn (1:1) at different pH values.

AEZNPB (Zn-tren) CTRENB (Cu-tren) XUZVET (Fe-tren)
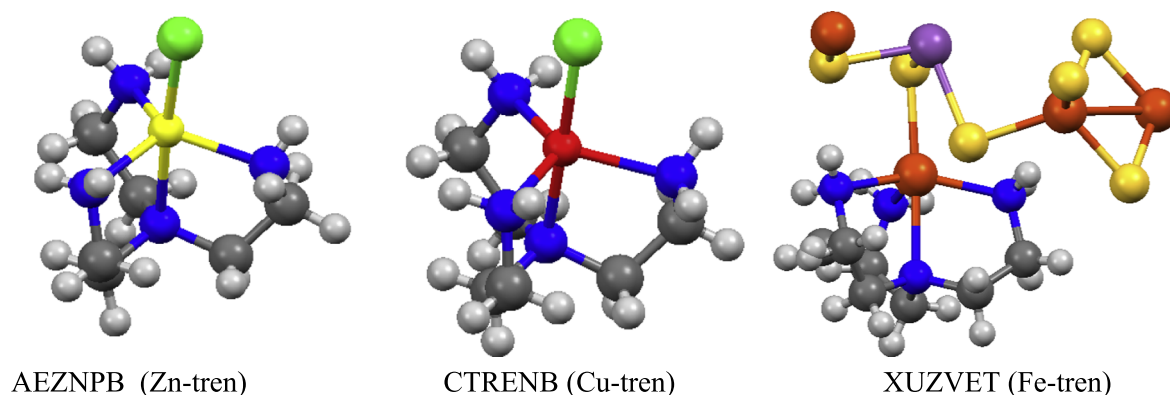
Fig. 19. X-Ray structures of the tren complexes with zinc, copper and iron. Coordinates obtained from the Cambridge Structural Database, images created with Mercury3.5.

Table 7
The length of the bonds between the metal ions (zinc, copper and iron) and the nitrogen atoms: the apical nitrogen atom, and the three terminal nitrogen atoms.

	Zinc	Copper	Iron
Apical N atom	2.325	2.080	2.302
NH_2 (1)	2.062	2.107	2.149
NH_2 (2)	2.067	2.066	2.135
NH_2 (3)	2.064	2.099	2.149

optimized without additional water molecules to saturate the first co-ordination sphere of the metal ion while three additional water were introduced in c). It results that the a) structure has an energy of ~ 55 kcal mol^{-1} higher than b) therefore the a) coordination mode can be discarded for this species. This result is in agreement with the ob-served changes of the aromatic F and G protons at pH > 8 (Fig. 17), supporting the hypothesis that at lower pH coordination occurs pre-ferentially at the N atoms of the linker, while at higher pH values the KA units are involved. Geometry searches always led to complexes where the KA moieties are not completely coordinated to the metal, but they can be either mono or bidentate. In the c) complex, the addition of the water molecules leads to the opening of the bidentate KA moiety.

In the case of Al^{3+}, the d) structure is less stable than e) by ~ 135 kcal mol^{-1} thus it is discarded also in this case and compatible with the observed preferential interaction with the oxygen atoms oc-curring at low pH yet. It should be noted that in e) the ligand can be bidentate with two KA units.

When also two water molecules are considered, one KA moiety opens to become monodentate. In summary, it can be concluded that: i)
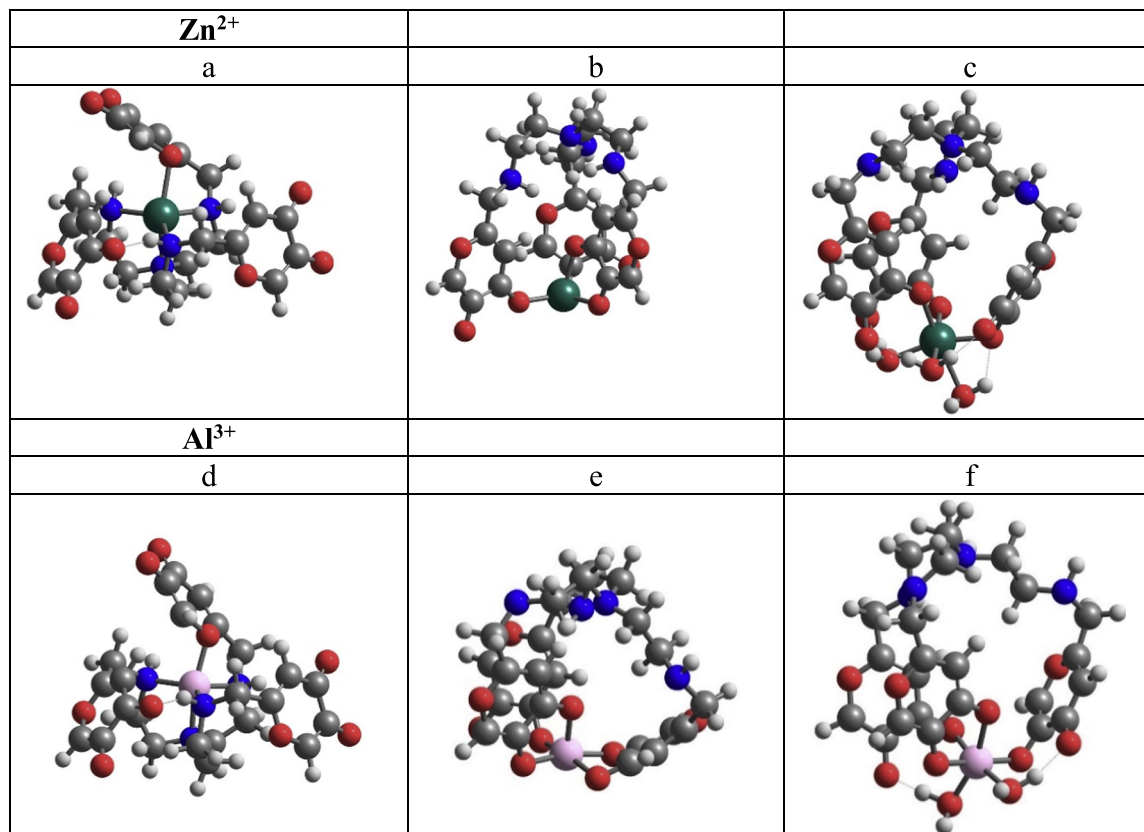
Fig. 20. Possible coordination modes of Zn^{2+} and Al^{3+} ions in the 1:1 complexes obtained in gas phase.

Table 8
Biodistribution of ^{67}Ga in the most relevant organs, expressed as percentage of I. A./g, after administration of ^{67}Ga-citrate with simultaneous intraperitoneal injection of SC ligand, at 1, and 24 h post-injection in female CD-1 mice (n = 3).

	^{67}Ga-SC	
	1 h	24 h
Blood	2.0 ± 0.6	0.8 ± 0.2
Liver	3.1 ± 0.6	1.1 ± 0.7
Intestine	2.1 ± 0.5	0.5 ± 0.4
Spleen	1.5 ± 0.4	0.5 ± 0.3
Heart	0.8 ± 0.2	0.7 ± 0.6
Lung	1.4 ± 0.4	1.2 ± 0.1
Kidney	3.6 ± 0.5	2.3 ± 0.5
Muscle	0.5 ± 0.1	0.21 ± 0.05
Bone	4.9 ± 1.3	0.6 ± 0.5
Stomach	1.2 ± 0.4	0.3 ± 0.2
Excretion (% I.A.)	49.9 ± 5.8	79.3 ± 5.5

the ligand is not flexible enough to encapsulate efficiently the metal ions ii) only the KA groups are involved in the complexation reaction, iii) Al^{3+} ion interacts more efficiently with the ligand due to the formation of more bonds with the KA units.

The same calculation carried out for Fe^{3+} ion provided a structure similar to that of Al^{3+} ion (Fig. 8S). By comparing the theoretical spectra of the FeSC complex (Fig. 9S) with that of the $Fe(KA)_3$ species it emerges that they are different confirming that the coordination mode should be different in the two cases.

3.9. Biological assays

Biodistribution studies were carried out in CD-1 mice to assess the efficacy of the ligand as chelating agent for the mobilization of gallium in ^{67}Ga-citrate injected mice. Since the biodistribution profile of the radiotracer ^{67}Ga-citrate in mice is well-known, we evaluated the effect of the ligand on the biokinetics and elimination of the radiometal by intraperitoneal administration of 0.5 μmole of the SC solution immediately after intravenous administration of the radiotracer. Tissue distribution of ^{67}Ga in major organs at 1 h and 24 h expressed as % I.A./

Fig. 21. Biodistribution data in the most relevant organs, expressed as % I. A. for ^{67}Ga-citrate and ^{67}Ga-citrate with co-administration of DFP or SC at 1 and 24 h after administration in female CD-1 mice (n = 3).

g is presented in Table 8 and Fig. 21.

These results indicate that the radiometal is rapidly cleared from the bloodstream through both the hepatobiliary and the urinary excretory pathways. Clearance from the major organs is rapid and most of the radioactivity was eliminated at 24 h after injection, except in the organs related with the excretory tracts, liver and kidneys. The overall rate of radioactivity excretion was moderate, 49.9 ± 5.8 and 79.3 ± 5.5% I.A, at 1 h and 24 h, respectively. Altogether, these results in mice demonstrated that the ligand has *in vivo* chelating ability promoting the elimination of the radiometal from the animal body.

To further evaluate the effect of our ligand on the ^{67}Ga distribution and excretion and its usefulness to complex *in vivo* and eliminate unwanted trivalent metal ions, we have compared our results with those found with the drug deferiprone (DFP) in the same animal model at 1 h and 24 h (Fig. 21). Biodistribution profile of the radiotracer ^{67}Ga-citrate without simultaneous administration of any ligand is also included in the graphic for comparative purposes.

Data analysis at 1 h and 24 h after administration evidenced that the co-administration of the ligand has enhanced the clearance of the radiometal ^{67}Ga from most organs, except in the kidneys and the overall excretion rate of radioactivity from whole animal body more efficiently than the drug (ρ < 0.01) at 24 h.

In conclusion, this ligand can efficiently chelate the radiometal in our animal model suggesting that it can be a promising candidate as chelating agent of other trivalent metals.

3.10. Pharmacokinetic properties

To evaluate the drug-likeness of the ligand SC, in comparison with the drug DFP (Fig. 1), some descriptors of their pharmacokinetic profiles were calculated using QikProp program, v. 2.5 [38], and are summarized in Table 9. Analysis of the data in this table shows that, although only DFP present no violations to the criteria of the Lipinski's rule [11], SC presents three minor violations of that rule, namely molecular weights (~518.5), lipophilicity (clog $P_{O/W}$ = −2.57), slightly exceed the number of H-bond acceptors (16) or H-bond donors (6). Furthermore SC present good capacity for membrane permeation as indicated by log BB values (> −3.113), good binding interaction with Human serum albumin (log K = −1.064), and moderate % Human oral absorption (32) by the gastrointestinal (GI) track [38].

Although some molecular descriptors as the molecular weight of the new ligand (572 Da) may put some limits to its possible use as an oral chelating agent, namely based on Lipinski rule [11], but we can consider other type of administration or the use of carriers (ex: nanoparticles, liposomes) to facilitate the drug crossing of the blood-brain barrier. On the other hand, it can find a number of applications in environmental remediation [2–4] and in agriculture for supplying essential elements to plants in an absorbable form, or making easily available those elements already present in the soil [5,6].

4. Concluding remarks

A new tripodal KA derivative (tris-3-hydroxy-4-pyrone) is presented herein and studied for its capacity to chelate iron and aluminium as well as the biometal ions copper and zinc. As compared with other reported tris-chelating ligands [25,32], it is remarkable the easy, cheap and high yield synthesis of this ligand as well as its hydrolytic stability due to absence of amide bonds. The measured protonation constants of

Table 9
Pharmacokinetic properties as predicted *in silico* by software QikProp v.2.5 [38].

Comp.	MW	Donors H bonds	Acceptors H bonds	clog$P$ O/W	log$K$ HSA serum binding	log BB	% Human oral absorpt. GI
DFP	139	1	3.25	0.601	−0.554	−0.296	78
SC	518.5	6	16.2	−2.571	−1.064	−3.113-	32

KA units do not move away significantly from that of KA, giving evidence of the absence of stabilizing hydrogen bonding. Analogously, the protonation constants related to the nitrogen atoms in the linker strictly resemble those of the tren parent molecule.

Concerning the iron and aluminium complexation, potentiometric, spectrophotometric and NMR results are clearly consistent with the formation of 1:1 metal complexes with differently protonated complexes, although DFT calculations indicate that the simultaneous coordination of the trivalent metal ions by three KA units on the same molecule appears difficult. The formation of differently protonated polynuclear complexes has to be assumed, even if no direct experimental evidence with ESI-MS was reached for the characteristic of SC ligand that prevented such measurements.

Biodistribution studies were carried out to assess the mobilization of gallium in ^{67}Ga-citrate injected mice. These studies demonstrated that this ligand efficiently chelates the radiometal in our animal model, which suggests that it can be a promising candidate as chelating agent of other trivalent metals. The calculated pM trend is $Fe^{3+} > Al^{3+} > Cu^{2+} > Zn^{2+}$ revealed for this ligand a higher chelating efficacy toward Fe^{3+} and Al^{3+} than the divalent biological metal cations, thus indicating that the sequestration of iron does not lead to the depletion of these bio relevant bi-charged metal ions. Furthermore, the high stability of Zn^{2+} complexes can open new perspectives for environmental and clinical applications of SC ligand.

Acknowledgements

Supplementary data

Supplementary data to this article can be found online at https://doi.org/10.1016/j.jinorgbio.2019.01.012.

References

[1] V.M. Nurchi, G. Crisponi, J.I. Lachowicz, S. Medici, M. Peana, M.A. Zoroddu, J. Trace Elem. Med. Biol. 38 (2016) 10–18.
[2] D. Leštan, C.L. Luo, X.D. Li, Environ. Pollut. 153 (1) (2008) 3–13.
[3] G. Chauhan, K. Pant, K. Nigam, Environ. Sci.: Processes Impacts 17 (1) (2015) 12–40.
[4] A. Serrano, F. Pinto-Ibieta, A. Braga, D. Jeison, R. Borja, F. Fermoso, Environ. Technol. 38 (24) (2017) 3137–3144.
[5] G. Dal Corso, A. Manara, S. Piasentin, A. Furini, Metallomics 6 (10) (2014) 1770–1788.
[6] E. Bloem, S. Haneklaus, R. Haensch, E. Schnug, Sci. Total Environ. 577 (2017) 166–173.
[7] V.M. Nurchi, J.I. Lachowicz, G. Crisponi, Murgia Sergio, M. Arca, A. Pintus, P. Gans, J. Niclos-Gutierrez, A. Domınguez-Martın, A. Castineiras, M. Remelli, Z. Szewczuk, T. Lis, Dalton Trans. 40 (2011) 5984–5998.
[8] L. Toso, G. Crisponi, V.M. Nurchi, M. Crespo-Alonso, J.I. Lachowicz, M.A. Santos, S.M. Marques, J. Niclós-Gutiérrez, J.M. González-Pérez, A. Domínguez-Martín, D. Choquesillo-Lazarte, Z. Szewczuk, J. Inorg. Biochem. 127 (2013) 220–231.
[9] V.M. Nurchi, G. Crisponi, J.I. Lachowicz, S. Murgia, T. Pivetta, M. Remelli, A. Rescigno, J. Niclós-Gutierrez, J.M. González-Pérez, A. Domínguez-Martín, J. Inorg. Biochem. 104 (2010) 560–569.
[10] V.M. Nurchi, G. Crisponi, J.I. Lachowicz, M.G. Jaraquemada-Pelaez, C. Bretti, M. Peana, S. Medici, M.A. Zoroddu, J. Inorg. Biochem. 189 (2018) 103–114.
[11] C.A. Lipinski, F. Lombardo, B.W. Dominy, P.J. Feeney, Adv. Drug Deliv. Rev. 23 (1997) 3–25.
[12] W.R. Harris, K.N. Raymond, F.L. Weitl, J. Am. Chem. Soc. 103 (1981) 2667–2675.
[13] A. Albert, E.P. Serjeant, Ionization Constants of Acids and Bases: A Laboratory Manual, Methuen, (1962).
[14] R. Silvagni, 2001 University of Sassari, PhD Thesis, pp. 57–58.
[15] G. Gran, Analyst 77 (1952) 661–671.
[16] P. Gans, A. Sabatini, A. Vacca, Talanta 43 (1996) 1739–1753 http://www.hyperquad.co.uk/HQ2013.htm.
[17] C. Frassineti, S. Ghelli, P. Gans, A. Sabatini, M.S. Moruzzi, A. Vacca, Anal. Biochem. 231 (1995) 374–382 http://www.hyperquad.co.uk/HypSpec2014.htm.
[18] M.A. Zoroddu, M. Peana, S. Medici, Dalton Trans. (2007) 379–384.
[19] J.I. Lachowicz, V.M. Nurchi, G. Crisponi, M.G. Jaraquemada-Pelaez, M. Arca, A. Pintus, M.A. Santos, C. Quintanova, L. Gano, Z. Szewczuk, M.A. Zoroddu, M. Peana, A. Dominguez-Martin, D. Choquesillo-Lazarte, Dalton Trans. 45 (2016) 6517–6528.
[20] M. Peana, S. Medici, V.M. Nurchi, J.I. Lachowicz, G. Crisponi, M. Crespo-Alonso, M.A. Santos, M.A. Zoroddu, J. Inorg. Biochem. 148 (2015) 69–77.
[21] A.D. Becke, J. Chem. Phys. 98 (1993) 1372–1377.
[22] C.T. Lee, W.T. Yang, R.G. Parr, Phys. Rev. B 37 (1988) 785–789.
[23] V.M. Nurchi, G. Crisponi, J.I. Lachowicz, M.A. Zoroddu, M. Peana, S. Medici, D. Veclani, M. Tolazzi, A. Melchior, Eur. J. Pharm. Sci. 93 (2016) 380–391.
[24] F. Piccinelli, M. Bettinelli, A. Melchior, C. Grazioli, M. Tolazzi, Dalton Trans. 44 (2015) 182–192.
[25] A.C. Mendonça, A.F. Martins, A. Melchior, S.M. Marques, S. Chaves, S. Villette, S. Petoud, P.L. Zanonato, M. Tolazzi, C.S. Bonnet, É. Tóth, P. Di Bernardo, C.F.G.C. Geraldes, M.A. Santos, Dalton Trans. 42 (2013) 6046–6057.
[26] S. Del Piero, P. Di Bernardo, R. Fedele, A. Melchior, P. Polese, M. Tolazzi, Eur. J. Inorg. Chem. 18 (2006) 3738–3745.
[27] A. Melchior, C. Gaillard, S. Gràcia Lanas, M. Tolazzi, I. Billard, S. Georg, L. Sarrasin, M. Boltoeva, Inorg. Chem. 55 (7) (2016) 3498–3507.
[28] P.J. Hay, W.R. Wadt, J. Chem. Phys. 82 (1985) 270–283.
[29] M.J. Frisch, G.W. Trucks, H.B. Schlegel, G.E. Scuseria, M.A. Robb, J.R. Cheeseman, G. Scalmani, V. Barone, G.A. Petersson, H. Nakatsuji, X. Li, M. Caricato, A.V. Marenich, J. Bloino, B.G. Janesko, R. Gomperts, B. Mennucci, H.P. Hratchian, J.V. Ortiz, A.F. Izmaylov, J.L. Sonnenberg, D. Williams-Young, F. Ding, F. Lipparini, F. Egidi, J. Goings, B. Peng, A. Petrone, T. Henderson, D. Ranasinghe, V.G. Zakrzewski, J. Gao, N. Rega, G. Zheng, W. Liang, M. Hada, M. Ehara, K. Toyota, R. Fukuda, J. Hasegawa, M. Ishida, T. Nakajima, Y. Honda, O. Kitao, H. Nakai, T. Vreven, K. Throssell, J.A. Montgomery, J.E. Peralta, F. Ogliaro, M.J. Bearpark, J.J. Heyd, E.N. Brothers, K.N. Kudin, V.N. Staroverov, T.A. Keith, R. Kobayashi, J. Normand, K. Raghavachari, A.P. Rendell, J.C. Burant, S.S. Iyengar, J. Tomasi, M. Cossi, J.M. Millam, M. Klene, C. Adamo, R. Cammi, J.W. Ochterski, R.L. Martin, K. Morokuma, O. Farkas, J.B. Foresman, D.J. Fox, Gaussian 16 Rev.A03 Wallingford, CT, (2016).
[30] F. Weigend, R. Ahlrichs, Phys. Chem. Chem. Phys. 7 (2005) 3297–3305.
[31] F. Neese, The ORCA program system, Wiley Interdiscip. Rev.: Comput. Mol. Sci. 2 (1) (2012) 73–78.
[32] R. Cappai, K. Chand, J.I. Lachowicz, S. Chaves, L. Gano, G. Crisponi, V.M. Nurchi, M. Peana, M.A. Zoroddu, M.A. Santos, New J. Chem. 42 (2018) 8050–8061.
[33] V.M. Nurchi, G. Crisponi, G. Sanna, M.I. Pérez-Toro, J. Niclos-Gutierrez, M.J. Gonzalez-Perez, A. Dominguez-Martin, Complex Formation Equilibria between polyamine ligands and copper(II) and zinc(II), J. Inorg. Biochem. (2019) (submitted for publication).
[34] http://www.hyperquad.co.uk/hyss.htm.
[35] A. Zalkin, R.J. Sime, R.P. Dodge, David H. Templeton, Inorg. Chem. 10 (3) (1971) 537–541.
[36] E.J. Laskowski, D.M. Duggan, D.N. Hendrickson, Inorg. Chem. 14 (10) (1975) 2449–2455.
[37] R. Kiebach, W. Bensch, R.D. Hoffmann, R. Pöttgen, Z. Anorg. Allg. Chem. 629 (2003) 532–538.
[38] QikProp, Version 2.5, Schrödinger, LLC, New York, NY, 2005.

Paper IV

Oxovanadium(IV) Coordination Compounds with Kojic Acid Derivatives in Aqueous solution

S. Berto, E. Alladio, P. G. Daniele, E. Laurenti, A. Bono, C. Sgarlata, G. Valora, R. Cappai, J. I. Lachowicz, V. M. Nurchi, *Molecules,* **2019***, 24,* 3767-3786.

Article

Oxovanadium(IV) Coordination Compounds with Kojic Acid Derivatives in Aqueous Solution

Silvia Berto [1,*], **Eugenio Alladio** [1], **Pier Giuseppe Daniele** [1], **Enzo Laurenti** [1], **Andrea Bono** [1,†], **Carmelo Sgarlata** [2], **Gabriele Valora** [2], **Rosita Cappai** [3], **Joanna Izabela Lachowicz** [4] **and Valeria Marina Nurchi** [3]

[1] Dipartimento di Chimica, Università di Torino, Via Pietro Giuria 7, 10125 Torino, Italy; eugenio.alladio@unito.it (E.A.); piergiuseppe.daniele@unito.it (P.G.D.); enzo.laurenti@unito.it (E.L.); bonoa94@gmail.com (A.B.)

[2] Dipartimento di Scienze Chimiche, Università degli Studi di Catania, Viale Andrea Doria 6, 95125 Catania, Italy; sgarlata@unict.it (C.S.); gabriele.valora@unict.it (G.V.)

[3] Dipartimento di Scienze della Vita e dell'Ambiente, Università di Cagliari, Cittadella Universitaria, 09042 Cagliari, Italy; cappai@unica.it (R.C.); nurchi@unica.it (V.M.N.)

[4] Dipartimento di Scienze Mediche e Sanità Pubblica, Università di Cagliari, Cittadella Universitaria, 09042 Monserrato, Italy; lachowicz@unica.it

* Correspondence: silvia.berto@unito.it; Tel.: +39-011-6705279

† Present address: Dipartimento di Chimica, Materiali e Ingegneria Chimica "Giulio Natta", Politecnico di Milano, via Mancinelli 7, 20131 Milano, Italy.

Abstract: Hydroxypyrone derivatives have a good bioavailability in rats and mice and have been used in drug development. Moreover, they show chelating properties towards vanadyl cation that could be used in insulin-mimetic compound development. In this work, the formation of coordination compounds of oxovanadium(IV) with four kojic acid (5-hydroxy-2-(hydroxymethyl)-4-pyrone) derivatives was studied. The synthetized studied ligands (S2, S3, S4, and SC) have two or three kojic acid units linked through diamines or tris(2-aminoethyl)amine chains, respectively. The chemical systems were studied by potentiometry (25 °C, ionic strength 0.1 mol L^{-1} with KCl), and UV-visible and EPR spectroscopy. The experimental data were analyzed by a thermodynamic and a chemometric (Multivariate Curve Resolution–Alternating Least Squares) approach. Chemical coordination models were proposed, together with the species formation constants and the pure estimated UV-vis and EPR spectra. In all systems, the coordination of the oxovanadium(IV) starts already under acidic conditions (the cation is totally bound at pH higher than 3–4) and the metal species remain stable even at pH 8. Ligands S3, S4, and SC form three coordination species. Two of them are probably due to the successive insertion of the kojate units in the coordination shell, whereas the third is most likely a hydrolytic species.

Keywords: vanadium; kojic acid; UV-visible spectroscopy; EPR spectroscopy; potentiometry; chemometry

---

1. Introduction

Vanadium plays different roles in biological systems [1] and shows a variety of pharmacological properties in humans [2,3], even if it is not an essential metal ion [4]. In particular, vanadyl salts and vanadyl coordination compounds exhibit insulin-mimetic activity and may be good candidates for the treatment of type II diabetes mellitus [3]. Bis(maltolato)oxovanadium(IV) (BMOV) and bis(ethylmaltolato)oxovanadium(IV) (BEOV) have undergone extensive pre-clinical testing, and BEOV

has been promoted to Phase II clinical trials [5,6]. These coordination compounds show a peculiar structure where two 3-hydroxy-4-pyrone units are linked in the equatorial plane of the vanadyl cation coordination sphere, as shown in Figure 1A [7].
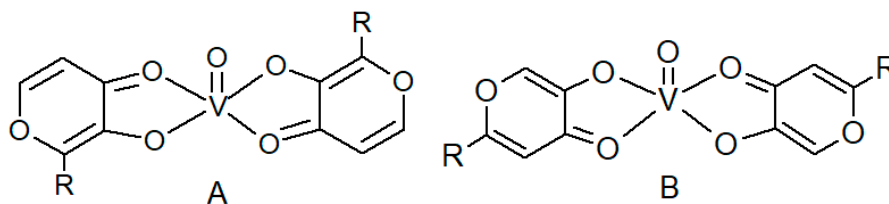
Figure 1. Structures of hydroxy-pyronato-oxovanadium(IV) coordination compounds. (**A**) Structure of bis(2-alkyl-3-hydroxy-4-pyronato)oxovanadium(IV); (**B**) structure of bis(2-alkyl-5-hydroxy-4-pyronato) oxovanadium(IV).

Hydroxypyrones are present in plant products, and many of their derivatives exhibit low toxicity, therefore good biocompatibility, and have been used for drug development [8]. Kojic acid (5-hydroxy-2-(hydroxymethyl)-4-pyrone, ka) is a fungal metabolite. ka and its derivatives are promising chelating agents for vanadyl cation and could be used in insulin-mimetic drug development. The coordination of ka or its derivatives with oxovanadium(IV) was previously studied. Yuen et al. [9] compared the glucose-lowering properties of BMOV and bis(kojiate)oxovanadium(IV) species, showing that the latter is effective but the BMOV is more potent. Sanna et al. [2] studied the chemical equilibria of ka–vanadyl species in blood serum and showed that the behavior of ka reflects that of maltol. Wei et al. [10,11] developed and tested a series of coordination compounds based on the ka structure for glucose control in blood, which showed similar glucose-lowering activity and lower toxicity with respect to BMOV.

In the present work, a series of ka-based ligands were employed for the coordination of the vanadyl cation. The synthesis and the characterization of the four investigated ligands were previously reported, as well as their coordination capability towards Fe^{3+}, Al^{3+}, Cu^{2+}, and Zn^{2+} cations [12,13]. The ligand structure presents two or three ka units linked through ethylene diamine, propylene diamine, butylene diamine, and tris(2-aminoethyl)amine, as shown in Figure 2. These molecules can be easily synthetized at high purity level and can interact with different metal cations through alcoholate, carbonyl, and amino groups. The presence of different donor groups gives the ligands a strong chelating ability towards both hard and soft metal cations. Moreover, the flexibility of the ligand chain permits the formation of 1:1 (metal:ligand) stoichiometry species [12]. The alkyl chains, which do not coordinate metal ions, could increase the lipophilicity of the molecules and, therefore, ameliorate the pharmacological effectiveness [10].

The coordination features of ligands S2–S4 and SC with oxovanadium(IV) were studied by potentiometry, and UV-visible and EPR spectroscopy. Chemical models were hypothesized on the basis of experimental data, which were analyzed by a thermodynamic approach and chemometric methods. The spectroscopic data, in particular, were analyzed by HypSpec® software [14] and by the Multivariate Curve Resolution–Alternating Least Squares (MCR–ALS) method [15]. The formation constants of the species and the pure UV-vis and EPR spectra were determined.
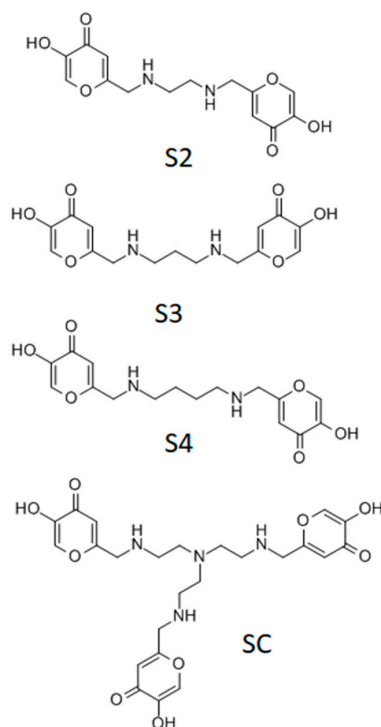
Figure 2. Molecular structure of the ka derivatives studied. S2: [ethane-1,2-diylbis (iminomethanediyl)]bis(5-hydroxy-4H-pyran-4-one), S3: [propane-1,3-diylbis(iminomethanediyl)] bis(5-hydroxy-4H-pyran-4-one); S4: [butane-1,4-diylbis(iminomethanediyl)]bis(5-hydroxy-4H-pyran-4-one); SC: 6,6′,6″-(((nitrilotris(ethane-2,1-diyl))tris(azanediyl))tris(methylene))tris(3-hydroxy-4H-pyran-4-one).

2. Results and Discussion

2.1. Potentiometric Data

pH-metric titrations were carried out in water solutions with different metal to ligand ratios (ionic strength 0.1 molL^{-1} with KCl, 25 °C) in the 2–11 pH range. As an example, some titration curves are shown in Figures S1–S8 in the Supplementary Material file. The curves obtained on all systems in the presence of the cation showed a marked acidification of the solution due to the formation of the coordination compounds (Figures S1–S4). The first equivalent point is correlated with the excess of H$^+$ in the solutions and with the protons released during the cation coordination. For all systems, it was possible observe the release of two protons for each ligand molecule (Figures S1–S4), except for S2. The solutions are yellow–green at acidic pH and yellow in alkaline conditions. The equilibrium becomes unachievable after the equivalent point for the solutions with a metal to ligand ratio of 1:1, except for the SC ligand, while instability starts above pH 8.5 with ligand excess. In any case, when instability occurs, the solutions acquire a dark-orange color. The typical browning of the solutions reveals that the vanadyl cation is being involved in reactions different from cation coordination (precipitation and/or oxidation of vanadium(IV) to vanadium(V)) [16]. Back titrations were conducted on each system, proving the reversibility of the equilibria in the pH range 2.0–8.0 (Figures S5–S8). For this reasons, the titrations were carried out preferentially in an excess of the ligand, and only the titration data collected between pH 2.0 and 8.0 were processed by the BSTAC program [17]. The chemical models proposed, with the formation constants of the species, are listed in Table 1.

The ligand S2 showed the formation of a main species, [VOLH$_3$]$^{3+}$, before the equivalent point and of a second one, [VOLH$_2$]$^{2+}$, above pH 5.

The titration curves obtained with S3 and S4 can be explained by the formation of two species, [VOLH$_3$]$^{3+}$ and [VOLH$_2$]$^{2+}$, in which the hydroxyl group of each ka units probably dissociate

successively at a very lower pH with respect to the free ligand molecules [12,13]. Both species are formed before the equivalent point. The buffer region of the titration curves could be explained on the basis of the ligand deprotonation only, but the trends of the UV-vis spectra recorded on the systems suggest the formation of a third species after pH 6.5 (see the next paragraph). Therefore, the species [VOLH]$^+$ was also included in the model. Their percentage formation is lower than 10% in the pH range considered; therefore, they can be considered as minor species and their formation constants are affected by larger uncertainties.

Table 1. Formation constants. Protonation constants [12,13] of the ligands and formation constants for the species of oxovanadium(IV). The formation constants are obtained from the analysis of pH-metric data (ionic strength: 0.1 mol L^{-1} in KCl; temperature: 25 °C).

Ligand	S2 [a]	S3 [a]	S4 [a]	SC [a]	
		log$K$ for the reaction H$^+$ + LH$_r^z$ ⇆ H$_{r+1}$L^{z+1} [b]				
Species				**Species**	
[LH]$^-$	9.85	10.20	10.59	[LH]$^{2-}$	10.18
[LH$_2$]^0	8.10 *	8.87	9.56	[LH$_2$]$^-$	9.65
[LH$_3$]$^+$	7.56 *	7.94 *	8.02 *	[LH$_3$]^0	8.72
[LH$_4$]$^{2+}$	6.89	7.27 *	7.38 *	[LH$_4$]$^+$	8.04*
				[LH$_5$]$^{2+}$	7.70*
				[LH$_6$]$^{3+}$	7.10*
		logβ ± std dev [c] for reaction pVO^{2+} + qL^{z-} + rH$^+$ ⇆ (VO)$_p$L$_q$H$_r^{2p+r-qz}$				
Species				**Species**	
[VOLH$_3$]$^{3+}$	31.64 ± 0.01	35.03 ± 0.08	36.6 ± 0.1	[VOLH$_5$]$^{4+}$	51.5 ± 0.08
[VOLH$_2$]$^{2+}$	24.57 ± 0.02	31.89 ± 0.08	33.20 ± 0.08	[VOLH$_4$]$^{3+}$	48.28 ± 0.03
[VOLH]$^+$	-	22.7 ± 0.1	23.5 ± 0.1	[VOLH$_3$]$^{2+}$	40.8 ± 0.08
		log$K$ for the reaction VO^{2+} + H$_r$L^z ⇆ (VO)LH$_r^{2-z}$				
Species				**Species**	
[VOLH$_3$]$^{3+}$	6.13	8.02	8.43	[VOLH$_5$]$^{4+}$	7.21
[VOLH$_2$]$^{2+}$	6.62	12.82	13.05	[VOLH$_4$]$^{3+}$	11.69
[VOLH]$^+$	-	12.50	12.91	[VOLH$_3$]$^{2+}$	12.25
	log$K$		**Experimental Conditions**	**Reference**	
VO^{2+} + ka$^-$ ⇆ VOka$^+$	7.63		I = 0.2 mol L^{-1} KCl	[18]	
	7.61		T = 25 °C	[9]	
VOka$^+$ + ka$^-$ ⇆ VO(ka)$_2$	6.74		I = 0.2 mol L^{-1} KCl	[18]	
	6.89		T = 25 °C	[9]	

[a] S2: [ethane-1,2-diylbis(iminomethanediyl)]bis(5-hydroxy-4H-pyran-4-one); S3: [propane-1,3-diylbis (iminomethanediyl)]bis(5-hydroxy-4H-pyran-4-one); S4: [butane-1,4-diylbis(iminomethanediyl)]bis(5-hydroxy-4H-pyran-4-one); SC: 6,6′,6″-(((nitrilotris(ethane-2,1-diyl))tris(azanediyl))tris(methylene))tris(3-hydroxy-4H-pyran-4-one). [b] The protonation constants were from refs. [12,13]. The symbol * indicates the protonation of ka unit. [c] ±standard deviation [17].

Regarding SC ligand, the formation of three different species, [VOLH$_5$]$^{+4}$, [VOLH$_4$]$^{+3}$, and [VOLH$_3$]$^{+2}$, was assumed. Both [VOLH$_5$]$^{+4}$ and [VOLH$_4$]$^{+3}$ are formed before the equivalent point.

The models proposed well explain the experimental titration curves (see Figures S5–S8); nevertheless, the uncertainty of the stability constants results to be quite high because their values are strictly correlated to each other, and the species start to be formed in quite acidic conditions where the variation of the proton concentration due to the formation of the coordination compounds is a small fraction of the total proton concentration in solution. The presence of dimeric species was tested, but their formation was excluded. On the other hand, if a stable dimeric species had been formed, the stability of solutions with a metal to ligand ratio of 1:1 would have been higher.

The general notation (VO)$_p$L$_q$H$_r^{2p+r-qz}$ used to define the coordination compounds does not allow differentiating a proton resulting from the dissociation of the ligand from a proton deriving from a water molecule, but it is possible to hypothesize on the basis of the partial formation constants obtained on the different metal–ligand systems. For all systems, it is reasonable assume that the species

[VOLH$_3$]$^{+3}$ of S2–S4, and the species [VOLH$_5$]$^{+4}$ of SC, are due to the insertion of one ka unit in the coordination sphere of the cation that bind the metal through the carbonyl oxygen atom and the phenolic group, (CO, O$^-$). Buglyó et al. [18] and Yuen et al. [9] reported formation constants of ~7.6 for the species [VOka]$^+$ (Table 1).

From the log$K$ of the species [VOLH$_2$]$^{+2}$ (S3–S4) and [VOLH$_4$]$^{+3}$ (SC), it is reasonable assume the coordination of the cation through two ka units, 2 × (CO, O$^-$), while, in the case of S2, it is more probable the formation of a hydrolytic species with the stoichiometry [VO(H$_3$S2)(OH)]$^{+2}$ because the log$K$ value is very low with respect to those estimated for the other ligands. On the other hand, S2 is the ligand with the shortest amine chain, and this may hinder the coordination by the second (CO, O$^-$) group. Moreover, S2 is the ligand with the highest proton dissociation constants of the ka units (Table 1).

Oxovanadium(IV) species with stoichiometry ML formed by the insertion of two units of 3-hydroxy-6-methyl-4-pyrone linked through an ethylenediamine chain were previously observed by Song et al. [19] for the ligand *N,N'*-bis(3-hydroxy-6-methyl-2-methylene-4-pyrone)ethylenediamine.

The third species of S3, S4, and SC ([VOLH]$^+$ or [VOLH$_3$]$^{+2}$) is probably a hydrolytic species with stoichiometry, [VO(H$_2$S3)(OH)]$^+$, [VO(H$_2$S4)(OH)]$^+$, and [VO(H$_4$SC)(OH)]$^{+2}$, respectively. In the cases of S3 and S4, the proton of the water molecule shows a dissociation constant quite similar to those of the protogenic groups of the ligands; therefore, on the basis of potentiometric data only, it is tricky to detect these species.

The species distribution diagrams of the four studied systems were calculated on the basis of the data in Table 1 and are shown in Figure 3. It can be observed that, for systems with S3, S4 and SC, above pH 4, the species that involves two (CO, O$^-$) donor sets is predominant.
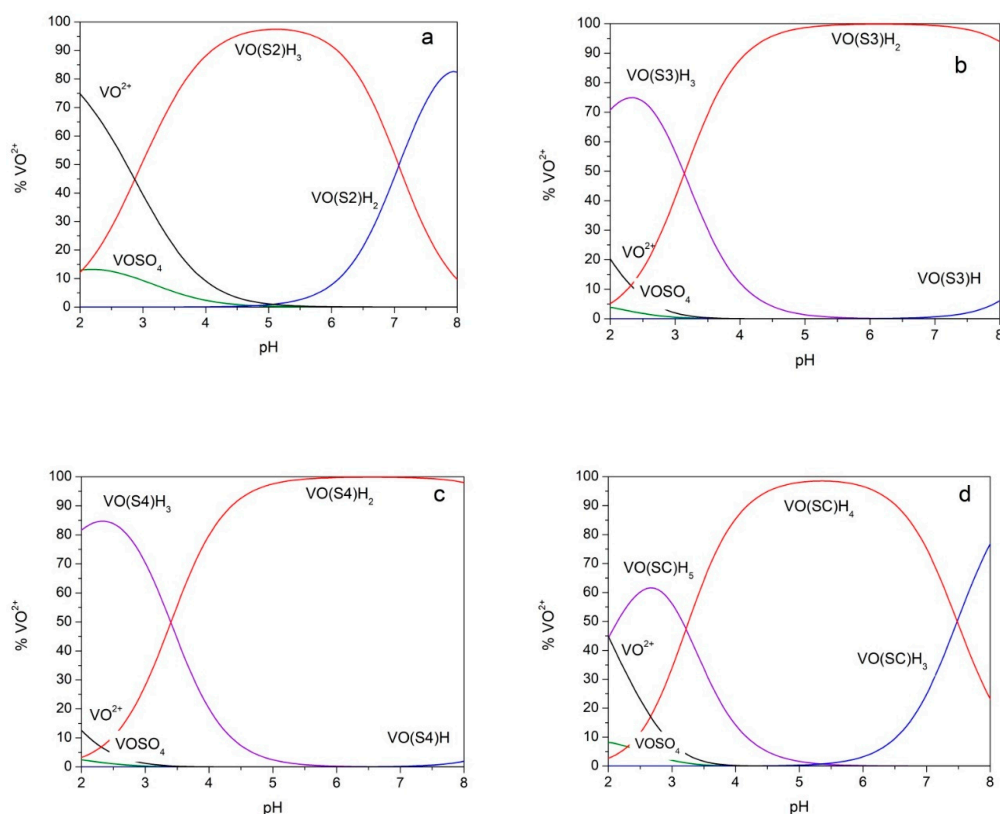
Figure 3. Species distribution diagrams. Species distribution diagrams for solutions of oxovanadium(IV) 5 mmolL^{-1} and ligand 10 mmol L^{-1} calculated on the basis of the formation constants reported in Table 1. (**a**) ligand = S2; (**b**) ligand = S3; (**c**) ligand = S4; (**d**) ligand = SC. VOSO$_4$: Vanadyl–sulphate ion pair.

2.2. UV-Visible Spectra

UV-vis absorption spectra were recorded on solutions of vanadyl cation and the different ligands as a function of pH. The experimental spectra of all studied systems show three absorption bands between 400 and 900 nm due to the cation species (namely band *I*, *II,* and *III* from the highest to the lowest wavelength). As shown in Figure 4, that reports the experimental spectra recorded on the systems with S2, S3, and SC, the λ_{max} values of the band *I* are between 820 and 890 nm. The band *I* is positioned at 765 nm for the pentaaquo ion $[VO(H_2O)_5]^{2+}$, therefore the chelation due to the (CO, O^-) donors provides a strong red shift, which is evident already at acidic pH (Figure 4a and Figures S9–S11). The second absorption band (band *II*) is positioned between 625 and 590 nm, whereas the corresponding λ_{max} of the pentaaquo ion is at 635 nm. The third band (band *III*) is visible at about 455 nm as a shoulder of the ligand absorption band tail. The coordination leads to a hyperchromic effect for all the three transitions. The systems showed stable potentials until pH 8. All systems showed a stability of the absorption values from pH 4.5 to 6.5 followed by a regular decrease in absorbance at higher pH associated with a further bathochromic shift of the band *III* (Figure 4c).

For each investigated system, from the whole of the spectra recorded on solutions at different concentrations and pH, the individual visible spectra were determined by the analysis of experimental data (wavelengths 550–900 nm) with HypSpec®. The principal spectral features of each species are listed in Table 2, and the entire spectra and the formation constants estimated are reported in the Supplementary Material file (Figures S12–S15 and Table S1). The percentage formation of the species $[VOLH]^+$ of S3 and S4 are lower than 10% in the pH range considered; therefore, the spectral parameters should be considered semi-quantitative. The position of the absorption maxima can be associated with the species proposed on the basis of the potentiometric data (see the donor set in Table 2). The entrance of one (CO, O^-) group in the coordination sphere moves the band *I* from 765 to 817–851 nm, whereas the metal chelation through two (CO, O^-) groups shifts the absorption maxima to the range 854–861 nm. The hydrolyzed species show absorption maxima in the range 884–898 nm. For the species due to the coordination of one (CO, O^-) group, it is not possible exclude the participation of a second ka unit through a CO group.

The position of the metal species bands is in quite good accordance with the absorption maxima obtained by Buglyó et al. [18] for the ka-oxovanadium(IV) species, and with those obtained by Chruscinska et al. [20] for the coordination compounds of the cation with maltol and L-mimosine (see Table 2). In the case of L-mimosine (α-amino-β-(3-hydroxy-4-oxo-1,4-dihydropyridin-1-yl)-propanoic acid), the participation of the amino groups in coordination was excluded [20]. These findings support the hypothesis that only the oxygenated functions of the ligands participate to the oxocation coordination.
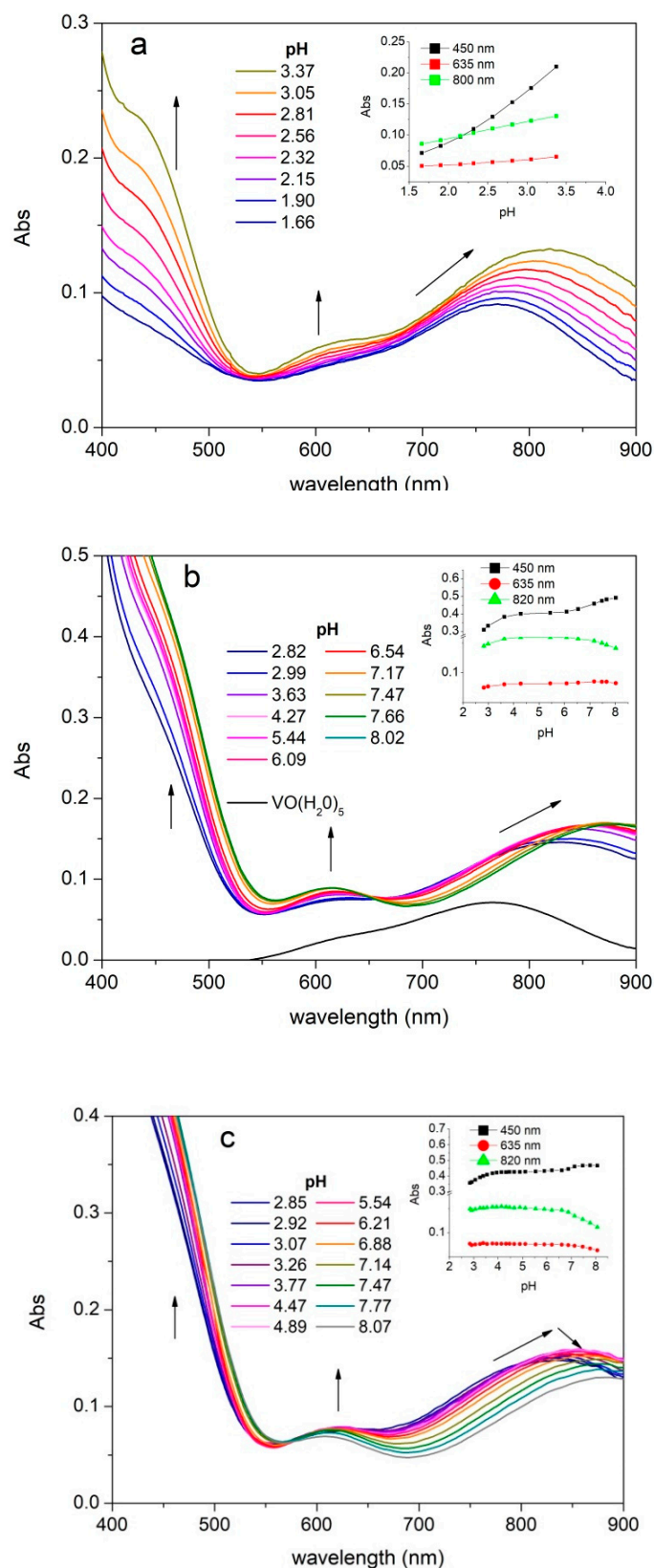
Figure 4. UV-vis absorption spectra. UV-vis absorption spectra of a solution containing oxovanadium(IV) 5 mmolL^{-1} and S2 5 mmolL^{-1} (batch titration) (**a**), S3 15 mmol L^{-1} (**b**), and SC 15 mmol L^{-1} (**c**). Inset graphs: Diagrams Abs vs. pH at different wavelengths.

Table 2. Spectrophotometric parameters. Values of λ_{max} (nm) and ε_{max} (mol^{-1} L cm^{-1}) of the species in solution.

Species [a]	Donor Set	Absorption Band						References
		Band I		Band II		Band III [b]		
		λ_{max}	ε_{max}	λ_{max}	ε_{max}	λ_{max}	ε_{max}	
[VO(H$_2$O)$_5$]$^{2+}$		765	16	635	7			[21]
VO(ka)$_2$	2 × (CO, O$^-$)	850	28	625	13	425	65	[18]
[VO(ka)$_2$OH]$^-$	2 × (CO, O$^-$), OH$^-$	870	27	595	20	450sh		
[VO(malt)]$^+$	(CO, O$^-$)	815	21	615	9	440	36	
VO(malt)$_2$	2 × (CO, O$^-$)	860	27	620	12	440	73	
[VO(malt)$_2$(OH)]$^-$	2 × (CO, O$^-$), OH$^-$	870	20	605	12	450	76	[20]
VO(HL-Mim)$_2$	2 × (CO, O$^-$)	860	24	620	16	540	11	
[VO(L-Mim)$_2$]$^{2-}$	2 × (CO, O$^-$)	880	18	615	15	535	11	
[VO(S2)H$_3$]$^{3+}$	(CO, O$^-$)	851	34.3 ± 0.1	~612 sh [c]		~440		This work
[VO(S2)H$_2$]$^{2+}$	(CO, O$^-$), OH$^-$	886	35.5 ± 0.3	612	19.1 ± 0.3	~455 sh		
[VO(S3)H$_3$]$^{3+}$	(CO, O$^-$)	817	28.7 ± 0.4	~613 sh		~452 sh		This work
[VO(S3)H$_2$]$^{2+}$	2 × (CO, O$^-$)	860	33.8 ± 0.2	622	16.8 ± 0.3	~455 sh		
[VO(S3)H]	2 × (CO, O$^-$), OH$^-$	897	35 ± 1	592	21 ± 2	~469		
[VO(S4)H$_3$]$^{3+}$	(CO, O$^-$)	819	28.6 ± 0.5	630	15.9 ± 0.6	-		This work
[VO(S4)H$_2$]$^{2+}$	2 × (CO, O$^-$)	861	33.1 ± 0.2	619	17.5 ± 0.3	~455 sh		
[VO(S4)H]	2 × (CO, O$^-$), OH$^-$	898	29 ± 2	~615 sh		~480 sh		
[VO(SC)H$_5$]$^{4+}$	(CO, O$^-$)	846	35.2 ± 09	612 sh		~455 sh		
[VO(SC)H$_4$]$^{3+}$	2 × (CO, O$^-$)	854	32.0 ± 0.4	619	16.7 ± 0.4	~455 sh		This work
[VO(SC)H$_3$]$^{2+}$	2 × (CO, O$^-$), OH$^-$	884	34.8 ± 0.5	606 sh		~480 sh		

[a] S2: [ethane-1,2-diylbis(iminomethanediyl)]bis(5-hydroxy-4H-pyran-4-one); S3: [propane-1,3-diylbis(iminomethanediyl)]bis(5-hydroxy-4H-pyran-4-one); S4: [butane-1,4-diylbis(iminomethanediyl)]bis(5-hydroxy-4H-pyran-4-one); SC: 6,6′,6″-(((nitrilotris(ethane-2,1-diyl))tris(azanediyl))tris(methylene))tris(3-hydroxy-4H-pyran-4-one). [b] The position of band III was estimated from the experimental spectra. [c] sh = shoulder.

2.3. EPR Spectra

EPR spectra of the different vanadyl–ligand systems were recorded at both room (RT) and low (LT) temperature.

The RT EPR spectra showed the typical eight line pattern of vanadyl mononuclear species, due to the coupling of the unpaired electron with ^{51}V nucleus ($S = 1/2$, $I = 7/2$). With increasing pH, the values of the isotropic hyperfine coupling constant A_0 decreased, revealing the progressive substitution of the water molecules in the pentaaquo ion $[VO(H_2O)_5]^{2+}$ with one or more ligand donor groups. Some of the experimental spectra obtained are reported in Figure 5 and Figure S16. At acidic pH (Figure 5), it is possible to note the presence of two partially overlapped signals that can be reasonably attributed to the pentaaquo ion and to the species $[VOLH_3]^{+3}$ (L = S2, S3 or S4) or $[VO(SC)H_5]^{+4}$. Increasing the pH only one signal can be observed. The experimental data were simulated with the program SIM32 [22,23] and deconvoluted by MCR–ALS as well [24]. The values of A_0 and g_0, derived from both the data treatments, are shown in Table 3.

The MCR–ALS approach provided good results. An example is reported in Figure S17 (in the Supplementary Material file) that shows extrapolated pure concentration profiles and spectra of a series of solutions involving oxovanadium(IV) 5 mmol L^{-1} and S3 15 mmol L^{-1} that were prepared at different pH values. MCR–ALS decompositions were performed by using the EPR spectrum of the pure oxovanadium(IV) as reference. Two- and three-component models were calculated and compared in terms of explained variance and lack of fit values. In all cases, the systems involving a three-component solution provided better results than those with two estimated components, showing satisfactory lack of fit and explaining variance values lower than 10% and higher than 99%, respectively. Moreover, a comparison between the pure EPR spectra of the standard of oxovanadium(IV) with the profile extracted by MCR–ALS (see Figure S18 reported in the Supplementary Material file) showed an almost complete overlap between the two spectra. The A_0 and g_0 values (Table 3) obtained by MCR–ALS were quite similar to those obtained from SIM32. Both SIM32 and MCR–ALS did not allow distinguishing between the signals due to species formed in alkaline conditions, but the decrease of the A_0 values with increasing pH suggests its presence.

LT EPR spectra were recorded on frozen VO^{2+}–ligand solutions at pH 6 and 8. The data show only little differences. According to the RT EPR spectra of the vanadyl compounds with SC ligand, a multispecies LT EPR spectrum is obtained at pH around 3 (see Figure S19 in the Supplementary Material file). Remarkably, low temperatures might change the species distribution determined at room temperature, as in the case of copper(II) complexes, generally favoring metal species with a higher coordination level [25]. Table 4 reports anisotropic magnetic parameters at different pH values for all the vanadyl species with ka derivatives, as well as those for the pentaaquo oxovanadium(IV) ion. Figure 6 shows, as an example, the LT frozen solution EPR spectra of the oxovanadium(IV) coordination compounds with the SC ligand at different pH values.

From inspection of the Table 4, it is quite evident that the ligands S3, S4, and SC replace equatorial water molecules of the pentaaquo oxovanadium cation with both the bidentate oxygen moieties of the ligands (CO, O$^-$). The shifts on g and A values are those expected in the case of bidentate ligands, as those observed for β-diketonates, in which oxygen atoms are more covalently bound than water molecules, and therefore higher $g_{\parallel}$ and lower $A_{\parallel}$ values are expected [26–28]. The $A_{\parallel}$ values approximately obey to the additivity relationship for equatorial ligands, as explained by Smith et al. [26], confirming the presence of four equatorial oxygen donors. Moreover, the values reported in Table 4 are in very good agreement with those proposed by Buglyò at al. [18] for the species VO(ka)$_2$ ($g_{\parallel} = 1.939$; $A_{\parallel} = 171 \times 10^{-4}$ cm^{-1}).

Table 3. RT EPR data. Isotropic hyperfine coupling constant (A_0) and isotropic g values (g_0) of the species obtained by the analysis of EPR spectra recorded on the different oxovanadium(IV)–ligand system, as a function of pH. Errors in g and A values were estimated to be ±0.002 and $\pm0.5 \times 10^{-4}$ cm^{-1}, respectively.

Ligand [a]	pH	SIM32			MCR–ALS		
		g_0	A_0 (cm$^{-1} \cdot 10^{-4}$)	R [b]	g_0	A_0 (cm$^{-1} \cdot 10^{-4}$)	R [b]
H$_2$O	-	1.965	106.9	0.993	1.970	105.9	0.990
		VO(H$_2$O)$_5$; VOLH$_{n \text{ and } n-1}$			VO(H$_2$O)$_5$; VOLH$_n$; VOLH$_{n-1}$		
S2	2.5	1.964; 1968	104.6; 96.9	0.989			0.986
	3.3	1.964; 1.967	104.3; 96.0	0.985			0.984
	6.5	1.967	95.8	0.989	1.970; 1.975; 1.966	105.9; 97.7; 90.5	0.992
	7.6	1.967	94.4	0.985			0.989
	8.1	1.967	93.7	0.983			0.991
S3	2.5	1.965; 1.968	104.8; 96.8	0.985			0.986
	3.3	1.967	96.9	0.989			0.987
	6.4	1.967	95.9	0.990	1.970; 1.975; 1.975	105.9; 96.5; 93.2	0.991
	7.4	1.967	94.9	0.970			0.986
	8.0	1.967	94.0	0.981			0.988
S4	2.5	1.964; 1.968	104.4; 96.7	0.990			0.988
	3.3	1.967	96.8	0.992			0.986
	6.6	1.967	95.8	0.989	1.970; 1.974; 1.976	105.9; 96.1; 92.9	0.989
	7.4	1.967	94.9	0.983			0.986
	8.1	1.967	93.8	0.985			0.984
		VO(H$_2$O)$_5$; VO(SC)H$_{5 \text{ and } 4}$			VO(H$_2$O)$_5$; VO(SC)H$_5$; VO(SC)H$_{4 \text{ or } 3}$		
SC	2.8	1.967; 1.966	104.2; 97.6	0.990			0.985
	3.1	1.967	96.9	0.994			0.991
	6.5	1.967	95.6	0.989	1.970; 1.974; 1.976	105.9; 96.7; 92.7	0.992
	7.5	1.967	94.3	0.980			0.987
	8.0	1.967	93.4	0.980			0.983

[a] S2: [ethane-1,2-diylbis(iminomethanediyl)]bis(5-hydroxy-4H-pyran-4-one); S3: [propane-1,3-diylbis(iminomethanediyl)]bis(5-hydroxy-4H-pyran-4-one); S4: [butane-1,4-diylbis(iminomethanediyl)]bis(5-hydroxy-4H-pyran-4-one); SC: 6,6′,6″-(((nitrilotris(ethane-2,1-diyl))tris(azanediyl))tris(methylene))tris(3-hydroxy-4H-pyran-4-one). [b] R = Pearson's correlation coefficient.

It was not possible to differentiate the signals of hydrolytic species, but little increase of the $g_\parallel$ values and decrease of $A_\parallel$ values can be observed for the data collected at pH 8, suggesting their presence. Moreover, the results obtained for S2 show little difference with respect to those obtained for other systems, despite potentiometric results suggesting the insertion of only one (CO, O$^-$) donor set. This could be due to the similar contribution of the hydrolytic species signal to the resultant $A_\parallel$ and $g_\parallel$ parameters.

Table 4. LT EPR data. Anisotropic magnetic parameters obtained by fitting the experimental frozen solution spectra of the oxovanadium(IV) species with ka derivatives at different pH values. Anisotropic magnetic parameters for the oxovanadium(IV) cation in water at pH 3 are also shown for comparison. Errors in *g* and *A* values were estimated to be ± 0.002 and $\pm 0.5 \times 10^{-4}$ cm^{-1}, respectively.

Ligand	pH	$g_\parallel$	$A_\parallel$ (cm^{-1} · 10^{-4})	$g_\perp$	$A_\perp$ (cm^{-1} · 10^{-4})
H$_2$O	3.0	1.933	180.8	1.978	70.2
S2	6.2	1.939	168.9	1.975	59.8
	8.2	1.941	167.2	1.974	57.1
S3	6.4	1.936	169.9	1.975	59.9
	8.2	1.939	167.1	1.972	56.3
S4	6.4	1.936	170.8	1.975	60.8
	8.0	1.940	166.9	1.973	56.9
SC	5.6	1.938	170.2	1.974	59.2
	8.0	1.938	167.0	1.971	56.8
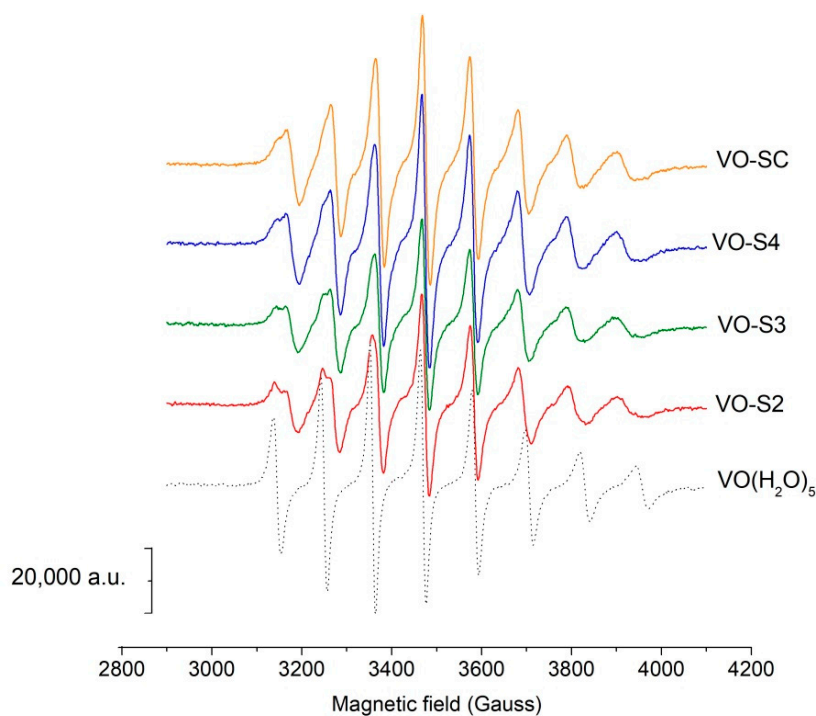
Figure 5. RT EPR spectra in acidic conditions. EPR spectra of solutions with oxovanadium(IV) 5 mmol L^{-1} and different ligands 15 mmol L^{-1} at pH 2.5.
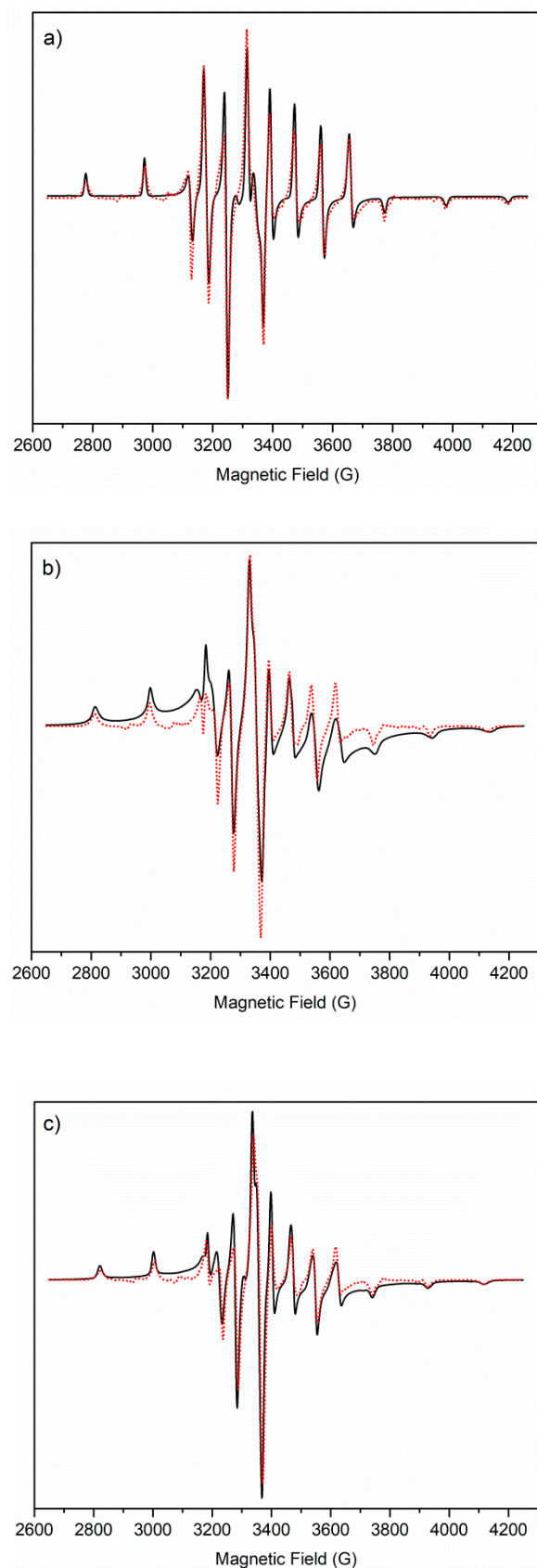
Figure 6. LT EPR spectra. Experimental (black solid line) and computed (red dot line) frozen solution EPR spectra of (**a**) VO^{2+} pentaaquo ion, (**b**) VO–SC at pH 5.6, and (**c**) VO–SC at pH 8.

3. Sequestering Capability

In order to define the sequestering ability of the ligands under study towards oxovanaium(IV) and compare it with those of ka and maltol, the sum of formation percentages of all metal–ligand species ($\Sigma\%VO^{2+}_{compl}$) was plotted versus the pL, where pL = $-\log_{10}[L]_{tot}$ ([L]$_{tot}$ is the total ligand concentration) for each metal–ligand system. This procedure was proposed by Crea et al. [29] and provides curves that show an exponential decay. The higher the pL necessary to bind a defined percentage of metal, the better the sequestering capability.

The obtained curves are shown in Figure 7. $\Sigma\%VO^{2+}_{compl}$ was calculated at pH 5.5 and I = 0.1 molL^{-1}. At this pH value, the ligands exhibit their maximum binding capacity. For ka and maltol, the chemical models proposed by Buglyó et al. [18] were used and the formation constants were extrapolated at ionic strength 0.1 molL^{-1} using an expanded Debye–Hückel equation [30]. The sequestering ability of the ligands S3, S4, and SC are very similar and their curves are overlaid; moreover, they show higher sequestering capability with respect to ka or maltol.
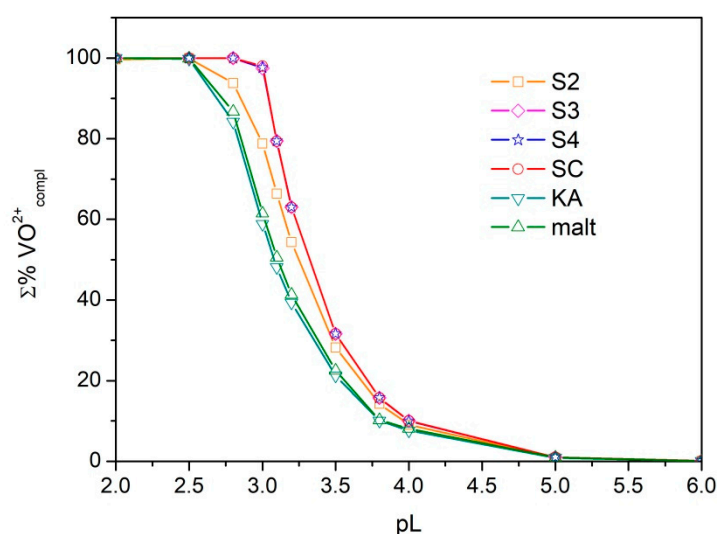
Figure 7. Sequestration diagram. Sum of formation percentages of all metal–ligand species vs. pL values, where L = S2–S4, SC, ka, or maltol. Experimental conditions: I = 0.1 mol L^{-1} in KCl, 25 °C, pH = 5.5.

4. Materials and Methods

4.1. Chemicals

The stock solution (~0.1 mol L^{-1}) of vanadyl sulphate (purity ~96%, Aldrich, St. Louis, MO, USA) was weekly prepared without previous purification of the salt; it was standardized by redox titration with permanganate solution (Carlo Erba, Milan, Italy), followed by photometric detection [21]. D$_2$O (99.9%), ethanol (99.9%), 5-hydroxy-2-hydroxymethyl-pyran-4-one (kojic acid, ka; purity 99%), ethylene diamine, propane-1,3-diamine, and butane-1,4-diamine were Sigma-Aldrich products. Ethane-1,2-diylbis(iminomethanediyl)]bis(5-hydroxy-4H-pyran-4-one), propane-1,3-diylbis (iminomethanediyl)]bis(5-hydroxy-4H-pyran-4-one), butane-1,4-diylbis(iminomethanediyl)]bis(5-hydroxy-4H-pyran-4-one), and 6,6′,6″-(((nitrilotris(ethane-2,1-diyl))tris(azanediyl))tris(methylene)) tris(3-hydroxy-4H-pyran-4-one) (hereinafter S2, S3, S4, and SC, respectively) were synthetized as reported in references. [12,13]. The identity and the purity of the synthetized ligands were evaluated by nmR spectroscopy (Bruker Ascend™ 400 MHz spectrometer; Bruker Italia, Milan, Italy) and the protonation level was checked by alkalimetric titration.

Potassium chloride solutions were prepared by weighing the pure salt (Fluka, p.a., Seelze, Germany). Standard KOH (0.1 and 0.5 mol L^{-1}) and HCl solutions (1.0 and 0.1 mol L^{-1}) were

prepared by diluting Merck (Darmstadt, Germany) concentrate products, and standardized against potassium hydrogenphthalate (Fluka, purity ≥99.5%) and sodium carbonate anhydrous (Fluka, purity 99.95–100.05%), respectively. All solutions were prepared using grade A glassware and ultrapure water (conductivity <0.1 μS).

4.2. Potentiometric Measurements

Potentiometric measurements were performed using the Metrohm (Herisau, Svizzera) automated titration system Titrando 888 controlled by the software *tiamo*^{TM} 2.5, or a Metrohm mod. 713 potentiometer (resolution of ±0.1 mV) coupled with a Metrohm 765 Dosimat burette (minimum volume deliverable of ±0.001 cm^3). Metrohm combined glass electrodes (mod. 6.0259.100 and mod. 6.0234.100) with internal reference Ag/AgCl/3M KCl were used. The potentiometric titrations were carried out in a stream of purified nitrogen gently bubbled in the titration cell to avoid O_2 and CO_2 contamination. The measurement cells were thermostated at (25.0 ± 0.1 °C) by means of water circulation from a thermocryostat (mod. D1-G Haake, Vreden, Deutschland). A maximum signal drift of 0.5 mVolt min^{-1} and a maximum waiting time of 100 s were imposed for each titration point. The Dynamic Titration mode was used, the minimum titrant increment was 0.01 mL, and the measuring point density was set in order to have ΔE < 15 mV for each titrant addition. The titration curves obtained by the automated titration system on each chemical system were compared to those recorded manually in order to verify the equilibrium condition. Some back titrations were conducted (titrant HCl 0.1 mol L^{-1}) on each system in order to check the reversibility of the equilibria.

The electrode couple was standardized, in terms of pH = −log[H$^+$], by titrating HCl 10 mmol L^{-1} solution (at the same ionic strength value as the solution under study) with standard KOH, in order to determine the formal potential E^0 before each experiment.

The potentiometric titrations were carried out in KCl aqueous solutions with 0.1 mol L^{-1} ionic strength. For the investigation of VO^{2+}–ligand systems, 25 or 50 mL of solution containing VO^{2+}, the ligand, and KCl were titrated with standard KOH. Each titration was repeated at least twice. The metal concentration ranged from 2 to 10 mmol L^{-1}. The ligand concentration ranged from 2 to 15 mmol L^{-1}. The metal to ligand ratios were 1:1, 1:2, 1:3, 2:1, and 3:1. The investigated pH range was 2.0–11.0 and, since the synthetized ligands were not completely protonated, the initial acidic condition was obtained by the addition of HCl 0.1 mol L^{-1}.

Before use, the ligands (S2–S4, SC) were kept at 60 °C for a night. This treatment enabled to remove most of the solvent derived from the synthetic procedure, and therefore, it allowed obtaining a constant weight.

4.3. Spectroscopic Measurements

The visible molecular absorption (400–900 nm) spectra were recorded by a V-550 Jasco double-beam spectrophotometer (JASCO Europe, Cremella, Italy), equipped with Hellma quartz cuvettes (1.000 cm optical path length, sample in a cell for flow-through measurements). The signal was collected each 1 nm, with a scan rate of 400 nm min^{-1}, and the baseline was taken in air before each absorbance measurement. Each absorbance spectrum was taken against the reference cuvette filled with KCl 0.1 mol L^{-1}. The solution being examined was transferred from the potentiometric to an optical cell using a peristaltic pump. Due to the low values of the molar absorptivity coefficients of the vanadyl-containing species, the concentration of oxocation was always higher than 5 mmol L^{-1}, with the suitable metal to ligand ratio. In order to better estimate the formation constants of the species, some batch titrations were conducted at very acidic conditions in a mixture of HCl and KCl, maintaining constant the ionic strength at 0.1 mol L^{-1}.

The EPR spectra of VO^{2+}-ligand systems were recorded at room temperature (RT) with an ESP-300E Bruker X-band spectrometer (Bruker Italia, Milan, Italy). Experimental parameters were as follows: Number of scans 5; microwave power 2 mW; microwave frequency 9.78 GHz; modulation amplitude 0.4 mT; modulation frequency 100 KHz; time constant 82 ms; sweep time 84 s.

Low temperature (LT) EPR spectra of oxovanadium(IV) frozen solutions were recorded by a Bruker Elexsys E500 CW-EPR spectrometer (Bruker Italia, Milan, Italy) driven by a PC running XEpr program under Linux, equipped with a Super-X microwave bridge operating at 9.3–9.9 GHz and a SHQE cavity. Instrumental settings of frozen solution EPR spectra were as follows: Number of scans 1–3; microwave frequency 9.42–9.45 GHz; modulation frequency 100 kHz; modulation amplitude 1 mT; time constant 164–327 ms; sweep time 6 min; microwave power 10–20 mW; linear receiver gain 1×10^4 to 1×10^5. All the EPR frozen solution spectra were recorded in quartz tubes at 150 K by means of a ER4131VT variable temperature apparatus.

The EPR spectra were recorded on solutions with a metal to ligand ratio of 1:3. The RT spectra were recorded on solutions with vanadyl 5 mmol L^{-1}, whereas the LT EPR spectra were recorded on solutions with vanadyl 1–4 mmol L^{-1}. The ionic strength was maintained at 0.1 mol L^{-1} with KCl and the pH of the solutions was comprised between 2.5 and 8.0. Methanol up to 5% was added to the aqueous solution in order to increase the resolution of LT frozen solution spectra.

4.4. Data Analysis and Calculations

The electrode calibration data were analyzed by the ESAB2M program [31] in order to refine the electrode parameters. This program was used to refine the formal potential E^0, the Nernstian slope, and the analytical concentration of the reagents.

The refinement of the formation constants was performed by the BSTAC software [17]. It employs an iterative and convergent numerical method, which is based upon the linear combination of the mass balance equations, minimizes the error squares sum on electromotive force values. The data refinement was performed by including in the model the protonation constants of the ligands, reported in previous papers [12,13] (see Table 1), the hydrolysis constants of the vanadyl cation ([VO(OH)]$^+$ logβ = −5.65; [(VO)$_2$(OH)$_2$]$^{+2}$ logβ = −7.02), and the formation constant of the vanadyl–sulphate ion pair ([VO(SO$_4$)]^0 logβ = 1.73) [21]. The pK_w was 13.78 and both total ligand and proton concentration were refined.

Spectrophotometric data were analyzed by means of the HypSpec$^®$ program [14] that optimizes the formation constants and the values of molar absorptivity coefficients (ε_λ/L mol^{-1} cm^{-1}) of the different species applying mass balance equations and Lambert–Beer's law. The experimental spectra (absorbance vs. wavelength λ/nm), the analytical concentrations of the reagents, and the proposed chemical model (stoichiometric coefficients and known stability constant values of all species) were the input data. The absorbance values comprised between 550 and 900 nm were considered in order to exclude from the data treatment the ligand absorption. The [VO(SO$_4$)]^0 was considered as an absorbing species during the elaboration process and the spectra obtained were compared with that presented in a previous paper [16].

RT EPR spectra of VO^{+2} solutions showed typical unequal spacing between the lines due to second order effects. Therefore, in order to obtain the correct values of g and A, experimental data were analyzed with the EPR simulation program SIM32, written by Spałek and Sojka [22,23].

Anisotropic magnetic parameters of the LT EPR spectra were obtained by simulating the experimental spectra through a modified program from Pilbrow et al. [32], in which the line width (LW) parameters are allowed to vary according to the general formula LW = LW ± aM$_i{}^b$, where a is a multiplication coefficient and b is an exponent of the nuclear magnetic component of the vanadium nucleus multiplet.

UV-vis and EPR spectra were computed by Multivariate Curve Resolution–Alternating Least Squares (MCR–ALS). MCR is a chemometric strategy that performs a bilinear decomposition of the original data set X, consisting of N spectra/samples, into the product of two distinct matrixes, C and S, plus the residual error E [33–36]. In particular, S is referred to contain a number of n pure spectra (where n < N) relative to the specific constituents that have been extracted from the samples under investigation. On the other hand, C includes the information about the signal-related concentration profiles of the pure aforementioned constituents of the samples. The general MCR

procedure is summarized by the following formula: $X = C\ S^T + E$. At the same time, the altering least squares (ALS) approach is performed in order to minimize the deconvolution error by involving specific constraints (such as, for instance, unimodality, non-negativity, equality, and concentration closure) [35–37] that allow to optimize the estimation of the pure spectra and the concentration profiles. In more detail, the whole MCR–ALS procedure starts with the estimation of the number of compounds (components) that constitute the examined samples, and this is performed by involving Principal Component Analysis (PCA) or Single Value Decomposition (SVD) protocols [36,38]. Then, a preliminary bilinear decomposition is done by employing a variable purity approach such as, for instance, the SIMPLISMA (SIMPLe-to-use Interactive Self Modeling Analysis) algorithm [39,40]. This method determines the most variant samples among the collected measurements data set to be employed as the first estimation of pure spectra or pure concentration profiles. Furthermore, the analyst can specify an arbitrary variability (15% here) on the estimated spectra and concentration profiles. After this step, ALS algorithms are exploited to optimize the model and diminish the residual error, setting an arbitrary convergence criterion and number of iterations as well. In the present study, the following non-negativity (non-negative least squares algorithm [41]) and concentration closure (equal to 5 mmolL^{-1}, i.e., the concentration of oxovanadium(IV), supposed to be the limiting reactant) constraints were employed for the calculation of the pure concentration profiles. Conversely, non-negativity constraint was also used for the estimation of the pure spectra of the components detected within the UV-visible spectra, while no constraints were taken into account for the assessment of the components of the recorded EPR spectra. For this purpose, the routines and the graphical user interface (GUI) developed by Jaumot et al. [38] were used on MATLAB software version R2018b.

5. Conclusions

The four ligands examined in this work are able to coordinate the oxovanadium(IV) cation through the bidentate kojate units, thus forming stable species in the 4–8 pH range. The shifts of the UV-vis absorption bands, as well as of the magnetic parameters (i.e., higher *g* values and lower hyperfine coupling constants) of the pentaaquo vanadyl ion $[VO(H_2O)_5]^{+2}$ in the presence of the S3, S4, and SC receptors, reveal that the four ligand oxygen atoms replace the water molecules in the equatorial coordination plane, leading to the formation of the dominant species in the 4–8 pH range. In the case of S2, it could be reasonable to exclude the insertion of the second ka unit in the coordination sphere of the cation. Hydrolyzed species become important after pH 6.5, particularly for the systems with S2 and SC.

The sequestering capability of the ligands S3, S4, and SC towards oxovanadium(IV) is very similar and it is higher than that of maltol and ka.

This study paves the way to further investigations on the properties of these VO^{+2}–ligand systems also in the presence of other metal cations naturally existing in physiological fluids. Moreover, additional studies to assess, both in vitro and in vivo, the toxicity, the bioavailability, and the pharmacokinetics of these species might be advisable to envisage clinical applications such as, for example, their use as insulin-mimetic compounds.

Author Contributions: S.B. organized the potentiometric and spectroscopic investigation, and wrote and edited the manuscript; E.A. applied chemometric techniques; P.G.D. provided advice on potentiometric data processing; E.L. collected and interpreted RT EPR data; A.B. carried out potentiometric and spectrophotometric experiments; C.S. organized and supervised the LT EPR measurements, revised the manuscript; G.V. carried out and interpreted the LT EPR measurements; R.C. synthetized the ligands; J.I.L. provided advice about the properties of the ligands; and V.M.N. supervised the work and revised the manuscript.

Conflicts of Interest: The authors declare no competing financial interests.

References

1. Crans, D.C.; Smee, J.J.; Gaidamauskas, E.; Yang, L. The chemistry and biochemistry of vanadium and the biological activities exerted by vanadium compounds. *Chem. Rev.* **2004**, *104*, 849–902. [CrossRef] [PubMed]

2. Sanna, D.; Bíró, L.; Buglyó, P.; Micera, G.; Garribba, E. Transport of the anti-diabetic VO^{2+} complexes formed by pyrone derivatives in the blood serum. *J. Inorg. Biochem.* **2012**, *115*, 87–99. [CrossRef] [PubMed]

3. Thompson, K.H.; Orvig, C. Coordination chemistry of vanadium in metallopharmaceutical candidate compounds. *Coord. Chem. Rev.* **2001**, *219–221*, 1033–1053. [CrossRef]

4. Zoroddu, M.A.; Aaseth, J.; Crisponi, G.; Medici, S.; Peana, M.; Nurchi, V.M. The essential metals for humans: A brief overview. *J. Inorg. Biochem.* **2019**, *195*, 120–129. [CrossRef] [PubMed]

5. Thompson, K.H.; Lichter, J.; LeBel, C.; Scaife, M.C.; McNeill, J.H.; Orvig, C. Vanadium treatment of type 2 diabetes: A view to the future. *J. Inorg. Biochem.* **2009**, *103*, 554–558. [CrossRef]

6. Crans, D.C.; LaRee, H.; Cardiff, G.; Posner, B. Essential metals in medicine: Therapeutic use and toxicity of metal ions in the clinic. In *Essential Metals in Medicine: Therapeutic Use and Toxicity of Metal*; Astrid Siegel, Ed.; De Gruyter: Berlin, Germany, 2019; pp. 203–230. ISBN 3110527871.

7. Yuen, V.G.; Caravan, P.; Gelmini, L.; Glover, N.; McNeill, J.H.; Setyawati, I.A.; Zhou, Y.; Orvig, C.; Chaudhary, J.; Pathak, A.N.; et al. Pyrone derivatives and metals: From natural products to metal-based drugs. *J. Inorg. Biochem.* **1997**, *104*, 94–106.

8. Kandioller, W.; Kurzwernhart, A.; Hanif, M.; Meier, S.M.; Henke, H.; Keppler, B.K.; Hartinger, C.G. Pyrone derivatives and metals: From natural products to metal-based drugs. *J. Organomet. Chem.* **2011**, *696*, 999–1010. [CrossRef]

9. Yuen, V.G.; Caravan, P.; Gelmini, L.; Glover, N.; McNeill, J.H.; Setyawati, I.A.; Zhou, Y.; Orvig, C. Glucose-lowering properties of vanadium compounds: Comparison of coordination complexes with maltol or kojic acid as ligands. *J. Inorg. Biochem.* **1997**, *68*, 109–116. [CrossRef]

10. Wei, Y.; Zhang, C.; Zhao, P.; Yang, X.; Wang, K. A new salicylic acid-derivatized kojic acid vanadyl complex: Synthesis, characterization and anti-diabetic therapeutic potential. *J. Inorg. Biochem.* **2011**, *105*, 1081–1085. [CrossRef]

11. Wei, Y.B.; Yang, X. Da Synthesis, characterization and anti-diabetic therapeutic potential of a new benzyl acid-derivatized kojic acid vanadyl complex. *BioMetals* **2012**, *25*, 1261–1268. [CrossRef]

12. Nurchi, V.M.; Crisponi, G.; Lachowicz, J.I.; de Guadalupe Jaraquemada-Pelaez, M.; Bretti, C.; Peana, M.; Medici, S.; Zoroddu, M.A. Equilibrium studies of new bis-hydroxypyrone derivatives with Fe^{3+}, Al^{3+}, Cu^{2+} and Zn^{2+}. *J. Inorg. Biochem.* **2018**, *189*, 103–114. [CrossRef] [PubMed]

13. Nurchi, V.M.; de Guadalupe Jaraquemada-Pelaez, M.; Crisponi, G.; Lachowicz, J.I.; Cappai, R.; Gano, L.; Santos, M.A.; Melchior, A.; Tolazzi, M.; Peana, M.; et al. A new tripodal kojic acid derivative for iron sequestration: Synthesis, and in vivo bioassays. *J. Inorg. Biochem.* **2019**, *193*, 152–165. [CrossRef] [PubMed]

14. Gans, P.; Sabatini, A.; Vacca, A. Investigation of equilibria in solution. Determination of equilibrium constants with the HYPERQUAD suite of programs. *Talanta* **1996**, *43*, 1739–1753. [CrossRef]

15. De Juan, A.; Jaumot, J.; Tauler, R. Multivariate curve resolution (MCR). Solving the mixture analysis problem. *Anal. Methods* **2014**, *6*, 4964–4976. [CrossRef]

16. Komura, A.; Hayashi, M.; Hiroto, I. Hydrolytic behavior of oxovanadium(IV) ions. *Bull. Chem. Soc. Jpn.* **1977**, *50*, 2927–2931. [CrossRef]

17. De Stefano, C.; Mineo, P.; Rigano, C.; Sammartano, S. Ionic strength dependence of formation constants. XVII: The calculation of equilibrium concentrations and formation. *Ann. Chim.* **1993**, *83*, 243–277.

18. Buglyó, P.; Kiss, E.; Fábián, I.; Kiss, T.; Sanna, D.; Garribba, E.; Micera, G. Speciation and nmR relaxation studies of VO(IV) complexes with several O-donor containing ligands: Oxalate, malonate, maltolate and kojate. *Inorganica Chim. Acta* **2000**, *306*, 174–183. [CrossRef]

19. Song, B.; Saatchi, K.; Rawji, G.H.; Orvig, C. Synthesis and solution studies of the complexes of pyrone analogue ligands with vanadium(IV) and vanadium(V). *Inorganica Chim. Acta* **2002**, *339*, 393–399. [CrossRef]

20. Chruscinska, E.; Garribba, E.; Micera, G.; Panzanelli, A. L-mimosine, an amino acid with maltol-type binding properties toward copper(II), oxovanadium(IV) and other metal ions. *J. Inorg. Biochem.* **1999**, *75*, 225–232. [CrossRef]

21. Berto, S.; Daniele, P.G.; Foti, C.; Prenesti, E.; Sammartano, S. Interaction of oxovanadium(IV) with carboxylic ligands in aqueous solution: A thermodynamic and visible spectrophotometric study. *J. Mol. Liq.* **2008**, *142*, 57–63. [CrossRef]

22. Mabbs, F.E.; Collins, D. The use of matrix diagonalization in the simulation of the EPR powder spectra of D-transition metal compounds. *Mol. Phys. Rep.* **1999**, *26*, 39–59. [CrossRef]

23. Spałek, T.; Pietrzyk, P.; Sojka, Z. Application of the genetic algorithm joint with the powell method to nonlinear least-squares fitting of powder EPR spectra. **2004**. [CrossRef]

24. Abou Fadel, M.; de Juan, A.; Touati, N.; Vezin, H.; Duponchel, L. New chemometric approach MCR-ALS to unmix EPR spectroscopic data from complex mixtures. *J. Magn. Reson.* **2014**, *248*, 27–35. [CrossRef] [PubMed]

25. Bonomo, R.P.; Riggi, F.; Di Bilio, A.J. EPR reinvestigation of the copper(II)-imidazole system. *Inorg. Chem.* **1988**, *27*, 2510–2512. [CrossRef]

26. Smith, T.S.; Lobrutto, R.; Pecoraro, V.L. Paramagnetic spectroscopy of vanadyl complexes and its applications to biological systems. *Coord. Chem. Rev.* **2002**, *228*, 1–18. [CrossRef]

27. Dessì, A.; Micera, G.; Sanna, D. EPR investigation of the oxovanadium(IV) complexes formed by the tripeptide glutathione and some related ligands in aqueous solution. *J. Inorg. Biochem.* **1993**, *52*, 275–286. [CrossRef]

28. Yen, T.F.; Bucher, L.J. *Electron Spin Resonance of Metal Complexes: Proceedings of the Symposium on ESR of Metal Chelates at the Pittsburgh Conference on Analytical Chemistry and Applied Spectroscopy, Held in Cleveland, Ohio, March 4–8, 1968*; Springer US: New York, NY, USA, 1969; ISBN 1468483234.

29. Crea, F.; De Stefano, C.; Foti, C.; Milea, D.; Sammartano, S. Chelating agents for the sequestration of mercury(II) and monomethyl mercury(II). *Curr. Med. Chem.* **2014**, *21*, 3819–3836. [CrossRef]

30. Casale, A.; Daniele, P.G.; De Robertis, A.; Sammartano, S. Ionic strength dependence of formation constants. Part XI. An analysis of literature data on carboxylate ligand complexes. *Ann. Chim. Chim.* **1988**, *78*, 249.

31. De Stefano, C.; Princi, P.; Rigano, C.; Sammartano, S. Computer-analysis of equilibrium data in solution Esab2M—An improved version of the Esab program. *Ann. Chim.* **1987**, *77*, 643–675.

32. Pilbrow, J.R.; Winfield, M.E. Computer simulation of low symmetry ESR spectra due to vitamin B 12r and model systems. *Mol. Phys.* **1973**, *25*, 1073–1092. [CrossRef]

33. Tauler, R. Multivariate curve resolution applied to second order data. *Chemom. Intell. Lab. Syst.* **1995**, *30*, 133–146. [CrossRef]

34. Elbergali, A.; Nygren, J.; Kubista, M. An automated procedure to predict the number of components in spectroscopic data. *Anal. Chim. Acta* **1999**, *379*, 143–158. [CrossRef]

35. De Juan, A.; Tauler, R. Chemometrics applied to unravel multicomponent processes and mixtures: Revisiting latest trends in multivariate resolution. *Anal. Chim. Acta* **2003**, *500*, 195–210. [CrossRef]

36. Jaumot, J.; Gargallo, R.; de Juan, A.; Tauler, R. A graphical user-friendly interface for MCR-ALS: A new tool for multivariate curve resolution in MATLAB. *Chemom. Intell. Lab. Syst.* **2005**, *76*, 101–110. [CrossRef]

37. Ruckebusch, C.; Blanchet, L. Multivariate curve resolution: A review of advanced and tailored applications and challenges. *Anal. Chim. Acta* **2013**, *765*, 28–36. [CrossRef]

38. Jaumot, J.; de Juan, A.; Tauler, R. MCR-ALS GUI 2.0: New features and applications. *Chemom. Intell. Lab. Syst.* **2015**, *140*, 1–12. [CrossRef]

39. Windig, W.; Guilment, J. Interactive self-modeling mixture analysis. *Anal. Chem.* **1991**, *63*, 1425–1432. [CrossRef]

40. Ruckebusch, C. *Resolving Spectral Mixtures: With Applications from Ultrafast Time-Resolved Spectroscopy to Super-Resolution Imaging*; Elsevier: Amsterdam, The Netherlands, 2016; ISBN 9780444636447.

41. Bro, R.; De Jong, S. A fast non-negativity-constrained least squares algorithm. *J. Chemom.* **1997**, *11*, 393–401. [CrossRef]

Sample Availability: Samples of the compounds S2, S3, S4 and SC are available from the authors.

Paper V

Metal self-assembly mimosine peptides with enhanced antimicrobial activity: towards a new generation of multitasking chelating agents

J. I. Lachowicz, G. Dalla Torre, R. Cappai, E. Randaccio, V. M. Nurchi, R. Bachor, Z. Szewczuk, L. Jaremko, M. Jaremko, M. B. Pisano, S. Cosentino, G. Orrù, A. Ibba, J. Mujika, X. Lopez, *Dalton Trans*., **2020**, *49*, 2862-2879.

.

PAPER

Metal self-assembly mimosine peptides with enhanced antimicrobial activity: towards a new generation of multitasking chelating agents†

Joanna Izabela Lachowicz, [iD] *[a] Gabriele Dalla Torre, [iD] [b,c] Rosita Cappai,[d]
Enrico Randaccio,[e] Valeria M. Nurchi, [iD] [d] Remigiusz Bachor,[e]
Zbigniew Szewczuk, [iD] [e] Lukasz Jaremko,[f] Mariusz Jaremko, [iD] [f]
Maria Barbara Pisano,[g] Sofia Cosentino,[g] Germano Orrù,[h] Antonella Ibba,[h]
Joni Mujika[b] and Xabier Lopez*[b]

Mimosine is a non-protein amino acid with various properties, such as antibacterial, anti-inflammatory, anti-cancer and anti-virus among others. Due to its structural similarity with deferiprone (**DFP**), mimosine is a potential excellent metal chelator. In the present work, we combine experimental and theoretical (DFT) approaches in order to investigate the properties of mimosine peptides. Six different peptides were synthesized and their complex stoichiometry and stability were characterized by means of UV-Vis spectrophotometry. Then, the binding mode and self-assembly features of the peptides were evaluated using a DFT approach, taking into account different number of mimosine amino acids and varying the length of the spacer between the mimosine residues, and there was good agreement between experimental data and computational calculations. Further elucidations of the structural properties of these peptides allowed us to propose improvements in the structure of the mimosine moiety which can lead to enhanced affinity for high-valent metals. Moreover, we demonstrate that these peptides show an antimicrobial activity against Gram positive bacteria that is enhanced by the formation of a complex with iron(III) ions. The mimosine peptides could be an alternative to antimicrobial peptides (AMPs), which are expensive and susceptible to proteolytic degradation. In summary, in the present work, we propose a new generation of multipurpose mimosine-based peptides as new metal self-assembly chelators which could be a turning point in biomedical and nanotechnological applications.

[a]*Department of Medical Sciences and Public Health, University of Cagliari, Cittadella Universitaria, 09042 Monserrato, Italy. E-mail: lachowicz@unica.it*
[b]*Kimika Fakultatea, Euskal Herriko Unibertsitatea UPV/EHU, Donostia International Physics Center (DIPC), P.K. 1072, Donostia, Euskadi, 20080 San Sebastian, Spain. E-mail: xabier.lopez@ehu.es*
[c]*UCIBIO/REQUIMTE, Departamento de Química e Bioquímica, Faculdade de Ciências, Universidade do Porto, Rua do Campo Alegre, s/n, 4169-007 Porto, Portugal*
[d]*Department of Life Sciences, University of Cagliari, Cittadella Universitaria, 09042 Monserrato, Italy*
[e]*Faculty of Chemistry, University of Wrocław, F. Joliot-Curie 14, 50-383 Wrocław, Poland*
[f]*Division of Biological and Environmental Sciences and Engineering, King Abdullah University of Science and Technology (KAUST), 23955 Thuwal, Saudi Arabia*
[g]*Department of Medical Sciences and Public Health, University of Cagliari, Cittadella Universitaria, 09042 Monserrato, Italy*
[h]*Department of Surgical Sciences, University of Cagliari, Cittadella Universitaria, 09042 Monserrato, Italy*
†Electronic supplementary information (ESI) available. See DOI: 10.1039/C9DT04545G

1. Introduction

One out of three proteins use metal ions as cofactors. The binding of metal ions to proteins changes their structures and properties, and it is a key feature for their structural, regulatory, and/or enzymatic functions. For example, peptides that self-assemble through metal–ligand complexes form nanostructures that possess very different structures and functions from the original peptides. This particular property was recently used for the synthesis of metal-triggered, self-assembled peptides in nanotechnology,[1] to synthesize nanofiber materials for cell culture and tissue engineering,[2] to assemble peptide nanotubes[3] and helical ribbons, *etc*. Thus, the formation of molecular building blocks that can spontaneously form regular and stable macroscopic structures, *via* covalent or noncovalent bonds is a very active and fast-growing process in nanotechnology.

In addition to the 22 amino-acids used by eukaryotes, there are more than 140 non-proteinogenic amino-acids that are not

naturally encoded or found in the genetic code of any organism. Some of them possess a biological function (*e.g.* components of bacterial cell walls, neurotransmitters and toxins) that may be used as natural or man-made pharmacological compounds.[4]

Antibiotics are among the most extensively used drugs. Their abuse in human medicine and in animal farming leads to bacteria resistance.[5] Now, we are witnessing the end of a golden epoch of antibiotics[6] and new solutions are critical for human health. Antimicrobial peptides (AMPs) have emerged as an alternative to antibiotics and in 2003 Daptomycin (MIC 32 μg ml^{-1} (ref. 7)) was approved by the FDA as an antibiotic against a variety of Gram-positive bacteria (methicillin-resistant *Staphylococcus aureus* (MRSA), vancomycin-resistant *enterococci* (VRE) and penicillin-resistant *Streptococcus pneumoniae*[8]

(PRSP)). The bactericidal activity of AMPs is triggered mainly by membrane disruption and reduction in bacterial resistance; however most AMPs are expensive, highly cytotoxic and susceptible to proteolytic degradation. AMPs can be improved by the design of peptide mimics (peptidomimetics), whose backbone is not based on the regular amino acid linked in a chain.[9,10] One of the strategies in peptidomimetics is the use of unnatural amino acids.[11]

Mimosine [β-[*N*-(3-hydroxy-4-oxypyridyl)]-α-aminopropionic acid] (**MIM**, Scheme 1) is a non-protein amino-acid biosynthesized by the *Mimosoideae* family of plants. The chemistry,[12] methods for estimation,[13] biosynthesis,[14] and the degradation of this secondary metabolite[15] have been extensively described in the literature. Over the past few years, mimosine has been found to be involved in different biological processes such as
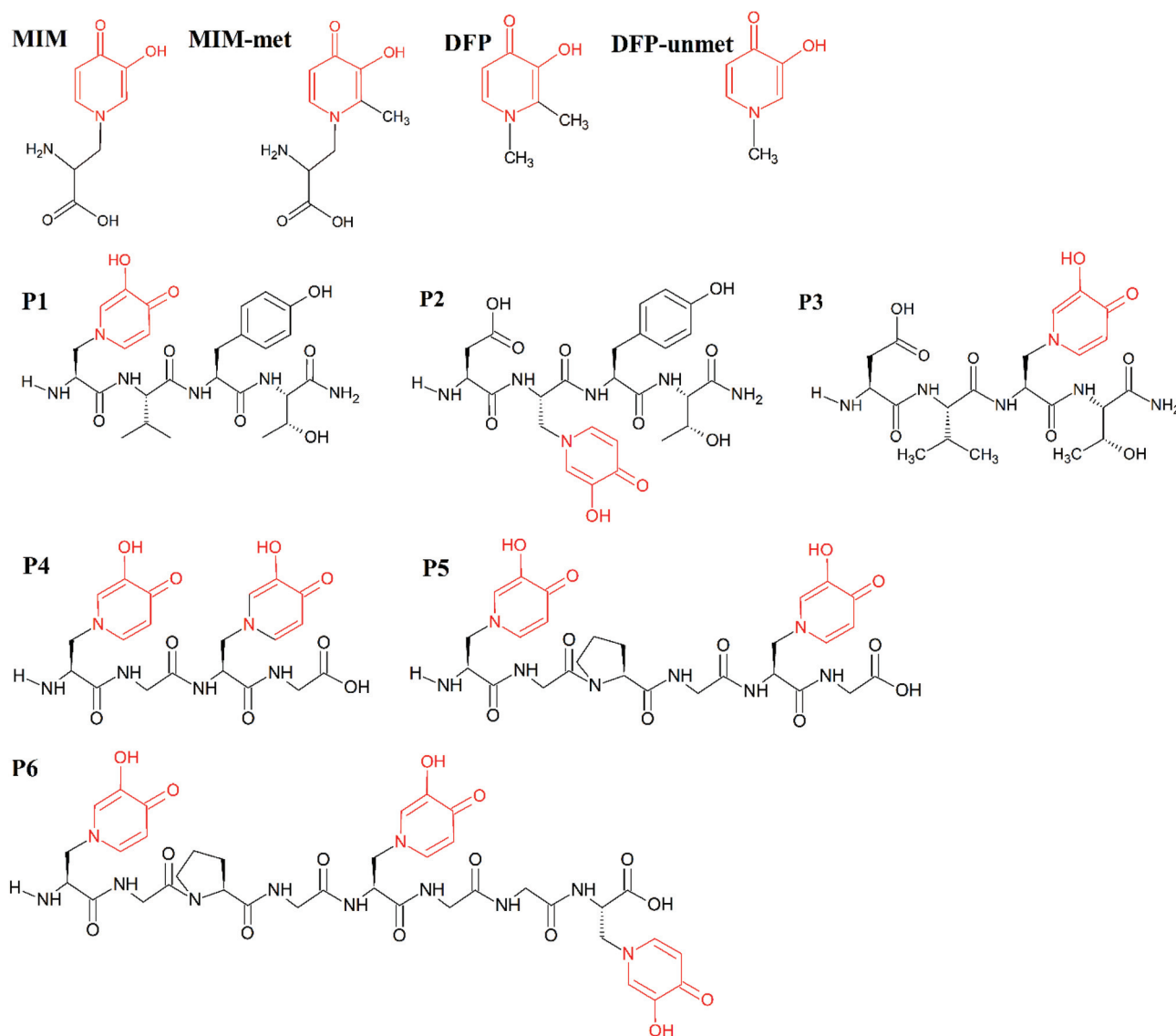
Scheme 1 Molecular structures of the studied molecules (**MIM**, **MIM-unmet**, **DFP**, **DFP-unmet**, **P1–P6**). Structural similarities between these molecules are indicated in red.

antibacterial,[16] anti-cancer,[17] anti-inflammatory,[18] anti-fibrosis,[19] anti-influenza,[20] anti-virus,[21] herbicidal[22] and insecticidal,[23] among others.[12] In the 90s, mimosine was investigated as a potential inhibitor of the G1/S phase,[24] and, over the last twenty years, as a potential drug for cancer.[25] The activity of mimosine-based peptides has been linked to its metal chelating properties. For instance, the coordination of the essential metal ions, in blood plasma, causes an inhibition of the growth of wool and defleecing in sheeps.[26]

The mimosine sidechain is structurally similar to that of deferiprone (DFP, Ferriprox, 1,2-dimethyl-3-hydroxy-4-pyridinone, Scheme 1) and therefore, they show similar features in their metal-coordination ability. DFP is used as a drug to remove the excess iron in thalassaemia major.[27] It has been used in the treatment of thalassaemia major in Europe and Asia since 1994, and was approved for its use in the US,[28] in 2011. Its coordination of Cu(II),[29,30] Cd(II),[31] Al(III),[32] Fe(III),[33] Ga(III),[34] Gd(III)[29] and In(III)[34] metal ions, as well as actinides[35] and lanthanides,[36] has been extensively described in the literature. DFP and its derivatives have been proposed as potential remedies for diseases related to metal disorders, e.g. anaemia, thalassemia, hemochromatosis, etc., for which the delivery, or removal, of metal ions is desirable. Recently, hydroxypyridinones have been used to improve the retention and tissue uptake of metal-based insulin-enhancing agents. DFP-based therapy protects against the toxicity of heavy metals (used in contrast agents), chemotherapeutics, exposition to harmful radioisotopes and the neurotoxicity of redox metals.[37] Fe(III)–, VO(IV)–, Cu(II)–, Zn(II)– and Ni(II)–mimosine complexes have been investigated by various research groups.[38,39] Mimosine dipeptides and tetrapeptides have been previously synthesized and investigated as potential neuraminidase,[40] tyrosinase[40,41] and cyclooxigenase[41] inhibitors. However, to our knowledge, no other applications have been considered, nor any synthesis of mimosine hexapeptides has been performed, to this day.

Recently, we have investigated by means of QM/MM and DFT calculations the potential application of several mimosine-based peptides as improved metal chelators.[42] We found that this class of ligands may reach a metal binding affinity comparable to or even higher than DFP.[42] In this paper, we present synthetic, DFT, and experimental iron(III)- and copper(II)-complex formation studies of tetra- and hexapeptides containing one, two or three mimosine residues. The antimicrobial activities of the synthesized complexes against Gram positive, Gram negative bacteria and dermatophytes are also investigated and reported here (Section 3.2). We found very good agreement between experimental and theoretical studies, which point to these mimosine-based peptides as effective iron(III) and copper(II) chelators. The effect on the affinity of key structural features of these peptides, such as the number of mimosine residues and length and flexibility of the spacer, is also discussed and rationalized. The DFT model established here can be used for the design of the self-assembly of metal ions and mimosine peptides for medical and nanotechnological applications.

2. Experimental

2.1. Reagents

All solvents and reagents were used as supplied. Fmoc amino acid derivatives were purchased from Novabiochem. $FeCl_3$, $CuCl_2 \times 2H_2O$, NaOH, HCl, L-mimosine was obtained from Sigma Aldrich. (Benzotriazol-1-yloxy)tris(pyrrolidino)phosphonium hexafluorophosphate (PyBOP), N-[(dimethylamino)(1H-1,2,3-triazolo-[4,5-b]pyridin-1-yl)methylene]-N-methylmethanaminium hexafluorophosphate N-oxide (HATU), and MBHA-Rink amide resin (0.69 mmol g^{-1}) were obtained from Merck Millipore. Fmoc-Gly-Wang resin (0.73 mmol g^{-1}), 2-chlorotrityl chloride resin (1.00 mmol g^{-1}) and trifluoroacetic acid (TFA) were obtained from IrisBiotech. Solvents for peptide synthesis (N,N-dimethylformamide (DMF), dichloromethane (DCM), and (N-ethyldiisopropylamine (DIEA)) were obtained from Sigma Aldrich.

2.2. Synthesis

The synthesis of the Fmoc-Mim derivative was performed using the method described by Upadhyay et al.[40] Briefly, mimosine (200 mg) and sodium carbonate (Na_2CO_3) (220 mg) were dissolved in distilled water (3 mL). Fmoc-Osu (500 mg) dissolved in 3.6 mL of 1,4-dioxane was added dropwise to the solution and stirred for 2 h at room temperature. Afterwards, 12 mL of Na_2CO_3 (0.1 M) was added. The mixture was stirred for 7 h at 26 °C and was then filtered and washed with 20 mL of ethyl acetate to remove the excess of Fmoc-Osu and by-products. The water fraction was kept in an ice bath, the pH was adjusted to 4.0 (by adding 6 N HCl) and the mixture was incubated overnight at 4 °C. The resulting precipitate was filtered, washed with distilled water, and dried under reduced pressure to give Fmoc mimosine. The obtained product was analyzed by ESI-MS.

The synthesis of peptides on the MBHA-Rink (peptides 1–3, Table S1†), Fmoc-Gly-Wang resin (peptide 4, Table S1†) and 2-chlorotrityl chloride resin was performed manually in polypropylene syringe reactors (intavis AG) equipped with polyethylene filters, according to a standard Fmoc (9-fluorenylmethoxycarbonyl) solid phase synthesis procedure.[43]

All products were purified using the analytical HPLC Thermo Separation system with UV detection (210 nm) having a YMAC-Pack RP C18 Column (4.6 × 250 mm, 5 µm), with a gradient elution of 0–40% B in A (A = 0.1% TFA in water; B = 0.1% TFA in acetonitrile/H_2O, 4 : 1) over 30 min (flow rate 1 mL min^{-1}). The main fraction, corresponding to the peptide, was collected and lyophilized.

All products were analyzed on a microTOF-Q mass spectrometer (Bruker Daltonics, Bremen, Germany) and on an FTICR (Fourier Transform Ion Cyclotron Resonance) PAex-Qe Ultra 7 T mass spectrometer (Bruker Daltonics, Bremen, Germany) equipped with a standard ESI source. The instruments were operated in the positive-ion mode and calibrated daily with a Tunemix™ mixture (Agilent Technologies, Palo Alto, CA, USA). The mass accuracy was better than 5 ppm. Analyte solutions (70 µl) were introduced at a flow rate of 3 µl min^{-1}. The parameters of the instruments were as follows: for microTOF-Q

Table 1 Constants of formation for the Iron(III)−DFP and Iron(III)−mimosine Systems, as determined at t = 25 °C and I = 0.1 M (KCl) by Nurchi,[32] and at t = 25 °C and I = 0.1 M Tsai and Ling,[58] respectively. Stability constants of the proton and Cu(II) complexes of DFP at t = 37 °C and I = 0.15 (KNO$_3$) by Stunzi et al.,[59] and at t = 25 °C and I = 0.1 M (KCl) by Nurchi et al.;[32] L-mimosine, t = 37 °C and I = 0.15 (KNO$_3$) by Stunzi et al.[59] and at t = 25 °C and I = 0.1 M (KNO$_3$) by Chruscinska et al.[38]

	DFP[32]			Mimosine[58]		**DFP**[59]	**DFP**[32]	Mimosine[59]			Mimosine[38]
Species	log K			log K	Species	log K	log K	log K			log K
LH	9.82			8.76	LH	8.80	9.82	8.86			9.02
LH$_2$	3.66			7.14	LH$_2$	3.35	3.66	7.00			7.18
LH$_3$				2.48	LH$_3$	—	—	2.62			2.56
					LH$_4$	—	—	1.1			<1
Species	log K	λ_{max}	ε	log K	Species	log K	log β	log β	λ_{max}	ε	log β
					CuLH$_2$			18.1			
FeLH				12.00	CuLH	1.60		16.36	755	34 ± 5	16.63
FeL	15.01	540	1700		CuL	9.35	10.42	9.48			
					CuLH$_{-2}$						−9.47
FeL$_2$H$_2$				9.50	CuL$_2$H$_2$	—		31.26	693 ± 10	37 ± 10	32.04
					CuL$_2$H		21.98	24.40			24.43
FeL$_2$	12.02	491	3700		CuL$_2$	7.58	19.09	16.81	690	33	17.23
					CuL$_2$H$_{-1}$		8.49				5.79
					Cu$_2$L			15.70	735 ± 15	28 ± 5	
					Cu$_2$L$_2$			32.2	662	50	29.98
					Cu$_2$L$_3$			29.52			
FeL$_3$H$_3$				8.00							
FeL$_3$H$_2$				6.28							
FeL$_3$H				7.43							
FeL$_3$	10.40	457	4400	7.42							

MS: scan range: 50–1600 m/z; drying gas: nitrogen; flow rate: 4.0 L min^{-1}, temperature: 200 °C; potential between the spray needle and the orifice: 4.2 kV; for FTICR MS: scan range: 100–1600 m/z; drying gas: nitrogen; flow rate: 1.5 L min^{-1}, temperature: 200 °C; potential between the spray needle and the orifice: 4.2 kV. For MS spectra analysis (Table 1), a Bruker Compass Data Analysis 4.0 software was used.

2.3. NMR measurements

2.0 mg of each peptide was dissolved in 500 μL of a mixture of 10% D$_2$O and 90% of H$_2$O (v/v). After the peptide was dissolved, the pH of the solution was manually adjusted to 7.40, prior to each measurement. All NMR experiments were performed using either 700 MHz (for peptides 1 and 2) or 950 MHz (for peptides 3–5) spectrometers at 25 °C. All NMR data were processed by NMRPipe[44] and analyzed by using Sparky[45] software. Complete assignments of the ^{1}H and ^{13}C resonances, for all the peptides (Tables S3–S7†), were done by the application of a standard procedure[46] based on the inspection of the 2D homonuclear TOCSY (with mixing times of 10 and 80 ms) and ROESY (with mixing times of 300) experiments. The NMR spectra were acquired after 2 months of synthesis and ESI-MS spectra acquisition. No peptide degradation was observed.

2.4. UV-Vis measurements

UV-Vis spectra were recorded using a SPECTROstar Nano (BMG LABTECH). 5 μl total volume of the peptide and metal water solutions were placed in multi-well plates, and spectra were collected, using a range of wavelengths from 200 to 900 nm. The final pH was a result of mixing peptide- and water solutions with metal acidic solutions. The peptide and metal concentrations, for each experiment, are reported in the Results and Discussion section. The pHs of the solutions were measured using a METROHM Microelectrode 6.0224.100 daily calibrated with a Mettler TOLEDO InLab® Solutions buffer (pHs 4.01 and 9.21).

2.5. ESI-MS measurements

The obtained mass spectra were recorded in the positive mode on a LCMS 9030 qTOF Shimadzu mass spectrometer (Shimadzu, Kyoto, Japan). The m/z range was between 100 and 1500, interface voltage (+) was 4.5 kV, interface temperature 300 °C, DL temperature 250 °C, heat block temperature 400 °C, nebulizing gas (nitrogen) flow 3 L min^{-1}, and total flow 0.4 mL min^{-1} of the H$_2$O/MeCN mixture (1 : 1, v : v). Equimolar ratios of the peptide and metal ions (Fe(III) ions (FeCl$_3$), Cu(II) (CuSO$_4$) were mixed in water, dissolved in methanol and analyzed by mass spectrometry.

2.6. DFT calculations

Optimization was carried out using the B3LYP functional[47,48] with Grimme's D3 dispersion correction[49] along with the Becke–Johnson (BJ) damping scheme and the 6-31+G(d) basis set. To confirm that the optimized structures were real minima on the potential energy surfaces, frequency calculations were carried out at the same level of theory. All structures showed positive force constants for all normal modes of vibration. The frequencies were then used to evaluate the zero-point vibrational energy (ZPVE) and thermal (T = 298°K) vibrational corrections to the Gibbs free energies within the harmonic oscillator approximation. To calculate the entropy, the

different contributions to the partition function were evaluated using the standard statistical mechanics expressions in the canonical ensemble and the harmonic oscillator and rigid rotor approximation. In addition, energies were refined with single point calculations at the B3LYP-D3(BJ)/6-311++G(3df,2p) level of theory. All calculations were performed with the IEFPCM solvation model[50] in order to properly investigate the thermodynamics of metal–ligand complexes in solution.

All calculations were performed with the Gaussian16 Rev. A03 package.[51]

Binding energies and enthalpies were calculated according to the following substitution reaction:

$$\left[M(H_2O)_6\right]^p + n[LIG]^q$$
$$\leftrightarrow \left[M(H_2O)_{6-m}(LIG)_n\right]^{p-nq} + m(H_2O) \quad (1)$$
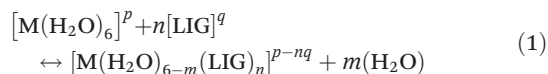
where M can be Fe(III)(sextuplet) or Cu(II)(doublet), p refers to the metal charge (+3 for Fe(III) and +2 for Cu(II)), LIG is one of the ligands (**DFT**, **DFT-unmet**, **MIM**, **MIM-unmet**, peptides 1–6) depicted in Scheme 1, n refers to the number of the ligand (n = 1,2,3), q is the total charge of the ligand, and m is the number of water molecules displaced from $M(H_2O)_6$ by the n ligands so that $m = 2n$ (note that every ligand binds bidentately to the metal).

Ligands were considered in their unprotonated form since this is the way that experimental stability constants are calculated, and good agreement was found between DFT binding energies and experimental log β values as in a previous work.[52]

The binding energies in solution associated with eqn (1) can be calculated as:

$$\Delta G_{aq}^{comp} = G_{aq}\left[M \cdot (H_2O)_6 - m(LIG)^n\right] + mG_{aq}(H_2O)$$
$$- G_{aq}\left[M(H_2O)_6\right] - nG_{aq}(LIG) \quad (2)$$
$$+ \Delta \nu RT \ln(24.46) + mRT \ln(55.34)$$

Since the energies were determined using an ideal gas at 1 atm as the standard state, the penultimate term in eqn (2) corresponds to the volume change due to the transformation from 1 atm to 1 M in solution, where $\Delta \nu$ refers to the change in the number of species in the reaction. The last term is the entropic factor that accounts for the concentration of 55.34 M of water in liquid water.[53] The $\Delta \nu RT \ln(24.46)$ and $mRT \ln(55.34)$ corrections correspond to the changes in the standard state, accounting, on the one hand, for the change due to the transformation from 1 atm to 1 M in solution, and to an entropic factor that accounts, on the other hand, for the concentration of 55.34 M of water in liquid.[53]

2.7. Antimicrobial activity

2.7.1. Bacterial and dermatophyte species and culture conditions. The antibacterial and antifungal activities of the six peptides were preliminarily evaluated by the agar-plate disk-diffusion method (CLSI) against the following bacterial and dermatophyte species: *Staphylococcus aureus* ATCC 25923, *Bacillus cereus* ATCC 11178, *Escherichia coli* ATCC 25922, *Microsporum canis* 10D, and *Trichophyton rubrum* 11D (from

the collection of the Department of Medical Science and Public Health). All bacterial strains were stored in a nutrient broth (NB, Microbiol, Cagliari, Italy) and 15% (v/v) glycerol, at −20 °C, except the dermatophyte strains that were maintained in Potato Dextrose broth (PDB, Microbiol) with 15% (v/v) glycerol. Before use, they were sub-cultured twice in an appropriate medium.

The bacterial and fungal suspensions, adjusted to a 0.5 McFarland standard turbidity (equivalent to 1.5×10^8 CFU mL^{-1} or 1–5×10^6 spores per mL^{-1}),[54] were prepared in NB and in sterile phosphate-buffered saline (PBS) with 0.05% Tween 80 (PBS-Tween), respectively.

A sterilized filter paper disc (5 mm in diameter) containing either a 10 µL of peptide or a Cu(II)–peptide complex sample was placed on Muller Hinton (MHA) or Sabouraud Dextrose agar (SDA) plates previously seeded with the prepared bacterial and fungal suspensions. Different stock solutions of peptides were prepared, depending on the residual amount. Peptides 1, 3 and 5 were dissolved in 0.2 mL of sterile distilled water to obtain the final concentrations of 50, 340, and 810 µg per disc, respectively. Peptides 2 and 4 were dissolved in 0.5 mL of sterile distilled water to obtain 84 and 149 µg per disc concentrations, respectively. The stock solution of peptide 6 prepared in DMSO (100%) was further diluted in NB to obtain the final concentrations of 140 and 14 µg per disc. These concentrations were chosen according to each peptide maximum-water solubility. The Cu(II)–peptide complexes involving peptides 2, 4 and 6 were prepared in 1 : 3, 1 : 1 and 1 : 1 metal-to-peptide molar ratios, respectively. 25 µg of amoxicillin, 5 µg of ofloxacin or 15 µg of Ketoconazole (Oxoid) and blank disc impregnated with 10 µL of NB or PBS-Tween were used as positive and negative controls, respectively.

Serial doubling dilutions of the different peptides and their metal complexes were prepared in 100 µL of NB, in 96-well microtiter plates. The following concentrations were tested: **P3**, 3400–106.25 µg mL^{-1}, **P4**, 7450–232.81 µg mL^{-1}, **P5**, 8100–253.125 µg mL^{-1}, **P6**, 6900–215.625 µg mL^{-1}, for the following metal–peptide complexes: Fe(III)–**P1** 333.7–3.0 µg mL^{-1}, Fe(III)–**P2** (1 : 3 metal : peptide molar ratio) 560–17.5 µg mL^{-1}, Fe(III)–**P4** (1 : 1 metal : peptide molar ratio) 967.5–30.2 µg mL^{-1}, Fe(III)–**P6** (1 : 1 metal : peptide molar ratio) 896.1–28.0 µg mL^{-1}. The bacterial suspensions, prepared as described above, were further diluted in the broth media, and 100 µL volume of this diluted inoculum was added to each well of the plate, resulting in the final inoculum of 5×10^5 CFU mL^{-1}. Controls for the sterility of the NB and the peptides, and the culture (inoculum) were included; DMSO (for **P6**) was also monitored to check the effect of the solvent on the growth of microorganisms. Furthermore, ofloxacin (8 µg mL^{-1}) was used as the positive control for Gram-positive and negative bacteria. MICs and MBCs were determined after 24 h of incubation of the plates, at 37 °C. Microbial growth was indicated by the presence of turbidity and a "pellet" on the well bottom. MICs were determined presumptively as the first well, in ascending order, which did not produce a pellet. To confirm MICs and to establish MBCs, 10 µL of broth was removed from each well and

inoculated on Tryptic Soy Agar (Microbiol) plates. After incubation under the conditions described above, the number of surviving bacteria was determined. The MIC was the lowest concentration that resulted in a significant decrease of the inoculum's viability (>90%), and the MBC concentration was found to be the one for which 99.9% (or more) of the initial inoculum was killed. All tests were conducted in triplicate, and the modal MIC and MBC values were selected.

The MIC dilutions were prepared with daily prepared solutions and with 2 month-old solutions (stored at −5 °C). No differences were observed in the experimental results.
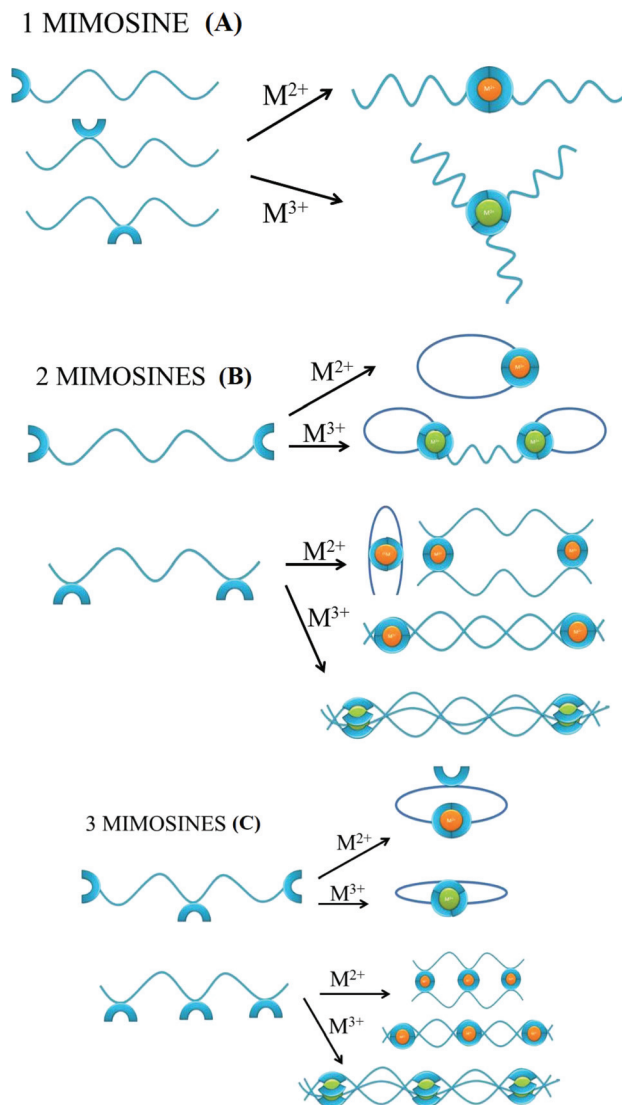
2.7.2. Antibiofilm activity. The following bacterial species were used: *Staphylococcus aureus* ATCC 6538 (American Type Culture Collection), *Streptococcus intermedius* DSMZ 20573 (German Collections of Microorganisms and Cell Cultures), *Pseudomonas aeruginosa*, strain ATCC 2783. These strains were cultured at 37 °C in the following: Mueller-Hinton broth for *S. aureus* and *P. aeruginosa*, and Schaedler broth for *S. intermedius*. All media were manufactured by Microbiol (Uta, Italy). The crystal violet staining protocol, previously described in the literature,[55] was used for biofilm evaluation. A microplate containing serial concentrations of the compound, inoculated with 10^6 CFU ml^{-1} bacterial cells, was incubated at 37 °C for 6 days, to permit biofilm formation. The plate samples were subsequently washed three times with phosphate-buffered saline GIBCO® PBS (ThermoFisher) to eliminate planktonic cells; thus the biofilm was stained with 100 μL of 0.1% w/v of crystal violet solution (Microbial, Uta, Italy) for 10 min at 25 °C; after washing with PBS solution three times, 200 μL of 30% v/v acetic acid was added in every well to solubilize the dye from the bacterial biomass. The biofilm amount was measured with a plate reader spectrophotometer (SLT-Spectra II, SLT Instruments, Germany) at 620 nm. For each formulation the experiment was performed in triplicate. For the same concentration, all values that showed a standard deviation (SD) within ±10% of the mean value were considered significant.

Scheme 2 Possible types of the self-assembled metal–peptide aggregates, according to the number of mimosine residues, the position of the mimosine in the backbone of the peptide, and the oxidation state of the metal.

3. Results and discussion

3.1. Metal coordination

The number of mimosine residues, their positions in the peptide backbone, and the length of the spacer between neighboring mimosine residues determine the stoichiometry of metal–peptide complexes and their structures (Scheme 2). Some of the predicted stoichiometries of the M^{2+} and M^{3+} metal-ion complexes with mimosine peptides are shown in Scheme 2, together with their possible structures.

In the peptide containing one mimosine residue (Scheme 2A), the most probable stoichiometry with M^{2+} is a 1 : 2 (metal : ligand) molar ratio, whereas in the trivalent metal ion, a 1 : 3 (metal : ligand) stoichiometry is expected. The position of the mimosine residue in the peptide backbone influences the ternary structure of the metal complex, and in some

cases, where the conformational constraints occur, even the changes in the metal–ligand stoichiometry.

The addition of the second mimosine residue in the peptide backbone (Scheme 2B) gives more possible stoichiometries of the metal complex and makes the coordination system more complicated. The peptide that contains mimosine amino acids at the N- and C-ends of the peptide can form cyclic complexes with divalent metal ions, if the length of the linker between mimosine residues is long enough for obtaining appropriate geometry of the metal complex. In the case of the short spacer between neighboring mimosine residues (*e.g.* mimosine residues in the middle of the peptide backbone), it is likely that bend, dimeric or polymeric structures will be formed. For trivalent metal ions, the two mimosine peptides will form 2 : 3 (metal : ligand) complexes of different ternary

structures (closed or linear) or polymers, depending on the length of the linker between mimosine units.

The presence of a third mimosine residue (Scheme 2C) makes the predictability of the complex stoichiometry harder. Two mimosine residues at the N- and C-ends of the peptide, and one in the middle, will form cyclic complexes with trivalent metal ions, but also with divalent ones. In the last case, one mimosine residue will have free binding sites, which could be the starting point to form higher stoichiometric complexes. Three mimosine residues in close proximity in the backbone will lead to the formation of $3:2$, $3:3$ (metal : ligand) linear complexes or polymeric structures with divalent and trivalent metal ions.

The possible formation of polymeric structures by mimosine peptides is intriguing. The two mimosine peptides (Scheme 3A) can form with M^{2+} metal ions in linear polymers, while three mimosine peptides can be assembled both in linear and in non-linear polymers (Scheme 3B).

The formation of polymeric structures instead of dimeric complexes depends on the length of the linker between neighbouring mimosine residues, as well as linker rigidity (peptide bonds or proline residues) and steric incumbrances in the metal complex. Moreover, the metal and peptide concentrations in the solution, pH, ionic strength, and temperature determining polymerization/aggregation process[56] influence the polymerization/aggregation process, but they are not the object of the present studies.

In order to predict accurately the stoichiometry and the structure of the investigated complexes, we establish a DFT cal-

A

Linear polymer

B

Linear polymer

Non-linear polymer

Scheme 3 Possible types of the self-assembled metal–peptide polymers with M^{2+}, according to the number of mimosine residues and the position of the mimosine in the backbone of the peptide.

culation protocol and probe peptides with a variable number of mimosine residues and different lengths of the linker.

3.1.1. DFP and mimosine Fe(III) and Cu(II) coordination models. The DFT protocol considers the metal coordination core, *i.e.* the hydroxypyridinone ring. As long as there are no crystal data for the mimosine complexes with copper(II) and iron(III) ions, the DFT model is prepared not only for **MIM** but also for **DFP**, which is the closest analogue of mimosine. The obtained data are then compared with the **DFP** crystal structure data.

The geometries of the $1:3$ Fe(III)–ligand complexes with **MIM** and **DFP** show a perfect octahedral coordination mode (Fig. S1†), in agreement with the X-ray structure of the $1:3$ Fe(**DFP**)$_3$ complex[34] (Fig. 1C). The octahedral geometry of the metal coordination shell is characterized by O–Fe–O angles between 80–90 and ~167 degrees, with the Fe–O distances 1.9–2.0 Å (Table S8†). Similarly, $1:2$ and $1:1$ Fe(III)–ligand complexes retain octahedral geometry with coordination sites filled by water molecules in the axial positions (Fig. S2 and S3†). On the other hand, in the $1:1$ Cu(II)–ligand complex, one water molecule leaves the copper coordination sphere (Fig. S5†), and the system shows a pentacoordinate binding mode. In the $1:2$ Cu(II)–ligand complex, two water molecules move away from their axial positions (Fig. S4†) and a stable tetrahedral complex is therefore formed, which is coherent with the X-ray structure for $1:2$ Cu(II)–**DFP** (Fig. 1D).[57] The calculations with our DFT model are in line with experimental data (Table S2 and Fig. S8†).

In aqueous solution, **DFP** forms complexes with a $1:1$ metal : ligand stoichiometry and at a pH lower than 1 (Fig. S6†) these complexes are transformed into $1:2$ stoichiometry complexes above pH 2 and $1:3$ complexes above pH 3.[32] The **DFP**–Fe(III) complexes are violet (at acidic pH) or red (neutral and basic pH), in water, and each complex is characterized by its specific absorptivity band (Fig. 1A). The crystal structure of **DFP** with Fe(III) ions (Fig. 1C) shows that the metal ion is coordinated in octahedral geometry by three pairs of carbonyl and dissociated hydroxyl groups.

With respect to L-mimosine, the protonation of the amino- and carboxylic groups makes the equilibrium of the iron complexation more complicated; nevertheless, electronic absorption spectra are similar to those obtained for **DFP** iron complexes, showing that amino- and carboxylic groups do not bind to the iron(III) ions.[39] The constants of formation for the **DFP** and **MIM** complexes with iron(III) ions, shown in Table 1, are in good correlation with the computed binding enthalpies (ΔH_{comp}) and free energies (ΔG_{comp}) for the complexes of similar stoichiometry, and with those calculated with our DFT model (Table S2 and Fig. S8†).

The aqueous solution complexes of **DFP** with copper(II) ions are green colored and the Vis spectra (Fig. 1B) in the 400–600 nm range show the charge transfer bands ($A_{max}\lambda \sim$ 480 nm) of O(phenol) to Cu(II) ions. Indeed, the crystal structure determined by A. El-Jammal *et al.*[57] (Fig. 1D) confirms the formation of a Cu(**DFP**)$_2$ complex and the coordination of copper ions by the pair of carbonyl and dissociated hydroxyl
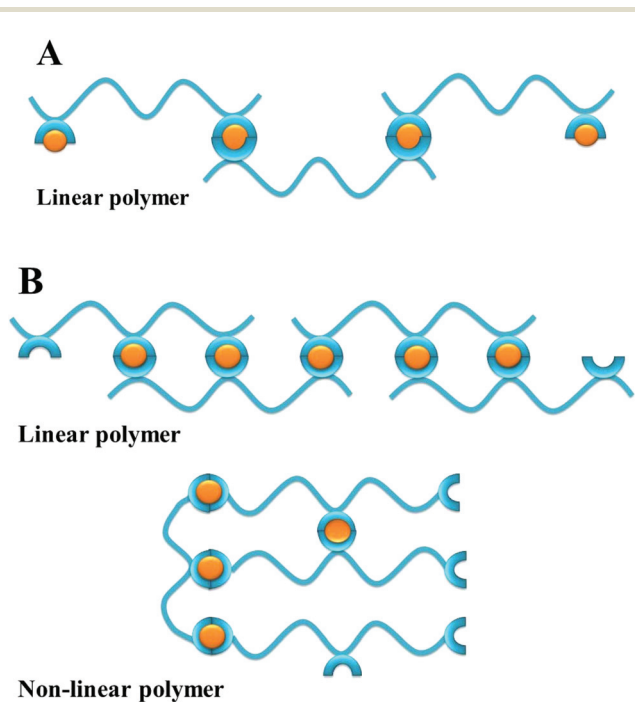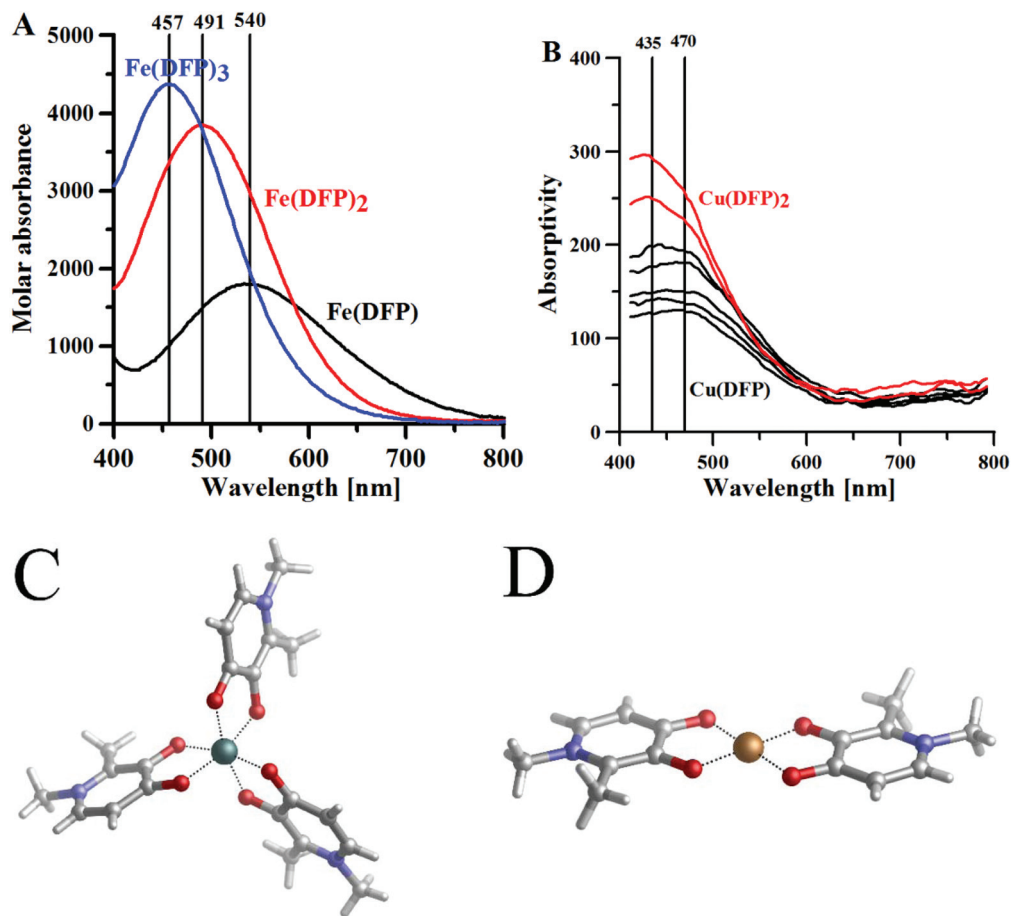
Fig. 1 The maximum absorptivity spectra of (A) Fe^{3+}–**DFP** complexes, [**DFP**] = 0.5 mM, l = 1 cm; (B) Cu(II)–**DFP** complexes, metal : ligand molar ratio 1 : 2, [**DFP**] = 0.5 mM, l = 10 cm. (C) Crystal structure CCDC (JAWSEF01, additional database identifier JUHXEP, 1183333) of Fe(**DFP**)$_3$ complexes by E. T. Clarke et al.[31] (D) The crystal structure (CCDC: 1291877, WELTEM) of the Cu(**DFP**)$_2$ complex by A. El-Jammal et al.[57]

groups in octahedral geometry, with two axial water ligands. As previously shown in the DFT calculations, the copper(II) complexes with **DFP** are less stable than the iron(III) complexes. The [Cu(**DFP**)]$^+$ forms at pH < 1 (Fig. S6†) and is replaced with the Cu(**DFP**)$_2$ complex above pH 2.5. The constants of stability of the copper(II)–**DFP** and mimosine complexes, presented in Table 1, are in good agreement with those calculated using our DFT model (Table S2†).

The copper(II)–**MIM** and copper(II)–**DFP** absorption spectra were studied by Stunzi et al.[59] According to the authors, the 1 : 1 (copper(II) : **MIM**) stoichiometry complexes have almost the same wavelength maxima (Table 1) as the corresponding **DFP** complexes. This finding confirms that the metal binding sites are similar for **MIM** and **DFP**. The addition of the spectra of CuDFP$^+$ and CuGly$^+$ (λ_{max} 715 nm)[60] reproduces approximately the spectrum of Cu$_2$(mimosine)$^{2+}$, whereas the spectrum of the dimeric 2 : 2 mimosine is similar to the mixed 1 : 1 : 1 Cu–Gly–**DFP** spectrum and has λ_{max} (660 nm) between those for the CuGly$_2$ (617 nm) and Cu(mimosine)$_2^{2-}$ (690 nm) complexes. The small extinction coefficient Cu$_2$(mimosine)$_2$ complex may be explained by a slightly distorted structure, essentially strain-free.

The formation of a dinuclear copper(II)–mimosine complex was confirmed by EPR studies, performed by Chruscinska et al.[38] A dinuclear species predominates in equimolar solution, for pHs ranging from pH 4 to 11 (Fig. S6†), and two sets of hyperfine components, each consisting of seven lines, at the approximate intensity ratio of 1 : 2 : 3 : 4 : 3 : 2 : 1, and in the parallel region of the ΔM_S = ±1 resonances, are present in the EPR spectrum. The measured zero field splitting corresponds to an intermetallic distance of approximately 5.0 Å. The atoms from the donor sets are as follows: (CO, O$^-$) and (NH$_2$, COO$^-$).

Our DFT calculations confirm the stability of the dinuclear copper(II)–**MIM** complex. Fig. 2 shows the characteristics of the structure in which both Cu(II) cations are pentacoordinated by interacting with the backbone NH$_2$, the COO$^-$ groups of one **MIM**, and the carbonyl and hydroxyl oxygen atoms of the side chain of the other **MIM**. The metal coordination shell is completed by an explicit water molecule. The distances and angles computed (Table S10†) confirmed that the ligands are placed in a near-optimum arrangement. Compared to the Cu(**DFP**)$_2$ structure, the Cu–O distances in the dinuclear mimosine complex are slightly longer (1.94–1.97 Å) and the Cu–metal binding site angles are slightly different (90° and 170°) than
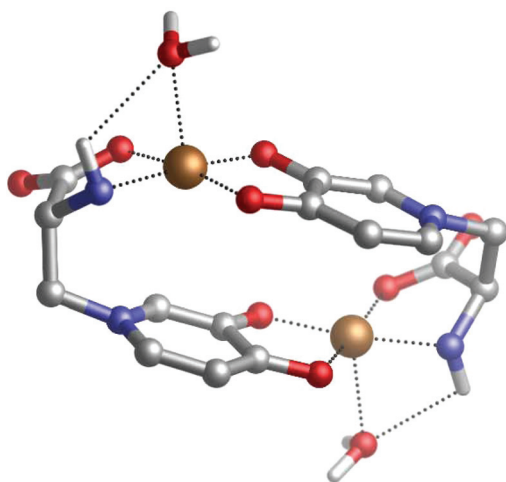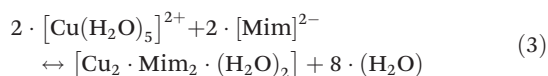
Fig. 2 DFT optimized structure of a dinuclear copper(II)−mimosine complex.

the corresponding distances (1.91–1.93 Å) and angles (90° and 180°) in the **DFP** copper complex (Table S10†). The DFT calculated distance between two copper ions in the dinuclear complex is 5.222 Å and stays in line with the EPR experimental data.[38] The stability of the complex was determined, *via* the following reaction:

$$2 \cdot \left[Cu(H_2O)_5 \right]^{2+} + 2 \cdot \left[Mim \right]^{2-}$$
$$\leftrightarrow \left[Cu_2 \cdot Mim_2 \cdot (H_2O)_2 \right] + 8 \cdot (H_2O) \tag{3}$$

in which Cu(II) is always pentacoordinated. The computed value of the free energy of the complex (in triplet state) is −163.1 kcal mol⁻¹ (ΔG_{aq}).

3.1.2. One-mimosine peptides: Peptide 1 (H-Mim-Val-Tyr-Thr-NH₂), Peptide 2 (H-Asp-Mim-Tyr-Thr-NH₂) and Peptide 3 (H-Asp-Val-Mim-Thr-NH₂). Here, we compare the metal complexes of four-amino acids peptides that contain only one **MIM** residue. According to the NMR data presented in Tables S3–S7,† none of the three peptides has a ternary structure. Peptide 1 contains one **MIM** residue at the N-end of the peptide, whereas peptide 2 and peptide 3 have **MIM** residues on the second and third positions, respectively.

The formation of metal complexes was studied experimentally using UV-Vis spectrometry, and the structure and stability of the formed complexes were determined by DFT calculations.

Electronic absorption spectra of the Peptide 1 (**P1**) and **P2** complexes with iron ions are shown in Fig. 3A. The **P1** peptide is considered to be a [LH₃]²⁺ ligand, where the amine, amide and hydroxyl groups are the dissociating groups. In the solution containing iron(III) and **P1** at a molar ratio 1 : 1, and at pH 1.0, one band with a maximum absorptivity at 540 nm can be seen on the Vis spectrum, and it can be associated with the [Fe(**P1**)H₂]⁴⁺ complex, as with the **DFP** complexes. The dissociated hydroxyl group is coordinating the iron ion, whereas both N-end and C-end (amide protected) of the peptide remain

protonated, at pH 1.0. Compared to amines, amides are weaker bases, and therefore do not present noticeable acid–base properties in water;[61] they are protonated only at a low pH (<4). In the solution of the metal and peptide at a 1 : 3 molar ratio, at pH 4.0, two additional bands appear, with maximum values at 491 and 457 nm; these bands can be attributed to the [Fe(**P1**)₂H₂]³⁺ and [Fe(**P1**)₃H₃]³⁺ complexes, respectively. The positive charge of the [Fe(**P1**)₂H₂]⁺ complex is associated with the metal ion and the protonated amine on the N-end of the peptides. The ESI-MS spectra (Fig. S9†) recorded in 50/50 H₂O/MeCN solution showed the formation of the [Fe(**P1**)H₋₁]⁺ ([C₂₆H₃₄FeN₆O₈]⁺; Fig. S9a†) and [Fe(**P1**)₂]⁺ ([C₅₂H₇₀FeN₁₂O₁₆]; Fig. S9b†) complexes.

The **P2** peptide is considered a [LH₄]²⁺ ligand with amine, amide, hydroxyl and carboxylic dissociating groups. Fig. 3A shows the absorptivity spectrum of the **P2** complex with iron(III) ions, at pH 4.6. The large band centered at 475 nm is composed of two bands (457 and 491 nm) of almost the same intensity, and one band at 540 nm of a lower intensity that represents the formation of all three types of complexes: [Fe(**P2**)H]²⁺, [Fe(**P2**)₂H₂]⁺ and [Fe(**P2**)₃].

The similarities between the UV-Vis spectra of the 1 : 3 (metal : ligand) stoichiometry, **P1**- and **P2**-peptide complexes (Fig. 3A) and that of **DFP** (Fig. 1A) suggest that only **MIM** residues are involved in the coordination of the iron, whereas carboxylic groups are not part of the metal coordination core. Indeed, the DFT optimized complexes in solution show that carboxylic acid groups are not involved in the coordination of the iron, and that the metal ions are bound by the oxygen atoms of **MIM** residues (Fig. 4). For each one-mimosine peptide, we optimized the most likely 1 : 1 metal–ligand geometry and calculated its binding energy (Table 2); even though in Table 2 we also reported the binding energies of 1 : 1, 1 : 2 and 1 : 3 metal–**DFP** complexes, it is important to bear in mind that a direct comparison of the stability of these compounds with mimosine-containing peptides is not reliable. Indeed, it is not correct to compare the stability of bidentate ligands (DPF complexes) with those of hexadentate ligands (**MIM**-peptides) because of different entropic contributions related to their respective chelate effects.

A comparison of the free energies of the 1 : 1 complexes (Table 2) shows that Peptide 3 (**P3**) forms the most stable complexes with either copper and iron when compared with Peptide 1 and Peptide 2.

The reason for this higher stability could be due to the intra-molecular H-bonds that are formed between the coordinating water molecules and backbone carbonyl and carboxylate residues of **P3** (Fig. 4F and G); these interactions are supposed to stabilize the overall system when compared with **P1** and **P2**, although a thorough conformational analysis of all peptides is beyond the scope of the present work.

Likewise, the 1 : 1 Fe(III)–**P2** complex is more stable (ΔG_{aq} = −76.4 kcal mol⁻¹) than the complex formed with **P1** (ΔG_{aq} = −65.4 kcal mol⁻¹), whereas the 1 : 1 Cu(II)–**P2** and Cu(II)–**P1** complexes have similar stability. Again, in the case of the Fe(II)–**P2** complex (Fig. 4C), intra-molecular hydrogen bonds are
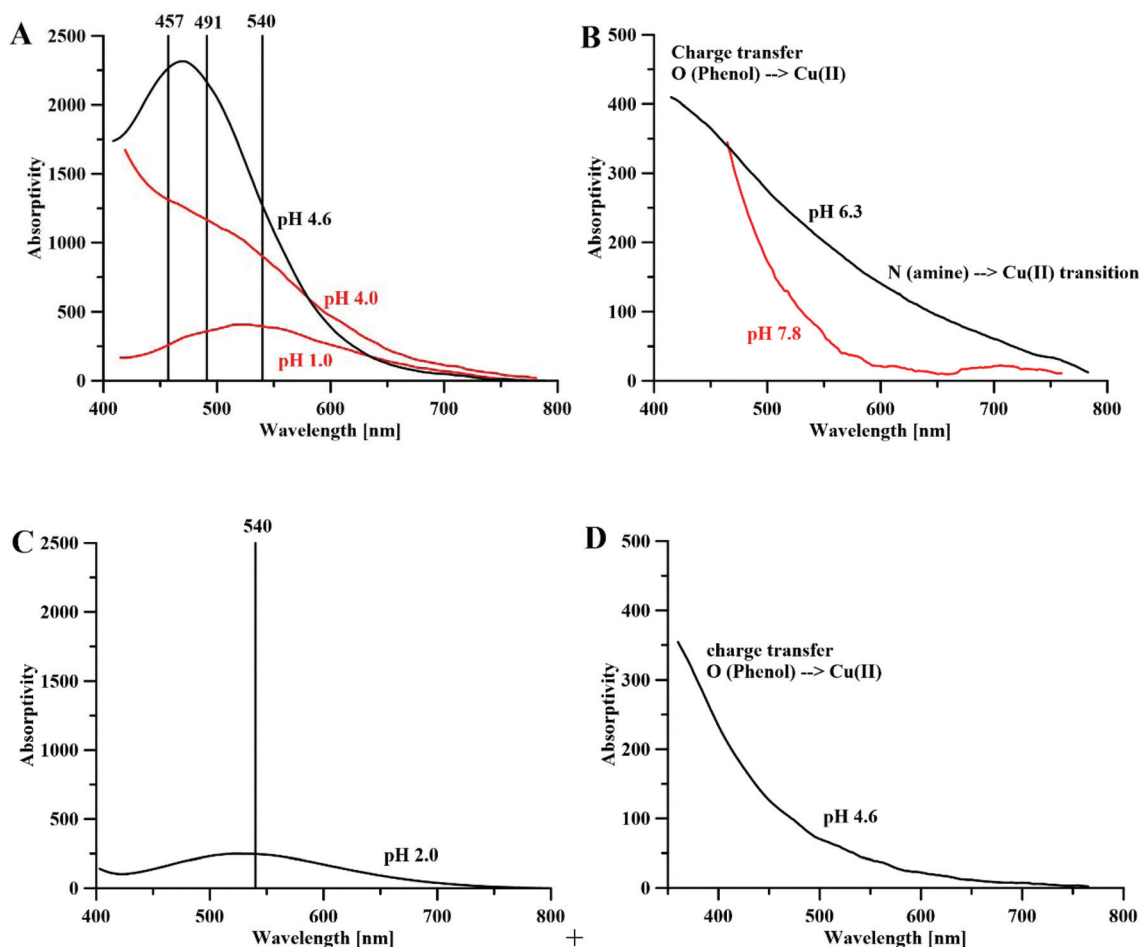
Fig. 3 Absorptivity spectra of (A) Fe^{3+}–**P1** (red) and Fe^{3+}–**P2** complexes (black), metal : ligand molar ratios 1 : 1 and 1 : 3 (for **P1**) and the ratio 1 : 3 (for **P2**), [**P1**] = [**P2**] 10 mM, l = 0.13 cm; (B) the Cu^{2+}–**P1** (red) and Cu^{2+}–**P2** (black) complexes, the metal : ligand molar ratio 1 : 2, [**P1**]=[**P2**] = 10 mM, l = 0.13 cm. (C) Fe^{3+}–**P4** complexes, the metal : peptide molar ratio 1 : 1, [**P4**] = 30 mM, l = 0.13 cm and (D) Cu^{2+}–**P4** complexes, the metal : peptide molar ratio 1 : 1, and [**P4**] = 30 mM and l = 0.13 cm.

additional forces that concur in the higher stabilization of the system.

For the same reasons outlined above, the 1 : 1 Fe(III)–**P3** and Cu(II)–**P3** complexes are remarkably more stable than the respective 1 : 1 metal–**DFP** complexes (Table 2).

The Vis spectra of the Cu^{2+}–**P1** complexes are shown in Fig. 3B. At a slightly basic pH, only the high intensity charge transfer O(phenol) → Cu^{2+} band appears to occur, which suggests the formation of a $[Cu(\text{P1})_2H_2]^{2+}$ complex. The absence of the bands in the 600–800 nm range implies that neither the amine group (N-end and C-end of the peptide) in the metal coordination shell nor the free metal ion in the solution is present. The ESI-MS spectra (in 50/50 H_2O/MeCN solution; Fig. S10†) showed the presence of the $[Cu(\text{P1})H_{-1}]^+$ ($[C_{26}H_{34}CuN_6O_8]^+$) complex (Fig. S10a†).

The **P2** complexes with copper(II) ions, at pH 6.3, are different from those of **P1** (Fig. 3B). Next to the band of charge transfer O(Phenol) → Cu^{2+}, we notice the presence of the d–d transition band (~650 nm) N(amine) → Cu^{2+} transition, which confirms the implication of the nitrogen atoms in the metal

coordination shell. The high intensity of the absorptivity spectrum (in agreement with the literature Cu(II)–mimosine complex data[59] in Table 1) suggests the formation of the dinuclear complex $[Cu_2(\text{P2})_2]$ (Fig. 4E), where each copper(II) ion is coordinated by the mimosine (CO, O^-) and aspartic acid (NH_2, COO^-) residues.

The copper(II) 1 : 1 stoichiometry complexes of **P1**, **P2** and **P3**, characterized by DFT calculations (Fig. 4A–D, F and G), confirm that the Cu(II) ion is coordinated by the pair of hydroxyl and carbonyl atoms of the **MIM** residue and three water molecules.

Considering the stability of the $Cu_2(\text{P2})_2$ complex, it is evident that unlike the dinuclear copper(II)–**MIM** complex where Cu(II) ions appear penta-coordinated, in the $Cu_2(\text{P2})_2$ system the two Cu(II) ions are tetra-coordinated by interacting with the **MIM** moiety of one peptide and the terminal carboxylic and amino groups of the other peptide (Fig. 4E). However, the interaction of Asp1 amino acid through its side chain carboxylic group and terminal amine slightly distorts the planarity between the metal ligands (Table S10†).
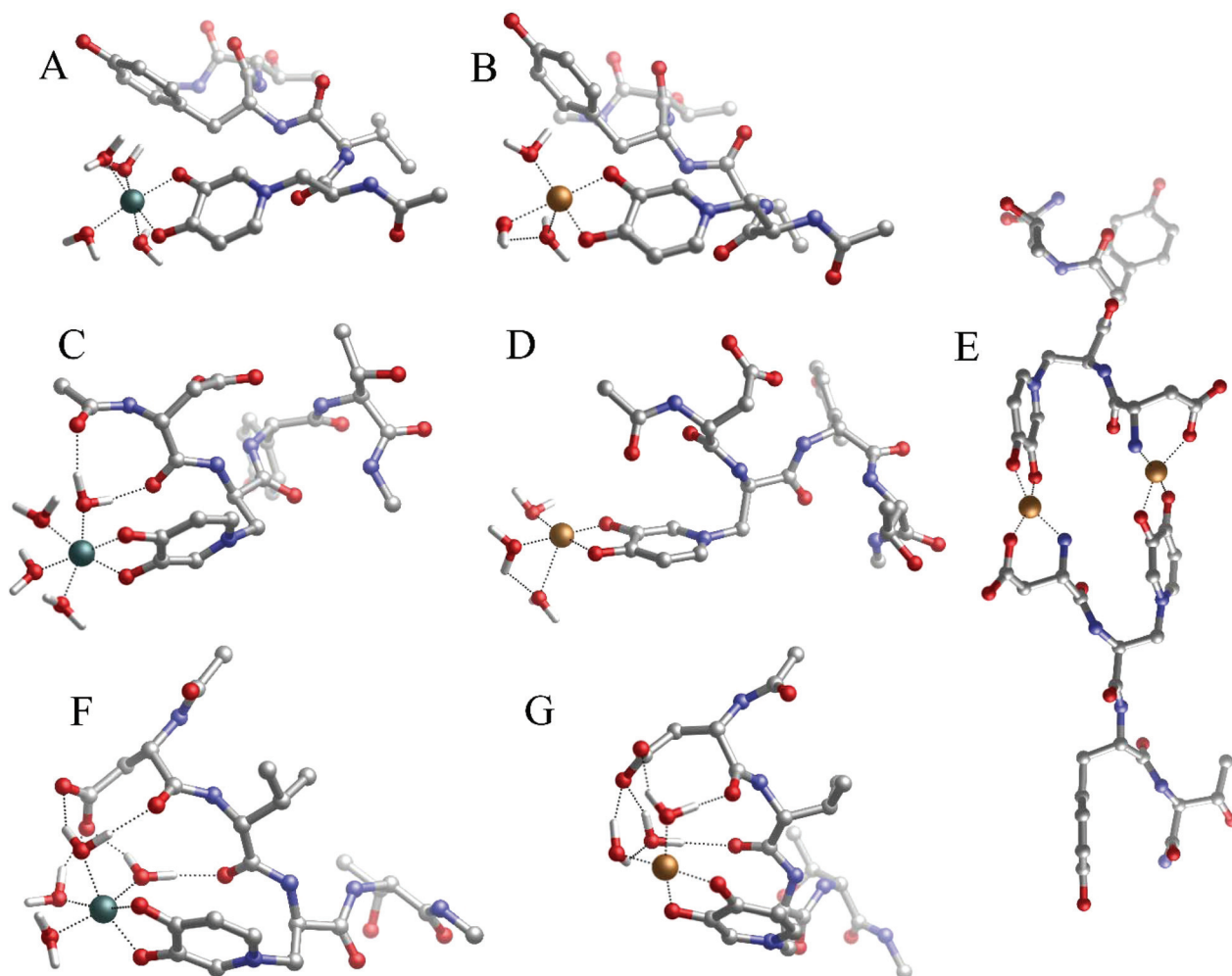
Fig. 4 Geometries of (A) Fe(**P1**), (B) Cu(**P1**), (C) Fe(**P2**), (D) Cu(**P2**), (E) Cu$_2$(**P2**)$_2$, (F) Fe(**P3**) and (G) Cu(**P3**) complexes optimized with DFT in solution.

Nevertheless, the metal coordination shell of the **P2** dinuclear complex is similar to that of the 2 : 2 copper(II)–**MIM** complex, with the Cu(II)–ligand binding site distances and angles being nearly the same (Table S10†). The stabilities of such complexes were computed according to eqn (3).

Cu(II) is tetra-coordinated both in solution and within the complex. The computed free energy value of the tetra-coordinated Cu$_2$(**P2**)$_2$ (−178.2 kcal mol^{-1}) complex is considerably more stable than the penta-coordinated Cu$_2$(**MIM**)$_2$ (−163.1 kcal mol^{-1}) one.

3.1.3.   Two-mimosine peptides: Peptide 4 (H-Mim-Gly-Mim-Gly-OH) and Peptide 5 (H-Mim-Gly-Pro-Gly-Mim-Gly-OH).
Peptide 4 has two **MIM** residues, spaced with glycine residues. The [LH$_4$]$^+$ ligand has four dissociating groups: amine (N-end), carboxylic (C-end) and two hydroxyl groups of **MIM** residues. Contrary to peptides **P1** and **P2**, peptide 4 contains two **MIM** residues, and, for this reason, the UV-Vis studies of iron(III) and copper(II) complexes are performed in solutions with a 1 : 1 metal-to-peptide molar ratio. Fig. 3C presents the

Table 2 Binding enthalpies (ΔH_{aq}) and free energies (ΔG_{aq}) in solution (in kcal mol^{-1}), computed according to eqn (2) on the DFT complexes formed by the six peptides given in Table 1, and by Fe(III) or Cu(II). For the sake of comparison, the energies of the copper(II) and iron(III) complexes in different molar ratios are also shown

Ligand name	Metal : ligand stoichiometry	Fe(III)		Cu(II)	
		ΔH_{aq}	ΔG_{aq}	ΔH_{aq}	ΔG_{aq}
DFP	1 : 3	−159.7	−165.3	—	—
DFP	1 : 2	−124.6	−131.2	−92.5	−97.6
DFP	1 : 1	−78.3	−81.5	−53.5	−56.1
Pept1	1 : 1	−70.2	−65.4	−51.8	−53.9
Pept2	1 : 1	−79.2	−76.4	−47.7	−50.9
Pept2	2 : 2			−159.7	−178.2
Pept3	1 : 1	−100.2	−91.4	−76.3	−69.5
Pept4	1 : 1	−109.7	−123.0	−74.3	−79.9
Pept4	2 : 2			−170.8	−187.0
Pept5	1 : 1	−106.7	−119.1	−65.3	−73.9
Pept5	2 : 2			−197.1	−205.9
Pept6	1 : 1	−121.9	−152.9	−60.9	−88.2

absorptivity spectrum of the iron(III) ions with the **P4** peptide, at pH 2.0. The single band with the maximum absorptivity at 540 nm suggests the formation of a monomeric $[Fe(P4)H_3]^{3+}$ species, positively charged due to its iron ion and amine group, whereas the second hydroxyl group and the carboxylic groups remain protonated at this low pH. It is unlikely that a dimeric complex is formed at such very low pH.

DFT calculations in water show the formation of a monomeric species Fe(III)/**P4** (Fig. 5A), where **MIM** residues are close enough to form a cyclic complex, and where two **MIM** and two water molecules form a complex exhibiting octahedral geometry (Table S11† and Fig. 5A).

Fig. 3D shows the absorptivity spectrum of the Cu(II)–**P4** system, in which only the band of charge transfer O(Phenol) → Cu^{2+} is present. This implies the existence of a coordination of the copper(II) by 2 (CO, O–) pairs of oxygen atoms of two **MIM** residues (Fig. 5B). The spacer between the two **MIM** residues is too short to allow both **MIM** residues participate in the coordination of the copper ion (Fig. 5B) and, due to the steric encumbrance, it is more likely that a dinuclear complex $[Cu_2(P4)_2]$ (Fig. 5C) is formed, instead of a monomeric species [Cu(**P4**)]. The formation of a dimeric complex, in which each metal ion is coordinated by two **MIM** residues (Fig. 5C), is consistent with the absorptivity spectrum of the Cu(II)/**P4** system obtained in our study (Fig. 3D).

Peptide 5 contains two **MIM** residues spaced by three amino acid residues. It has the same dissociating groups as peptide 4, and is considered to be a $[LH_4]^+$ ligand, but it is longer than **P4** due to the presence of additional glycine and

proline residue. The proline residue was introduced in the middle of the peptide's backbone to support turn formation upon metal complexation.[1]

DFT calculations highlight that the 1 : 1 iron to **P5** complex has two **MIM** residues and two water molecules in the metal-coordination core (Fig. 5D). The Fe(III) coordination shells are very similar, with both **P4** and **P5** systems satisfying the optimal octahedral coordination mode of iron (geometric data are given in Table S11†). Therefore the slightly lower stability of Fe(III)–**P5** compared to the Fe(III)–**P4** complex (Table 2) could be due to the rigidity of the peptide backbone that contains the proline residue; however, we reiterate that a careful conformational analysis (beyond the scope of this work) is pivotal in order to examine this point.

According to DFT calculations, **P5** can form a monomeric Cu(II)–**P5** complex in which two **MIM** residues and two water molecules coordinate copper ions in the distorted octahedral complex (Fig. 5E). Also in this case, the stability of the monomeric Cu(II)–**P5** complex is lower than that of the monomeric Cu(II)–**P4** system (Table 2) and, analogously to **P4**, it is highly possible that copper dimeric species (Fig. 5F) are formed. Finally, a comparison of the stabilities of the **P5** and **P4** dimeric complexes with the copper(II) ion reveals that the former is remarkably more stable than the latter.

3.1.4. Three mimosine peptide: Peptide 6 (H-Mim-Gly-Pro-Gly-Mim-Gly-Gly-Mim-OH). Peptide 6 has three mimosine residues spaced by glycine and one proline. It is a $[LH_5]^+$ ligand with three dissociating hydroxyl groups of **MIM** residues, one amine group at the N-end, and one carboxylic group at the C-end of the peptide.

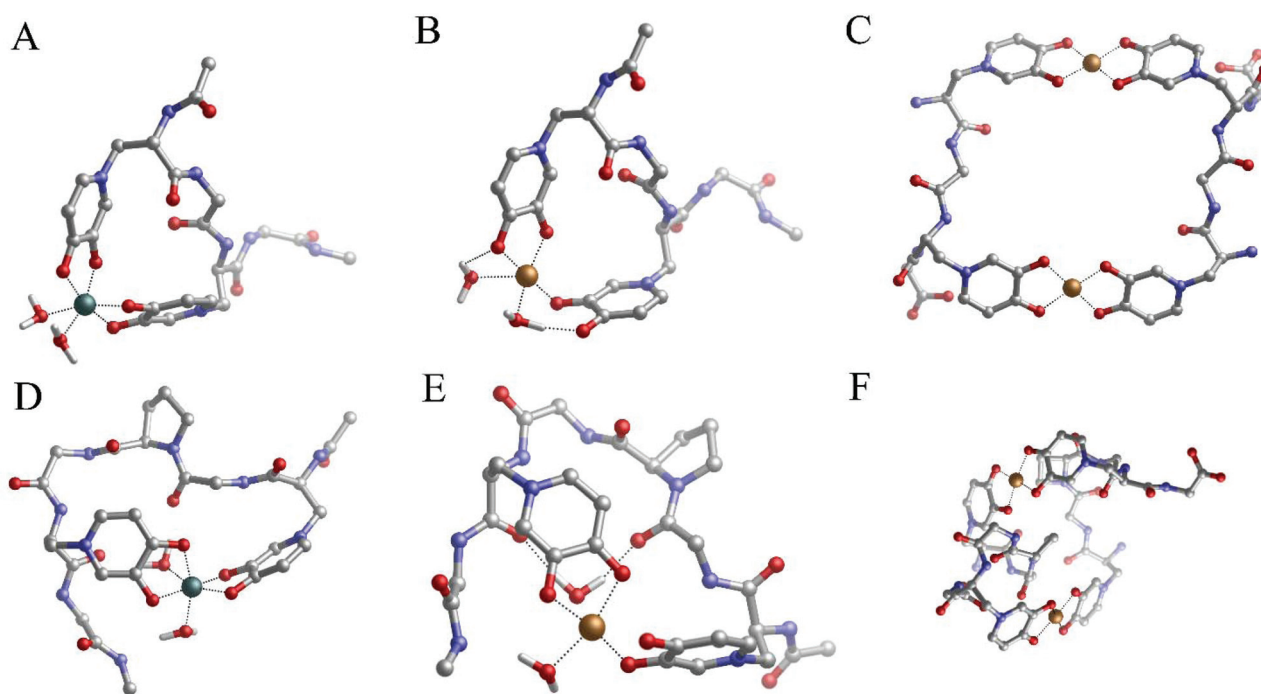**Fig. 5** Geometries of (A) the Fe(III)/**P4** 1 : 1 complex, (B) the Cu(II)–**P4** 1 : 1 complex, (C) the Cu(II)–**P4** 2 : 2 complex, (D) the Fe(III)–**P5** 1 : 1 complex, (E) the Cu(II)–**P5** 1 : 1 complex and (F) the Cu(II)–**P5** 2 : 2 complex optimized with DFT in solution.
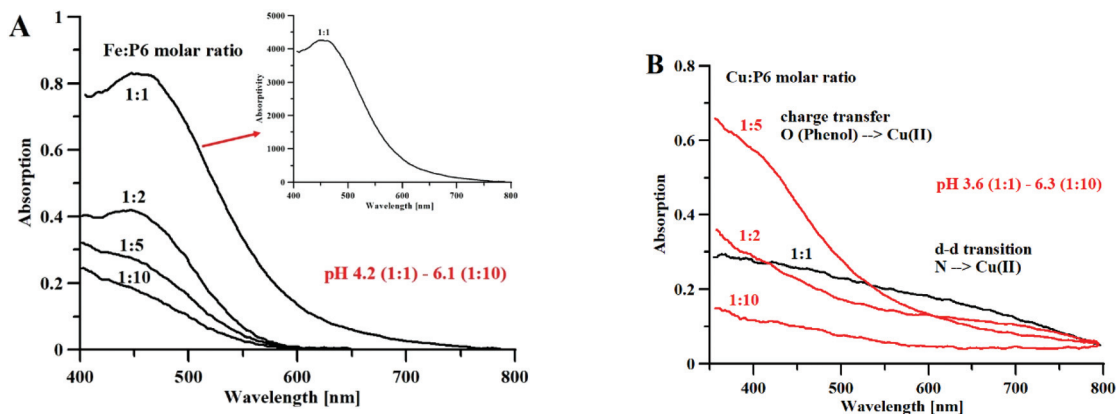
Fig. 6 (A) Absorption and absorptivity spectra of Fe^{3+}–**P6** complexes, [**P6**] = 1.5 mM, l = 0.13 cm (B) Absorption spectra of Cu^{2+}–**P6** complexes, [**P6**] = 3.5 mM, l = 1.0 cm.

Fig. 6A shows the Vis spectra of the iron(III)–**P6** system titration with the growing quantity of iron ions. We can clearly see that the spectrum reaches its highest absorptivity for a 1 : 1 metal to peptide molar ratio, which is equivalent to the maximum absorptivity of the Fe(**DFP**)$_3$ complex (Fig. 1A). Based on this result, we can hypothesize the formation of a monomeric Fe(**P6**) complex, where the metal ion is coordinated by six oxygen atoms of three mimosine residues (Fig. 7A).

Fig. 6B shows the results of an analog experiment with copper(II) ions. At a high metal-to-ligand molar ratio (1 : 10), and a pH of 6.3, only the band of charge transfer O(Phenol) → Cu^{2+} can be observed. In the solutions of 1 : 5 and 1 : 2 metal to ligand molar ratios, the band of charge transfer is predominant (over the band of the N(amine) → Cu^{2+} d–d transition). In the solution containing equimolar concentrations of metal and peptide, at pH 3.6, the intensity of the charge transfer band is almost equal to the band of the d–d transition, which makes it likely that mixed coordination complexes are formed.

The 1 : 1 complexes formed by peptide 6 and Fe(III) or Cu(II) were characterized by DFT methods and their binding energies computed, according to eqn (2). For both complexes, the optimized structures are shown in Fig. 7A and B respectively, and their computed binding energies in solution are presented in Table 2.

The spacers between the mimosine residues are long enough to involve three mimosine residues in the metal-coordination process. In fact, the angles computed on the metal coordination shell of Fe(**P6**) are very similar to the ones computed on Fe(**DFP**)$_3$ (see Table S11†), indicating that the peptide is long enough to allow the three mimosine side chain to arrange in a near-optimum disposition. Interestingly, the free energy (Table 2) of the Fe(III)–**P6** complex (−152.9 kcal mol^{-1}) is less negative compared to that of the 1 : 3 Fe(III)–**DFP** (−165.3 kcal mol^{-1}) and very similar to that of the 1 : 3 Fe(III)–**MIM** complex (−151.8 kcal mol^{-1}, Table S2†). Such a situation indicates that, in the case of **P6**, the entropic contribution related to the chelate effect is not a major driving force in the stabilization of 1 : 1 Fe(III)–**P6**, as highlighted by the very
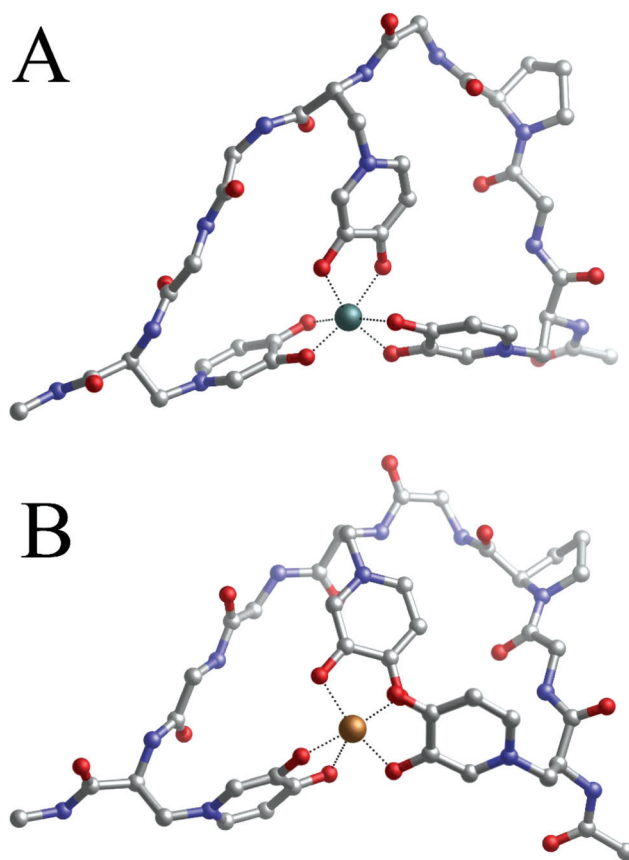
Fig. 7 Geometries of Fe(III)–**P6** (A) and the Cu(II) (B)–**P6** 1 : 1 complex optimized with DFT in solution.

similar free energy of the 1 : 3 Fe(III)–**MIM** complex. A possible explanation could be that the introduction of one proline residue turns the backbone of the peptide, but makes it more rigid and decreases its overall complex stability. Clearly, the addition of a proline residue is not a good strategy for the design of novel mimosine-containing chelating agents with

improved chelation performance. These findings are in agreement with the results obtained in our previous work involving proline-containing and proline-free mimosine peptides coordinating Al(III) ions.[42]

Regarding the Cu/**P6** monomeric complex, apparently the metal adopts octahedral coordination mode because the angles between the oxygen ligands are appropriate for this coordination mode (see Table S12†). However, one of the mimosine residues interacts only though one oxygen atom (Cu–O distances of 1.98 and 2.80 Å), and a second one is in the mono-/bidentate borderline (Cu–O distances of 1.97 and 2.41 Å). Even if two **MIM** residues are involved in the coordination of copper, the geometry of the complex is distorted, and two of the **MIM** residues are not in planar position, with respect to the central metal ion. It is evident that the length of the linker between the neighboring metal binding **MIM** residues is too short to allow the formation of a complex of octahedral geometry, similar to that of Cu(**DFP**)$_2$, where two ligand molecules are in planar and equatorial positions. It is more likely that stoichiometries different than 1 : 1 are formed with the co-participation of the amine group in the complex core, as it can be deduced from Vis spectra with the evident N(amine) → Cu^{2+} d–d transition band (Fig. 6B).

Theoretical TDDFT spectra of metal complexes with **DFP** and all studied peptides confirmed our analysis of the UV/Vis experimental spectra and showed good agreement with the experiments. For a complete analysis of the theoretical spectra, we refer to the ESI (Fig. S11–S15†).

3.1.5. Improving the metal binding affinity: the role of the methyl group. Looking at Scheme 1, a clear difference between the **DFP** and **MIM** ligands indicates the presence of a methyl group in the ring of the former, but not of the latter. In order to assess the effect of the CH$_3$ substituent towards the stability of the Fe(III) and Cu(II) complexes with deferiprone (**DFP**) and mimosine (**MIM**) ligands, we calculated DFT models of the complexes formed by Fe(III) and Cu(II) with **DFP**- and mimosine-based complexes, using our previously validated computational protocol.[52] We also compared the experimental stability constants from our study with those reported in the literature (Table S2 and Fig. S8†). Finally, we characterized two model compounds, one with and one without the –CH$_3$ substituent placed in the ring, for both **DFP** and **MIM** ligands, providing a total of four different ligands (**DFP**, **DFP-unmet**, **MIM**, and **MIM-unmet**; Scheme 1). It is worth noting that the methyl group is an electron-donating (ED) substituent through inductive effect that is expected to increase the ligand's affinity towards trivalent metals, due to a slight increase in the (minor) covalent character of the metal–ligand dative interactions.[52]

As seen in Fig. S8,† the binding energies computed in solution (ΔG_{comp}, see Table S2†) are in very good agreement with the available $\log \beta$ values with a correlation coefficient of 0.9873, confirming the suitability of our methodology for the characterization of the complexes investigated in this study. Interestingly, the **DFP** ligand interacts more tightly with the two metals than it does with the **MIM** residue; with Fe(III) and

the 1 : 1, 1 : 2 and 1 : 3 complexes containing **DFP** being, respectively, 9.2, 15.4 and 15.6 kcal mol^{-1} more stable than the **MIM**-containing ligands. In the case of Cu(II), the 1 : 1 and 1 : 2 ligands that contain **DFP** are, respectively, 6.1 and 13.2 kcal mol^{-1} more stable than their **MIM**-containing counterparts.

Considering both families of ligands (deferiprone-based and mimosine-based), the introduction of a methyl group significantly increases the stability of the formed complexes, especially the stability of the iron complexes (Table S2†). For Fe(III), for example, the Fe–**DFP** 1 : 1, 1 : 2 and 1 : 3 complexes are 4.3, 8.0 and 7.0 kcal mol^{-1} more stable than the corresponding Fe–**DFP-unmet** (Table S2†). Similarly, in the case of Cu(II), the presence of methyl in the Cu(II)–**DFP** complexes also leads to more stable complexes than the Cu(II)–**DFP-unmet** complexes (2.7 and 3.5 kcal mol^{-1} for the 1 : 1 and 1 : 2 complexes). However, the increase in stability, upon addition of the methyl group, is lower than that obtained with the Fe(III)–ligand complexes. Interestingly, a similar trend is also observed for the **MIM**-based ligands, for which the inclusion of the –CH$_3$ substituent stabilizes all complexes in a similar fashion. The addition of a methyl in position 2 in the mimosine ligand (**MIM-met**) stabilizes the Fe(III) 1 : 1, 1 : 2 and 1 : 3 complexes by 4.5, 7.5 and 4.9 kcal mol^{-1}, respectively; the Cu(II) 1 : 1 and 1 : 2 complexes are stabilized by 2.4 and 6.5 kcal mol^{-1}, respectively.

In general, we can conclude that the addition of a 2-methyl group is important for augmenting the affinity of **DFP** to the metal, but the introduction of the 3-methyl substituent in mimosine would lead to a lower increase in affinity. This is probably due to the positively charged amino group of the **MIM** residue, which acts as an electron-withdrawing group (EW), thus lowering the electron density from the coordination site of the ligands. As a result, the EW amino group (positively charged) partially compensates the ED effect of the methyl group. Nevertheless, the addition of this 2-methyl group could help in the improvement of the chelation performance of these compounds.

3.2. Antimicrobial activity

Antimicrobial peptides (AMPs) (also known as host defence peptides, HDPs) are part of the innate immune response, in all classes of life, produced to kill bacteria, viruses, fungi and even cancer cells.[62–65] Most AMPs have a positive charge (+2 to +9) and hydrophobic amino acids (more than 30%), while the length varies between 10 and 50 amino acid residues. The mechanism of AMP action against microbials is complicated and the same AMP may act on different targets.[63] One of the best known mechanisms is through membrane permeabilization, which consequently leads to a loss of cellular components and cell death.[64] The non-specific membrane interactions between AMPs and bacteria differ from those of antibiotics, and they target specific molecular receptors of pathogens and make it difficult for bacteria to acquire resistance to AMPs.[64]

Different approaches have been used to ameliorate AMP bactericidal activity with a short half-time and at the same

time reduce hemolytic activity, *e.g.* changes in the amino acids' sequence, cyclization, and synthesis of multivalent constructs. It was observed that the proline-rich peptides have a higher membrane internalization, while Gly-rich peptides are more selective for Gram-negative bacteria, fungi and cancer cells.[65,66] Also many short-chain pro-rich peptides showed a high activity against Gram-negative bacteria.[67] The long peptides with a high ratio of Pro and Gly amino acids usually exhibit linear, rather than secondary, structures.[68–70] AMPs have mostly a positive charge (from +2 to +9), which allows AMPs to interact with negatively charged lipid head groups.[71] The increase of the positively charged amino acids in the peptides' sequence increases the affinity for the microbial membrane and improves the overall antimicrobial activity. However, also anionic AMPs (containing Gln and Asp) participate in the eukaryotic innate immune system.[72] Their negative charge ranges from −1 to −2, and they generally need cations (*e.g.* Zn^{2+}) as cofactors for antibiotic activity.[73]

AMPs with high hydrophobicity can damage the membrane structure, which results in cell lysis or the formation of transient pores and the transport of peptides inside the cell; this property enables them to interact with intracellular targets.[74]

3.2.1. Antibacterial and antidermatophytic activity. Mimosine peptides are stable in solid state and in water solution for weeks. No experimental changes were observed in repeated NMR spectra nor in microbiological studies conducted over three months. The high stability could be associated with the non-protein mimosine amino acid, which is not recognized by the proteolytic enzymes.

The preliminary screening carried out on the six peptides by the disk diffusion method (Table S14†) reveals that the peptides tested at higher concentrations possess an antibacterial activity. In particular, **P5** (810 μg per disk equivalent to 81 mg mL^{-1}) exhibits an inhibitory effect against *S. aureus* and *B. cereus*, and **P3** (340 μg per disk) against *S. aureus*. The other four peptides tested with lower concentrations show no inhibition activity against the microbial strains used as indicators.

The physicochemical properties of the peptide, with respect to charge, amphipathic nature, hydrophobicity capacity, are key factors impacting on their mode of action and selectivity towards microbial cells.[75] The binding of the metal may induce changes to net charge and the conformational plasticity of the peptides that may favor the interaction with the bacterial cell wall and the phospholipid bilayer component of the membrane, resulting in the potentiation of antibacterial activity; however, additional experiments need to be performed to confirm such hypothesis.

In order to better investigate the antibacterial activity of the mimosine-derived peptides and their complexes, the MIC and MBC values were determined following the broth microdilution method. The results are reported in Tables S15 and S16.† The copper complexes with the peptides investigated in our study showed no antibacterial activity, whereas the iron(III) complexes with the **P4** and **P6** peptides gave a positive antibacterial response. The free **P4** shows an MIC of 7450 μg mL^{-1}, and the iron(III) complex of **P4** shows up to fifteen times lower

MIC values against *S. aureus* (484 μg mL^{-1}), *B. cereus* (484 μg mL^{-1}), and *E. coli* (967 μg mL^{-1}). A good inhibition activity was recorded against the strains *S. aureus* and *B. cereus* by the **P6** Fe complex, with MIC values of 448 μg mL^{-1}, which are much lower than the MIC activity of the free **P6** peptide (>6900 μg ml^{-1}).

The enhanced antagonistic activity of the iron complexes against *Bacillus* could be due to the siderophore mimicking property of the mimosine peptides, these being structurally similar to the siderophores produced by *Bacillus* strains (*e.g.* petrobactin), but more in-depth studies aimed at understanding the mechanism of action are needed for supporting this hypothesis. The siderophore mimicking property of mimosine peptides could be applied for diagnostic and theragnostic treatment of bacterial infections,[76] while mimosine is structurally similar to that of **DFP** and could form stable complexes with Gd(III)[77] and other lanthanide metals.[37]

Mimosine based peptides are structurally and functionally different from classical antibiotics and their MIC activity should be compared with AMPs rather than antibiotics. The MIC comparative studies of different AMPs made by Ebbensgaard *et al.*[5] showed that unstructured AMPs (Myxinidin-NH2, Pyrrhocoricin, Apidaecin IA, Metalnikowin I) are less effective than α-helical and β-sheet structured peptides and their MIC activity requires more than 256 μg mL^{-1} concentration. Such a value is comparable with the results reported for the Fe(III)–**P6** complexes.

Even if mimosine peptides require high doses to reach MIC activity, their month-long stability, both in the solid state and in solution, makes them good candidates for being an alternative to antibiotics (or mixed) therapies. Recent studies point out that the contemporary use of different antibiotic agents can reduce the dose of each drug in the combination. Such mixed therapies may lower the development of bacterial resistance *in vitro* (compared to monotherapy). AMPs/peptidomimetics are well suited for synergic combinations with conventional antibiotics,[64] while disrupting bacterial membranes and facilitating antibiotics to reach their cytosolic targets.[78]

3.2.2. Antibiofilm activity. Biofilm-associated-bacteria are responsible for up to 65% of infections in humans and at the same time are highly adaptively resistant to classical antibiotics. Biofilm forms on living tissues, medical devices, industrial or potable water system piping, or in the natural aquatic environment.[79] Almost 80% of human infections are caused by biofilms.[80–82] Biofilm infection can be classified into two groups, non-device and device associated infections.[83,84] About 60–70% of nosocomial infections are related to biomaterials or implants.[85] It is difficult to remove biofilm formation on medical devices, therefore necessitating the removal of the infected device or use of high doses of antibiotics,[86] which increases costs and further antibiotic resistance and cytotoxicity.[87] Therefore, the identification of new compounds (*e.g.* peptides) capable of inhibiting biofilm formation is required.

Natural and synthetic antimicrobial peptides have been shown to prevent biofilm formation, kill bacteria or disrupt

the biofilm structure.[88] AMPs prevent bacteria adhesion on surfaces[89] and damage mature biofilms by detachment or killing bacteria.[90] The exact mechanism of biofilm degradation is poorly understood, but the fast destruction of biofilm embedded cells[90] may indicate that they act by disrupting the membranes of the bacteria.

In this study the antibiofilm activity of the most effective inhibitor (peptide 6) and its Fe complex is evaluated. Three different strains of bacterial pathogens (*S. aureus*, *S. intermedius*, and *P. aeruginosa*), described in the literature as linked to biofilm-associated diseases in humans and animals,[91,92] are used to examine the antibiofilm activity of peptide 6 and its iron complex. A preliminary evaluation of **P6** against bacteria in Planktonic status shows (Table S17†) an antimicrobial activity (MIC > 1 mM L^{-1}; MBC > 1 mM L^{-1}), whereas **P6** in sessile form shows a slightly different behavior. Peptide 6 is found unable to completely inhibit the formation of biofilms, but a consistent reduction (up to 70%) related to the peptide's concentration is observed for *S. aureus* (from 1 to 0.5 mM peptide concentration range). The antibiofilm data show that the **P6** Biofilm–interaction is not iron-dependent (*P* > 0.05 between two conditions +Fe/−Fe), as seen in Fig. S7A,† suggesting that **P6** activity against biofilm formation is rather not related to siderophore mimicking. With respect to the other bacterial strains, *S. intermedius* and *P. aeruginosa*, the obtained values, at different peptide concentrations, with and without iron, are not significant; nevertheless, the addition of iron ions to the peptide solution slightly reduces the formation of a biofilm (Fig. S7B and C†). The antibiofilm results reported here are preliminary, and should be more thoroughly examined by the genic expression of biofilm-related genes, for example those involved in the bacteria quorum-sensing network.[92]

The anti-biofilm activity of AMPs can be enhanced by mixed therapy with antibiotics.[93–95] Combine use of AMPs with known antibiotics is useful since they can target different strains of bacteria with different metabolisms cells in low pH, hypoxic or low nutritious environments.[96]

4.   Conclusions

We have presented a series of mimosine-based peptides, which according to our experimental and theoretical data, are effective iron(III) and copper(II) chelators. These peptides bind Fe(III) more strongly than Cu(II), as non-peptidic complexes based on deferiprone. Quite interestingly, the binding energies of these peptide complexes can be modulated by a number of key structural factors, such as the number of mimosine residues in the peptide, and length and flexibility of the spacer between mimosine residues. In this sense, peptide 6, with three mimosine residues, forms the most stable complexes with both Fe(III) and Cu(II), followed by peptides 4 and 5, with two mimosine residues.

For each peptide, the basic metal : peptide stoichiometry was investigated. The formation of oligomeric and polymeric

structures depends on environmental factors (peptide and metal concentration, pH, ionic strength and temperature) and needs further investigation in diffusion NMR studies. The present results and the combination of theoretical and experimental methodologies can be helpful for the design of self-assembly between metal ions and mimosine peptides, which could lead to various medical and nanotechnological applications. In fact, we have also proved that Fe–mimosine complexes can display a significant antimicrobial activity, which highlights the potential interest of the compounds presented in this work.

Conflicts of interest

There are no conflicts to declare.

Acknowledgements

References

1 R. Zou, Q. Wang, J. Wu, J. Wu, C. Schmuck and H. Tian, *Chem. Soc. Rev.*, 2015, **44**, 5200–5219.
2 D. E. Przybyla and J. Chmielewski, *Biochemistry*, 2010, **49**, 4411–4419.
3 M. Panciera, M. Amorín and J. R. Granja, *Chem. – Eur. J.*, 2014, **20**, 10260–10265.
4 A. Ambrogelly, S. Palioura and D. Söll, *Nat. Chem. Biol.*, 2007, **3**, 29–35.
5 A. Ebbensgaard, H. Mordhorst, M. T. Overgaard, C. G. Nielsen, F. M. Aarestrup and E. B. Hansen, *PLoS One*, 2015, **10**, e0144611.
6 A. Lewies, L. H. Du Plessis and J. F. Wentzel, *Probiotics Antimicrob. Proteins*, 2019, **11**, 370–381.
7 K. Sabol, J. E. Patterson, J. S. Lewis, A. Owens, J. Cadena and J. H. Jorgensen, *Antimicrob. Agents Chemother.*, 2005, **49**, 1664–1665.
8 J. N. Steenbergen, J. Alder, G. M. Thorne and F. P. Tally, *J. Antimicrob. Chemother.*, 2005, **55**, 283–288.
9 S. Rotem and A. Mor, *Biochim. Biophys. Acta, Biomembr.*, 2009, **1788**, 1582–1592.
10 B. Findlay, G. G. Zhanel and F. Schweizer, *Antimicrob. Agents Chemother.*, 2010, **54**, 4049–4058.
11 N. Molchanova, P. Hansen and H. Franzyk, *Molecules*, 2017, **22**, 1430.
12 B. C. Q. Nguyen and S. Tawata, *Phytother. Res.*, 2016, **30**, 1230–1242.

13 S. Tawata, in *Pesticide and Alternatives*, ed. J.E Casida, Elsevier Science Publishers, Amsterdam, Netherlands, 1990, pp. 541–544.

14 J. W. Hylin, *Phytochemistry*, 1964, **3**, 161–164.

15 B. Tangendjaja, J. Hogan and R. Wills, *Aust. J. Agric. Res.*, 1983, **34**, 289–293.

16 R. Anitha, S. Jayavelu and K. Murugesan, *Phytother. Res.*, 2005, **19**, 992–993.

17 A. Zalatnai and J. Bocsi, *Anticancer Res.*, 2003, **23**, 4007–4009.

18 S. Frydas, N. Papaioannou, M. Papazahariadou, M. Hatzistilianou, E. Karagouni, M. Trakatelli, G. Brellou, C. Petrarca, M. Castellani and P. Conti, *Int. J. Immunopathol. Pharmacol.*, 2005, **18**, 85–93.

19 C. Baltazar, R. Mun, H. Tajmir-Riahi and J. Bariyanga, *J. Mol. Struct.*, 2018, **1161**, 273–278.

20 Y. Shan, Y. Ma, M. Wang and Y. Dong, *Curr. Med. Chem.*, 2012, **19**, 5885–5894.

21 Y. Dai, B. Gold, J. K. Vishwanatha and S. L. Rhode, *Virology*, 1994, **205**, 210–216.

22 T. Xuan, A. Elzaawely, F. Deba, M. Fukuta and S. Tawata, *Agron. Sustainable Dev.*, 2006, **26**, 89–97.

23 R. Williams and R. Hoagland, *Allelopathy J.*, 2007, **19**, 423–430.

24 M. Lalande, *Exp. Cell Res.*, 1990, **186**, 332–339.

25 A. Restivo, L. Brard, C. Granai and N. Swamy, *J. Clin. Oncol.*, 2005, **23**, 3200–3200.

26 K. Ward and R. N. Harris, *Aust. J. Biol. Sci.*, 1976, **29**, 189–196.

27 J. Savulescu, *Br. Med. J.*, 2004, **328**, 358.

28 FDA NEWS RELEASE: FDA Approves Ferripox (deferiprone) to Treat Patients with Excess Iron in the Body, Oct. 14, 2011, http://www.fda.gov/NewsEvents/Newsroom/PressAnnouncements/ucm275814.htm.

29 R. Ma, J. J. Reibenspies and A. E. Martell, *Inorg. Chim. Acta*, 1994, **223**, 21–29.

30 R. J. Motekaitis and A. E. Martell, *Inorg. Chim. Acta*, 1991, **183**, 71–80.

31 E. T. Clarke and A. E. Martell, *Inorg. Chim. Acta*, 1992, **191**, 57–63.

32 V. M. Nurchi, G. Crisponi, T. Pivetta, M. Donatoni and M. Remelli, *J. Inorg. Biochem.*, 2008, **102**, 684–692.

33 J. Lachowicz, V. Nurchi, G. Crisponi, M. Jaraquemada-Pelaez, M. Arca, A. Pintus, M. Santos, C. Quintanova, L. Gano and Z. Szewczuk, *Dalton Trans.*, 2016, **45**, 6517–6528.

34 E. T. Clarke, A. E. Martell and J. Reibenspies, *Inorg. Chim. Acta*, 1992, **196**, 177–183.

35 A. E. Gorden, J. Xu, K. N. Raymond and P. Durbin, *Chem. Rev.*, 2003, **103**, 4207–4282.

36 D. M. Doble, M. Melchior, B. O'Sullivan, C. Siering, J. Xu, V. C. Pierre and K. N. Raymond, *Inorg. Chem.*, 2003, **42**, 4930–4937.

37 K. H. Thompson, C. A. Barta and C. Orvig, *Chem. Soc. Rev.*, 2006, **35**, 545–556.

38 E. Chruscinska, E. Garribba, G. Micera and A. Panzanelli, *J. Inorg. Biochem.*, 1999, **75**, 225–232.

39 R. C. Scarrow, P. E. Riley, K. Abu-Dari, D. L. White and K. N. Raymond, *Inorg. Chem.*, 1985, **24**, 954–967.

40 A. Upadhyay, J. Chompoo, N. Taira, M. Fukuta, S. Gima and S. Tawata, *J. Agric. Food Chem.*, 2011, **59**, 12858–12863.

41 B. C. Q. Nguyen and S. Tawata, *Molecules*, 2015, **20**, 14334–14347.

42 J. Mujika, G. Dalla Torre, J. Lachowicz and X. Lopez, *RSC Adv.*, 2019, **9**, 7688–7697.

43 W. C. Chan and P. D. White, *Fmoc solid phase peptide synthesis*, Oxford University Press, 2000.

44 F. Delaglio, S. Grzesiek, G. W. Vuister, G. Zhu, J. Pfeifer and A. Bax, *J. Biomol. NMR*, 1995, **6**, 277–293.

45 T. Goddard and D. Kneller, *SPARKY 3.114*, University of California, San Francisco, USA, 2007.

46 K. Wüthrich, *Europhys. News*, 1986, **17**, 11–13.

47 A. D. Becke, *J. Chem. Phys.*, 1993, **98**, 5648–5652.

48 P. Stephens, F. Devlin, C. Chabalowski and M. J. Frisch, *J. Phys. Chem.*, 1994, **98**, 11623–11627.

49 S. Grimme, J. Antony, S. Ehrlich and H. Krieg, *J. Chem. Phys.*, 2010, **132**, 154104.

50 J. Tomasi, B. Mennucci and R. Cammi, *Chem. Rev.*, 2005, **105**, 2999–3094.

51 M. Frisch, G. Trucks, H. Schlegel, G. Scuseria, M. Robb, J. Cheeseman, G. Scalmani, V. Barone, G. Petersson and H. Nakatsuji, *Gaussian 16, Revision A*, 2016, vol. 3.

52 G. Dalla Torre, J. I. Mujika, E. Formoso, E. Matito, M. J. Ramos and X. Lopez, *Dalton Trans.*, 2018, **47**, 9592–9607.

53 J. Alí-Torres, L. Rodríguez-Santiago and M. Sodupe, *Phys. Chem. Chem. Phys.*, 2011, **13**, 7852–7861.

54 B. Gandhi, R. Summerbell and T. Mazzulli, *J. Clin. Microbiol.*, 2018, **56**, e01481–e01417.

55 G. Orru, C. Demontis, A. Mameli, E. Tuveri, P. Coni, G. Pichiri, F. Coghe, A. Rosa, P. Rossi and G. D'Hallewin, *Front. Microbiol.*, 2017, **8**, 2067–2078.

56 W. Wang, S. Nema and D. Teagarden, *Int. J. Pharm.*, 2010, **390**, 89–99.

57 A. El-Jammal, P. L. Howell, M. A. Turner, N. Li and D. M. Templeton, *J. Med. Chem.*, 1994, **37**, 461–466.

58 W. C. Tsai and K. H. Ling, *J. Chin. Biochem. Soc.*, 1973, **2**, 70–86.

59 H. Stunzi, D. Perrin, T. Teitei and R. Harris, *Aust. J. Chem.*, 1979, **32**, 21–30.

60 R. P. Martin, L. Mosoni and B. Sarkar, *J. Biol. Chem.*, 1971, **246**, 5944–5951.

61 J. I. Lachowicz, M. Crespo-Alonso, F. Secci, C. Caltagirone, G. Alberti, R. Biesuz, J. O. Orton and V. M. Nurchi, *J. Trace Elem. Med. Biol.*, 2018, **50**, 580–588.

62 K. Reddy, R. Yedery and C. Aranha, *Int. J. Antimicrob. Agents*, 2004, **24**, 536–547.

63 K. A. Brogden, *Nat. Rev. Microbiol.*, 2005, **3**, 238–250.

64 J. Wang, X. Dou, J. Song, Y. Lyu, X. Zhu, L. Xu, W. Li and A. Shan, *Med. Res. Rev.*, 2019, **39**, 831–859.

65 E. de Souza Cândido, D. A. Sousa, J. C. Viana, N. G. de Oliveira-Júnior, V. Miranda and O. L. Franco, *Peptides*, 2014, **55**, 65–78.

66 N. Ilić, M. Novković, F. Guida, D. Xhindoli, M. Benincasa, A. Tossi and D. Juretić, *Biochim. Biophys. Acta, Biomembr.*, 2013, **1828**, 1004–1012.

67 W. Li, J. Tailhades, N. M. O'Brien-Simpson, F. Separovic, L. Otvos, M. A. Hossain and J. D. Wade, *Amino Acids*, 2014, **46**, 2287–2294.

68 E. Sikorska and E. Kamysz, *J. Pept. Sci.*, 2014, **20**, 952–957.

69 T. Niidome, H. Mihara, M. Oka, T. Hayashi, T. S. Kazutoshiyoshida and H. Aoyagi, *J. Pept. Res.*, 1998, **51**, 337–345.

70 E. J. Veldhuizen, V. A. Schneider, H. Agustiandari, A. Van Dijk, J. L. Tjeerdsma-van Bokhoven, F. J. Bikker and H. P. Haagsman, *PLoS One*, 2014, **9**, e95939.

71 X. Wang, J. C. B. Junior, B. Mishra, T. Lushnikova, R. M. Epand and G. Wang, *Biochim. Biophys. Acta, Biomembr.*, 2017, **1859**, 1350–1361.

72 N. B. Leite, L. C. Da Costa, D. dos Santos Alvares, M. P. dos Santos Cabrera, B. M. de Souza, M. S. Palma and J. R. Neto, *Amino Acids*, 2011, **40**, 91–100.

73 S. G. Dashper, N. M. O'Brien-Simpson, K. J. Cross, R. A. Paolini, B. Hoffmann, D. V. Catmull, M. Malkoski and E. C. Reynolds, *Antimicrob. Agents Chemother.*, 2005, **49**, 2322–2328.

74 A. Schmidtchen, M. Pasupuleti and M. Malmsten, *Adv. Colloid Interface Sci.*, 2014, **205**, 265–274.

75 N. Malanovic and K. Lohner, *Pharmaceuticals*, 2016, **9**, 59–92.

76 H. Kornreich-Leshem, C. Ziv, E. Gumienna-Kontecka, R. Arad-Yellin, Y. Chen, M. Elhabiri, A.-M. Albrecht-Gary, Y. Hadar and A. Shanzer, *J. Am. Chem. Soc.*, 2005, **127**, 1137–1145.

77 M. Rogosnitzky and S. Branch, *BioMetals*, 2016, **29**, 365–376.

78 R. Domalaon, T. Idowu, G. G. Zhanel and F. Schweizer, *Clin. Microbiol. Rev.*, 2018, **31**, e00077–e00017.

79 R. M. Donlan, *Emerging Infect. Dis.*, 2002, **8**, 881–890.

80 J. W. Costerton, P. S. Stewart and E. P. Greenberg, *Science*, 1999, **284**, 1318–1322.

81 L. Hall-Stoodley, J. W. Costerton and P. Stoodley, *Nat. Rev. Microbiol.*, 2004, **2**, 95–108.

82 F. Reffuveille, C. de la Fuente-Núñez, S. Mansour and R. E. Hancock, *Antimicrob. Agents Chemother.*, 2014, **58**, 5363–5371.

83 N. Høiby, T. Bjarnsholt, C. Moser, G. Bassi, T. Coenye, G. Donelli, L. Hall-Stoodley, V. Hola, C. Imbert and K. Kirketerp-Møller, *Clin. Microbiol. Infect.*, 2015, **21**, S1–S25.

84 U. Römling, S. Kjelleberg, S. Normark, L. Nyman, B. E. Uhlin and B. Åkerlund, *J. Intern. Med.*, 2014, **276**, 98–110.

85 J. D. Bryers, *Biotechnol. Bioeng.*, 2008, **100**, 1–18.

86 J. C. Carmen, B. L. Roeder, J. L. Nelson, R. L. R. Ogilvie, R. A. Robison, G. B. Schaalje and W. G. Pitt, *Am. J. Infect. Control*, 2005, **33**, 78–82.

87 I. K. Paterson, A. Hoyle, G. Ochoa, C. Baker-Austin and N. G. Taylor, *Sci. Rep.*, 2016, **6**, 37853–37863.

88 M. Yasir, M. Willcox and D. Dutta, *Materials*, 2018, **11**, 2468–2483.

89 G. Batoni, G. Maisetta and S. Esin, *Biochim. Biophys. Acta, Biomembr.*, 2016, **1858**, 1044–1060.

90 L. A. Segev-Zarko, R. Saar-Dover, V. Brumfeld, M. L. Mangoni and Y. Shai, *Biochem. J.*, 2015, **468**, 259–270.

91 L. Montanaro, A. Poggi, L. Visai, S. Ravaioli, D. Campoccia, P. Speziale and C. R. Arciola, *Int. J. Artif. Organs*, 2011, **34**, 824–831.

92 M. Erriu, C. Blus, S. Szmukler-Moncler, S. Buogo, R. Levi, G. Barbato, D. Madonnaripa, G. Denotti, V. Piras and G. Orrù, *Ultrason. Sonochem.*, 2014, **21**, 15–22.

93 N. M. Mishra, Y. Briers, C. Lamberigts, H. Steenackers, S. Robijns, B. Landuyt, J. Vanderleyden, L. Schoofs, R. Lavigne and W. Luyten, *Org. Biomol. Chem.*, 2015, **13**, 7477–7486.

94 H. Rudilla, E. Fusté, Y. Cajal, F. Rabanal, T. Vinuesa and M. Viñas, *Molecules*, 2016, **21**, 1223–1235.

95 S. M. Ribeiro, C. de la Fuente-Núñez, B. Baquir, C. Faria-Junior, O. L. Franco and R. E. Hancock, *Antimicrob. Agents Chemother.*, 2015, **59**, 3906–3912.

96 L. Grassi, G. Maisetta, S. Esin and G. Batoni, *Front. Microbiol.*, 2017, **8**, 2409–2417.

Paper VI

A Review on Coordination Properties of Thiol Containing Chelating Agents Towards Mercury, Cadmium, and Lead

G. Bjorklund, G. Crisponi, V.M. Nurchi, R. Cappai, A. B. Djordjevic, J. Aaseth

A Review on Coordination Properties of Thiol-Containing Chelating Agents Towards Mercury, Cadmium, and Lead

Geir Bjørklund [1,*], Guido Crisponi [2], Valeria Marina Nurchi [3], Rosita Cappai [3], Aleksandra Buha Djordjevic [4] and Jan Aaseth [5,6,7,*]

[1]   Council for Nutritional and Environmental Medicine, N-8610 Mo i Rana, Norway
[2]   Cittadella Universitaria, University of Cagliari, 09042 Cagliari, Italy
[3]   Department of Life and Environmental Sciences, University of Cagliari, 09042 Cagliari, Italy
[4]   Department of Toxicology "Akademik Danilo Soldatović", Faculty of Pharmacy, University of Belgrade, 11000 Belgrade, Serbia
[5]   Research Department, Innlandet Hospital, N-2380 Brumunddal, Norway
[6]   Inland Norway University of Applied Sciences, N-2411 Elverum, Norway
[7]   IM Sechenov First Moscow State Medical University (Sechenov University), 119146 Moscow, Russia
[*]   Correspondence: bjorklund@conem.org (G.B.); jaol-aas@online.no (J.A.)

Abstract: The present article reviews the clinical use of thiol-based metal chelators in intoxications and overexposure with mercury (Hg), cadmium (Cd), and lead (Pb). Currently, very few commercially available pharmaceuticals can successfully reduce or prevent the toxicity of these metals. The metal chelator meso-2,3-dimercaptosuccinic acid (DMSA) is considerably less toxic than the classical agent British anti-Lewisite (BAL, 2,3-dimercaptopropanol) and is the recommended agent in poisonings with Pb and organic Hg. Its toxicity is also lower than that of DMPS (dimercaptopropane sulfonate), although DMPS is the recommended agent in acute poisonings with Hg salts. It is suggested that intracellular Cd deposits and cerebral deposits of inorganic Hg, to some extent, can be mobilized by a combination of antidotes, but clinical experience with such combinations are lacking. Alpha-lipoic acid (α-LA) has been suggested for toxic metal detoxification but is not considered a drug of choice in clinical practice. The molecular mechanisms and chemical equilibria of complex formation of the chelators with the metal ions Hg^{2+}, Cd^{2+}, and Pb^{2+} are reviewed since insight into these reactions can provide a basis for further development of therapeutics.

Keywords: BAL; DMPS; DMSA; metal chelator; metal ion

1. Introduction

The US Agency for Toxic Substances and Disease Registry assembles a list of the substances that can cause the most significant problems to human health for their toxicity and potential for human exposure. It should be noticed that this priority list is not a list of "the most toxic" substances, but rather a prioritization of substances based on a combination of their frequency, toxicity, and potential for human exposure. This list is regularly revised to take into account any new information on toxic substances [1].

On these bases, lead (Pb), mercury (Hg), and cadmium (Cd) are classified not only as the most relevant toxic metals, but also as the most relevant toxic substances in general. Furthermore, the World Health Organization (WHO) has also included these three toxic metals in the top 10 chemicals of major public health concern [2].

Therefore, in the present review, we will take into consideration the chelating agents that can be useful for the clinical treatment of Pb, Hg, and Cd intoxication. In particular, since the sulfhydryl (SH) groups of proteins furnish the vehicle for both the toxicity and detoxification of the majority of heavy metal ions, we will take into consideration chelating agents characterized by thiol groups. The review aims to delineate principles that can be used in the search for improved antidotal treatments of these three toxic metals. We will start by recalling the hard–soft properties of these metal ions [3] reported in Table 1.

Table 1. Classification of the toxic metals, and the coordinating groups, according to their hard, intermediate (borderline), and soft character. The implied metal ions and coordinating groups are marked in red.

Metal Ions			Coordinating Groups		
Hard	**Borderline**	**Soft**	**Hard**	**Borderline**	**Soft**
Li^+, Na^+, K^+, Be^{2+} Mg^{2+}, Ca^{2+}, Sr^{2+}, Mn^{2+}, Al^{3+}, Ga^{3+}, Cr^{3+}, Fe^{3+}, Sn^{4+}, $(CH_3)_2Sn^{2+}$, UO_2^{2+}, VO^{2+}	Fe^{2+}, Co^{2+}, Ni^{2+}, Cu^{2+}, Zn^{2+}, Pb^{2+}, Sn^{2+}, Sb^{3+}, Bi^{3+}	Cu^+, Ag^+, Au^+, Hg^+, Pd^{2+}, Cd^{2+}, Pt^{2+}, Hg^{2+}, CH_3Hg^+, Pt^{4+}	H_2O, OH^-, F^-, $RCOO^-$, Cl^-, RO^-, NH_3, RNH_2	$C_6H_5NH_2$	R_2S, RSH, RS^-

It can be observed that Cd^{2+} and Hg^{2+}, both belonging to group 12 in the periodic table of elements, are classified as soft metal ions, preferring the coordination by ligands characterized by soft groups such as R_2S, RSH, and RS [4]. On the other hand, Pb^{2+}, which belongs to group 14 in the periodic table, is classified as an intermediate metal ion, indicating that above all it will be coordinated by amino groups, even if the interaction with hard oxygen groups and soft thiol groups is observed in a number of complexes. Furthermore, different structural coordination modes characterize these metal ions, such as linear coordination for Hg with thiol groups, or tetrahedral for Cd, but these considerations will be further developed in the last sections of the present paper.

2. Exposure and Effects

Table 2 reports some exposure sources and target organs for Hg, Cd, and Pb, which will be discussed in the following lines.

Table 2. Some exposure sources and target organs for Hg, Cd, and Pb.

	Important Sources of Occupational Exposure	Routes of Exposure	Important Sources of Environmental Exposure	Routes of Exposure	Target Organs of Toxicity
Elemental mercury	Coal-burning, waste incineration, gold extraction, dental amalgam handling, fluorescent lamp manufacturing	Inhalation	Dental amalgam in teeth	Inhalation	Central and peripheral nervous system
Inorganic mercury salts	-	-	Use of skin lightening products and medicinal use of mercury salts	Gastrointestinal ingestion, transdermal	Kidneys
Methyl mercury	-	-	Food (fish, seafood)	Gastrointestinal ingestion	Central nervous system
Cadmium	Production of nickel-Cd batteries, Cd plating, Cd-containing paint production	Inhalation	Food (rice, potato, and wheat, offal, seafood) Tobacco smoke	Gastrointestinal ingestion Inhalation	Kidneys Skeleton
Lead	Mining, smelting, battery manufacturing, traditional printing technology	Inhalation	Food, drinking water, dust and soil (in children)	Gastrointestinal ingestion	Central nervous system, hematopoietic system, kidneys

2.1. Mercury

Environmental Hg exists in three chemical forms, viz. elemental Hg (metallic Hg^0 liquid), inorganic mercuric salts (e.g., Hg chloride, $HgCl_2$), and organic Hg compounds (e.g., methylmercury (MeHg, CH_3Hg) and ethylmercury (EtHg, C_2H_5Hg)) [5,6]. Humans are exposed to low chronic levels of mercurial compounds via various routes: Oral, inhalation, and dermal [7], to MeHg mainly through fish, Hg vapor from dental amalgams, and EtHg through vaccines [8].

Although organic Hg is regarded as the most frequent and toxic one, elemental Hg is more volatile and, hence, more dangerous than generally perceived. Elemental Hg^0 exists as liquid metal and can vaporize at room temperature due to high vapor pressure. For example, a worker who stays for about eight hours in a Hg-saturated place can inhale up to about 100 mg of Hg per day [9]. Major sources of elemental Hg emissions to the air are coal burning, metal smelting, crematoriums, waste incineration, and small-scale gold extraction [10]. Emitted Hg vapor is oxidized to ionic form (Hg^{2+}) in the air layers, which falls to the ground with rain, often far from the emission point. This makes Hg exposure a global concern. In the soil layers and sediments, Hg has a very long half-life [11,12]. Also, Hg occurs naturally as a result of volcanic activities, forest fire, water movement, etc. [13]. Other important sources of Hg exposure is the use of Hg in measuring instruments and as a disinfectant. Regulatory measures during the last decades have reduced the Hg emissions to the environment significantly [12]. However, still, some hot spots of Hg pollution exist. Mainly in developing countries, Hg poses a threat to the environment and health of nearby living residents. Hence, environmental and human Hg exposure assessments are needed in these regions [11].

The main sources of elemental Hg in humans are Hg released from dental amalgams batteries, and incineration of medical waste [14,15]. In the 1830s, dental amalgam was introduced in the Western World and has since then been subject to recurrent concerns and controversies [16]. Today, many countries, including the Scandinavian countries and Italy, have in principle ceased the use of dental amalgam. However, this filling material is still in widespread use, particularly in developing countries [14].

Elemental Hg is oxidized to divalent inorganic Hg in red blood cells and tissues [17]. However, some Hg vapor passes the blood–brain barrier and enters the brain. Elemental Hg, which is highly diffusible and lipid-soluble, is oxidized and accumulated in the human brain. Its half-life in the brain is several years to several decades [18]. Numerous toxic effects and conditions have been linked to Hg vapor exposure. It has been suggested that inhaled Hg vapor from amalgam fillings is a predisposing factor to Alzheimer's disease [19]. However, this hypothesis remains to be verified [20]. Research has also shown that Hg vapor passes the placenta and is taken up by the fetus. The inorganic Hg concentrations in the placenta and umbilical cord have been found to correlate with the mother's number of amalgam fillings [21,22]. Dental personnel who are occupationally exposed to Hg have a higher Hg body burden than unexposed individuals., Recently this was reviewed by Aaseth et al. [23] and Bjørklund et al. [24]. Also, dental personnel more often develop uncharacterized symptoms like fatigue, weakness, and anorexia than unexposed people [23]. A similar trend was shown for neurobehavioral effects, like idiopathic disturbances in cognitive skills, affective reactions, and motor functions [24].

In addition to dental personnel, occupational Hg exposure also occurs in the chloralkali industry (if Hg electrodes are used) and in the manufacture of fluorescent lamps and batteries. Adverse effects in the central nervous system of chloralkali workers may persist for ten years or more after high Hg vapor exposure has ceased. Mathiesen et al. [25] found that a group of 70 previously H-exposed chloralkali workers (time passed after the last exposure was on average 12.7 years) had decreased performance on a number of neuropsychological tests compared to an unexposed control group of 52 workers. Comparable results were shown in another study of high-level Hg vapor-exposed workers [26]. It has been demonstrated that adverse Hg effects in the peripheral nervous system are detectable even decades after cessation of exposure [27]. The major clinical feature of chronic elemental Hg poisoning is a triad of tremors, erethism, and gingivitis [28]. Long-term chronic Hg vapor exposure led to

mercurial erethism, characterized by excessive shyness and social phobia [29]. In the 19th century, mercuric nitrate was commonly used in felt hat production. At that time in England and the US, the syndrome of erethism was common among exposed hatters. More on historical perspectives of Hg poisoning is given by Brooks et al. and Buckell et al. [30,31]. Apart from the central nervous system toxicity, elemental Hg can affect the human immune system or cause toxic pulmonary, reproductive, or cardiovascular effects [15].

Inorganic Hg^{2+} is absorbed from the gastrointestinal tract after ingestion and also through the skin [32]. The highest inorganic Hg levels are found in kidneys. In the kidneys, inorganic Hg can give many effects, including proteinuria and polyuria. This can further progress into nephritic syndrome [33]. Chronic inorganic Hg poisoning can also cause acrodynia, which is considered a hypersensitivity reaction, characterized by profuse sweating and erythematous rashes of the palms and soles [32].

Of serious concern is Hg exposure via fish and seafood. Mercury bioaccumulates and biomagnifies in the food chain, after biomethylation to MeHg [11,13]. Usually, the MeHg levels increase with the age of the fish [34]. Methylmercury has caused major environmental disasters [35]; the most serious happened in Minamata Bay, in Japan. In the 1950s, the plastic plant belonging to the Chisso Corporation group emitted wastewater containing Hg into this sea bay [36,37]. Over time, this caused a massive Hg accumulation in the food chain. Minamata disease is a neurological syndrome encompassing symptoms of sensory disturbances, ataxia, dysarthria, constriction of the visual field, auditory disturbances, and tremor. Another poisoning incident happened 20 years later in Iraq when the sensory, motor and visual disturbance were developed after ingestion of bread contaminated with organomercury fungicide [38]. After ingestion and rapid absorption of MeHg in the gastrointestinal tract, it circulates in the blood bound to SH-containing amino acid residues and distributed to the central nervous system and other parts of the organism [39,40]. By the use of molecular mimicry, MeHg, bound to the SH group of cysteine, crosses the blood–brain barrier and arrives at glial cells and neurons, where it is slowly converted to inorganic Hg [41]. Epidemiological studies have shown that pregnant women who are exposed to large MeHg concentrations give birth to children with severe brain damage even without having any poisoning symptoms themselves [11,42]. Furthermore, MeHg has been implicated in many neurodegenerative diseases, and a possible role in autism spectrum disorder has been suggested [20,41,43].

According to the International Agency for Research on Cancer, MeHg compounds are possibly carcinogenic to humans (group 2B), while metallic Hg and inorganic Hg compounds are not considered carcinogenic to humans [44].

Mercury compounds exert toxic actions through various mechanisms. Research indicates that toxic effects of organic Hg in the nervous system may be caused or worsened by the oxidized form, Hg^{2+}, that binds to the thiol (-SH) groups and thereby alters protein structure and/or inhibits enzymatic functions [41]. Numerous studies have also suggested other mechanisms of Hg toxicity such as induction of oxidative stress, damage of Ca homeostasis, and changes in glutamate homeostasis [6].

2.2. Cadmium

Metallic Cd is, to a significant extent, a by-product of zinc (Zn) production and to some degree, also a by-product from copper (Cu) and Pb production [45]. Since 1990, the annual use of Cd is about 20,000 tons worldwide. Recycling accounts for ca. 18% of the production. A majority of Cd is used in nickel-Cd batteries. Also, Cd is used for corrosion protection of steel (cadmium plating), as a solder and weld metal in alloys, in polyvinyl chloride plastics, and as a pigment in paint colors, different types of paint, and glazes [46].

Numerous studies have reported health effects of Cd exposure in the general population, even in subjects without particular industrial exposure. The estimated Cd exposure in many areas, particularly industrial ones, is high enough to represent a human health threat [47–49]. Environmental Cd contamination is mainly a result of anthropogenic activities, but can also be of natural origin [50]. Due

to high rate soil-to-plant transfer, Cd enters and accumulates in the food chain [51]. In most parts of the world, food is the primary Cd source for non-smokers [47].

Foods rich in Cd include offal, seafood, cocoa powder, and wild mushrooms. However, due to the larger consumption, 80% of Cd in food comes from staples (rice, potato, and wheat) [52,53]. The average daily Cd intake from food is 8–25 µg [50,52]. Currently, the Food and Agriculture Organization (FAO) and World Health Organization (WHO) Joint Expert Committee on Food Additives and Contaminants consider 25 µg Cd per kg body weight/month as a tolerable intake level [54]. However, certain subpopulations can have a much higher Cd intake than the average population (vegetarians, populations that consume rice as a dominant energy source) [52]. Tobacco leaves accumulate Cd. Therefore, cigarette smoke is a significant Cd source in the general population [55]. Cadmium in drinking water typically only contributes a few percent of the total Cd intake [53]. In the air, Cd is present in trace amounts [56]. Therefore, exposure from air generally provides less than a few percent of the total Cd body burden. However, Cd-polluted water and air and even house dust may occur in areas close to some metal industries. Itai-itai disease is the documented case of a mass Cd poisoning in Toyama Prefecture, Japan. What became the world's first large Cd poisoning disaster started around 1912 and caused a crippling and very painful form of osteomalacia including severe kidney damage and multiple bone fractures [57] The disease got its name due to the pain moans.

After Cd uptake in the body, it is transported via the hepatic portal system to the liver, where Cd induces synthesis of metal-binding proteins, metallothioneins (MTs). Inhaled Cd induces MTs in the lungs, where CdMT complexes are formed directly. CdMTs are released from the liver, enterocytes, and lungs into the systematic circulation. Thus, Cd is transported primarily to the kidneys where it accumulates. A recent review by Satarug presents a detailed overview of Cd kinetics [51]. The half-life of renal Cd is 7–16 years [58] or longer [59]. However, the accumulation of Cd in the organism varies with age, gender, smoking status, and certain co-morbidities.

Long-term Cd exposure affects many organs. The kidneys have been considered the critical organ of Cd toxicity. Even low-level, long-term Cd exposure may induce various kidney dysfunctions [60]. Also, the liver is critical to Cd accumulation. In both sexes, both acute and chronic Cd exposure is linked to various liver-related diseases [60,61]. Recent epidemiological studies confirm the association between Cd exposure and increased risk of osteoporosis-related fractures [62], which originally was observed during the Itai-itai epidemic in Japan. Also, associations between Cd exposure and cardiovascular diseases [63], reproductive disorders in both sexes [64–66], thyroid disorders [67], gestational diabetes, and diabetes mellitus type 2 [68,69] have been shown. Also, Cd may produce hormesis phenomena [70]. IARC classifies Cd and Cd compounds as known human carcinogens [44], based on a causal relationship between exposure and lung cancer. New research has also shown positive associations between chronic Cd exposure and kidney and prostate cancers [71]. Studies have implied a possible role of Cd in pancreatic [72,73], bladder [74], prostate [75], and breast cancer [76].

The mechanisms of Cd toxicity are various and include binding to SH groups, oxidative stress induction [77,78], interactions with bioelements [79–82], mitochondrial toxicity [83], and altered microRNA expression [84].

2.3. Lead

For several decades, the use of Pb-containing gasoline was an environmental and human exposure source of organic Pb compounds [85,86]. Since the 1920s, Pb usually added as tetraethyl lead (TEL) to gasoline caused significant exposure via inhalation of car exhaust [87]. Since Pb is toxic, this gasoline was gradually phased out in most countries of the world. In the US, Pb in gasoline was banned from 1996, and in the EU, organolead was entirely phased out in 2000 [87]. The removal of Pb from gasoline is regarded as one of the major public health triumphs of the 20th century. Also, much work has been done to phase out Pb from various other products completely. To completely eliminate Pb from gasoline and water pipes took a long time but effectively reduced Pb pollution in the environment [86,88]. However, due to the persistence of Pb, it is still present in the environment. Although food generally

contains low Pb levels, most of the Pb exposure in many countries nowadays occurs through food and drinking water [86,89]. In Europe, the average exposure via diet is about 0.50 µg Pb/kg body weight/day [90]. Cereal products contribute most to dietary Pb exposure, while Pb in dust and soil can be important sources for children. Also, Pb in old paint dust and soil can be a source of increased Pb exposure for small children, due to their tendency for licking, chewing, and swallowing foreign bodies [91,92]. Residual paints that contain significant quantities of Pb is a problem in many countries of the world, especially for children [93].

Lead exposure mainly happens through the gastrointestinal and respiratory tract. Approximately 30%–40% of Pb from the respiratory tract is absorbed into the bloodstream while the gastrointestinal absorption depends mainly on age and nutritional status [86,94]. Hence, while adults absorb around 10%–15% of ingested Pb, this amount increases up to 50% in infants, young children, and pregnant woman [85,94,95]. Once absorbed, Pb is transported by the bloodstream mainly bound to erythrocytes and distributed to other tissues such as liver, kidneys, brain, lungs, spleen, teeth, and bones. More than 95% of Pb is deposited in skeletal bones while in children, this percentage is less resulting in more Pb in soft tissues [85,86]. Furthermore, Pb passes the placental barrier during pregnancy and can cause damage to the fetus. Concentrations of Pb found in the umbilical cord blood are 80%–100% of the maternal blood levels [96].

Toxic effects of Pb have been detected in virtually every body system. Children are generally more vulnerable to Pb toxicity than adults, especially for neurological Pb toxicity. The most deleterious effects of Pb are detected on erythropoiesis, kidney function, and the central nervous system [85,86,97]. Other toxic effects of Pb include hypertension and hearing impairment, infertility, abdominal pain ("lead colic"), and anorexia [97]. Recent research has linked the level of Pb in drinking water to increased risk of cardiovascular pathologies [98]. For children, Pb exposure may impair cognitive abilities, attention, mental development, and skeletal growth [99]. Also, disturbed blood formation and renal effects may occur in children at relatively low Pb exposure [100]. A lower threshold for children that provides complete safety against Pb poisoning has not been established. The International Agency for Cancer Research classified inorganic Pb as probably carcinogenic to humans (Group 2A) [101].

Many in vivo and in vitro studies have been performed to identify the exact mechanisms of Pb toxicity. Some of them are oxidative stress induction [77,102], binding to sulfur ligands that can affect many enzymes and proteins [77], interaction with bioelements [102], changes in DNA structure, and inhibition of DNA repair [103].

3. Endogenous Protective SH-Compounds: Metallothioneins and Glutathione

3.1. Metallothioneins (MTs)

The metallothionein (MT) family is cysteine-rich and consists of proteins with low molecular weight (mol. wt. ranging from about 1000 to 14,000 kDa). They are localized intracellularly and can bind both essential and non-essential heavy metals, e.g., Zn, Cu, Cd, Hg, silver (Ag), and As, through the thiol group of its cysteine residues. Approximately 30% of the amino acids in MTs are cysteine. MTs are found in yeasts, plants, invertebrates, as well as vertebrates including humans.

Margoshes and Vallee [104] discovered MT when they purified a Cd-binding protein from the renal cortex of horses. Still, the MTs functions are not entirely understood, but apparently, they protect against the effects of toxic metals as well as being involved in the physiological regulation of Cu and Zn. MTs also protect against oxidative stress [105]. In principle, four isoforms of MTs are present in humans (i.e., MT1 with subtypes, MT2, MT3, and MT4) [106]. All isoforms contain polynuclear metal-sulfur coordination sites. In mammals, MT1 and MT2 are the most common isoforms. In the liver and also in the gut, these MTs get induced by many different metals, especially by Zn ions. MT3 has been found in the central nervous system, and MT4 has been found in epithelial cells. MT3 appears to have a protective function against oxidative stress in the brain [107].

For the production of MT1 and MT2 in the liver, dietary Cu and Zn, as well as the amino acids cysteine and histidine, are needed. The content of the metals in MTs depends on their stability constants and their amount in the body. MTs can tie up many different metals, including Cd, Zn, Hg, and Cu.

Through their binding and release of Zn, MTs can regulate the cellular levels of Zn. According to their affinity constants with MTs, many toxic metal ions, including Hg^{2+}, Cu^+, Ag^+, Cd^{2+}, Bi^{2+}, and Pb^{2+}, might displace Zn^{2+} from MT. The free Zn, in turn, plays a key role for the binding and activation of transcription factors, especially the metal-regulatory transcription factor 1 (MTF-1), and Zn release induces more MT being synthesized.

Residues of cysteine from MTs may also capture oxidant radicals, including the harmful hydroxyl and superoxide radicals [108]. In such reactions, cysteine oxidizes to cystine, and the Zn ions that were cysteine bound are disconnected. Released Zn can activate the synthesis of further MTs. Various factors induce the gene expression of MTs, including metal exposure, oxidative stress, and glucocorticoids. The MT gene controls the response level of these inducers. MTs can also carry Zn ions between different parts of the cell. When Zn enters into a cell, thionein can take up the trace element and carry it to other cellular parts. This kind of signaling system is considered of particular importance in the brain, where Zn signaling appears crucial both within and between nerve cells [109].

3.2. Glutathione (GSH)

Glutathione (GSH), the tripeptide γ-glutamyl-cysteinyl-glycine, is a crucial antioxidant for animals, plants, as well as for some bacteria, in preventing damage on essential cellular components due to some metal ions and peroxides. GSH is the crucial intracellular reducing agent in animal cells. GSH is biosynthesized in the body from its amino acid constituents. Its cysteine thiol group (SH) functions as an electron donor in its interactions with metal ions or oxygen radicals. Cysteine is considered the rate-limiting factor in cellular GSH biosynthesis due to its relatively little presence in foods. The cellular biosynthesis of GSH involves two ATP-dependent steps: First, γ-glutamyl-cysteine is synthesized from L-glutamate and cysteine through the action of the enzyme gamma-glutamyl-cysteine synthetase. This initial step in the GSH synthesis is rate-limiting in the synthesis. In the second reaction, the enzyme glutathione synthetase adds glycine to the γ-glutamylcysteine. GSH exists in two different states, i.e., both as oxidized (GSSG) and reduced (GSH) states. In its reduced state, a reducing equivalent (H^++ e^-) can be donated by the SH group to unstable molecules such as reactive oxygen species. When an electron gets donated, a GSH molecule becomes reactive but reacts readily with another reactive molecule of GSH to create glutathione disulfide (GSSG). Oxidized GSSG is reduced rapidly back to GSH by glutathione reductase, in a reaction where NADPH is used as a donor of electrons [110].

Some important functions of GSH are as follows:

1. It is the principal endogenous antioxidant that the cells produce, it participates directly in the neutralization of ROS and free radicals, and it is a cofactor of the selenoenzyme glutathione peroxidase (GPx).
2. GSH is an important substrate for conjugation reactions, catalyzed by the glutathione-S-transferase enzyme. Thus, in the case of the reactive metabolite formed by a paracetamol overdose, GSH acts as an antidote. GSH can also conjugate and detoxify organometallic compounds, such as MeHg [111].
3. It has important roles in binding, transport, and storing of several metals, thus affecting the homeostasis of metals in biological systems [112].

Here, we will concentrate on its ability to bind toxic metals [113]. Among metals reported to bind to GSH are Cu, Hg, Cd, and Pb. Metals bound by GSH can be exchanged with other ligands. This leads to a fast metal redistribution in the body. The bile appears to be a main excretory pathway for some metal–GSH complexes, which was early indicated for the CH_3Hg–GSH conjugate. When GSH reacts with a metal, there are two possible outcomes: The metal gets either stabilized as a nonreactive conjugate or the metal, such as transition metals, can undergo a redox reaction paralleled by oxidation

of GSH and formation of ROS. Most frequently, GSH binds to metals and protects against the toxicity, e.g., of Hg^{2+}.

In healthy tissue and cells, more than 90% of GSH exists in the reduced form (GSH), and less than 10% exists in the disulfide form (GSSG). Increased GSSG/GSH ratio is considered indicative of oxidative stress.

4. SH-Containing Chelating Agents: Clinical Use and Environmental Remediation

In 1920, Morgan and Drew suggested the term *chelate* [114], which originates from the Greek word *chele* (claw of a lobster). The term was suggested to be used on the caliper-like groups that function together as two units, which connect a central atom and create heterocyclic rings. In therapeutic use, chelators remove metals from chemical compounds through the formation of complexes. An excellent chelator should be characterized by high solubility in both lipids and water, resistance to biotransformation, ability to reach the sites of metal storage, retain chelating ability at the pH of body fluids, as well as being able to form metal complexes with lower toxicity than the free metal ions [115–117]. Unfortunately, even today, most chelators are not able to cross the blood–brain barrier and therefore have limited ability to remove the metals from the brain tissue [4,118].

For more than a century, chelating agents were used by Ehrlich and Werner to decrease the toxicity of arsenic (As)-containing syphilis drugs. During 1920–1940, similar trials to reduce the toxicity of antimony drugs for schistosomiasis and trypanosomiasis were done by Voegtlin et al. [119]. In 1941, Kety and Letonoff used citrate as an antidote towards acute Pb intoxication [120]. This experiment started a new era in treating metal intoxications caused by environmental exposure or genetic disturbances in metal metabolism.

During World War II, Sir Rudolph Peters and colleagues developed the antidote BAL (British anti Lewisite) against the war gas dichlorovinyl arsine (Lewisite) [121]. The next chelator, EDTA (ethylenediamine tetraacetate) was developed for radionuclide decorporation and clinical treatment of Pb intoxication [122]. EDTA must be administered parenterally. Since the intestinal uptake it low, its action is almost exclusively extracellular. To some essential metals, its stability constants are high.

During the 1950s, DMSA (*meso*-dimercaptosuccinic acid) and DMPS (2,3-dimercapto-1-propanesulfonic acid) were used in China [123] and the former Soviet Union [124]. These drugs have been available in the Western world for decades. DMSA is a registered drug in USA and DMPS in Germany. Several decades passed until Western clinicians fully realized their value. Today, they are first-line antidotes in acute or chronic intoxications with many divalent metal salts. The clinical use of DMSA and DMPS in metal intoxications was reviewed by Aaseth [115] and Aposhian et al. [125].

Originally, BAL was a general antidote particularly used in acute As [126] and inorganic Hg poisonings [127]. Earlier, alternative antidotes did not exist. However, BAL is not considered a good chelator today due to its high toxicity. BAL can increase the deposition of Hg and As in the brain [128]. DMSA and DMPS, which are less toxic, are suited for both oral and parenteral administration. Previously, EDTA was used in childhood and occupational Pb intoxications. However, it is no longer recommended due to a possible redistribution of Pb to the brain [129].

4.1. BAL (2,3 dimercaptopropan-1-ol)

BAL, which is a dithiol compound, was originally used to treat poisonings caused by the war gas Lewisite [121]. It competes successfully with protein SH groups for the treatment of Lewisite and other As poisonings. Also, BAL forms stable chelates with other toxic metals. For several decades after World War II, it was recommended for inorganic Hg, arsenic, antimony, gold, and bismuth poisonings [130]. In cases of elevated intracranial pressure and encephalopathy due to acute Pb poisonings, BAL was earlier recommended given i.m. in the initial phase in combination with calcium EDTA infusion [131]. However, this advice is now outdated [129]. BAL has a short half-life. Within four hours, its metabolism and excretion are completed. Given in full dose, BAL has severe and sometimes very serious adverse effects, including elevated blood pressure followed by tachycardia.

Due to the high toxicity, BAL is currently only used for a few days in life-threatening and acute Pb or As intoxications [132]. Due to BAL's small safety margin, tendency to redistribute toxic elements to the brain, and painful intramuscular injections, it is, in most cases of metal poisoning, replaced by DMSA and DMPS [4]. In the few cases when BAL is used, it is given as deep intramuscularly injections (2.5 mg BAL/kg every four hours). BAL is contraindicated in the treatment of poisonings with Cd, as well as alkyl- and aryl-Hg compounds.

4.2. DMSA (meso-dimercaptosuccinic acid, Succimer)

DMSA (*meso*-dimercaptosuccinic acid, Succimer) and DMPS (2,3-dimercaptopropane-1-sulfonic acid, Unitiol) are water-soluble dithiols, derived from dimercaprol (2,3-dimercapto-1-propanol, BAL) [133].

DMSA can be administered as intravenous, oral, transdermal, or suppository preparations. Plasma and whole-blood half-lives and urinary elimination half-life of DMSA are less than four hours in humans [134,135]; longer in Hg-intoxicated persons [136]. Since DMSA is hydrophilic, it can be administered orally. About 20% of it is absorbed in the gastrointestinal tract, depending on the gut's health status. About 95% of the absorbed drug bind to plasma proteins (albumin). It probably binds by one of its SH groups on a cysteine residue of albumin. Thereby, DMSA leaves its other SH group free to bind metals [137]. Of the free drug, only a tiny amount remains [135]. Only 10%–25% of the oral application is excreted through urine. The other part is excreted via feces. In the body, it is largely metabolized to various disulfides with cysteine [138–140]. DMSA is confined to the extracellular space and does not enter red blood cells [134]. It increases the excretion of Ag, Cd, Pb, and Hg via the urine. Also, it can remove MeHg and Pb from animal brains [141]. Children have a lower renal clearance for DMSA than healthy adults [135].

DMSA is considered the drug of choice in organic Hg poisonings [130,142]. It does not pass the blood–brain barrier but appears to indirectly reduce the MeHg brain burden by changing the brain-to-blood equilibrium [129,141,143–145].

Compared to other dithiol antidotes, DMSA is less toxic [146]. It also has the advantage that practically no essential metal is lost (Fe, Ca, magnesium (Mg)). Only minor changes in Cu metabolism is observed [144]. Side effects range from skin reactions, mild neutropenia, and gastrointestinal discomfort, to increased liver enzymes [138]. Rare adverse effects of DMSA treatment are toxic epidermal necrosis and mucocutaneous eruptions [143,147].

In 1991, Roels et al. [148] found that intake of two grams DMSA significantly elevated urinary Hg excretion in occupationally Hg-exposed people. A meta-analysis by Miller et al. [137] proved DMSA safe and efficient. They concluded that DMSA, due to its efficacy, urinary Hg excretion, and safety, is the preferred antidote against Pb. On average, oral DMSA treatment increases the excretion of Pb by a factor of 12. In 17 Pb-poisoned adults, DMSA reversed the gastrointestinal and neurological symptoms of Pb poisoning [140]. Excretion of Pb after DMSA administration increased significantly in chronically exposed adults and children [130]. A patient reported by Gustavsson and Gerhardsson had severe symptoms of Pb poisoning from an accidentally ingested Pb bullet during a game meal. Years after the incident, the patient was cured after removal of the bullet from the bowel and over one year of therapy with DMSA [149].

4.3. DMPS (2,3-dimercaptopropane-1-sulfonic acid, Unitiol)

In different countries, DMPS can be prescribed as a drug in capsules for oral antidote treatment (one capsule Dimaval® contains 100 mg DMPS) or in ampoules for intravenous treatment (5 mL ampoule DMPS-Heyl® contains 250 mg DMPS). In Germany, DMPS is a registered drug for treatments of Hg intoxication. However, it is not an approved drug in the US, so unless the U.S. Food and Drug Administration gives special permission, DMPS cannot be legally used by physicians in the US, nor can pharmacies compound it [150]. The daily dose is usually 3–10 mg DMPS/kg body weight.

Many studies have proven its efficiency to chelate toxic metals in the body [145]. DMPS is considered an optimal antidote in inorganic Hg poisonings [130]. For Pb and organic Hg poisonings, it is less efficient than DMSA [151].

The fraction of absorption of oral DMPS is less than 40% [152]. DMPS can be administered orally or intravenously. DMPS converts quickly to disulfide form. The half-life in different organs for DMPS is approximately 20 min [153]. In animal experiments, relatively small DMPS concentrations were detected in the brain and other organs [144]. DMPS is primarily excreted via urine and to some part via the bile. Its use is usually accompanied by some loss of Zn and Cu. Therefore, it is recommended to monitor and replace these trace elements before and after the treatment [154]. DMPS, which is hydrophilic, is distributed primarily in the extracellular space, but a fraction can pass into the intracellular compartment [130]. DMPS removes Hg better from the kidney than DMSA. In cases of acute poisonings with inorganic mercuric salts, DMSA is considered the drug of choice [141,144].

4.4. Penicillamine (D-2-amino-3-mercapto-3-methylbutanoic acid)

D-Penicillamine (D-2-amino-3-mercapto-3-methylbutanoic acid, Cuprimine) was introduced in the racemic form (PA) for the treatment of Wilson disease by John Walshe [155]. It is a product of penicillin degradation. Its structure represents a dimethylated cysteine where two methyl groups surround the SH group and give the molecule a higher resistance than cysteine against in vivo interactions. The D-form of penicillamine has fewer side effects than the L-form and is currently the preferred therapeutic form [156]. Penicillamine's distribution volume consists primarily of the extracellular space. Accidentally, penicillamine may give rise to serious adverse effects [157]. Also, D-penicillamine has been used as an antidote in Hg and Pb poisonings, before DMSA and DMPS were clinically introduced [130].

4.5. Lipoic and dihydrolipoic acids

Alpha-lipoic acid ((R)-5-(1,2-Dithiolan-3-yl)pentanoic acid, LA) is an organo-sulfur compound also known as thioctic acid. It is usually produced in the body, and it is essential for aerobic metabolism. The reduced form of LA, called dihydrolipoic acid (DHLA), contains a pair of thiol groups. Here again, the R-enantiomer is the biologically and therapeutically active form. DHLA has high affinity to Hg and has been proposed as an effective Hg antidote [158,159].

4.6. MiADMSA (monoisoamyl 2, 3-dimercaptosuccinic acid)

Monoisoamyl 2, 3-dimercaptosuccinic acid (MiADMSA) is currently in development as a future chelating agent. In contrast to DMSA and DMPS, which effectively remove extracellularly distributed Cd [160], MiADMSA can also chelate intracellular Cd [161]. This analog of DMSA can cross biomembranes and is more efficient than DMSA in reducing the burden of subchronic and acute arsenic intoxications [162]. Also, MiADMSA has lower toxicity than DMSA [163]. When used together with N-acetylcysteine, it reduces significantly oxidative stress during chelation therapy [164].

4.7. Thiocarbamates (Diethyldithiocarbamate and Derivatives)

Depending on the lipophilicity of a metal-chelator complex, chelating agents may change the metal's organ distribution, and thereby potentially increase its toxicity. Diethyldithiocarbamate (DDC) was originally suggested as an efficient chelator for acute Cd intoxication, as parenteral DDC administration decreased mortality induced by parenteral Cd in animal experiments, even at protracted time after Cd administration [165]. In general, DDC forms highly lipophilic complexes with divalent metal ions. Increased brain deposition caused by exposure to DDC has been documented for organic and inorganic Hg [166], as well as for Pb [167].

However, some derivatives of DDC with higher molecular weight appear promising in mobilizing aged Cd deposits. Thus, N(methoxybenzyl)-Dglucamine dithiocarbamate in studies on animals effectively reduced the retention of Cd both in organs and the entire body. This agent's effects were shown to be less pronounced in younger than in older animals. The highest administered Cd fraction retained in the liver, and the strongest chelation therapy effect observed was also on liver deposits. Mobilized Cd was almost exclusively excreted through feces [168].

5. Combination of Chelating Agents

It has been shown that DMSA, used in combination with Monensin (the sodium salt of monensic acid, an antibiotic used in ruminant animal feeds [45]), is even more efficient than when it is used alone, in particular in removing Pb deposited in the brain. The suggested mechanism to explain this is that there may be a cotransport of Pb and OH ions leaving the cells, in exchange with external sodium ions; this would promote transport of intracellular Pb to extracellular DMSA, thereby enhancing its effectiveness [169]. Thus, Monensin acts as a shuttling agent for DMSA [118]. The combination of EDTA and BAL was, for many years, recommended in inorganic Pb poisonings [170–172]. It is reasonable to assume that the tightly bound Hg-ions in the brain after long-term Hg^0 vapor exposure, to some extent, can be mobilized by using minor doses of BAL as a brain-to-blood shuttle, in combination with DMPS to promote the final elimination from the body [118]. Furthermore, a combination of MiADMSA and DMSA may be proven more efficient than each agent alone to promote Cd mobilization, although this metal is tightly bound to MTs intracellularly [160].
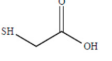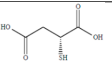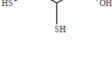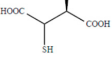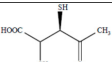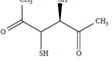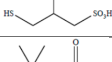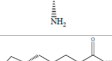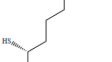
In cases with acute Hg salt poisonings, venous hemodiafiltration (CVVHDF) is suggested in combination with DMPS. In a case reported by Dargan, a man who had severe Hg poisoning after the ingestion of one gram mercuric sulfate in a suicide attempt, presented acute hematemesis and deteriorated rapidly. The treatment with the combined strategy saved him. He developed no neurological symptoms and was symptom-free five months after being 50 days under hospital care [173].

6. Chemical Features of BAL, DMSA, DMPS, Penicillamine, Lipoic Acid, Dihydrolipoic Acid, and their Metal Chelates

6.1. Protonation of the Thiolate Anions

In the following, we report the acidic properties of the chelating agents BAL, DMSA, DMPS, penicillamine, lipoic acid, and dihydrolipoic acid, together with those of the simpler ligands thioglycolic acid and thiomalic acid related to DMSA, to obtain insight into the behavior of the parent molecules. Table 3 reports selected protonation constants of these ligands (those concerning the mercapto groups are marked in red) together with their structure, the used acronyms, the formula, and the molecular weights. The protonation constants are of particular importance since they determine the biological properties of a drug, such as its solubility, absorption, cell penetration, and bioavailability. Furthermore, protonation constants are also of primary importance in determining the speciation of the complexes formed with the toxic metal ions of interest.

Table 3. Protonation constants of thioglycolic acid, thiomalic acid, meso-2,3-dimercaptosuccinic acid (DMSA), dimercaptopropane sulfonate (DMPS), penicillamine, lipoic acid, dihydrolipoic acid, and some other simple ligands useful to characterize the acid behavior of SH ligands.

Structure	Name	Acronym	Formula	MW	log K_1	log K_2	log K_3	log K_4
	Thioglycolic acid	TGA	$C_2H_4O_2S$	92.11	[174] 9.96	3.44		
	Thiomalic acid	TMA	$C_4H_6O_4S$	150.15	[174] 10.24	4.52	3.12	
	2,3 Dimercapto propan-1-ol	BAL	$C_3H_8OS_2$	124.23	10.8	8.7		
	meso-Dimercapto succinic acid	DMSA	$C_4H_6O_4S_2$	182.22	[174] 12.05	9.65	3.43	2.71
	Methyl-DMSA	MDMSA	$C_5H_8O_4S_2$	196.22	[174] 9.98	7.15	2.8	
	Dimethyl-DMSA	DDMSA	$C_6H_{10}O_4S_2$	210.22	[174] 7.31	5.23		
	Unitiol	DMPS	$C_3H_8O_3S_3$	188.289	[175] 11.38	8.69		
	d-Penicillamine	DPEN	$C_5H_{11}NO_2S$	149.212	[176] 10.35	7.91	2.19	
	Lipoic acid	LA	$C_8H_{14}O_2S_2$	206.343	[177] 6.37 * $^\$$ 4.704(1)			
	Dihydrolipoic acid	DHLA	$C_8H_{16}O_2S_2$	208.343	[178] 11.02	9.86	4.73	

The protonation constants related to the SH groups are marked in red. * Determined in non-aqueous solvent, $^\$$ determined in this work.

6.1.1. TGA and TMA

The speciation plots of thioglycolic acid (TGA) and thiomalic acid (TMA) are reported in Figure 1. In the case of TGA, the negatively charged $[LH]^-$ species with protonated mercapto group is the prevailing one at physiological pH. In the case of TMA, the $[LH]^{2-}$ species, which has lost two protons from the carboxylic groups, is the prevailing one.
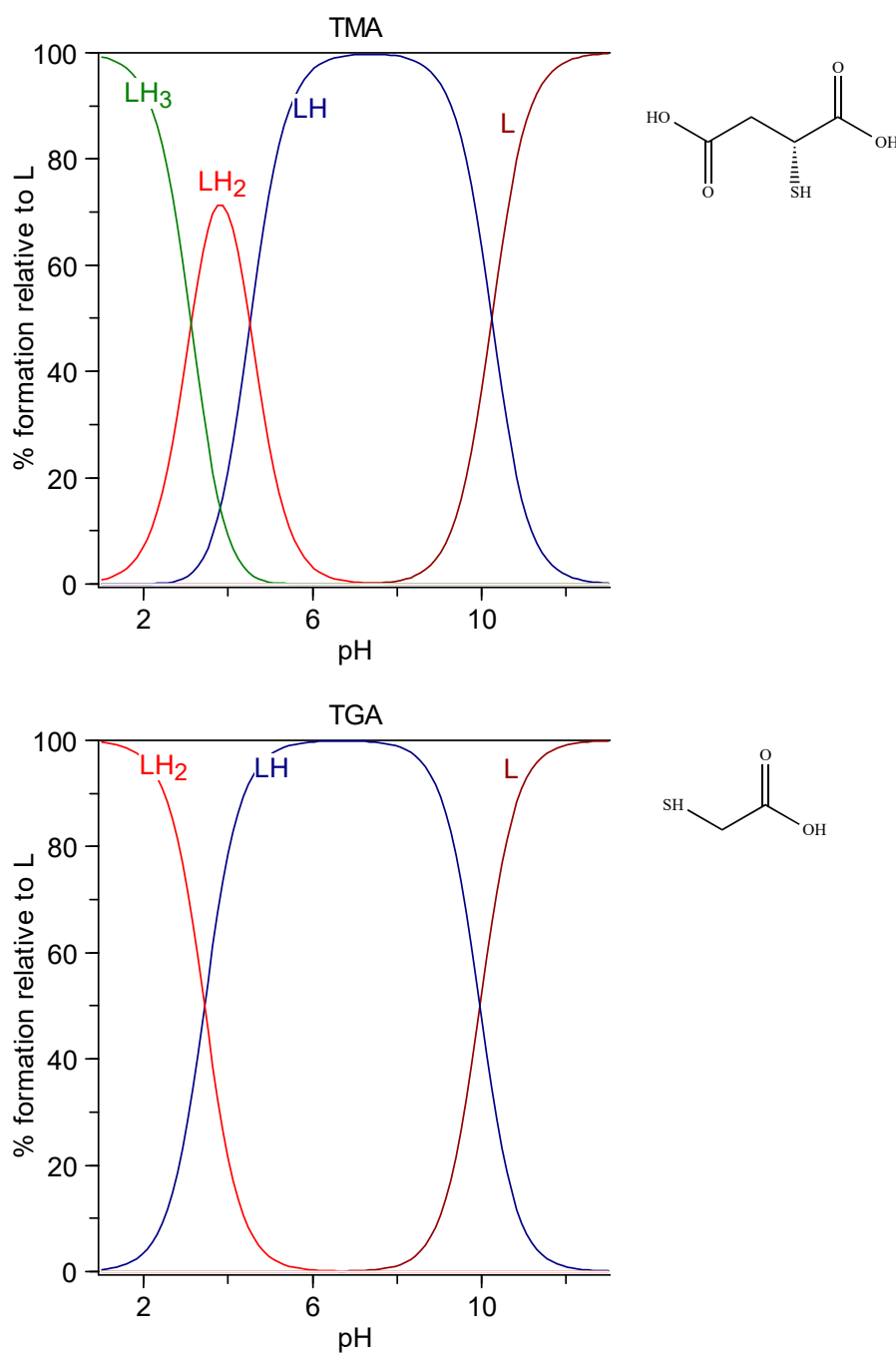
Figure 1. Speciation plots of TGA (top) and TMA (bottom).

6.1.2. BAL

BAL (2,3 dimercaptopropan-1-ol, dimercaprol) is a viscous oily liquid with a pungent odor of mercaptan, density 1.23985 g/mL, solubility in water 87 g/L, or 0.7 M [179,180]. It is characterized by two protonation constants (log K_1 10.8 and log K_2 8.7 obtained as the mean values among the cases reported at 25 °C and 0.1 M in the IUPAC Stability Constant Database [181]. The speciation plot is reported in Figure 2. The completely protonated form LH_2 is prevalent at pH 7.4 (95.2%) together with the monoprotonated form $(LH)^-$ (4.8%).
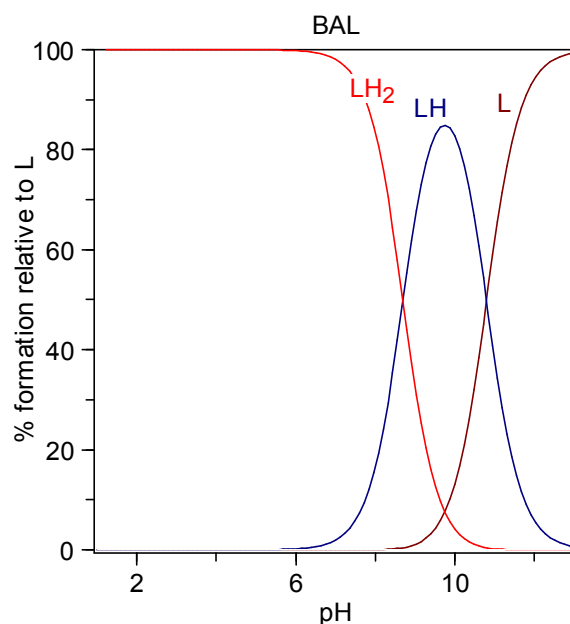
Figure 2. Speciation plots of British anti-Lewisite (BAL).

6.1.3. DMSA

DMSA (*meso*-2,3-dimercaptosuccinic acid, Succimer) is a white crystalline powder with mercaptan odor and taste, water-solubility 2.43 g/L (DMSA is sparingly soluble; it must be titrated with alkali to pH 5.5 to go into solution, i.e., it must be salified on both carboxylic groups, as can be seen in the speciation plot in Figure 3), log P = −0.3. It is characterized by four protonation constants, $\log K_1 = 12.05$, $\log K_2 = 9.65$, $\log K_3 = 3.43$, and $\log K_4 = 2.71$. Its formula and the related speciation plot are presented in Figure 3. The form $[LH_2]^{2-}$ that has lost both the carboxylic protons is the prevalent form at pH 7.4 (99.4%).
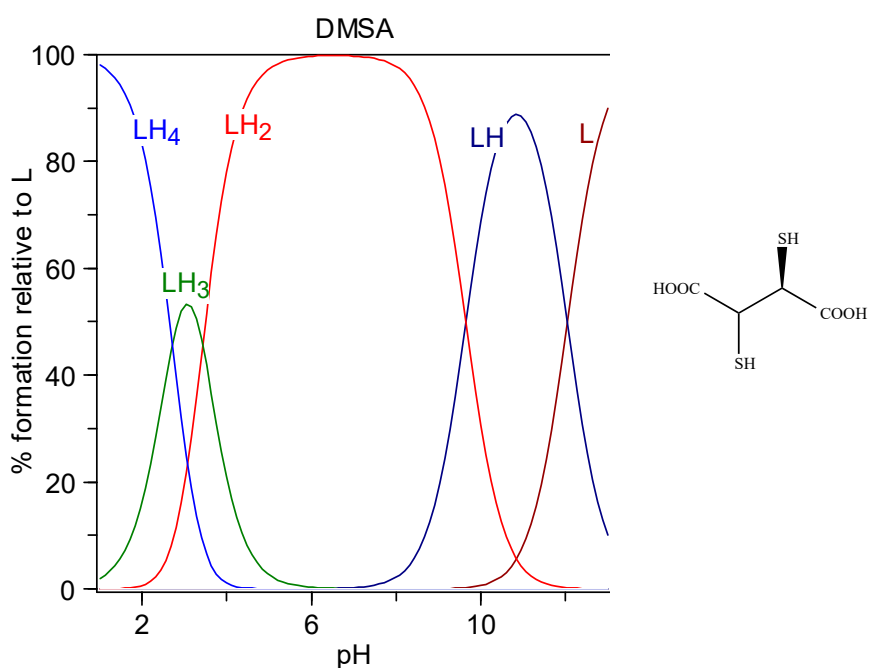

Figure 3. Speciation plots of DMSA.

Esters of DMSA, more effective than DMSA at clearing Hg and Cd from the intracellular space, have been developed successively. Their better chelating properties are attributed to their higher lipophilicity, favoring cell penetration. Despite the esterification of carboxylic groups, the net charge at pH 7.4 is almost the same as that of the parent molecule, due to the resulting increased acidity of mercapto groups (Figure 4) [174].

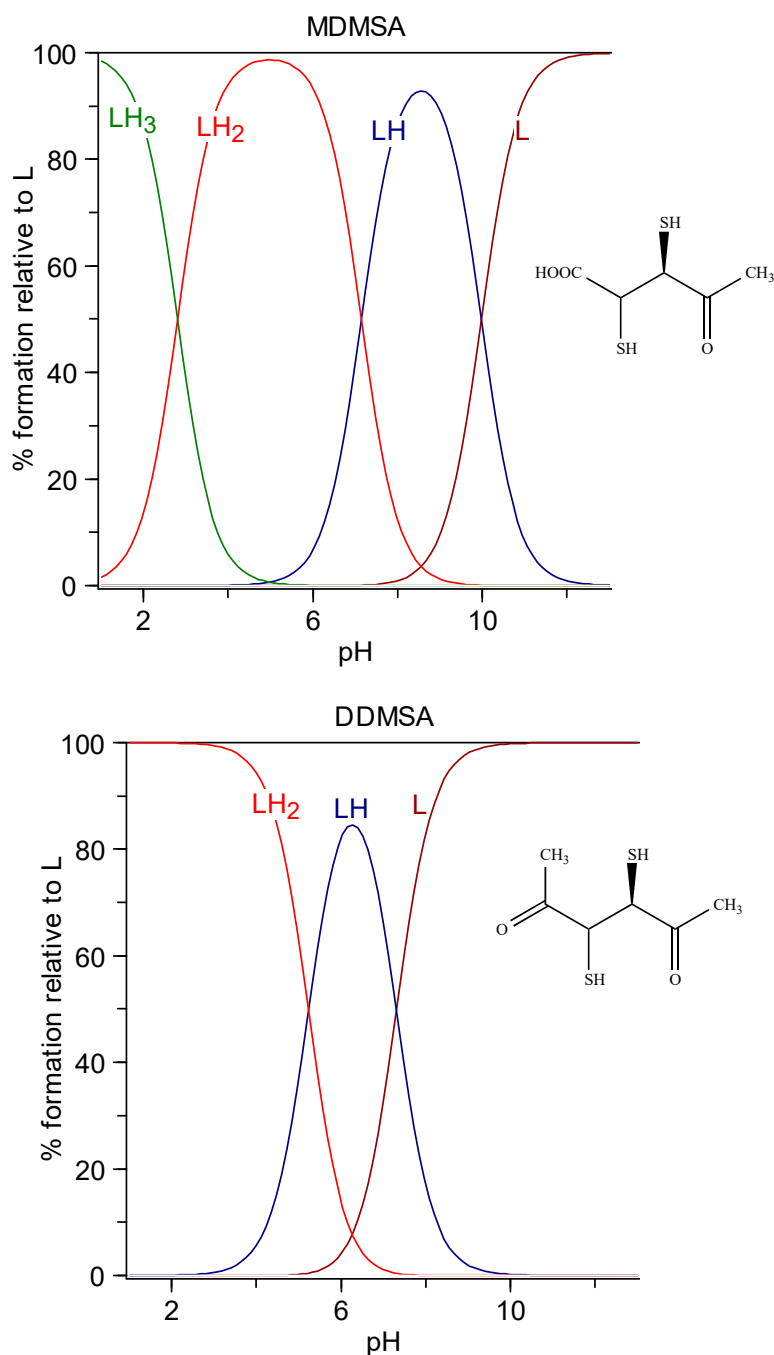
Figure 4. Speciation plots of methyl-DMSA (top) and dimethyl-DMSA (bottom).

6.1.4. DMPS

DMPS (2,3-dimercaptopropane-1-sulfonic acid) is used as the sodium salt that presents as a white crystalline powder with one molecule of crystallization water of general formula $C_3H_7NaO_3S_3 \cdot H_2O$, MW 228.26, produced in Germany by Heyl Chemisch-pharmazeutische Fabrik GmbH, with the trade

name of Dimaval®. It has a high water solubility of 350 g/L, corresponding to a 1.54 M solution. It is commercially available as ampules for injection (250 mg as $C_3H_7NaO_3S_3$ in a sterile solution under nitrogen atmosphere to protect against oxidation) or as 100 mg capsules for oral use (always as $C_3H_7NaO_3S_3$). It is characterized by two protonation constants, $logK_1 = 11.62$ and $logK_2 = 8.53$, behaving in the sulfonic group as a strong acid. Its formula and the related speciation plot are presented in Figure 5. The form $[LH_2]^-$ deprotonated on the sulfonic group is the prevalent form at pH 7.4 (99.4%) [182].
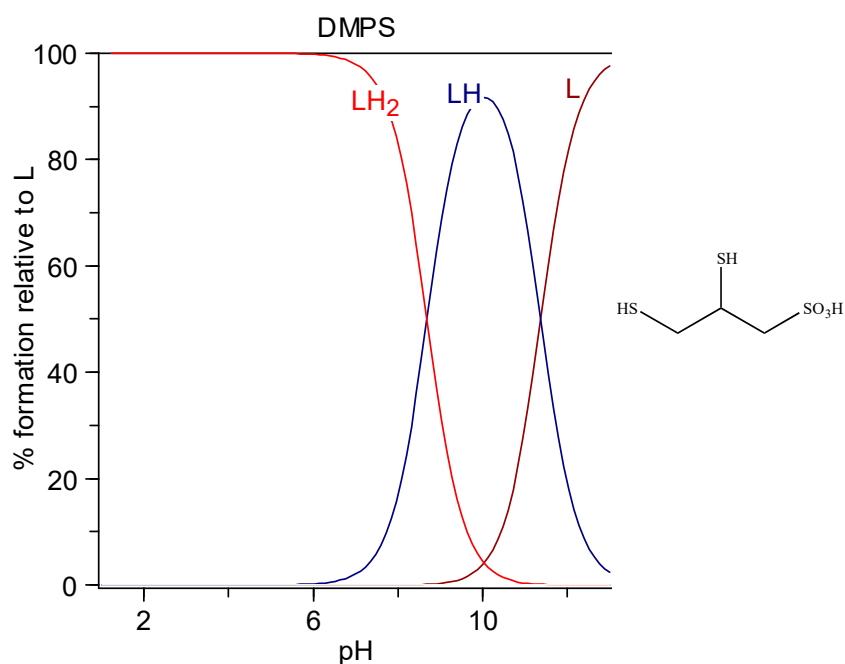

Figure 5. Speciation plots of DMPS.

6.1.5. D-penicillamine

D-penicillamine (DPEN), D-2-amino-3-mercapto-3-methylbutanoic acid, Cuprimine, is a colorless crystalline powder with a weak odor of sulfur-containing amino acids. It is relatively soluble in water [183]. It is characterized by three protonation constants, imputable to SH, NH_3^+, and COOH groups respectively, $logK_1 = 10.8$, $logK_2 = 8.1$, and $logK_3 = 2.2$. These were obtained as the mean values among the cases reported at 25 °C and 0.1 M in the IUPAC Stability Constant Database [181]. The speciation plot of DPEN is reported in Figure 6. The zwitterionic form $HS-C(CH_3)_2-CHNH_3^+–COO^-$ (LH_2 76.4%) and the negatively charged $HS-C(CH_3)_2-CHNH_2–COO^-$ (LH 23.6%) are the species existing at physiological pH.
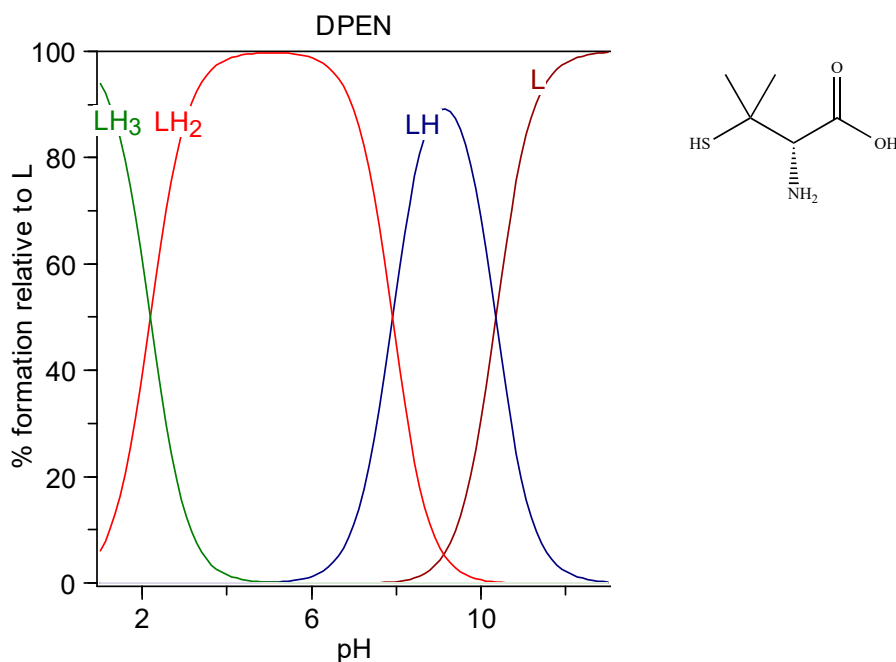
Figure 6. Speciation plots of D-penicillamine (DPEN).

6.1.6. Lipoic and dihydrolipoic acids

Lipoic acid, (R)-5-(1,2-Dithiolan-3-yl)pentanoic acid, known as α-lipoic acid, (LA) or thioctic acid, appears as yellow needle-like crystals. It is reported to be very slightly soluble in water (0.224 g/L, corresponding to a solution 1.16 mM).

Since no protonation constant in water solution is reported in the literature for the carboxylic acid, we determined it at 25 °C and 0.1 M NaCl ionic strength through potentiometric measurements. The lipoic acid was a reagent-grade Aldrich product, used without further purification. The operating conditions were those generally used by our research group [184]. The solution of ligand to be titrated was obtained by dissolving an excess of lipoic acid in 0.1 M NaCl solution in an ultrasound bath for 3 h. This solution resulted in 6.1 mM of lipoic acid, corresponding to a solubility of 1.26 g/L, about six times greater than that reported above. The log K of protonation resulted in 4.704 (1), very similar to the value 4.73 for DHLA found by Bonomi et al. at the same experimental conditions [178].

Dihydrolipoic acid (DHLA), 6,8-Bis(sulfanyl)octanoic acid, is the reduced form of lipoic acid. It is freely soluble in water (103 g/L corresponding to a 0.49 M solution), it has a log P 2.24, and it is characterized by the three protonation constants $\log K_1 = 11.02$, $\log K_2 = 9.86$, and $\log K_3 = 4.73$ at 25 °C and 0.1 M ionic strength [178]. The speciation plots of lipoic acid and DHLA are reported in Figure 7.

Some general features on the results for the protonation constants of mercapto groups (Table 3) can be remarked. In molecules with a single SH group, the log K value presents a low variability, ranging from 9.96 for TGA to 10.35 for DPEN. There is instead a large difference in both the first (10.38 BAL, 11.35 DMPS, and 12.05 DMSA) and also the second protonation constants (8.7 BAL, 8.69 DMPS, and 9.65 DMSA) when two SH groups are present in the molecule. These differences are to a large extent due to the different charges on the entire molecule. The solid-state structures of a number of examined chelating agents are presented in Table S1.
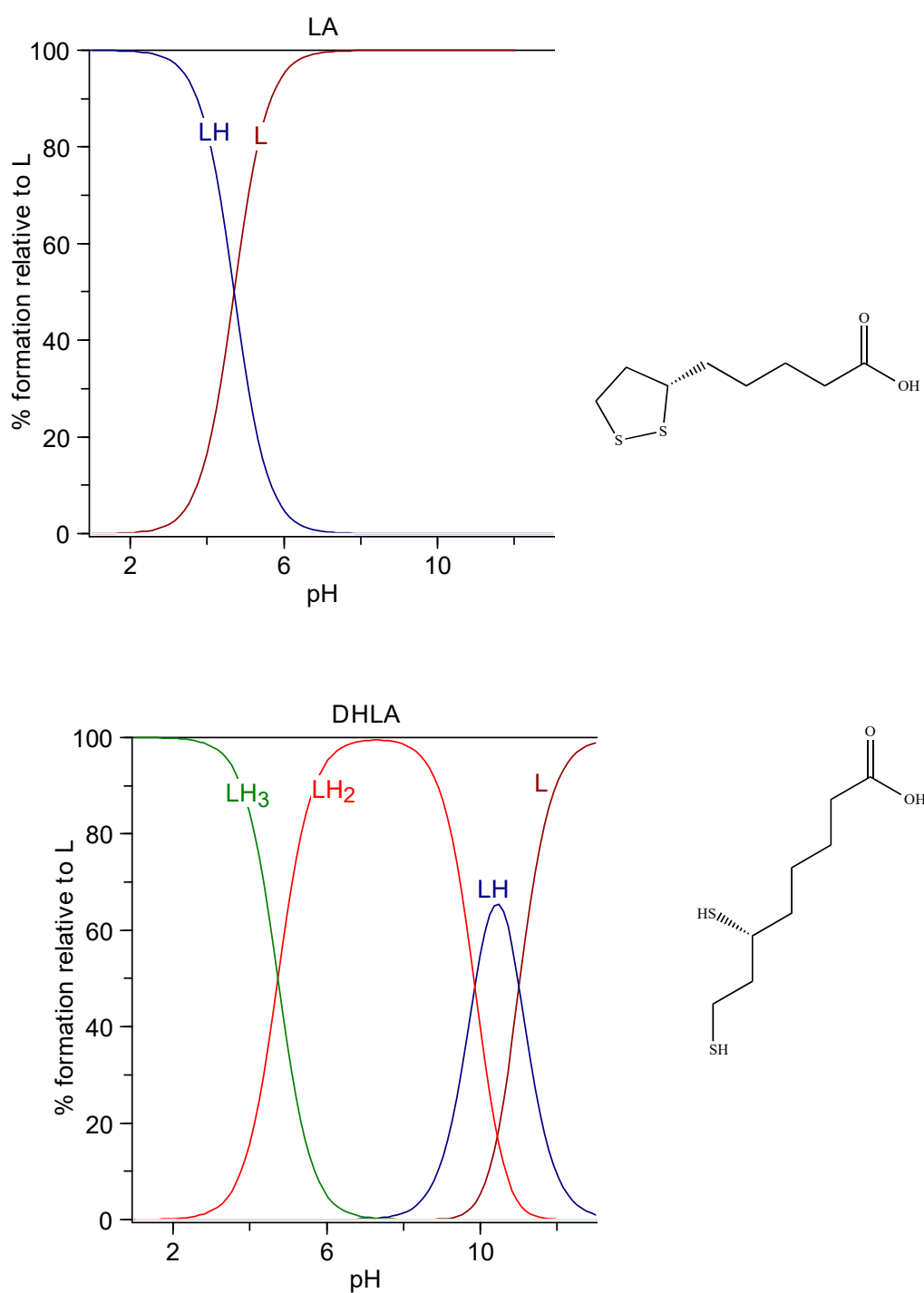
Figure 7. Speciation plots of Lipoic acid (top) and dihydrolipoic acid (DHLA) (bottom).

6.2. Complex Formation Reactions between Hg^{2+}, Cd^{2+}, and Pb^{2+} and Thiol Chelating Agents

As remarked in a previous work [185], the literature reports only a few data on the complex formation equilibria between Hg^{2+}, Cd^{2+}, Pb^{2+}, and the thiol chelating agents in Table 4. The literature complex formation constants are reported in Table 4. In the same table, the corresponding pM values are reported for each ligand–metal ion system. Irrespective of the complexation model, the pM values permit us to develop some consideration on the general behavior of each metal ion. The speciation plots for the systems are shown in Figure S1.

Table 4. Complex formation constants of thioglycolic acid, thiomalic acid, DMSA, DMPS, penicillamine, lipoic acid, dihydrolipoic acid with Hg^{2+}, $Cd^{2+,}$ and Pb^{2+}. The pM values for each system are also reported in red.

Ligand	Hg^{2+}		Cd^{2+}		Pb^{2+}		Temp./Ion. Str.	Method
	Species	Logβ	Species	Logβ	Species	Logβ		
TGA	[186] HgL	34.5	[187] CdLH	11.08	[188] PbL	8.5	[186] 25, 0.1 M NaClO₄	EMF
	HgL₂	40.5	CdL	4.34			[187] 25, 3 M LiClO₄	gl
			CdL₂	6.49			[188] 25, 0.15 M	gl
pM	32.9		6.00		6.95			
TMA	[189] HgL	9.94	[190] CdL	10.05	[181] PbL	10.80	[189] 25, 0.1 M KNO₃	gl
	HgL₂	18.07	CdL₂	13.51			[190] 25, 0.2 M KNO₃	gl
			Cd₃L₄	41.59			[181] 30, 0.007 ClO₄⁻	gl
pM	8.24		7.78		8.90			
DMSA	§	—	[181] CdLH₃	28.73	[191] PbL	17.4	[181] 25, 0.1 M KCl	gl
			CdLH	23.50			[191] 25, 0.1 M	Spect.
			CdL	17.11				
pM			11.48		11.45			
DMPS	[192] HgL	42.2	[193] CdL₂	28.27	[181] PbL	16.38	[192] 25, 0.1 M NaClO₄	ISE
	HgL₂	53.1	Cd₃L₃	59.9	PbL₂	22.21	[193] 25, 0.2 M KNO₃	gl
			Cd₃L₄	71.9			[181] 20, 0.1 KNO₃	EMF
			Cd₅L₆	114.3				
			Cd₇L₈	156.7				
pM	37.60		13.24		12.00			
	[181] HgL	39.71	[181] CdL	17.32			[181] 20, 0.1 KNO₃	EMF
			CdL₂H	35.19			[181] 37, 0.15 NaCl	gl
			CdL₂	28.22				
			Cd₂L2	37.72				
			Cd₃L₃H	61.91				
pM	34.80		12.14					
DPEN	[194] HgL	37.6	[190] CdL	11.53	[181] PbLH	15.87	[194] 25, 0.1 M KNO₃	
	HgL₂H	52.31	CdL₂	19.64	PbL	13.12	[190] 25, 0.2 M KNO₃	gl
	HgL₂	43.69	Cd₃L₄	50.22	PbL₂H	26.19	[181] 25, 0.1 M KCl	gl
					PbL₂	17.7		
pM	34.50		8.61		10.50			
	[186] HgL	37.8	[194] CdL	11.51			[186] 25, 0.1 M NaClO₄	gl
	HgL₂H	53.6	CdL₂H	15.94			[194] 25, 0.1 M KNO₃	
	HgL₂	44.50	CdL₂	19.52				
			CdL₃	22.35				
pM	35.30		8.46					

§ Precipitation occurs [195].

In the case of Hg complexes, apart from the pHg value 8.24 for the Hg–TMA complexes studied by Lenz and Martell [189], the pHg values are all extremely high, regardless of the number of SH groups in the molecule. Contrarily, the pM values of Cd^{2+} and Pb^{2+}·complexes with the ligands containing two SH binding groups are higher than those with ligands with a SH group alone. The pCd and pPb values are lower than the corresponding pHg values of more than 20 pM units. In a work of Basinger et al. [186], the authors stated "(a) the structural chemistry of Hg^{2+} complexes with thiol-containing ligands, (b) the stability constants for such systems and (c) the relative efficacy of 29 compounds as antidotes for Hg poisoning has been carried out to determine the structural requirements for Hg^{2+}

antidotes. This leads to the suggestion that instances in which two thiol groups on the same chelate molecule are simultaneously bonded to the same Hg^{2+} species in a complex, water-soluble or otherwise, are not found, and Hg^{2+} species bearing two sulfur donors generally have a bond angle of 180° or so between these two bonds. It was hypothesized, from this, that chelating agents bearing a single SH group might be almost as effective as Hg antidotes as those bearing two groups. Data on the stability constants and antidotal effectiveness are presented for such structures, but in general, molecules which do not have the potential ability to chelate are also inferior as antidotes. From the data assembled, it would appear that the presence of a second donor group is required. Because of the lability of the Hg-SH bond, this second site seems necessary to provide the required kinetic stability for the complex. In the case of dithiols, the Hg may move back and forth from one sulfur donor site to another but may not (and possibly cannot) bind firmly and simultaneously to both donor sites."

In their potentiometric equilibrium study on the complex formation reaction between Hg^{2+} and dithiol chelating agents, Rivera et al. [195] pointed out the formation of a 1:1 complex in which both the two thiol groups were involved in coordination. In the case of DMSA, they proposed the structure in Figure 8, as well as Aposhian et al. [125] six years later.
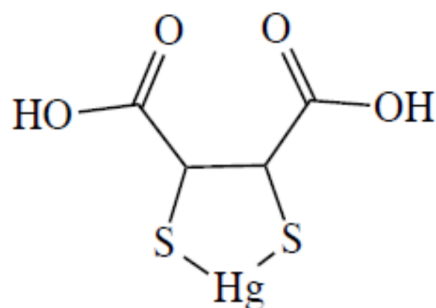

Figure 8. The molecular formula of DMSA–Hg complex proposed by Rivera et al. [193].

In a work of 2004, George et al. [145] presented a study of the solution chemistry of mercuric ions with DMSA and DMPS, employing X-ray absorption spectroscopy and density functional theory calculations (DFT). The reported complexes were Hg_2L_2 and Hg_3L_3 for DMSA, and Hg_2L_2 for DMPS, at 1:1 M/L ratio. With DMPS at 1:4 M/L ratio, HgL_4 was also observed. Contrary to established thinking reported above, the authors stated that the two functional groups of the chelator molecule cannot bind a common atom of *Hg* because the distance between the two sulfur atoms in the molecule of DMSA or DMPS does not allow the accommodation of a linear two-coordinate S–Hg–S species (Figure 8). Therefore, they concluded that more complex structures must be occurring with at least two DMSA or DMPS molecules and at least two Hg atoms, and based on DFT studies; they proposed the structures in Figure 9 in which the two coordinated species are both close to linear.

Chekmeneva et al. used differential pulse voltammetry (DPV) and electrospray ionization mass spectrometry (ESI-MS) to the study of the binding of DMSA, DMPS, and DPEN with Hg^{2+} metal ions [196]. The use of voltammetric titrations allowed obtaining a thorough picture of the complexation schemes in a concentration range extremely low. The main formed complexes were $Hg(DPEN)_2$, $Hg_2(DMSA)_2$, and $Hg(DMPS)_2$. Further minor species were also evidenced; Hg_2L species for DMSA and DMPS by DPV; HgL_2, Hg_2L_3, Hg_3L_3 for DMSA; and Hg_2L_2, Hg_2L_3, Hg_3L_3 for DMPS by ESI-MS.
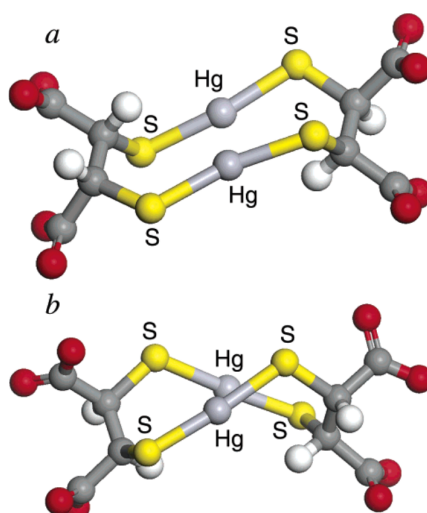
Figure 9. Calculated structures of the two diastereomers of the smallest possible DMSA:Hg^{2+} complex. The carbon atoms are depicted as dark gray, oxygen atoms as red, hydrogen atoms as white, mercury atoms as light gray, and sulfur atoms as yellow. Reproduced from reference [144].

The system Hg-DPEN was previously studied by Koszegi-Szalai and Paal [197], who by potentiometric methods and Raman spectroscopy showed that variously protonated $Hg(DPEN)_2$ complexes are the dominant species in a wide range of pH, and by Leung et al. [198]. These last authors studied the complexation of Hg^{2+} by DPEN using EXAFS and ^{199}Hg NMR, giving evidence of the formation of HgL_2, and HgL_3 in excess of DPEN.

The structure of the complex formed by two DHLA molecules, one Hg^{2+} ion, and two phenyl-Hg groups, shown in Figure 10, presents a similar linear binding coordination mode [199].
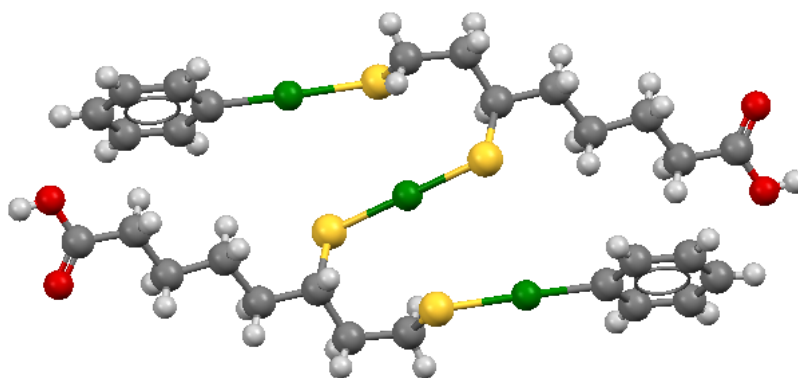

Figure 10. Mercury in green, sulfur in yellow, and oxygen in red. Coordinates obtained from the Cambridge Structural Database (Reference Code LIMNUQ; the image was created with Mercury3.5.

The linear coordination of Hg^{2+} is also indirectly reported by Chekmeneva et al. [200], who remarks the formation of 1:1 and 1:2 metal:ligand complexes through DPV, and give evidence of the more complex stoichiometries $Hg_2(DHLA)_2$, $Hg(DHLA)_2$, $Hg_2(DHLA)_4$, and $Hg_4(DHLA)_4$ through ESI-MS spectroscopy. The formation of polynuclear species can be explained, taking into consideration the short distance between the two thiol-groups in the chelating agent. Only the participation of several ligand moieties can provide a stable linear conformation with two thiol groups for each Hg^{2+} metal ion. The structures presented in Table S2 for a number of Hg–SH complexes confirm the preferred linear coordination of the Hg^{2+} metal ion.

In the case of Cd^{2+} complexes with thiol-containing ligands (Table 4), a significant difference can be observed between the pCd values of ligands containing a single SH group (TGA 6.00, TMA 7.78,

DPEN 8.61, 8.46) and those containing two vicinal SH groups (DMSA 11.48, DMPS 13.24, 12.14). In this last case, the possibility of forming tetrahedral chelates favors their stability. This is confirmed by the solid-state structures presented in Table S3. In a recent study, Jahromi et al. [201] report a structural study of the solution equilibria between Cd^{2+} and DMSA and DMPS. They make use of different techniques, X-ray absorption spectroscopy (XAS), size exclusion chromatography, and density functional theory (DFT). The results indicate complex chemistry consistent with both DMPS and DMSA acting as true chelators, using two thiolates for DMPS and one thiolate and one carboxylate for DMSA [201].

A behavior analogous to that of Cd^{2+} is presented by Pb^{2+} complexes, which show a definite difference among the ligands bearing a single SH group (TGA 6.95, TMA 8.9) and those with two vicinal SH groups (DMSA 11.45 and DMPS 12.00), while DPEN presents an intermediate behavior with pPb 10.5, presumably for the involvement in coordination of NH_2 or COO^- groups. A paper by Gala Morales et al. [202] presented a work where cyclic voltammetry (CV) and DPV were used to study the complex formation of Pb^{2+} with DMSA and DMPS. Multivariate curve resolution was applied to voltammetric results to estimate the stoichiometries and stability constants of the formed complexes. In both systems, the ML_2 was found as the predominant species. Table S4 presents a number of solid-state structures of Pb^{2+} complexes with mercapto ligands.

7. Conclusions

Based on clinical, experimental, and in vitro studies discussed in the present review, some up-to-date recommendations can be given with regard to drugs of choice in metal intoxications with Hg, Cd, and Pb (Table 5). The metal chelator DMSA is considerably less toxic than the classical metal antidote BAL, and today DMSA is the recommended agent in poisonings with Pb and organic Hg. Its toxicity is also lower than that of DMPS, although DMPS is the recommended agent in acute poisonings with mercuric salts. We have suggested that intracellular Cd deposits and cerebral deposits of inorganic Hg, to some extent, can be mobilized by a combination of antidotes (Table 5), but clinical experience with such combinations are lacking. The agent MiADMSA is not yet commercially available, and its possible use in Pb poisonings must await further research. Moreover, the clinical combination of minor doses of BAL with DMPS in cases of Hg vapor overexposure is also insufficiently studied.

Table 5. Recommended chelation treatment in poisonings with mercury, cadmium, and lead.

Toxic Agent	Recommended Chelation Treatment
Inorganic mercuric salts	DMPS
Methyl mercury	DMSA
Elemental mercury vapor	DMPS (initially combined with BAL)
Cadmium	DMSA (combined with MiADMSA)
Lead	DMSA (combined with Monensin)

Conflicts of Interest: The authors declare that they have no conflict of interest.

References

1. ATSDR. *ATSDR Substance Priority List*; ATSDR: Atlanta, GA, USA, 2017.
2. World Health Organisation. *Ten Chemicals of Major Public Health Concern*; WHO: Geneva, Switzerland, 2010; pp. 1–4.
3. Pearson, R.G. Hard and Soft Acids and Bases. *J. Am. Chem. Soc.* **1963**, *85*, 3533–3539. [CrossRef]
4. Aaseth, J.; Skaug, M.A.; Cao, Y.; Andersen, O. Chelation in metal intoxication-Principles and paradigms. *J. Trace Elem. Med. Biol.* **2015**, *31*, 260–266. [CrossRef]
5. Clarkson, T.W. The toxicology of mercury. *Crit. Rev. Clin. Lab. Sci.* **1997**, *34*, 369–403. [CrossRef] [PubMed]
6. Bjørklund, G.; Dadar, M.; Mutter, J.; Aaseth, J. The toxicology of mercury: Current research and emerging trends. *Environ. Res.* **2017**, *159*, 545–554. [CrossRef] [PubMed]
7. Maqbool, F.; Niaz, K.; Hassan, F.I.; Khan, F.; Abdollahi, M. Immunotoxicity of mercury: Pathological and toxicological effects. *J. Environ. Sci. Health Part C* **2017**, *35*, 29–46. [CrossRef] [PubMed]
8. Branco, V.; Caito, S.; Farina, M.; Teixeira da Rocha, J.; Aschner, M.; Carvalho, C. Biomarkers of mercury toxicity: Past, present, and future trends. *J. Toxicol. Environ. Health Part B* **2017**, *20*, 119–154. [CrossRef]
9. Scott, R.A. (Ed.) *Encyclopedia of Inorganic and Bioinorganic Chemistry*; John Wiley and Sons: Hoboken, NJ, USA, 2011.
10. Nordberg, G.F.; Fowler, B.A.; Nordberg, M. *Handbook on the Toxicology of Metals: Fourth Edition*; Academic Press: Cambridge, MA, USA, 2014; ISBN 9780123973399.
11. Bose-O'Reilly, S.; McCarty, K.M.; Steckling, N.; Lettmeier, B. Mercury exposure and children's health. *Curr. Probl. Pediatric Adolesc. Health Care* **2010**, *40*, 186–215. [CrossRef]
12. Selin, N.E. Global Biogeochemical Cycling of Mercury: A Review Noelle Eckley Selin. *Annu. Rev. Environ. Resour.* **2009**, *34*, 43–63. [CrossRef]
13. UNEP. *Global Mercury Assessment 2013: Sources, Emissions, Releases, and Environmental Transport*; UNEP Chemicals Branch: Geneva, Switzerland, 2013.
14. Bjørklund, G.; Lindh, U.; Aaseth, J.; Mutter, J.; Chirumbolo, S. Mercury in dental amalgams: A great concern for clinical toxicology in developing countries? *J. Trace Elem. Med. Biol.* **2019**, *51*, 9–11. [CrossRef]
15. Rice, K.M.; Walker, E.M.; Wu, M.; Gillette, C.; Blough, E.R. Environmental mercury and its toxic effects. *J. Prev. Med. Public Heal.* **2014**, *47*, 74–83. [CrossRef]
16. Bjørklund, G. The history of dental amalgam. *Tidsskr. Nor. Laegeforen.* **1989**, *109*, 3582–3585. (In Norwegian)
17. Risher, J. Toxicological Profile for Mercury. In *ATSDR's Toxicological Profiles*; ATSDR: Atlanta, GA, USA, 2010.
18. Rooney, J.P.K. The retention time of inorganic mercury in the brain—A systematic review of the evidence. *Toxicol. Appl. Pharmacol.* **2014**, *274*, 425–435. [CrossRef] [PubMed]
19. Pendergrass, J.C.; Haley, B.E.; Vimy, M.J.; Winfield, S.A.; Lorscheider, F.L. Mercury vapor inhalation inhibits binding of GTP to tubulin in rat brain: Similarity to a molecular lesion in Alzheimer diseased brain. *Neurotoxicology* **1997**, *18*, 315–324. [PubMed]
20. Bjørklund, G.; Tinkov, A.A.; Dadar, M.; Rahman, M.M.; Chirumbolo, S.; Skalny, A.V.; Skalnaya, M.G.; Haley, B.E.; Ajsuvakova, O.P.; Aaseth, J. Insights into the Potential Role of Mercury in Alzheimer's Disease. *J. Mol. Neurosci.* **2019**, *67*, 511–533. [CrossRef] [PubMed]
21. Ask, K.; Åkesson, A.; Berglund, M.; Vahter, M. Inorganic mercury and methylmercury in placentas of Swedish women. *Environ. Health Perspect.* **2002**, *110*, 523–526. [CrossRef]
22. Björnberg, K.A.; Vahter, M.; Petersson-Grawé, K.; Glynn, A.; Cnattingius, S.; Darnerud, P.O.; Atuma, S.; Aune, M.; Becker, W.; Berglund, M. Methyl mercury and inorganic mercury in Swedish pregnant women and in cord blood: Influence of fish consumption. *Environ. Health Perspect.* **2003**, *111*, 637–641.
23. Aaseth, J.; Hilt, B.; Bjørklund, G. Mercury exposure and health impacts in dental personnel. *Environ. Res.* **2018**, *164*, 65–69. [CrossRef] [PubMed]
24. Bjørklund, G.; Hilt, B.; Dadar, M.; Lindh, U.; Aaseth, J. Neurotoxic effects of mercury exposure in dental personnel. *Basic Clin. Pharmacol. Toxicol.* **2019**, *124*, 568–574. [CrossRef]
25. Mathiesen, T.; Ellingsen, D.G.; Kjuus, H. Neuropsychological effects associated with exposure to mercury vapor among former chloralkali workers. *Scand. J. Work Environ. Health* **1999**, *25*, 342–350. [CrossRef]
26. Albers, J.W.; Kallenbach, L.R.; Fine, L.J.; Langolf, G.D.; Wolfe, R.A.; Donofrio, P.D.; Alessi, A.G.; Stolp-Smith, K.A.; Bromberg, M.B. Neurological abnormalities associated with remote occupational elemental mercury exposure. *Ann. Neurol.* **1988**, *24*, 651–659. [CrossRef]

27. Letz, R.; Gerr, F.; Cragle, D.; Green, R.; Watkins, J.; Fidler, A. Residual neurologic deficits 30 years after occupational exposure to elemental mercury. *Neurotoxicology* **2000**, *21*, 459–474. [PubMed]

28. Clarkson, T.W.; Magos, L. The toxicology of mercury and its chemical compounds. *Crit. Rev. Toxicol.* **2006**, *36*, 609–662. [CrossRef] [PubMed]

29. International Programme on Chemical Safety (IPCS). *Inorganic Mercury, Environmental Health Criteria 118*; World Health Organization: Geneva, Switzerland, 1991.

30. Brooks, W.E. Industrial Use of Mercury in the Ancient World. In *Mercury in the Environment*; USGS: Reston, VA, USA, 2012.

31. Buckell, M.; Hunter, D.; Milton, R.; Perry, K.M. Chronic mercury poisoning. *Br. J. Ind. Med.* **1993**, *50*, 97–106. [CrossRef] [PubMed]

32. Park, J.D.; Zheng, W. Human exposure and health effects of inorganic and elemental mercury. *J. Prev. Med. Public Health* **2012**, *45*, 344–352. [CrossRef] [PubMed]

33. WHO. *Exposure to Mercury: A Major Public Health Concern*; WHO: Geneva, Switzerland, 2006.

34. Likens, G.E. *Biogeochemistry of Inland Waters*; Academic Press: Cambridge, MA, USA, 2010; ISBN 9780123819963.

35. Grandjean, P.; Satoh, H.; Murata, K.; Eto, K. Adverse effects of methylmercury: Environmental health research implications. *Environ. Health Perspect.* **2010**, *118*, 1137–1145. [CrossRef] [PubMed]

36. Harada, M. Minamata Disease: Methylmercury Poisoning in Japan Caused by Environmental Pollution. *Crit. Rev. Toxicol.* **1995**, *25*, 1–24. [CrossRef]

37. Hinton, J.; Veiga, M. Mercury contaminated sites: A review of remedial solutions. In Proceedings of the National Institute for Minamata Disease, Kumamoto, Japan, 1 March 2001.

38. Amin Zaki, L.; Elhassani, S.; Majeed, M.A.; Clarkson, T.W.; Doherty, R.A.; Greenwood, M.R.; Giovanoli-Jakubczak, T. Perinatal Methylmercury Poisoning in Iraq. *Am. J. Dis. Child.* **1976**, *130*, 1070–1076. [CrossRef] [PubMed]

39. Clarkson, T.W.; Vyas, J.B.; Ballatori, N. Mechanisms of mercury disposition in the body. *Am. J. Ind. Med.* **2007**, *50*, 757–764. [CrossRef] [PubMed]

40. Fernandes Azevedo, B.; Barros Furieri, L.; Peçanha, F.M.; Wiggers, G.A.; Frizera Vassallo, P.; Ronacher Simões, M.; Fiorim, J.; Rossi de Batista, P.; Fioresi, M.; Rossoni, L.; et al. Toxic Effects of Mercury on the Cardiovascular and Central Nervous Systems. *J. Biomed. Biotechnol.* **2012**. [CrossRef]

41. Cariccio, V.L.; Samà, A.; Bramanti, P.; Mazzon, E. Mercury Involvement in Neuronal Damage and in Neurodegenerative Diseases. *Biol. Trace Elem. Res.* **2019**, *187*, 341–356. [CrossRef] [PubMed]

42. Vejrup, K.; Brandlistuen, R.E.; Brantsæter, A.L.; Knutsen, H.K.; Caspersen, I.H.; Alexander, J.; Lundh, T.; Meltzer, H.M.; Magnus, P.; Haugen, M. Prenatal mercury exposure, maternal seafood consumption and associations with child language at five years. *Environ. Int.* **2018**, *110*, 71–79. [CrossRef] [PubMed]

43. Bjørklund, G.; Skalny, A.V.; Rahman, M.M.; Dadar, M.; Yassa, H.A.; Aaseth, J.; Chirumbolo, S.; Skalnaya, M.G.; Tinkov, A.A. Toxic metal (loid)-based pollutants and their possible role in autism spectrum disorder. *Environ. Res.* **2018**, *166*, 234–250. [CrossRef] [PubMed]

44. IARC. *IARC Monographs on the Evaluation of the Carcinogenic Risk of Chemicals to Man*; IARC: Lyon, France, 1993.

45. Remelli, M.; Nurchi, V.M.; Lachowicz, J.I.; Medici, S.; Zoroddu, M.A.; Peana, M. Competition between Cd (II) and other divalent transition metal ions during complex formation with amino acids, peptides, and chelating agents. *Coord. Chem. Rev.* **2016**, *327–328*, 55–69. [CrossRef]

46. IARC. *IARC Monographs on the Evaluation of Carcinogenic Risks to Humans. Painting, Firefighting, and Shiftwork*; IARC: Lyon, France, 2010; Volume 100.

47. EFSA. Cadmium in food-Scientific opinion of the Panel on Contaminants in the Food Chain: Cadmium in food-Scientific opinion of the Panel on Contaminants in the Food Chain. *EFSA J.* **2009**, *7*, 980.

48. WHO. *Exposure to Cadmium: A Major Public Health Concern*; WHO: Geneva, Switzerland, 2010.

49. Crea, F.; Foti, C.; Milea, D.; Sammartano, S. Speciation of Cadmium in the Environment. In *Cadmium: From Toxicity to Essentiality*; Sigel, A., Sigel, H., Sigel, R.K.O., Eds.; Springer Science & Business Media: Dordrecht, The Netherlands, 2013; Chapter 3; Volume 11, pp. 63–83.

50. Järup, L.; Åkesson, A. Current status of cadmium as an environmental health problem. *Toxicol. Appl. Pharmacol.* **2009**, *238*, 201–208. [CrossRef] [PubMed]

51. Satarug, S. Dietary Cadmium Intake and Its Effects on Kidneys. *Toxics* **2018**, *6*, 15. [CrossRef]

52. Satarug, S.; Vesey, D.A.; Gobe, G.C. Current health risk assessment practice for dietary cadmium: Data from different countries. *Food Chem. Toxicol.* **2017**, *106*, 430–445. [CrossRef]

53. Olsson, I.M.; Bensryd, I.; Lundh, T.; Ottosson, H.; Skerfving, S.; Oskarsson, A. Cadmium in blood and urine —Impact of sex, age, dietary intake, iron status, and former smoking—Association of renal effects. *Environ. Health Perspect.* **2002**, *110*, 1185–1190. [CrossRef]

54. FAO/WHO; Food and Agriculture Organization of the United Nations; World Health Organization. *Seventy-third Meeting, Geneva, 8–17 June 2010. Summary and Conclusions. JECFA/73/SC.* 2010. Available online: http://www.who.int/foodsafety/publications/chem/summary73.pdf (accessed on 28 July 2019).

55. Mortensen, M.E.; Wong, L.Y.; Osterloh, J.D. Smoking status and urine cadmium above levels associated with subclinical renal effects in U.S. adults without chronic kidney disease. *Int. J. Hyg. Environ. Health* **2011**, *214*, 305–310. [CrossRef]

56. Zhang, H.; Reynolds, M. Cadmium exposure in living organisms: A short review. *Sci. Total Environ.* **2019**, *678*, 761–767. [CrossRef]

57. Aoshima, K. Itai-itai disease: Renal tubular osteomalacia induced by environmental exposure to cadmium—Historical review and perspectives. *Soil Sci. Plant Nutr.* **2016**, *62*, 319–326. [CrossRef]

58. Suwazono, Y.; Kido, T.; Nakagawa, H.; Nishijo, M.; Honda, R.; Kobayashi, E.; Dochi, M.; Nogawa, K. Biological half-life of cadmium in the urine of inhabitants after cessation of cadmium exposure. *Biomarkers* **2009**, *14*, 77–81. [CrossRef] [PubMed]

59. Fransson, M.N.; Barregard, L.; Sallsten, G.; Akerstrom, M.; Johanson, G. Physiologically-based toxicokinetic model for cadmium using markov-chain monte carlo analysis of concentrations in blood, urine, and kidney cortex from living kidney donors. *Toxicol. Sci.* **2014**, *141*, 365–376. [CrossRef] [PubMed]

60. Mezynska, M.; Brzóska, M.M. Environmental exposure to cadmium—A risk for health of the general population in industrialized countries and preventive strategies. *Environ. Sci. Pollut. Res.* **2018**, *25*, 3211–3232. [CrossRef] [PubMed]

61. Hyder, O.; Chung, M.; Cosgrove, D.; Herman, J.M.; Li, Z.; Firoozmand, A.; Gurakar, A.; Koteish, A.; Pawlik, T.M. Cadmium Exposure and Liver Disease among US Adults. *J. Gastrointest. Surg.* **2013**, *17*, 1265–1273. [CrossRef] [PubMed]

62. James, K.A.; Meliker, J.R. Environmental cadmium exposure and osteoporosis: A review. *Int. J. Public Health* **2013**, *58*, 737–745. [CrossRef] [PubMed]

63. Deering, K.E.; Callan, A.C.; Prince, R.L.; Lim, W.H.; Thompson, P.L.; Lewis, J.R.; Hinwood, A.L.; Devine, A. Low-level cadmium exposure and cardiovascular outcomes in elderly Australian women: A cohort study. *Int. J. Hyg. Environ. Health* **2018**, *221*, 347–354. [CrossRef] [PubMed]

64. Wang, Y.X.; Sun, Y.; Feng, W.; Wang, P.; Yang, P.; Li, J.; Huang, Z.; Chen, Y.J.; Liu, C.; Sun, L.; et al. Association of urinary metal levels with human semen quality: A cross-sectional study in China. *Environ. Int.* **2016**, *91*, 51–59. [CrossRef]

65. Silva, N.; Peiris-John, R.; Wickremasinghe, R.; Senanayake, H.; Sathiakumar, N. Cadmium a metalloestrogen: Are we convinced? *J. Appl. Toxicol.* **2012**, *32*, 318–332. [CrossRef]

66. Chen, X.; Zhu, G.; Jin, T. Effects of Cadmium Exposure on Age of Menarche and Menopause. *Toxics* **2017**, *6*, 6. [CrossRef]

67. Buha, A.; Matovic, V.; Antonijevic, B.; Bulat, Z.; Curcic, M.; Renieri, E.A.; Tsatsakis, A.M.; Schweitzer, A.; Wallace, D. Overview of cadmium thyroid disrupting effects and mechanisms. *Int. J. Mol. Sci.* **2018**, *19*, 1501. [CrossRef] [PubMed]

68. Xing, Y.; Xia, W.; Zhang, B.; Zhou, A.; Huang, Z.; Zhang, H.; Liu, H.; Jiang, Y.; Hu, C.; Chen, X.; et al. Relation between cadmium exposure and gestational diabetes mellitus. *Environ. Int.* **2018**, *113*, 300–305. [CrossRef] [PubMed]

69. Jacquet, A.; Ounnas, F.; Lénon, M.; Arnaud, J.; Demeilliers, C.; Moulis, J.-M. Chronic Exposure to Low-Level Cadmium in Diabetes: Role of Oxidative Stress and Comparison with Polychlorinated Biphenyls. *Curr. Drug Targets* **2016**, *17*, 1385–1413. [CrossRef] [PubMed]

70. Renieri, E.A.; Sfakianakis, D.G.; Alegakis, A.A.; Safenkova, I.V.; Buha, A.; Matović, V.; Tzardi, M.; Dzantiev, B.B.; Divanach, P.; Kentouri, M.; et al. Nonlinear responses to waterborne cadmium exposure in zebrafish. An in vivo study. *Environ. Res.* **2017**, *157*, 173–181. [CrossRef] [PubMed]

71. International Agency for Research on Cancer (IARC). *IARC Cadmium and Cadmium Compounds*; 100C ed.; WHO Press: Lyon, France, 2012; Volume 100C.

72. Buha, A.; Wallace, D.; Matovic, V.; Schweitzer, A.; Oluic, B.; Micic, D.; Djordjevic, V. Cadmium Exposure as a Putative Risk Factor for the Development of Pancreatic Cancer: Three Different Lines of Evidence. *BioMed Res. Int.* **2017**, *2017*, 1981837. [CrossRef] [PubMed]

73. Djordjevic, V.R.; Wallace, D.R.; Schweitzer, A.; Boricic, N.; Knezevic, D.; Matic, S.; Grubor, N.; Kerkez, M.; Radenkovic, D.; Bulat, Z.; et al. Environmental cadmium exposure and pancreatic cancer: Evidence from case control, animal and in vitro studies. *Environ. Int.* **2019**, *128*, 353–361. [CrossRef] [PubMed]

74. Feki-Tounsi, M.; Hamza-Chaffai, A. Cadmium as a possible cause of bladder cancer: A review of accumulated evidence. *Environ. Sci. Pollut. Res.* **2014**, *21*, 10561–10573. [CrossRef]

75. Vinceti, M.; Venturelli, M.; Sighinolfi, C.; Trerotoli, P.; Bonvicini, F.; Ferrari, A.; Bianchi, G.; Serio, G.; Bergomi, M.; Vivoli, G. Case-control study of toenail cadmium and prostate cancer risk in Italy. *Sci. Total Environ.* **2007**, *373*, 77–81. [CrossRef]

76. Van Maele-Fabry, G.; Lombaert, N.; Lison, D. Dietary exposure to cadmium and risk of breast cancer in postmenopausal women: A systematic review and meta-analysis. *Environ. Int.* **2016**, *86*, 1–13. [CrossRef]

77. Matović, V.; Buha, A.; Dukić-Ćosić, D.; Bulat, Z. Insight into the oxidative stress induced by lead and/or cadmium in blood, liver and kidneys. *Food Chem. Toxicol.* **2015**, *78*, 130–140. [CrossRef]

78. Matović, V.; Buha, A.; Bulat, Z.; Đukić-Ćosić, D. Cadmium Toxicity Revisited: Focus on Oxidative Stress Induction and Interactions with Zinc and Magnesium. *Arch. Ind. Hyg. Toxicol.* **2011**, *62*, 65–76. [CrossRef] [PubMed]

79. Bulat, Z.; Dukić-Ćosić, D.; Antonijević, B.; Buha, A.; Bulat, P.; Pavlović, Z.; Matović, V. Can zinc supplementation ameliorate cadmium-induced alterations in the bioelement content in rabbits? *Arh. Hig. Rada Toksikol.* **2017**, *68*, 38–45. [CrossRef] [PubMed]

80. Bulat, Z.; Đukić-Ćosić, D.; Antonijević, B.; Bulat, P.; Vujanović, D.; Buha, A.; Matović, V. Effect of Magnesium Supplementation on the Distribution Patterns of Zinc, Copper, and Magnesium in Rabbits Exposed to Prolonged Cadmium Intoxication. *Sci. World J.* **2012**, *2012*, 572514. [CrossRef] [PubMed]

81. Buha, A.; Bulat, Z.; Dukic-Cosic, D.; Matovic, V. Effects of oral and intraperitoneal magnesium treatment against cadmium-induced oxidative stress in plasma of rats. *Arch. Ind. Hyg. Toxicol.* **2012**, *63*, 247–254. [CrossRef] [PubMed]

82. Buha, A.; Jugdaohsingh, R.; Matovic, V.; Bulat, Z.; Antonijevic, B.; Kerns, J.G.; Goodship, A.; Hart, A.; Powell, J.J. Bone mineral health is sensitively related to environmental cadmium exposure-experimental and human data. *Environ. Res.* **2019**, *176*, 108539. [CrossRef] [PubMed]

83. Wallace, D.; Spandidos, D.; Tsatsakis, A.; Schweitzer, A.; Djordjevic, V.; Djordjevic, A. Potential interaction of cadmium chloride with pancreatic mitochondria: Implications for pancreatic cancer. *Int. J. Mol. Med.* **2019**, *44*, 145–156. [CrossRef] [PubMed]

84. Fay, M.; Alt, L.; Ryba, D.; Salamah, R.; Peach, R.; Papaeliou, A.; Zawadzka, S.; Weiss, A.; Patel, N.; Rahman, A.; et al. Cadmium Nephrotoxicity Is Associated with Altered MicroRNA Expression in the Rat Renal Cortex. *Toxics* **2018**, *6*, 16. [CrossRef] [PubMed]

85. Papanikolaou, N.C.; Hatzidaki, E.G.; Belivanis, S.; Tzanakakis, G.N.; Tsatsakis, A.M. Lead toxicity update. A brief review. *Med. Sci. Monit.* **2005**, *11*, 329–336.

86. Patrick, L. Lead toxicity, a review of the literature. Part I: Exposure, evaluation, and treatment. *Altern. Med. Rev.* **2006**, *11*, 2–22.

87. Oudijk, G. The rise and fall of organometallic additives in automotive gasoline. *Environ. Forensics* **2010**, *11*, 17–49. [CrossRef]

88. Maas, R.P.; Patch, S.C.; Morgan, D.M.; Pandolfo, T.J. Reducing lead exposure from drinking water: Recent history and current status. *Public Health Rep.* **2005**, *120*, 316–321. [CrossRef] [PubMed]

89. Casas, S.J.; Sordo, J. *Lead Chemistry, Analytical Aspects, Environmental Impact and Health Effects*; Elsevier: Amsterdam, The Netherlands, 2006; ISBN 9780444529459.

90. EFSA (European Food Safety Authority). Scientific Opinion on Lead in Food. *EFSA J.* **2010**, *8*, 1570. [CrossRef]

91. Laidlaw, M.A.S.; Filippelli, G.M.; Sadler, R.C.; Gonzales, C.R.; Ball, A.S.; Mielke, H.W. Children's blood lead seasonality in flint, Michigan (USA), and soil-sourced lead hazard risks. *Int. J. Environ. Res. Public Health* **2016**, *13*, 358. [CrossRef]

92. Safruk, A.M.; McGregor, E.; Whitfield Aslund, M.L.; Cheung, P.H.; Pinsent, C.; Jackson, B.J.; Hair, A.T.; Lee, M.; Sigal, E.A. The influence of lead content in drinking water, household dust, soil, and paint on blood lead levels of children in Flin Flon, Manitoba and Creighton, Saskatchewan. *Sci. Total Environ.* **2017**, *593–594*, 202–210. [CrossRef] [PubMed]

93. O'Connor, D.; Hou, D.; Ye, J.; Zhang, Y.; Ok, Y.S.; Song, Y.; Coulon, F.; Peng, T.; Tian, L. Lead-based paint remains a major public health concern: A critical review of global production, trade, use, exposure, health risk, and implications. *Environ. Int.* **2018**, *121*, 85–101. [CrossRef] [PubMed]

94. Philip, A.T.; Gerson, B. Lead poisoning—Part I. Incidence, etiology, and toxicokinetics. *Clin. Lab. Med.* **1994**, *14*, 423–444. [CrossRef]

95. Markowitz, M. Lead poisoning: A disease for the next millennium. *Curr. Probl. Pediatr.* **2000**, *30*, 62–70. [CrossRef] [PubMed]

96. Gulson, B.L.; Mizon, K.J.; Korsch, M.J.; Palmer, J.M.; Donnelly, J.B. Mobilization of lead from human bone tissue during pregnancy and lactation—A summary of long-term research. *Sci. Total Environ.* **2003**, *303*, 79–104. [CrossRef]

97. Abadin, H.; Ashizawa, A.; Llados, F.; Stevens, Y.W. Toxicological Profile for Lead. In *ATSDR's Toxicological Profiles*; ATSDR: Atlanta, GA, USA, 2010.

98. Bjørklund, G.; Dadar, M.; Chirumbolo, S.; Aaseth, J. High content of lead is associated with the softness of drinking water and raised cardiovascular morbidity: A review. *Biol. Trace Elem. Res.* **2018**, *186*, 384–394. [CrossRef] [PubMed]

99. American Academy of Pediatrics Committee on Environmental Health. Lead exposure in children: Prevention, detection, and management; CCHMC guideline. *Pediatrics* **2005**, *116*, 1036. [CrossRef]

100. Grandjean, P. Even low-dose lead exposure is hazardous. *Lancet* **2010**, *376*, 855–856. [CrossRef]

101. IARC Working Group on the Evaluation of Carcinogenic Risks to Humans. Inorganic and Organic Lead Compounds. *IARC Monogr. Eval. Carcinog. Risks Hum.* **2006**, *87*, 1.

102. Andjelkovic, M.; Djordjevic, A.B.; Antonijevic, E.; Antonijevic, B.; Stanic, M.; Kotur-Stevuljevic, J.; Spasojevic-Kalimanovska, V.; Jovanovic, M.; Boricic, N.; Wallace, D.; et al. Toxic effect of acute cadmium and lead exposure in rat blood, liver, and kidney. *Int. J. Environ. Res. Public Health* **2019**, *16*, 274. [CrossRef] [PubMed]

103. Ahmed, Y.F.; Eldebaky, H.A.A.; Mahmoud, K.G.M.; Nawito, M. Effects of lead exposure on DNA damage and apoptosis in reproductive and vital organs in female rabbits. *Glob. Vet.* **2012**, *9*, 401–408.

104. Margoshes, M.; Valiee, B.L. A Cadmium Protein from Equine Kidney Cortex. *J. Am. Chem. Soc.* **1957**, *79*, 4813–4814. [CrossRef]

105. Felizola, S.J.A.; Nakamura, Y.; Arata, Y.; Ise, K.; Satoh, F.; Rainey, W.E.; Midorikawa, S.; Suzuki, S.; Sasano, H. Metallothionein-3 (MT-3) in the Human Adrenal Cortex and its Disorders. *Endocr. Pathol.* **2013**, *25*, 229–235. [CrossRef]

106. Coyle, P.; Philcox, J.C.; Carey, L.C.; Rofe, A.M. Metallothionein: The multipurpose protein. *Cell. Mol. Life Sci.* **2002**, *59*, 627–647. [CrossRef] [PubMed]

107. Lee, S.J.; Koh, J.Y. Roles of zinc and metallothionein-3 in oxidative stress-induced lysosomal dysfunction, cell death, and autophagy in neurons and astrocytes. *Mol. Brain* **2010**, *3*, 30. [CrossRef]

108. Kumari, M.V.R.; Hiramatsu, M.; Ebadi, M. Free radical scavenging actions of metallothionein isoforms I and II. *Free Radic. Res.* **1998**, *29*, 93–101. [CrossRef]

109. Bolognin, S.; Cozzi, B.; Zambenedetti, P.; Zatta, P. Metallothioneins and the central nervous system: From a deregulation in neurodegenerative diseases to the development of new therapeutic approaches. *J. Alzheimer's Dis.* **2014**, *41*, 29–42. [CrossRef]

110. Couto, N.; Malys, N.; Gaskell, S.J.; Barber, J. Partition and turnover of glutathione reductase from saccharomyces cerevisiae: A proteomic approach. *J. Proteome Res.* **2013**, *12*, 2885–2894. [CrossRef] [PubMed]

111. Ballatori, N.; Clarkson, T.W. Sulfobromophthalein inhibition of glutathione and methylmercury secretion into bile. *Am. J. Physiol. Liver Physiol.* **2017**, *248*, 238–245. [CrossRef] [PubMed]

112. Alexander, J.; Aaseth, J. Biliary excretion of copper and zinc in the rat as influenced by diethylmaleate, selenite and diethyldithiocarbamate. *Biochem. Pharmacol.* **1980**, *29*, 2129–2133. [CrossRef]

113. Cigala, R.M.; Crea, F.; De Stefano, C.; Lando, G.; Milea, D.; Sammartano, S. Modeling the acid-base properties of glutathione in different ionic media, with particular reference to natural waters and biological fluids. *Amino Acids* **2013**, *43*, 629–648. [CrossRef] [PubMed]

114. Morgan, G.T.; Drew, H.D.K. CLXII.—Researches on residual affinity and co-ordination. Part II. Acetylacetones of selenium and tellurium. *J. Chem. Soc. Trans.* **1920**, *117*, 1456–1465. [CrossRef]

115. Aaseth, J. Recent Advance in the Therapy of Metal Poisonings with Chelating Agents. *Hum. Exp. Toxicol.* **1983**, *2*, 257–272. [CrossRef]

116. Aaseth, J.; Crisponi, G.; Anderson, O. *Chelation Therapy in the Treatment of Metal Intoxication*; Academic Press: Cambridge, MA, USA, 2016; ISBN 9780128030721.

117. Crisponi, G.; M Nurchi, V.; Crespo-Alonso, M.; Toso, L. Chelating Agents for Metal Intoxication. *Curr. Med. Chem.* **2012**, *7*, 2745–2788.

118. Aaseth, J.; Ajsuvakova, O.P.; Skalny, A.V.; Skalnaya, M.G.; Tinkov, A.A. Chelator combination as therapeutic strategy in mercury and lead poisonings. *Coord. Chem. Rev.* **2018**, *358*, 1–12. [CrossRef]

119. Voegtlin, C.; Smith, H.W.; Crane, M.M.; Wright, K.D.; Connell, M.A. Quantitative Studies in Chemotherapy: I. *The Trypanocidal Action of Arsenic and Antimony Compounds. J. Pharmacol. Exp. Ther.* **1920**, *15*, 453–473.

120. Kety, S.S.; Letonoff, T.V. Treatment of lead poisoning by sodium citrate. *Amer. J.Med. Sci.* **1943**, *205*, 406–414. [CrossRef]

121. Peters, R.A. Development and theortical significance of british anti-lewisite (bal). *Br. Med. Bull.* **1948**, *5*, 313–318. [CrossRef] [PubMed]

122. Smith, H.D. Lead poisoning in children and its therapy with EDTA. *Ind. Med. Surg.* **1959**, *28*, 148–151. [PubMed]

123. Ding, G.-S.; Liang, Y.-Y. Antidotal effects of dimercaptosuccinic acid. *J. Appl. Toxicol.* **1991**, *11*, 7–14. [CrossRef] [PubMed]

124. Oginski, M. Use of unitiol for speeding up renal excretion of Chlormerodrin203Hg. *Int. Urol. Nephrol.* **1971**, *3*, 203–208. [CrossRef] [PubMed]

125. Aposhian, H.V.; Maiorino, R.M.; Gonzalez-Ramirez, D.; Zuniga-Charles, M.; Xu, Z.; Hurlbut, K.M.; Junco-Munoz, P.; Dart, R.C.; Aposhian, M.M. Mobilization of heavy metals by newer, therapeutically useful chelating agents. *Toxicology* **1995**, *97*, 23–38. [CrossRef]

126. Luetscher, J.A.; Eagle, H.; Long-cope, W.T. Clinical uses of 2,3-dimercaptopropanol (BAL); the effect of BAL on the excretion of arsenic in arsenical intoxication. *J. Clin. Investig.* **1946**, *25*, 534–540. [CrossRef] [PubMed]

127. Longcope, W.T.; Luetscher, J.A. Clinical uses of 2,3-dimercaptopropanol (BAL); the treatment of acute mercury poisoning by BAL. *J. Clin. Investig.* **1946**, *25*, 557–567. [CrossRef] [PubMed]

128. Berlin, M.; Ullrebg, S. Increased uptake of mercury in mouse brain caused by 2,3-dimercaptopropanol. *Nature* **1963**, *197*, 84–85. [CrossRef] [PubMed]

129. Cao, Y.; Skaug, M.A.; Andersen, O.; Aaseth, J. Chelation therapy in intoxications with mercury, lead and copper. *J. Trace Elem. Med. Biol.* **2015**, *31*, 188–192. [CrossRef]

130. Andersen, O. Principles and recent developments in chelation treatment of metal intoxication. *Chem. Rev.* **1999**, *99*, 2683–2710. [CrossRef]

131. Chisolm, J.J. The use of chelating agents in the treatment of acute and chronic lead intoxication in childhood. *J. Pediatr.* **1968**, *73*, 1–38. [CrossRef]

132. Andersen, O.; Aaseth, J. Molecular mechanisms of in vivo metal chelation: Implications for clinical treatment of metal intoxications. *Environ. Health Perspect.* **2002**, *110*, 887–890. [CrossRef] [PubMed]

133. Bjørklund, G.; Mutter, J.; Aaseth, J. Metal chelators and neurotoxicity: Lead, mercury, and arsenic. *Arch. Toxicol.* **2017**, *91*, 3787–3797. [CrossRef] [PubMed]

134. Maiorino, R.M.; Akins, J.M.; Blaha, K.; Carter, D.E.; Aposhian, H.V. Determination and metabolism of dithiol chelating agents: X. In humans, meso-2,3-dimercaptosuccinic acid is bound to plasma proteins via mixed disulfide formation. *J. Pharmacol. Exp. Ther.* **1990**, *254*, 570–577. [PubMed]

135. Dart, R.C.; Hurlbut, K.M.; Maiorino, R.M.; Mayersohn, M.; Aposhian, H.V.; Hassen, L.V.B. Pharmacokinetics of meso-2,3-dimercaptosuccinic acid in patients with lead poisoning and in healthy adults. *J. Pediatr.* **1994**, *125*, 309–316. [CrossRef]

136. Sears, M.E. Chelation: Harnessing and Enhancing Heavy Metal Detoxification—A Review. *Sci. World J.* **2013**, *2013*, 219840. [CrossRef] [PubMed]

137. Miller, A.L. Dimercaptosuccinic acid (DMSA), a non-toxic, water-soluble treatment for heavy metal toxicity. *Altern. Med. Rev.* **1998**, *3*, 199–207.

138. Aposhian, H.V.; Maiorino, R.M.; Dart, R.C.; Perry, D.F. Urinary excretion of meso-2,3-dimercaptosuccinic acid in human subjects. *Clin. Pharmacol. Ther.* **1989**, *45*, 520–526. [CrossRef]

139. Asledu, P.; Moulton, T.; Blum, C.B.; Roldan, E.; Lolacono, N.J.; Graziano, J.H. Metabolism of meso-2,3-dimercaptosuccinic acid in lead-poisoned children and normal adults. *Environ. Health Perspect.* **1995**, *103*, 734–739.

140. Bradberry, S.; Vale, A. Dimercaptosuccinic acid (succimer; DMSA) in inorganic lead poisoning. *Clin. Toxicol.* **2009**, *47*, 617–631. [CrossRef]

141. Aaseth, J.; Jacobsen, D.; Andersen, O.; Wickstrøm, E. Treatment of mercury and lead poisonings with dimercaptosuccinic acid and sodium dimercaptopropanesulfonate: A review. *Analyst* **1995**, *120*, 853–854. [CrossRef] [PubMed]

142. Aaseth, J.; Friedheim, E.A.H. Treatment of Methyl Mercury Poisoning in Mice with 2,3-dimercaptosuccinic Acid and other Complexing Thiols. *Acta Pharmacol. Toxicol.* **1978**, *42*, 248–252. [CrossRef] [PubMed]

143. Grandjean, P.; Guldager, B.; Larsen, I.B.; Jørgensen, P.J.; Holmstrup, P. Placebo response in environmental disease: Chelation therapy of patients with symptoms attributed to amalgam fillings. *J. Occup. Environ. Med.* **1997**, *39*, 707–714. [CrossRef] [PubMed]

144. Aposhian, H.V. DMSA and DMPS-Water Soluble Antidotes for Heavy Metal Poisoning. *Annu. Rev. Pharmacol. Toxicol.* **2003**, *23*, 193–215. [CrossRef] [PubMed]

145. George, G.N.; Prince, R.C.; Gailer, J.; Buttigieg, G.A.; Denton, M.B.; Harris, H.H.; Pickering, I.J. Mercury binding to the chelation therapy agents DMSA and DMPS and the rational design of custom chelators for mercury. *Chem. Res. Toxicol.* **2004**, *17*, 999–1006. [CrossRef] [PubMed]

146. Graziano, J.H. Role of 2,3-Dimercaptosuccinic Acid in the Treatment of Heavy Metal Poisoning. *Med. Toxicol.* **1986**, *1*, 155–162. [CrossRef] [PubMed]

147. Ramsey, D.T.; Casteel, S.W.; Faggella, A.M.; Chastain, C.B.; Nunn, J.W.; Schaeffer, D.J. Use of orally administered succimer (meso-2,3-dimercaptosuccinic acid) for treatment of lead poisoning in dogs. *J. Am. Vet. Med. Assoc.* **1996**, *208*, 371–375.

148. Roels, H.A.; Boeckx, M.; Ceulemans, E.; Lauwerys, R.R. Urinary excretion of mercury after occupational exposure to mercury vapour and influence of the chelating agent meso-2,3-dimercaptosuccinic acid (DMSA). *Occup. Environ. Med.* **2008**, *48*, 247–253. [CrossRef] [PubMed]

149. Gustavsson, P.; Gerhardsson, L. Intoxication from an accidentally ingested lead shot retained in the gastrointestinal tract. *Environ. Health Perspect.* **2005**, *113*, 491–493. [CrossRef]

150. Flora, S.J.S.; Pachauri, V. Chelation in metal intoxication. *Int. J. Environ. Res. Public Health* **2010**, *7*, 2745–2788. [CrossRef]

151. Gersl, V.; Hrdina, R.; Vavrova, J.; Holeckova, M.; Palicka, V.; Vogkova, J.; Mazurova, Y.; Bajgar, J. Effects of repeated administration of dithiol chelating agent-sodium 2,3-dimercapto 1-propanesulphonate (DMPS)-on biochemical and hematological parameters in rabbits. *Acta. Medica.* **1997**, *40*, 3–8. [PubMed]

152. Hurlbut, K.M.; Maiorino, R.M.; Mayersohn, M.; Dart, R.C.; Bruce, D.C.; Aposhian, H.V. Determination and metabolism of dithiol chelating agents. XVI: Pharmacokinetics of 2,3-dimercapto-1-propanesulfonate after intravenous administration to human volunteers. *J. Pharmacol. Exp. Ther.* **1994**, *268*, 662–668.

153. Gabard, B. Distribution and excretion of the mercury chelating agent sodium 2,3-dimercaptopropane-1-sulfonate in the rat. *Arch. Toxicol.* **1978**, *39*, 289–298. [CrossRef] [PubMed]

154. Torres-Alanís, O.; Garza-Ocañas, L.; Bernal, M.A.; Piñeyro-López, A. Urinary excretion of trace elements in humans after sodium 2,3-dimercaptopropane-1-sulfonate challenge test. *J. Toxicol. Clin. Toxicol.* **2000**, *38*, 697–700. [CrossRef]

155. Walshe, J.M. Penicillamine, a new oral therapy for Wilson's disease. *Am. J. Med.* **1956**, *21*, 487–495. [CrossRef]

156. Rodriguez-Castro, K.I.; Hevia-Urrutia, F.J.; Sturniolo, G.C. Wilson's disease: A review of what we have learned. *World J. Hepatol.* **2015**, *7*, 2859–2870. [CrossRef] [PubMed]

157. Horn, N.; Møller, L.B.; Nurchi, V.M.; Aaseth, J. Chelating principles in Menkes and Wilson diseases: Choosing the right compounds in the right combinations at the right time. *J. Inorg. Biochem.* **2019**, *190*, 98–112. [CrossRef] [PubMed]

158. Patrick, L. Mercury toxicity and antioxidants: Part I: Role of glutathione and alpha-lipoic acid in the treatment of mercury toxicity. *Altern. Med. Rev.* **2002**, *7*, 456–471. [PubMed]

159. Bjørklund, G.; Aaseth, J.; Crisponi, G.; Rahman, M.M.; Chirumbolo, S. Insights on alpha lipoic and dihydrolipoic acids as promising scavengers of oxidative stress and possible chelators in mercury toxicology. *J. Inorg. Biochem.* **2019**, *195*, 111–119. [CrossRef] [PubMed]

160. Bakka, A.; Aaseth, J.; Rugstad, H.E. Influence of Certain Chelating Agents on Egress of Cadmium from Cultured Epithelial Cells Containing High Amounts of Metallothionein: A Screening of Cd-Releasing and Toxic Effects. *Acta Pharmacol. Toxicol.* **1981**, *49*, 432–437. [CrossRef] [PubMed]

161. Jones, M.M.; Singh, P.K.; Gale, G.R.; Smith, A.B.; Atkins, L.M. Cadmium Mobilization in Vivo by Intraperitoneal or Oral Administration of Monoalkyl Esters of meso–2, 3–Dmercaptosuccinic Acid in the Mouse. *Pharmacol. Toxicol.* **1992**, *70*, 336–343. [CrossRef] [PubMed]

162. Ram Kumar, M.; Flora, S.J.S.; Reddy, G.R. Monoisoamyl 2,3-dimercaptosuccinic acid attenuates arsenic induced toxicity: Behavioral and neurochemical approach. *Environ. Toxicol. Pharmacol.* **2013**, *36*, 231–242. [CrossRef] [PubMed]

163. Flora, S.J.S.; Bhadauria, S.; Pachauri, V.; Yadav, A. Monoisoamyl 2, 3-Dimercaptosuccinic Acid (MiADMSA) Demonstrates Higher Efficacy by Oral Route in Reversing Arsenic Toxicity: A Pharmacokinetic Approach. *Basic Clin. Pharmacol. Toxicol.* **2012**, *110*, 449–459. [CrossRef] [PubMed]

164. Kannan, G.M.; Flora, S.J.S. Combined administration of N-acetylcysteine and monoisoamyl DMSA on tissue oxidative stress during arsenic chelation therapy. *Biol. Trace Elem. Res.* **2006**, *110*, 43–59. [CrossRef]

165. Gale, G.R.; Smith, A.B.; Walker, E.M. Diethyldithiocarbamate in treatment of acute cadmium poisoning. *Ann. Clin. Lab. Sci.* **1981**, *11*, 476–483. [PubMed]

166. Aaseth, J.; Alexander, J.; Raknerud, N. Treatment of mercuric chloride poisoning with dimercaptosuccinic acid and diuretics: Preliminary studies. *Clin. Toxicol.* **1982**, *19*, 173–186. [CrossRef]

167. Oskarsson, A.; Lind, B. Increased Lead Levels in Brain after Long-term Treatment with Lead and Dithiocarbamate or Thiuram Derivatives in Rats. *Acta Pharmacol. Toxicol.* **1985**, *56*, 309–315. [CrossRef]

168. Kargačin, B.; Kostial, K.; Arežina, R.; Singh, P.K.; Jones, M.M.; Cikrt, M. Influence of age and time of administration of dithiocarbamate analogues on cadmium retention in rats. *J. Appl. Toxicol.* **1991**, *11*, 273–277. [CrossRef]

169. Hamidinia, S.A.; Erdahl, W.L.; Chapman, C.J.; Steinbaugh, G.E.; Taylor, R.W.; Pfeiffer, D.R. Monensin improves the effectiveness of meso-dimercaptosuccinate when used to treat lead intoxication in rats. *Environ. Health Perspect.* **2006**, *114*, 484–493. [CrossRef]

170. Chisolm, J.J. BAL, EDTA, DMSA and DMPS in the treatment of lead poisoning in children. *Clin. Toxicol.* **1992**, *30*, 493–504. [CrossRef]

171. Lee, B.K.; Schwartz, B.S.; Stewart, W.; Ahn, K.D. Provocative chelation with DMSA and EDTA: Evidence for differential access to lead storage sites. *Occup. Environ. Med.* **1995**, *52*, 13–19. [CrossRef] [PubMed]

172. Besunder, J.B.; Super, D.M.; Anderson, R.L. Comparison of dimercaptosuccinic acid and calcium disodium ethylenediaminetetraacetic acid versus dimercaptopropanol and ethylenediaminetetraacetic acid in children with lead poisoning. *J. Pediatr.* **1997**, *130*, 966–971. [CrossRef]

173. Dargan, P.I.; Giles, L.J.; Wallace, C.I.; House, I.M.; Thomson, A.H.; Beale, R.J.; Jones, A.L. Case report: Severe mercuric sulphate poisoning treated with 2,3-dimercaptopropane-1-sulphonate and haemodiafiltration. *Crit. Care* **2003**, *7*, R1–R6. [CrossRef]

174. Aragoni, M.C.; Arca, M.; Crisponi, G.; Cristiani, F.; Isaia, F.; Nurchi, V.M. Characterization of the ionization and spectral properties of mercapto-carboxylic acids. Correlation with substituents and structural features. *Talanta* **1996**, *43*, 1357–1366.

175. Arnold, A.P.; Canty, A.J.; Reid, R.S.; Rabenstein, D.L. Nuclear magnetic resonance and potentiometric studies of the complexation of methylmercury (II) by dithiols. *Can. J. Chem.* **2006**, *63*, 2430–2436. [CrossRef]

176. Sallam, S.A.; Bahgat, K.M.; El-Tanany, A.Z.; Mahmoud, M.A. Lanthanide complexes of D-penicillamine: Formation constants, spectral and thermal properties. *J. Coord. Chem.* **2006**, *59*, 2055–2073. [CrossRef]

177. Sigel, H.; Prijs, B.; McCormick, D.B.; Shih, J.C.H. Stability and structure of binary and ternary complexes of α-lipoate and lipoate derivatives with Mn2+, Cu2+, and Zn2+ in solution. *Arch. Biochem. Biophys.* **1978**, *187*, 208–214. [CrossRef]

178. Bonomi, F.; Pagani, S.; Cariati, F.; Pozzi, A.; Crisponi, G.; Cristiani, F.; Diaz, A.; Zanoni, R. Synthesis and characterization of metal derivatives of dihydrolipoic acid and dihydrolipoamide. *Inorg. Chim. Acta* **1992**, *192*, 237–242. [CrossRef]

179. *The Merck Index*, 12th ed.; Merck: New York, NY, USA, 1996.

180. Williams, M. *The Merck Index: An Encyclopedia of Chemicals, Drugs, and Biologicals*, 14th ed.; Merck Inc.: Kenilworth, NJ, USA, 2006; p. 2564.

181. Pettit, L.D.; Powell, K.J. *The IUPAC Stability Constants Database (SC-Database)*; Timble: Otley, Yorks, UK, 2008.

182. Ruprecht, J. *Dimaval®: Scientific Product Monograph*, 7th ed.; Heyl Chem.-Pharm Fabrik: Berlin, Germany, 2008.

183. Weigert, W.M.; Offermanns, H.; Degussa, P.S. D-Penicillamine—Production and Properties. *Angew. Chem. Int. Ed. Engl.* **1975**, *14*, 330–336. [CrossRef]

184. Nurchi, V.M.; Crisponi, G.; Lachowicz, J.I.; Jaraquemada-Pelaez, M.D.G.; Bretti, C.; Peana, M.; Medici, S.; Zoroddu, M.A. Equilibrium studies of new bis-hydroxypyrone derivatives with Fe^{3+}, Al^{3+}, Cu^{2+} and Zn^{2+}. *J. Inorg. Biochem.* **2018**, *189*, 103–114. [CrossRef]

185. Nurchi, V.M.; Crespo-Alonso, M.; Toso, L.; Lachowicz, J.I.; Crisponi, G. Chelation Therapy for Metal Intoxication: Comments from a Thermodynamic Viewpoint. *Mini-Rev. Med. Chem* **2013**, *13*, 1541–1549. [CrossRef] [PubMed]

186. Basinger, M.A.; Casas, J.S.; Jones, M.M.; Weaver, A.D.; Weinstein, N.H. Structural requirements for Hg (II) antidotes. *J. Inorg. Nucl. Chem.* **1981**, *43*, 1419–1425. [CrossRef]

187. Matsui, H.; Ohtaki, H. A potentiometric study on complex formation of cadmium (II) ion with 2-mercaptoacetic and 2-mercaptopropionic acids. *Polyhedron* **1983**, *2*, 631–633. [CrossRef]

188. Li, N.C.; Manning, R.A. Some Metal Complexes of Sulfur-containing Amino Acids. *J. Am. Chem. Soc.* **1955**, *77*, 5225–5228. [CrossRef]

189. Lenz, G.R.; Martell, A.E. Metal Chelates of Some Sulfur-Containing Amino Acids. *Biochemistry* **1964**, *3*, 745–750. [CrossRef] [PubMed]

190. Urbańska, J.; Kozlowski, H.; Kurzak, B. Polarographic and potentiometric study of ternary complexes of cadmium with penicillamine and histidine. *J. Coord. Chem.* **1992**, *25*, 149–154. [CrossRef]

191. Harris, W.R.; Chen, Y.; Stenback, J.; Shah, B. Stability constants for dimercaptosuccinic acid with bismuth (III), zinc (II), and lead (II). *J. Coord. Chem.* **1991**, *23*, 173–186. [CrossRef]

192. Casas, J.S.; Jones, M.M. Mercury (II) complexes with sulfhydryl containing chelating agents: Stability constant inconsistencies and their resolution. *J. Inorg. Nucl. Chem.* **1980**, *42*, 99–102. [CrossRef]

193. Avdeef, A.; Chemotti, A.R. Cadmium binding by biological ligands. Part 4. Polynuclear complexes of cadmium with 2,3-dimercaptopropane-1-sulphonic acid. *J. Chem. Soc. Dalt. Trans.* **1991**, *5*, 1189–1194. [CrossRef]

194. Strand, R.; Lund, W.; Aaseth, J. Complex formation of zinc, cadmium, and mercury with penicillamine. *J. Inorg. Biochem.* **1983**, *19*, 301–309. [CrossRef]

195. Rivera, M.; Zheng, W.; Aposhian, H.V.; Fernando, Q. Determination and metabolism of dithiol chelating agents. VIII. Metal complexes of meso-dimercaptosuccinic acid. *Toxicol. Appl. Pharmacol.* **1989**, *100*, 96–106. [CrossRef]

196. Chekmeneva, E.; Díaz-Cruz, J.M.; Ariño, C.; Esteban, M. Study of the Hg2+ binding with chelation therapy agents by differential pulse voltammetry on rotating Au-disk electrode and electrospray ionization mass-spectrometry. *Anal. Chim. Acta* **2009**, *653*, 77–85. [CrossRef] [PubMed]

197. Kõszegi-Szalai, H.; Paál, T.L. Equilibrium studies of mercury (II) complexes with penicillamine. *Talanta* **1999**, *48*, 393–402. [CrossRef]

198. Leung, B.O.; Jalilehvand, F.; Mah, V. Mercury (II) penicillamine complex formation in alkaline aqueous solution. *Dalt. Trans.* **2007**, *41*, 4666–4674. [CrossRef] [PubMed]

199. Strasdeit, H.; von Döllen, A.; Saak, W.; Wilhelm, M. Intracellular Degradation of Diorganomercury Compounds by Biological Thiols—Insights from Model Reactions. *Angew. Chem. Int. Ed.* **2000**, *39*, 784–786. [CrossRef]

200. Chekmeneva, E.; Díaz-Cruz, J.M.; Ariño, C.; Esteban, M. Complexation of Hg2+ with α-Lipoic and dihydrolipoic acids: Study by differential pulse voltammetry on rotating Au-Disk electrode and ESI-MS. *Electroanalysis* **2010**, *22*, 177–184. [CrossRef]

201. Zeini Jahromi, E.; Gailer, J.; Pickering, I.J.; George, G.N. Structural characterization of Cd2+ complexes in solution with DMSA and DMPS. *J. Inorg. Biochem.* **2014**. [CrossRef] [PubMed]

202. De La Gala Morales, M.; Ariño, C.; Díaz-Cruz, J.M.; Esteban, M. Study of the complexation of Pb (II) with meso-2,3-dimercaptosuccinic acid (DMSA) and 2,3-dimercapto-1-propanesulfonic acid (DMPS) using a bismuth-bulk rotating disk electrode. *Electroanalysis* **2014**, *26*, 1912–1919. [CrossRef]

UNIONE EUROPEA
Fondo Sociale Europeo

Ministero dell'Università e della Ricerca

PON
RICERCA
E INNOVAZIONE
2014 - 2020